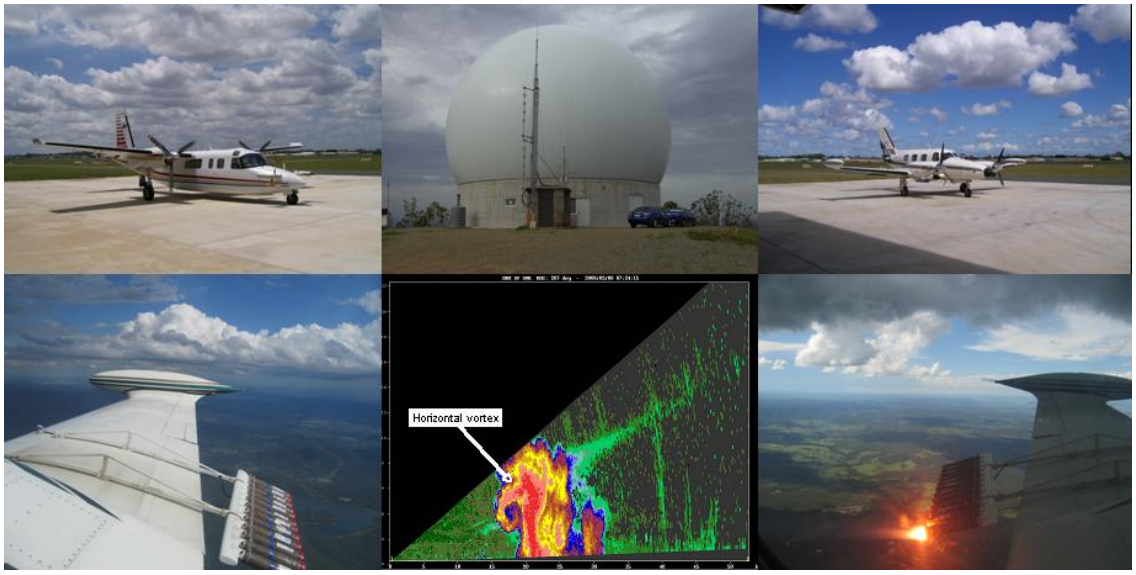

Interim report on

Southeast Queensland Cloud Seeding Research Program

22 July 2008

Australian Government
Bureau of Meteorology

Queensland Government

WEATHER MODIFICATION INC.

South African Weather Service

MONASH University

USQ
AUSTRALIA

NCAR

CSIRO

Interim report on

Southeast Queensland Cloud Seeding Research Program

Sarah Tessendorf, Roelof Bruintjes, Mike Dixon, Matt Pocernich, Ed Brandes, Jim Wilson, Rita Roberts, Kyoko Ikeda, Duncan Axisa, Ian Craig (USQ), Justin Peter (Monash), Peter May (BOM), Tom Keenan (BOM), Michael Manton (Monash), Roger Stone (USQ), David Yates, Erin Towler, V. Bringi (CSU), M. Thurai (CSU)

Research Applications Laboratory

NCAR
National Center for Atmospheric Research

2008-07-22

Report prepared by NCAR for the
State Government of Queensland

This research is in response to requirements and funding by the State Government of Queensland. The views expressed are those of the authors and do not necessarily represent the official policy or position of the Queensland Government.

TABLE OF CONTENTS

EXECUTIVE SUMMARY

Water stresses are occurring in Southeast Queensland. In order to assess the feasibility of any future precipitation enhancement potential in clouds in the Southeast Queensland region, it is extremely important to obtain observations in a well-designed measurement program. Aerosol and microphysical measurements, in particular, can help determine if seeding could be beneficial and also help determine what the optimal seeding method would be with regards to potential for enhancing precipitation in local clouds.

The potential for such manmade increases is strongly dependent on the natural microphysics and dynamics of the clouds that are being seeded (in this case microphysics means the size and concentration of water droplets and ice inside clouds). These factors can differ significantly from one geographical region to another, as well as during and between seasons in the same region. In some instances, clouds may not be suitable for seeding, or the frequency of occurrence of suitable clouds may be too low to warrant the investment in a cloud seeding program. Both factors need to be evaluated from a climatological perspective. It is therefore important to conduct preliminary studies on the microphysics and dynamics of the naturally forming clouds prior to commencing a larger, operational experiment. It is also important to conduct hydrological studies relating rainfall with river flows and reservoir levels, and to determine hydrological regions where reservoir catchments are most efficient. Seeding could then be optimized by preferentially targeting the most efficient watersheds.

The following is a summary of key preliminary results derived from the analysis of data collected during the 2007-2008 season in Southeast Queensland.

Climatology:

1. This has been a unique year for Queensland rainfall with the strong La Nina situation and many parts of Queensland subjected to flooding. (Usually most pronounced from Late December to March).
2. The current year is not representative of the previous years in terms of rainfall (normal years and El Nino years).
3. La Nina years are usually associated with abundant moisture through deep levels of the atmosphere and above normal rainfall with locally heavy rainfalls.
4. Because the air during La Nina years usually comes from the Pacific Ocean, it is also associated with very clean air resulting in generally more efficient natural rain processes.
5. During the early part of the rainy season (October to December), clouds are usually different with more deep convective cores. All the major flooding events this year took place between December and February.

Radar summary:

1. The measurement season was characterized by a variety of cloud systems (deep convective, shallow convective and deep stratiform). The shallow convective systems were the most predominant, while the deep convective and stratiform systems occurred on fewer days.
2. Although the shallow convective systems occurred on more days than the deep convective and stratiform systems, the total seasonal rainfall was about equally split

between the two types indicating the deep cloud systems usually produced more rain than the shallow convective system if individual systems are compared.

3. Shallow convective showers associated with the easterly trade winds were the most frequent cloud systems experienced during the last season. The systems consisted of shallow convective cloud systems that still could produce >50 dBZ echoes as measured by the radars and produce locally light to moderate rainfalls.
4. Because of the higher frequency of occurrence of the shallow convective systems they were better and more often observed than the other cloud systems. Due to their shallow nature they were usually shorter lived than the deep convective systems. On the other hand they provided the opportunity to study the warm rain process in a relatively simple dynamic framework.

Aircraft measurements:

1. Although the initial measurements seem to point to a very clean environment, aerosol measurements as measured by the Differential Mobility Analyzer (DMA) instrument seem to indicate higher concentrations of aerosols more in agreement with the cloud droplet concentrations that were measured in all cloud systems during the field measurement period.
2. Based on the DMA and cloud droplet concentration measurements, the clouds seem to be more of a modified maritime and continental nature than purely maritime as was originally anticipated.
3. Cloud droplet concentrations in clouds were similar to those observed in the South African and Mexican experiments in the 1990's ranging between 400 and 600 cm^{-3}. Hygroscopic randomized seeding experiments indicated positive effects of seeding on rainfall in those experiments. The South African and Mexican experiments only focused on deep convective systems.
4. Based on these conditions and the previous results from South Africa and Mexico, deep convective systems could be amenable to hygroscopic seeding to enhance rainfall (a few occasions in December, January and February). The enhancement factor should be dependent on the cleanness of the atmosphere and may increase with more polluted air. Only a few deep convective systems were studied this past season and even fewer were seeded because of seeding restrictions in place due to flooding. We do not have sufficient data at this time to assess the seeding effects on deep convective systems.
5. The deep stratiform systems (La Nina types) as experienced during several days in January and February are generally efficient naturally and cloud seeding may only make a marginal difference. Aircraft measurements have indicated that only on some occasions supercooled liquid water existed in clouds during these conditions.
6. Cloud bases during the shallow convective systems were usually between 15 and 20 °C and cloud tops between +10 and 0 °C with some tops reaching to -10 °C. These clouds always produced rain through a "warm-rain/condensation-coalescence" process and no ice process was observed in these clouds. Hygroscopic seeding attempts to create a more efficient "warm-rain" process.

Randomized experiment:

1. Because of their more frequent occurrence randomized seeding experiments using hygroscopic seeding was most often conducted in these shallow cloud systems. Although 62 storms were selected for randomized seeding, only 27 cases could be analyzed as part of the statistical analyses. The reasons for the smaller sample are explained in the report.
2. It is clear that due to the small sample size none of the results are statistically significant and no definitive conclusions can be drawn from the results. Having said this, however, it is important to note that similar tendencies observed in the Mexican data after such a small sample set during the first year are also observed in the current sample set. These tendencies, although not statistically significant, are:
    - More seeded storms had larger precipitation fluxes after seeding than unseeded storms.
    - More seeded storms had larger mean values of precipitation flux after seeding than unseeded storms.
    - More seeded storms tended to live longer than unseeded storms.
3. Although these results are not statistically significant and still could be due to chance alone, it is important to note that the responses are very similar to those observed in previous hygroscopic seeding experiments.
4. These preliminary results provide encouragement to continue with the experimentation and further analyses that are currently ongoing.

1. INTRODUCTION

Certain parts of Australia have been experiencing a severe drought over the past few years. In response, the Queensland government has decided to explore the potential for cloud seeding to enhance rainfall and an initial feasibility study took place in the Brisbane area December 2007-March 2008. Several comprehensive issues arise when considering technology within the context of rainfall enhancement: How are water resources currently used? Are the existing hydrological studies sufficient for assessing rainfall contributions or are more directed hydrological studies required? How does a weather modification (cloud seeding) program fit into water resource management? What are the ultimate economic benefits? Is the infrastructure of weather and hydrology observations adequate for assessing these and similar issues? Answers to these questions ought to shape the goals envisioned for Queensland, of which cloud seeding is a part.

The potential for such man-made increases in rainfall using cloud seeding is strongly dependent on the natural microphysics and dynamics of the clouds that are being seeded. Microphysics refers to the size and concentration of water droplets and ice particles inside clouds. Dynamics refers to the forces affecting air motions in and around clouds. Microphysics is in turn dependent on background aerosol levels, because it is the aerosol particles that attract water vapor to form cloud droplets, and in cold clouds, ice particles. Furthermore, the types and concentrations of aerosol particles can be influenced by trace gases (i.e., air pollution). Given these dependencies, the microphysics of clouds can differ significantly from one geographical region to another, and even between seasons in the same region. In some instances, clouds may not be suitable for seeding, or the frequency of occurrence of suitable clouds may be too low to warrant the investment in a cloud seeding program. Both factors need to be evaluated in a climatological sense or at least they should be evaluated over a sufficient period of time to account for natural variations. This requires conducting preliminary studies on atmospheric aerosols, pollution levels, and cloud microphysics and dynamics prior to commencing a large cloud seeding effort. If the targeted measurements and additional data show sufficient evidence that clouds would be positively affected by cloud seeding, the cloud seeding technique(s) should then be evaluated using a randomization procedure to statistically demonstrate that the seeding method is effective and measurable. This approach is similar, for example, to what is commonly done in medical trials with a new drug. Such a preliminary study was conducted in the Southeast Queensland region December 2007-March 2008, and an initial randomized study was also performed. This randomized study needs to be expanded and further measurements are still needed, especially in the early summer months of October-December.

The Queensland program provides a unique opportunity to address some of the outstanding issues such as growth of hygroscopic particles into drizzle drops and glaciation and graupel growth in silver iodide seeded clouds identified in previous rainfall enhancement experiments. The reason for this unique opportunity is the existence of a dual polarization, dual wavelength advanced weather radar (called CP2) that includes some of the latest technologies. This type of advanced radar has been identified in a report (National Academy of Sciences, 2003) by the U. S. National Research Council (NRC) of the National Academy of Sciences (NAS) as essential to address some of the outstanding questions related to the assessment of rainfall enhancement. The CP2 was acquired by the Bureau of Meteorology (BOM) as part of a joint agreement with the National Center for Atmospheric Research (NCAR) continuing

previous joint research activities. The considerable radar expertise within BMRC and NCAR is a major factor contributing to this program. Along with additional scientific expertise available in Australia through Monash University, the University of Southern Queensland, and CSIRO, and together with NCAR's expertise in cloud seeding, a solid basis exists for a world-class observational program supporting cloud seeding activities in the region. It should be noted that the particular combination of scientific expertise and observing capacity has never been available to previous weather modification activities and fills important gaps in such programs. Hence the potential exists for a unique world class scientific program to evaluate the effectiveness of weather modification in Southeast Queensland.

Scientists from the NCAR and the South African Weather Services (SAWS) in collaboration with the aforementioned Australian groups conducted a feasibility study for rainfall enhancement via cloud seeding in a summer rainfall regime in Southeast Queensland in Australia. The feasibility study included a range of measurement systems, some using novel technologies. The collaborative work entailed all necessary aspects of the project, including: airborne chemistry, aerosol, and cloud physics measurements; assessment and enhancement of weather radar capabilities (additional hardware and software for collection of quantitative data); and analyses of field data. These efforts build on the experience gained from programs in other parts of the world.

This report describes the preliminary results of the scientifically-based program conducted to evaluate the feasibility for using cloud seeding technology, specifically hygroscopic seeding, to enhance rainfall. The following chapters include preliminary climatological studies, summaries of the feasibility study operations, and preliminary results from aerosol, cloud, precipitation process, and cloud seeding assessment studies.

2. PROJECT OBJECTIVES

Based on previous Australian and other studies that demonstrated the importance of thoroughly designing future experiments using knowledge of the meteorology (trace gases, aerosols, clouds and rainfall) in the region, the Queensland program was designed to be conducted in several phases.

2.1 PHASE I

Pre-field phase climatological and meteorological studies (based on radar, satellite and other meteorological information) were conducted to define the overall characteristics of precipitation and its relation to the environment. This was followed by an initial field phase including radar and airborne observations (trace gases, aerosols, and cloud physics) to gain additional knowledge about cloud and precipitation characteristics in the Brisbane region. These studies enable assessment of the potential for seeding and evaluation of the effectiveness different seeding techniques. Experimental seeding and some randomized seeding was also done during this period. Information from such a Phase I study helps guard against repeating mistakes made in previous experiments around the world. This phase also involved implementing upgraded infrastructure, particularly weather radar and radar data display capabilities that are necessary for research and operations. The Phase I study took a full season of collecting data and we are in the data analysis portion of this phase at present. Particularly important during this phase was the use of the polarimetric and Doppler radar data to evaluate the affects cloud seeding may have on cloud dynamics.

The scientific objectives for Phase I were to make preliminary assessments of:

1) the climatological characteristics of precipitation and in particular the frequency of clouds suitable for seeding
2) the approaches necessary to obtain robust estimates of precipitation amount and retrieve microphysical properties of the clouds
3) the effect of cloud seeding on storm microphysics and dynamics. This includes precipitation particle types, number and size of precipitation particles and horizontal and vertical air motions
4) evidence from cloud seeding of increased secondary convective storm initiation
5) evidence of precipitation enhancement from cloud seeding

2.2 PHASE II

Based on the results of the Phase I studies, a randomized experiment will be designed to quantitatively assess the possible increases in precipitation due to seeding and to assess the impacts on water resources in the region. This experiment would use the most appropriate statistical methods in conjunction with numerical model simulations. This phase could take several years, depending on conditions and opportunities for cloud seeding but may need three or four years to complete.

2.3 PHASE III

Based on the results from Phase II, a possible operational seeding program will be designed.

Other possible side benefits of the program are:

- training and technology transfer that could be applied to other applications such as weather forecasting, aviation meteorology, air pollution monitoring and forecasting, etc.
- air pollution assessment and associated impacts over Southeast Queensland (health, visibility, climate)
- aviation forecasting of convective weather
- hydrology studies
- water resources
- enhancing research infrastructure (human resources and technology)
- updated and enhanced infrastructure for all meteorological and air quality applications and the ability to use these new tools.
- improved understanding of convective processes

3. PERSONNEL, TRAINING

3.1 OVERVIEW

There are numerous components to a successful field project, including forecasting, operational decision making, performing cloud seeding, performing the physical studies, maintaining the instrumentation, and doing post-processing. Various personnel were involved in these efforts, and specific duties are described in detail in the Operations Plan (see Appendix).

Key duties performed included: Operations Director, Radar Operator, Forecasters, Aircraft and Instrument Technicians, Pilots, and Data Managers. During the 2007-2008 field season NCAR personnel were responsible for the day-to-day operations.

3.2 PERSONNEL

3.2.1 Operations Director

Roelof Bruintjes and Sarah Tessendorf acted as the primary Operations Directors, with brief periods of leave covered by Mike Dixon. The Operations Director worked from the Operations Center, managing and directing the day-to-day operations and personnel. Decisions were made after assessment of the forecast and the designation or code for the day, including calling for aircraft operations (coordinating with the personnel at the Archerfield hangar), guiding the aircraft to suitable areas/clouds for investigation and seeding, and ensuring that proper data collection was taking place. The Operations Director worked closely with all personnel, particularly those at the Archerfield hangar and CP2 Operations Center.

3.2.2 Radar Operations

The Operations Director oversaw radar operations, however, at least one radar scientist was on site to handle the responsibility of changing scanning strategies according to the mission objectives. The radar scientist was also responsible for monitoring the development of clouds/storms, as well as the progress of the current radar objective/mission. The radar scientists during the 2007-2008 project included Justin Peter, Jim Wilson, Ed Brandes, Rita Roberts, Mike Dixon, Peter May, and Alan Seed. The radar hardware and software were regularly maintained by the CP2 radar engineer, Ken Glasson. This included periodic maintenance, calibration checks, general troubleshooting, and radar data archival.

3.2.3 Forecaster

Justin Peter provided the daily forecasts, which resulted in designating the flight plan options for the day. The plan for the day was communicated by the Operations Director to the pilots and crew at the Archerfield hangar by around 10 AM each day and plans for flights were decided at this time. Changes in meteorological conditions were monitored throughout the day and occasionally the plan was adjusted to reflect significant changes. Besides the daily forecast, outlooks for the following 2-3 days were issued by the forecaster to assist in staffing decisions for future operations. Another important function of the forecaster was to archive weather data, such as upper air soundings, synoptic charts, satellite imagery, and local meteorological observations.

3.2.4 Pilots

Pilots experienced in cloud seeding operations are critical to the successful implementation of the operations plan. For the SAWS research aircraft, Ret Orsmond, a pilot with a long history of cloud seeding operations, was available to the project for carrying out research flight operations along with his crew of pilots (Hans Krueger, Gary Wiggins, and John Hingst). The MIPD/WMI pilots conducted the primary cloud seeding operations, and included experienced in cloud seeding operations pilots from WMI (Jim Carr) and from MIPD (Neville O'Donnell, Paul Brady, and Greg Choma). Pilots were also responsible for taking in flight notes and submitting their flight notes/reports to the Data Managers on a daily basis.

3.2.5 Aircraft and Instrument Maintenance

Periodic calibration checks, aircraft instrument maintenance, and general troubleshooting of aircraft instrumentation were performed by the instrument technician, Steve Edwards. Aircraft maintenance was monitored and performed on each aircraft by Harold McGarry (ZS-JRA) and Rafe Zerby (N747RE). An instrument scientist flew on each research flight, to operate and monitor instrument function during flight. These personnel included Stephen Broccardo, Xolile Ncipha, and Shaazia Bhailall.

3.2.6 Data Managers

Data management was distributed among all the personnel, under the direction of the Operations Director. An important part of this effort involved regular reporting of the instrument and data status to the Operations Director and throughout the project staff. Ian Craig and Li Fitzmaurice were the primary contacts for the gathering and archiving of project data. Aircraft operations report writing duties were shared by Ian Craig, Martin van Nierop, Nico Kroese, Karel de Waal, and Stuart Piketh. Radar report writing duties were shared by the Radar Scientists and Operations Director. Roelof Burger and Duncan Axisa provided assistance with aircraft data processing and quality checks.

3.3 TRAINING

A ground school was led by Roelof Bruintjes in November 2007 to go over the operational procedures for the field portion of the project.

A short course on cloud physics instrumentation was led by Roelof Bruintjes in February 2008 at the Archerfield hangar. The purpose of this short course was to train the personnel at the hangar to process and quality control the collected aircraft data while in the field. This course helped train the flight scientists and others interested on each of the aircraft instruments, including how they operate, data checks, and calibration. The participants wrote reports at the end of this course on each of the instruments on board the ZS-JRA research aircraft.

Ian Craig (USQ) has been a scientific visitor at NCAR since April 16, 2008. During this time he has assisted with the post-processing and data analysis for the Queensland project. He has been under the guidance and training of Roelof Bruintjes, Sarah Tessendorf, and Duncan Axisa (Figure 3.1).

On-site training in radar meteorology and the use of the radar software was provided by NCAR personnel to scientists and engineers at the CP2 radar site prior to and during the field project.

Figure 3.1. Ian Craig with Duncan Axisa at NCAR, discussing DMA data from the Queensland project.

4. FACILITIES

4.1 AIRBORNE MEASUREMENTS

Two aircraft were used during the project: one was primarily a research aircraft, but also could serve as a secondary seeding aircraft if conditions warranted; the second aircraft was the primary seeding aircraft. The research aircraft was the South African Weather Service (SAWS) Aerocommander (ZS-JRA; call sign SEEDA1). It carried flare racks on each wing (10 burn-in-place hygroscopic or silver iodide flare capacity each), and had a full suite of atmospheric instrumentation (see section 4.1.1). The primary seeding aircraft was the Weather Modification Inc (WMI)/MIPD Piper Cheyenne II (N747RE; call sign WXMOD). It carried flare racks on each wing (12 burn-in-place hygroscopic or silver iodide flare capacity each) and an undercarriage ejectable silver iodide flare rack (306 flare capacity).

Aircraft operations were based out of Archerfield Airport, where daily weather and flight planning briefings were held for the pilots. During flights, operations were coordinated via radio communications between the pilots and the Operations Director at the CP2 radar facility and operations center.

4.1.1 Instrumentation

The research aircraft had a suite of instruments capable of taking trace gas, aerosol, and microphysical measurements in the Brisbane region, and in treated or untreated clouds (see Table 4.1). These instruments were monitored by an in-flight scientist, and maintained by an instrument technician to ensure all instruments were functioning properly.

Table 4.1. List of instrumentation on SEEDA1 (ZS-JRA Aerocommander).

Instrument	Purpose/Comment	Range
	State Variables	
Rosemount Temperature, Static and Dynamic Pressure, and GPS parameters	Temperature, pressure, altitude, TAS, and location – recorded on telemetry box and on the data system (SAWS)	*multiple*
EG&G Dewpoint sensor (optional)	Moisture content (NCAR)	-50 to 50 C
Vaisala Temperature and Relative Humidity	Secondary temperature and moisture content (SAWS)	-50 to 50 C, 0-100%
	Cloud Physics	
PMS FSSP	Cloud droplet spectra (SAWS)	.5-47 μm
DMT SPP-100 FSSP	Cloud droplet spectra	.5-47 μm
PMS 2D-C	Small precipitation particle size, concentration and shape (SAWS)	25-800 μm
PMS 2D-P	Large precipitation particle size, concentration and shape (SAWS)	200 -6400 μm
PMS Hot-wire (King) Liquid Water Content Probe	Liquid water content (SAWS)	0.01 – 3 g m^{-3}
DMT CAPS probe	Aerosol through precipitation size spectrometer; LWC; static and dynamic pressure; temperature (NCAR)	*multiple*
	Aerosols	
DMT CCN Counter	Cloud condensation nuclei concentration and spectra (WITS)	Depends on Supersaturation
Texas A&M DMA	Fine mode aerosol spectra and concentration (NCAR)	0.01 to 1 μm

PCASP	Aerosol concentration and spectra (WITS)	0.1 to 3 μm
	Trace Gases	
TECO SO_2 (43c)	Sulphur dioxide (WITS)	0-100 ppm
TECO CO (48c)	Carbon monoxide (WITS)	0-10,000 ppm
TECO O_3 (49i)	Ozone (WITS)	0-200 ppm
TECO NO_y (42c)	Nitrogen oxides (NCAR)	0-100 ppm
	Cloud and Situation Imagery	
Digital still camera	To show development of clouds and treatment situations for historical purposes	N/A

4.1.2 Aircraft data quality

Data quality checks on the aircraft instrument data are ongoing. To date, quality checks have been performed in a qualitative manner on the cloud drop size measurements from the FSSP, SPP-100, and Cloud Aerosol Spectrometer (CAS; part of the CAPS probe). Figure 4.1 and Figure 4.2 show comparisons between the results obtained using these three different instruments aboard ZS-JRA. These comparisons show broad agreement in terms of the modal droplet size and number concentration of that model size bin, especially in the sample from 16 March 2008 (Figure 4.2). These comparisons will be performed more quantitatively as we continue to quality control the data. Data from all other instruments are currently undergoing further quality checks as well.

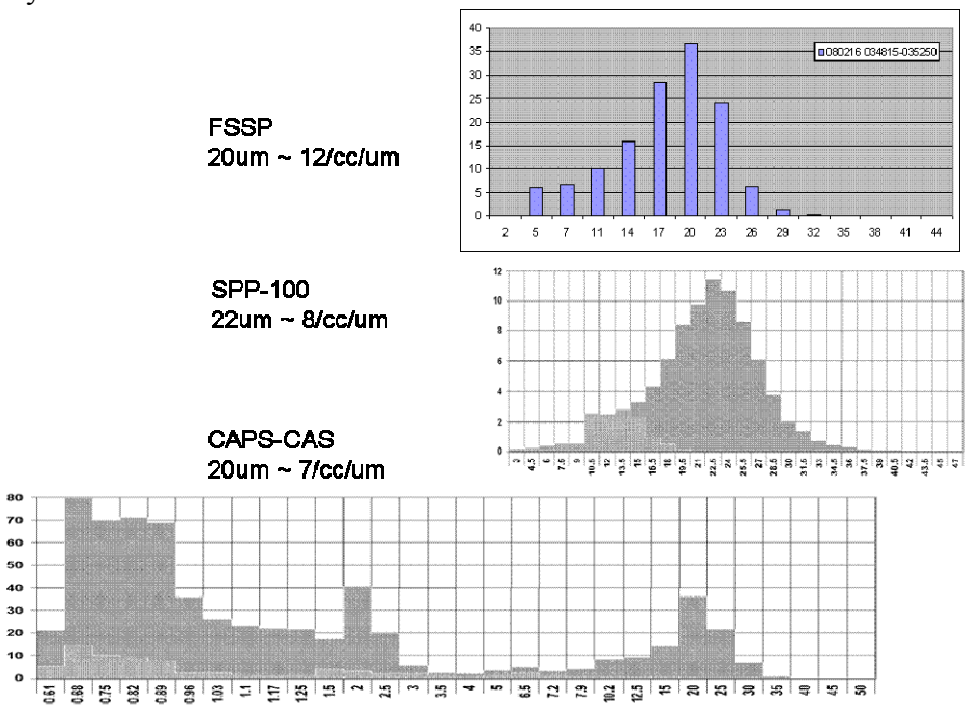

Figure 4.1. Qualitative graphical comparison of the results from three different instruments aboard ZS-JRA used to measure cloud droplet size during the period 034815-035250 on 16 February 2008. From top to bottom are the drop size distributions from the FSSP, the SPP-100 and the CAPS CAS. The modal droplet size and number concentration in that modal size bin are listed for each instrument.

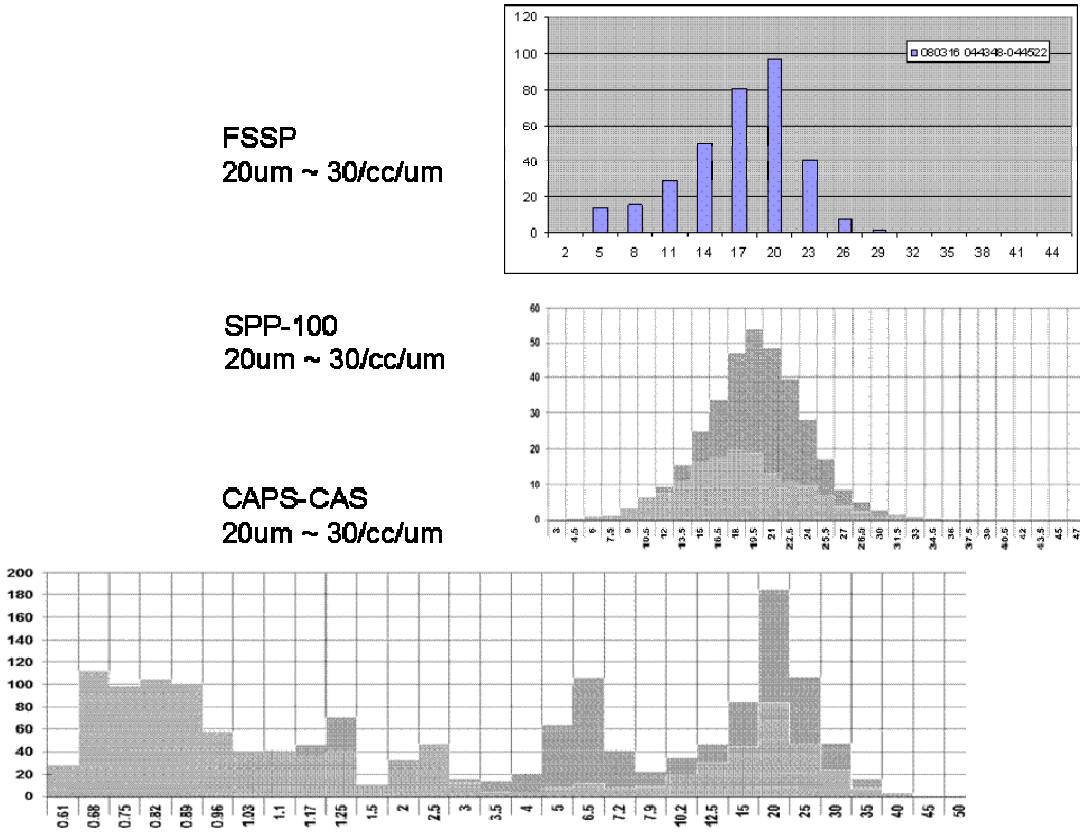

Figure 4.2. Same as Figure 4.1, except for the period 044348-044522 on 16 March 2008.

4.2 RADAR MEASUREMENTS

4.2.1 BOM operational radar network

The Australian Bureau of Meteorology (BOM) runs a large network of weather radars, predominantly around the coast of Australia. A number of these radars cover the area around Brisbane. These are listed in Table 4.2.

Table 4.2. BOM radars in the Brisbane region

Site	Latitude (deg)	Longitude (deg)	Type	Wavelength	Scan interval
Grafton	29.620 S	152.970 E	WSR 74S	10 cm	10 min
Moree	29.500 S	149.850 E	WF100C	5 cm	10 min
Mt Stapylton	27.718 S	153.240 E	Gematronik Doppler	10 cm	6 min
Marburg	27.61 S	152.54 E	EEC WSR 74S	10 cm	10 min
Mt Kanigan	25.957	152.577	EEC DWSR 8502S	10 cm	10 min

Some of the BOM radars scan a full volume once every 10 minutes, while others do this once every 6 minutes. In order to get more frequent data for this project, the Bureau modified the

scanning strategy for the Mount Stapylton radar to once every 6 minutes. This was important for dual-Doppler coordination with the CP2 research radar.

4.2.2 CP2 research radar

The CP2 radar, originally developed and owned by NCAR, was obtained by the BOM 2 years ago and set in Redbank Plains to the southeast of Brisbane. CP2 is actually two co-located radars, the main radar being an S-band (10 cm) unit and the smaller radar being an X-band (3 cm unit). The X-band antenna piggy-backs on the main S-band antenna, and is designed to view the same sample volume as the S-band radar. The technical characteristics of CP2 are described by Bringi and Hendry (1990) and summarized in Table 4.3.

Table 4.3. Technical Characteristics of the CP2 radar

Characteristic	CP2 S-Band	CP2 X-Band
Wavelength (cm)	10.7	3.2
Peak Power (kW)	1200	200
Pulse length(μs)	0.15-1.2	1.0
PRF (s-1)	<1700	<1000
Antenna Type	Centre feed paraboloid	Two Cassegrain paraboloids
Feed Type	Potter horn	Rectangular waveguide
Beamwidth (0)	0.93	0.94
Azimuth coverage (0)	360	360
Elevation Coverage (0)	90	90
Polarizations radiated	LIN H, LINV	LIN H
Simultaneous 2 channel reception	No	Yes
Polarization Received	Copolar to TX	LIN H & LIN V
Max Sidelobe level (dB)	-21	~-30
Max Antenna Linear X-POL lobes (dB)	-21	-36
Polarisation Control Method	Ferrite Switch	NA
Polarization Control rate	Pulse by pulse	NA
Channel to Channel Isolation (db) ex Antenna	>30	>30
Doppler Capability	Yes	No
Number of Range Gates	1024	1024
Range Resolution (m)	>30 typically 150	>30 typically 150
Polarization Quantities measured	ZHH, ZDR, Φdp, ρHV	Z, LDR,

CP2 is capable of measuring Doppler velocity and dual-frequency reflectivity at S- and X-band along matched beams. Polarimetric variables are also derived at S- and X-band. Further details of CP2 are summarized by Keeler et al. (1984) and the three co-aligned antennae configuration is shown in Figure 4.3.

Figure 4.3. CP2 S-band and X-band antennae

The CP2 system was subjected to major refurbishment work at NCAR. As part of the joint activities all drive gearboxes were refurbished, a new transmitter focus coil assembly power supply was installed, along with a new ceramic thyatron with associated solid state trigger drive circuitry. Following system acceptance tests, CP2 was shipped to Australia for installation with spare modules and components for all updated systems. A modern digital receiver and signal processing system is employed based on the NCAR PIRAQ III signal processing unit along with a new antenna control and data display system.

The site for the radar comprises the radar antenna and pedestal installed on a concrete foundation with a pressurized inflated fabric radome, as shown in Figure 4.4. The thirteen ton (plus) antenna structure requires significant reinforced concrete foundations on stable ground. The radome must remain pressurized at all times and this is maintained by a primary air blower, with a second higher capacity blower used to add extra pressurization in the event of high winds. The receiver and transmitter are located underneath the pedestal along with office space. This configuration minimizes waveguide runs and subsequent losses. Communications to the facility will be in the form of normal telephone and high-speed internet access (1Mbs) to provide control of the radar and transmission of various data and products.

Figure 4.4. CP2 site infrastructure at Redbank Plains. Antenna and pedestal are within an inflated radome mounted over housing for office, storage and transceiver.

The CP2 facility is supported by BOM personnel who visit the site regularly for routine maintenance and repairs. When unattended, CP2 operates in volume-scan mode synchronized with Mt. Stapylton, producing a volume once every 6 minutes. During operations, CP2 also operated in sector-scan mode, in which a segment of the 360-degree circle is scanned, or Range-Height Indicator (RHI) mode, in which the antenna scans vertically through a storm.

4.2.3 Data collection

Data from operational radars

The data from each BOM radar is stored in the RAPIC (RAdar PICture) data format. Each RAPIC file contains data from a single radar volume. The RAPIC data is transmitted from each radar site to a number of central BOM data servers. The BOM set up software to copy RAPIC data from the radars listed in Table 4.2 from the Brisbane office to the CP2 radar operations center. NCAR software running at CP2 converts the RAPIC data into NCAR Meteorological Data Volume (MDV) files.

Data from CP2

The data from the CP2 radars is obtained using the NCAR PC-based Integrated Radar Acquisition (PIRAQ) system. This PIRAQ system produces radar time series data that is transmitted to computers running the NCAR TITAN software system, which then computes the radar fields from the time series and stores the data in MDV files.

4.2.4 Merging data from single radars into a combined mosaic

In order to get the 'big picture' about the weather in the Brisbane area, data from the individual operational radars were combined into a regional 'radar mosaic'. Of the five operational radars, four were operated on a 10-minute cycle, and one (Mt. Stapylton) was operated on a 6-minute cycle. Therefore it was decided to create a mosaic once every 10 minutes. To create the mosaic, the data from each radar was interpolated from its respective radar space grid to a common Cartesian grid, and the merged reflectivity field was then calculated by taking the maximum reflectivity at each grid point.

Figure 4.5 and Figure 4.6 show the extent of the data in the merged radar grid for heights of 1.0 km MSL and 1.75 km MSL respectively. Because of earth curvature effects, radars are not

able to ‘see’ weather close to the ground at longer ranges. Therefore, full coverage is only obtained at some finite height above the ground, in this case 1.75 km.

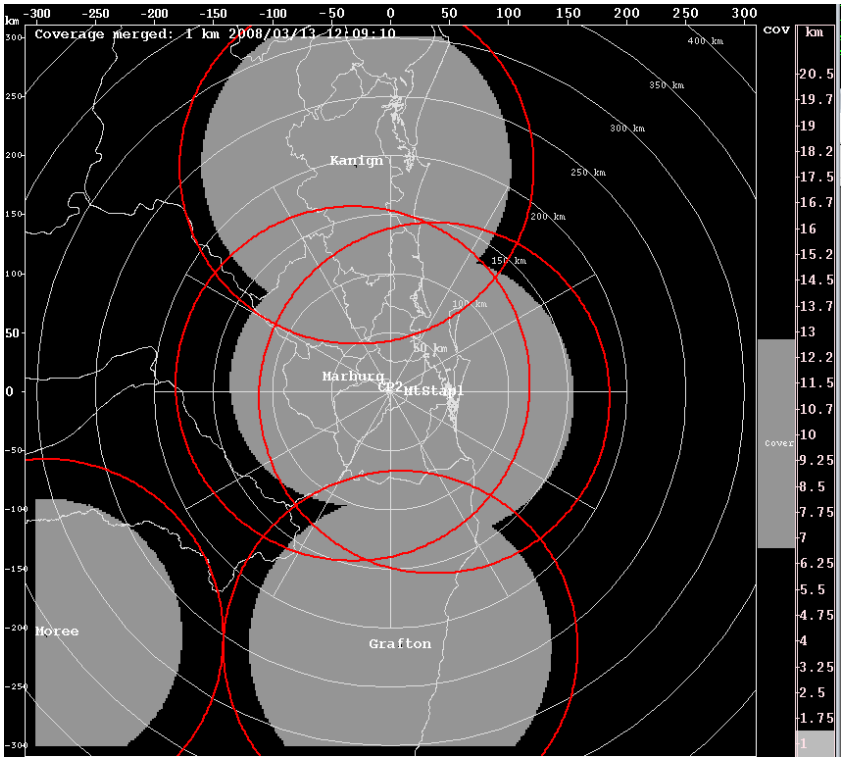

Figure 4.5. Coverage of the merged BOM radars, at a height of 1.0 km. MSL.

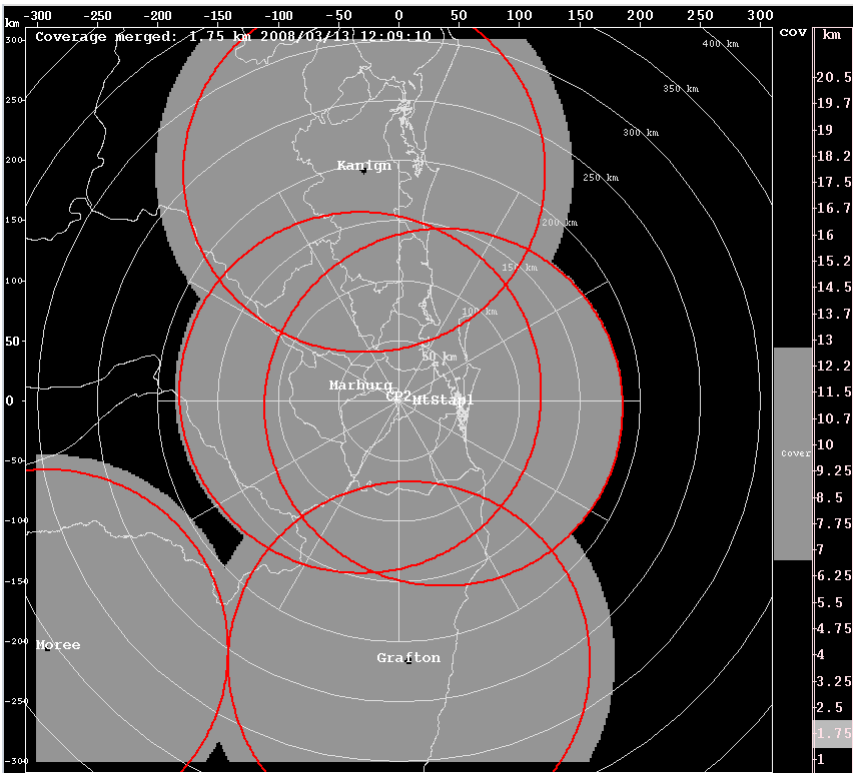

Figure 4.6. Coverage of the merged BOM radar, at a height of 1.75 km MSL.

4.2.5 Merged data example

Figure 4.7 shows an example of the merged radar coverage of storms that occurred on 2008/02/05 just before 0700 UTC. The storms at that time were quite widespread and were detected by all 5 operational radars. Figure 4.8-Figure 4.12 show the storms as seen by each of the 5 radars individually.

The merged data is a three-dimensional grid which covers an area of 600 km by 600 km centered on the CP2 radar site. The lowest grid plane in the gird is at 1 km MSL and the top plane is at 10.5 km MSL. The resolution of the grid is 0.75 km in each of the three coordinate directions (x, y, z).

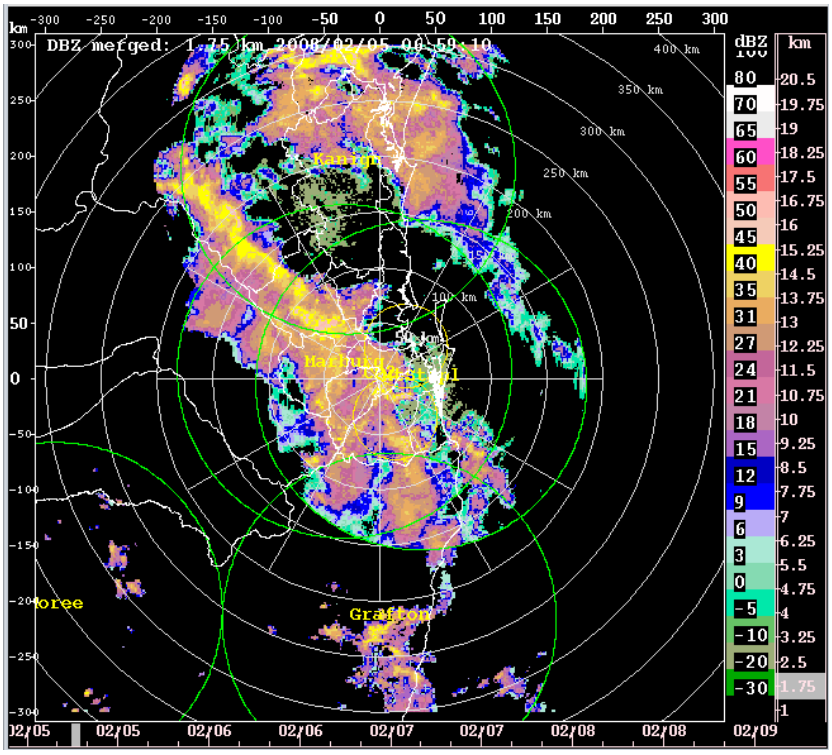

Figure 4.7. Example of merged radar coverage, 2008/02/05 06:56:08

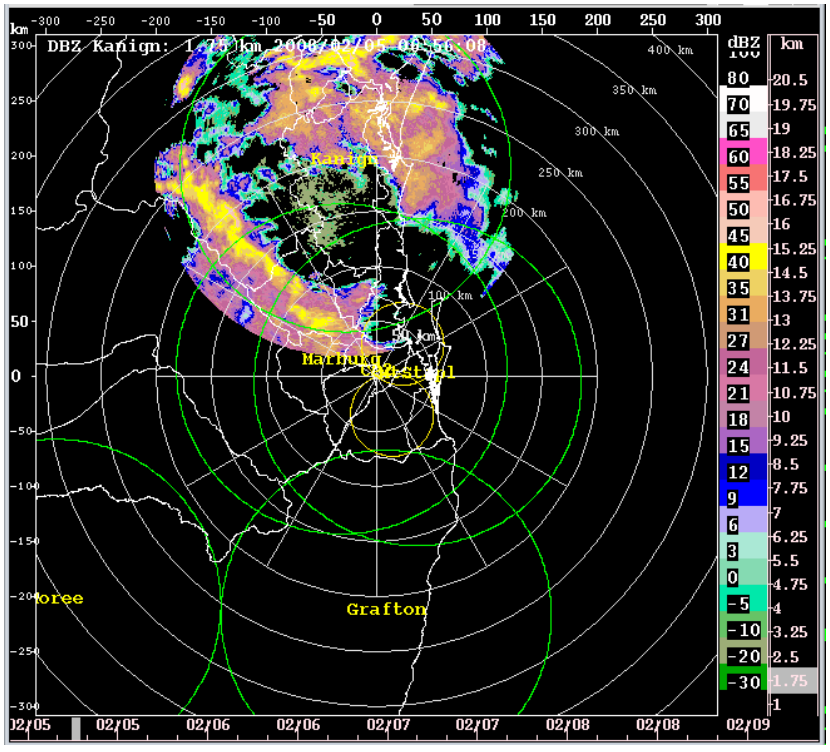

Figure 4.8. Example of radar coverage from Mt. Kanigan, 2008/02/05 06:56:08

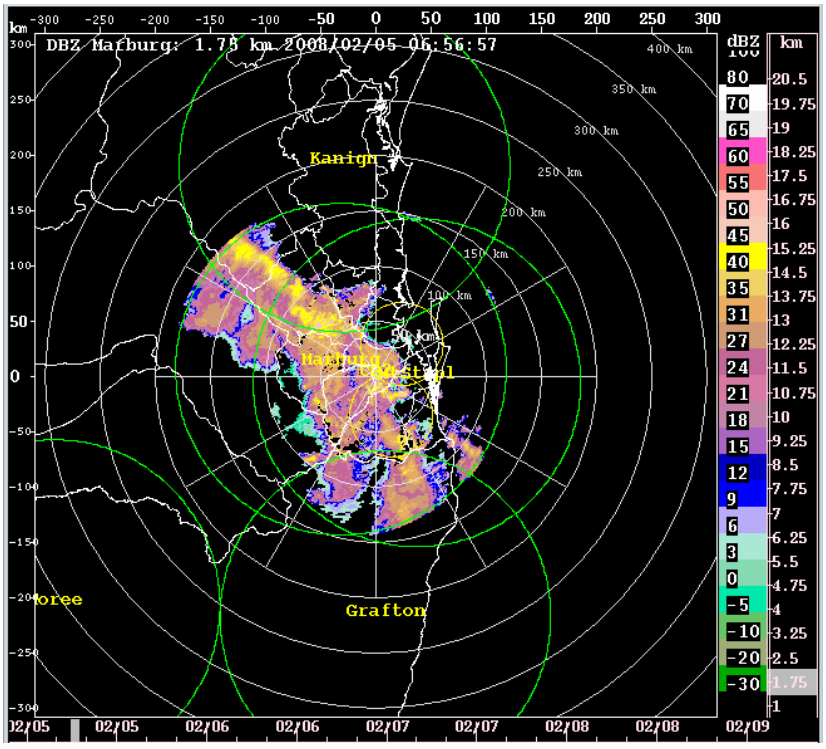

Figure 4.9. Example of radar coverage from Marburg, 2008/02/05 06:56:08

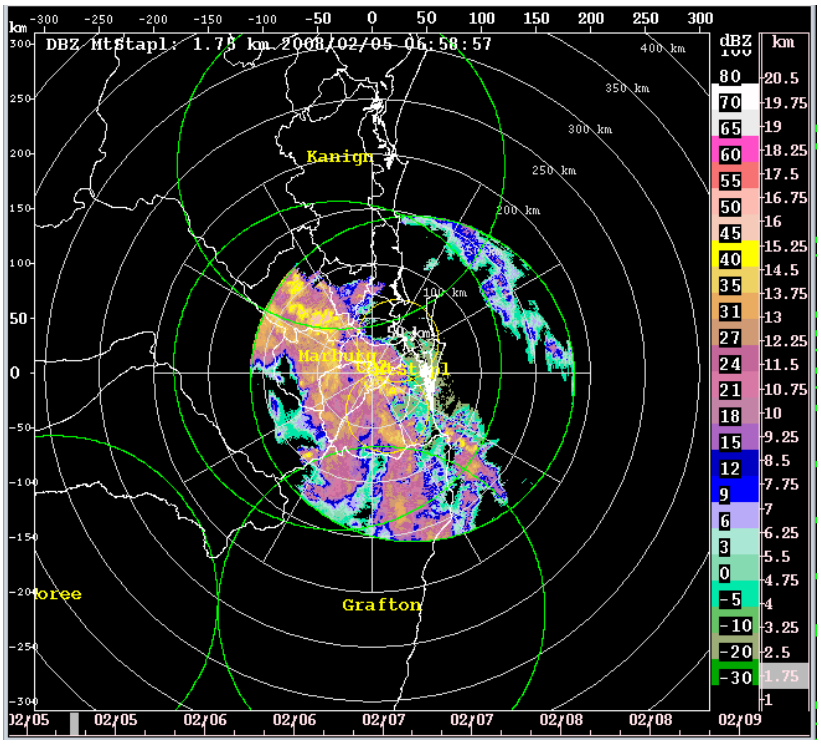

Figure 4.10. Example of radar coverage from Mt Stapylton, 2008/02/05 06:56:08

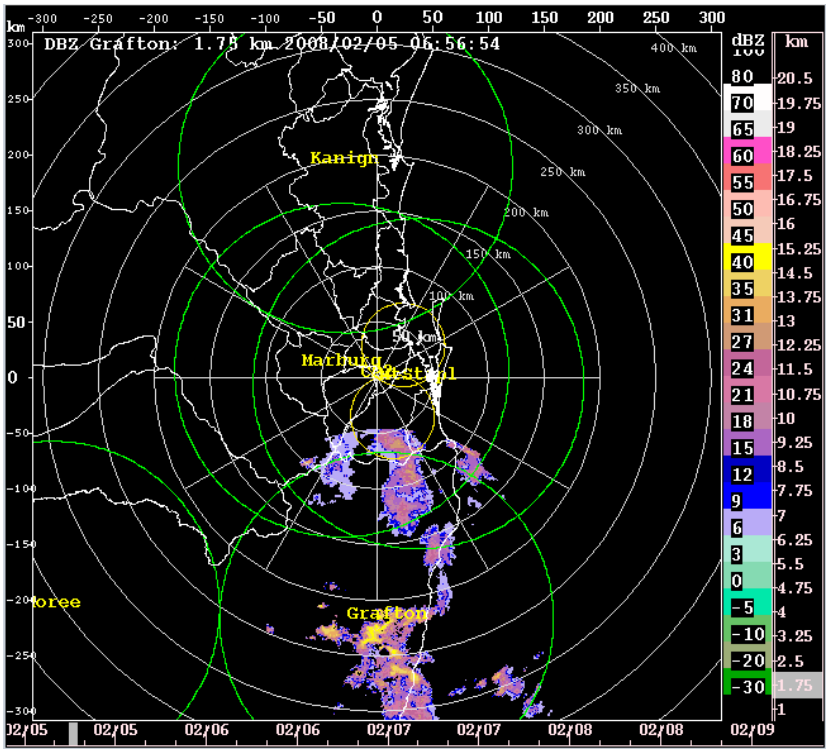

Figure 4.11. Example of radar coverage from Grafton, 2008/02/05 06:56:08

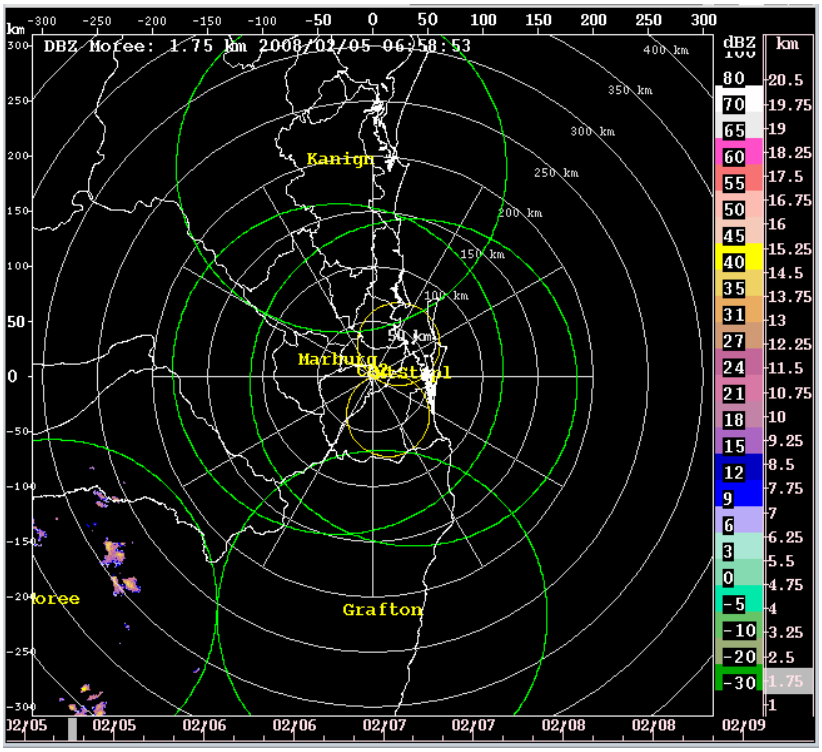

Figure 4.12. Example of radar coverage from Moree, 2008/02/05 06:56:08

4.2.6 Dual-Doppler capabilities

Figure 4.13 shows the dual-Doppler coverage for the pair of Doppler radars, CP2 and Mt. Stapylton. Each Doppler radar is only able to measure winds in a one-dimensional sense aligned with the radar beam, with motion measured either toward or away from the radar (called radial velocities). In order to resolve winds in two dimensions, overlapping data from two adjacent radars are used. The circles shown in Figure 4.13 represent the outer limits at which the wind vectors from the pair of radars intersects at an angle of 30 degrees or greater, which is considered a reasonable limit for dual-Doppler analysis. Thus, dual-Doppler analysis can be performed on radar features occurring within these so-called dual-Doppler lobes.

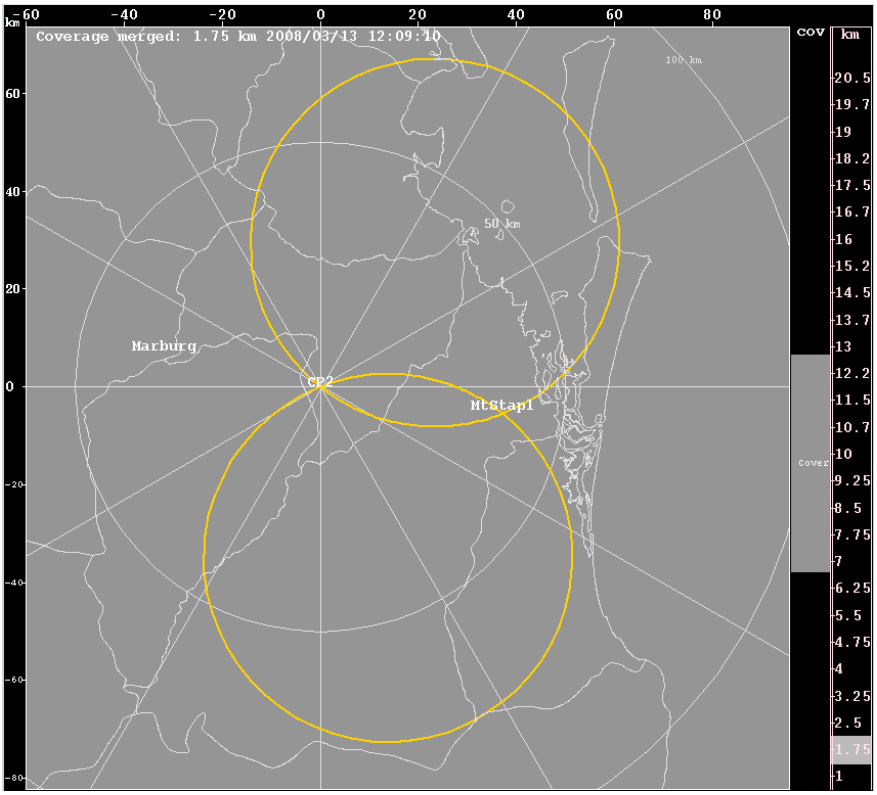

Figure 4.13. Dual-Doppler 30 degree coverage lobes (orange) for the CP2/Mt. Stapylton radar pair.

4.2.7 Storm tracking and display software

The TITAN system includes the capability to automatically identify and track storms in three-dimensional radar data, such as the merged mosaic. These storm tracks can then be displayed on a special purpose TITAN display called Rview. For a full description of the TITAN storm tracking and analysis capabilities, see:

http://www.rap.ucar.edu/projects/titan/home/index.php

Rview is actually a pair of displays. The main Rview display shows the radar data grid, both in plan view and in a vertical section through the 3-D radar data. Superimposed on these data are the identified storm shapes, including the current, past, and future (or forecast) storm shapes depending on the operational mode of the display (Figure 4.14). A secondary display,

TimeHist (for Time History) shows the time history of tracks selected on the main Rview display (Figure 4.15-Figure 4.17).

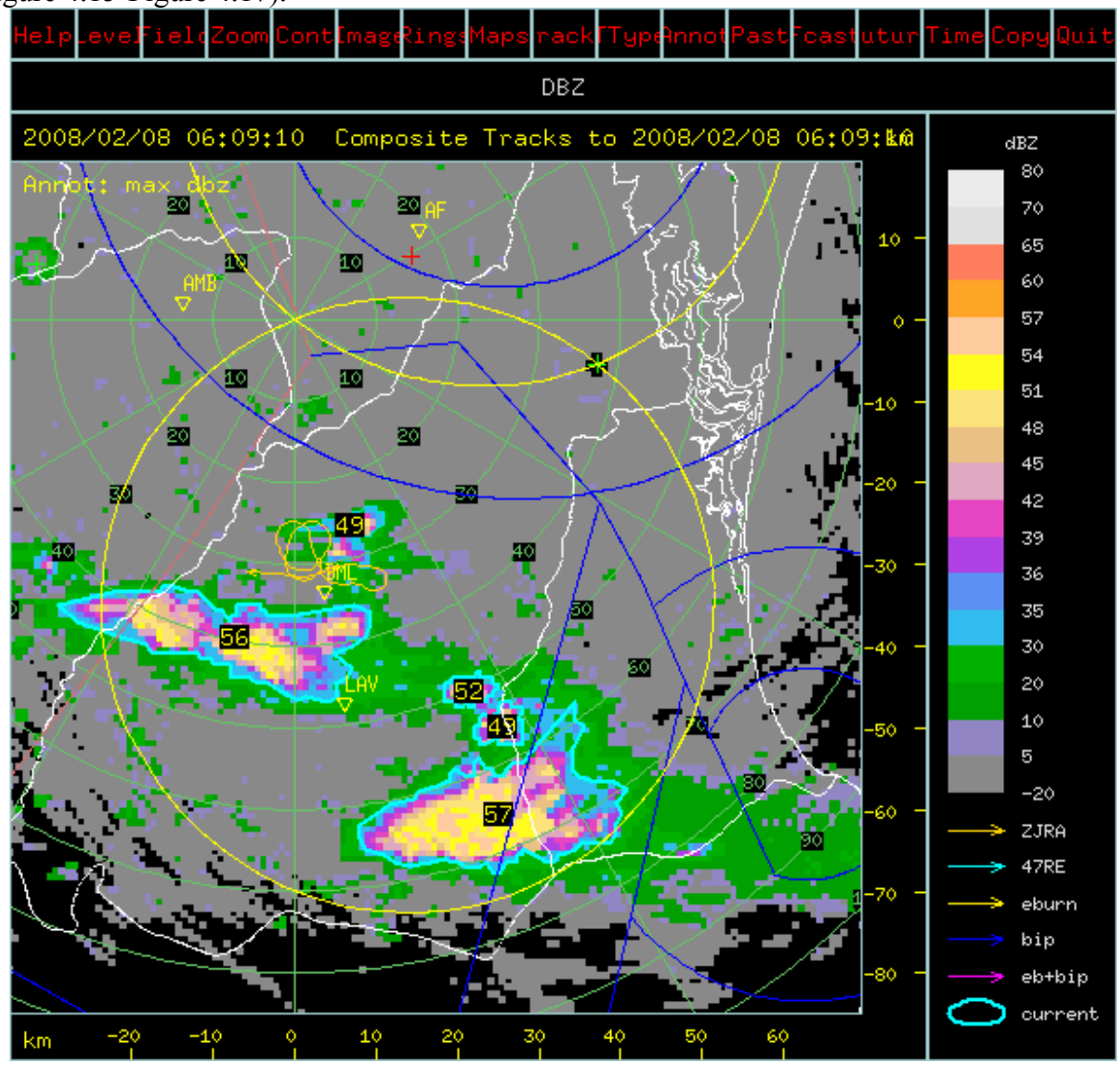

Figure 4.14. Rview display, showing storms in the southern dual-Doppler lobe (yellow circles). Orange line shows aircraft flight track for SEEDA1. Yellow numbers over the storm area show the maximum radar reflectivity. Cyan lines outline the storm shape at the current time.

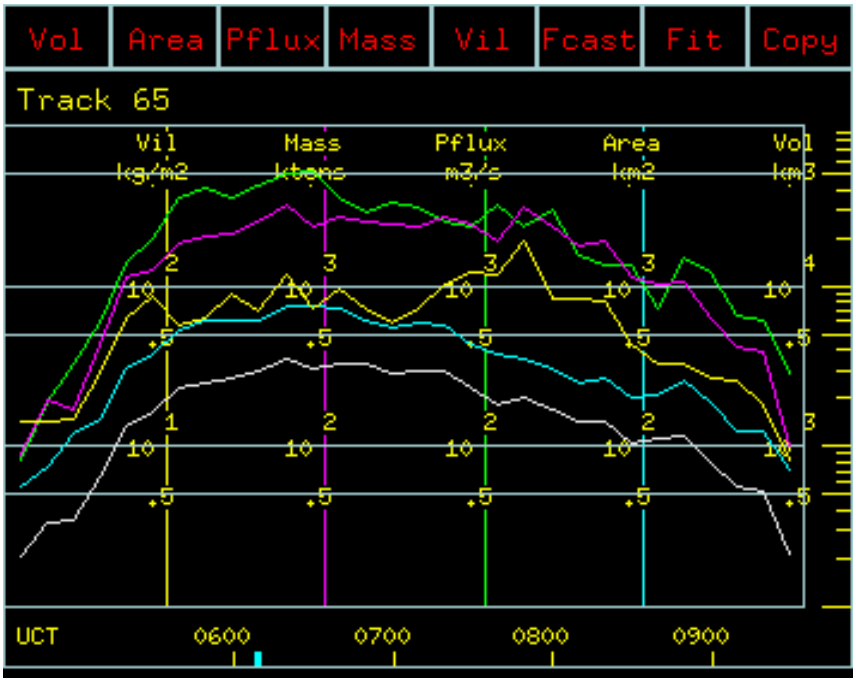

Figure 4.15. TimeHist window showing time history of storm: volume (gray), area (cyan), radar-estimated precipitation flux (green), radar-estimated mass (magenta) and vertically-integrate liquid (VIL) (yellow).

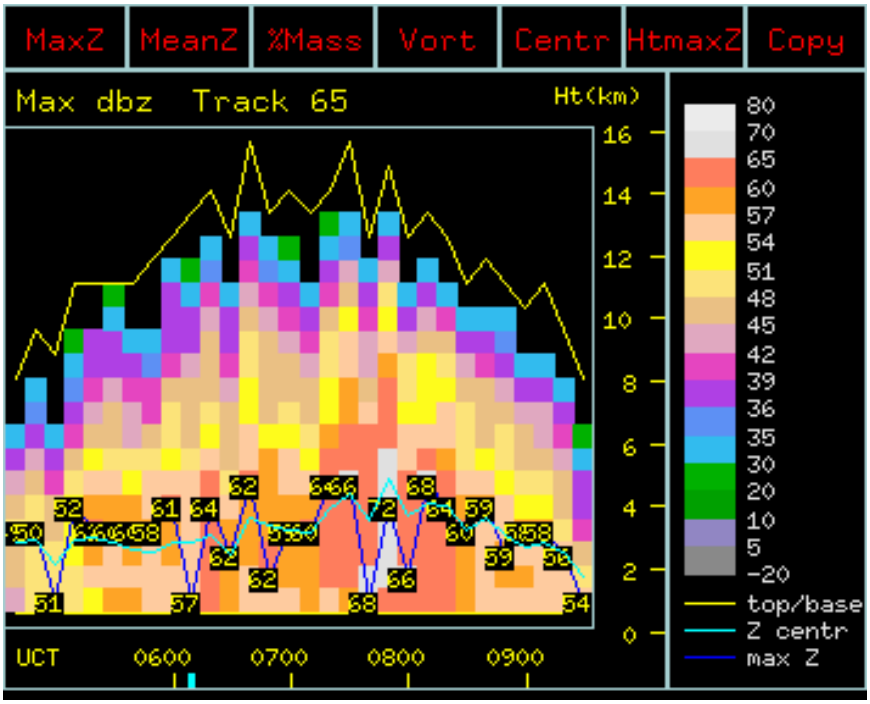

Figure 4.16. TimeHist window showing the time-height profile of storm reflectivity. The yellow line shows the storm top as estimated by the 18 dBZ contour. The numbers indicate the height of the maximum reflectivity over time.

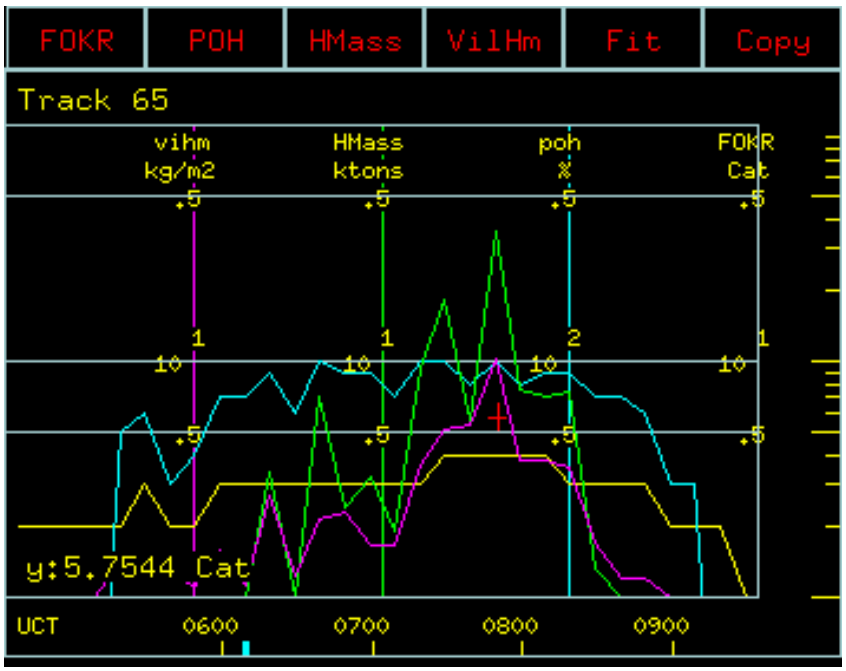

Figure 4.17. TimeHist plot showing various estimates of hail severity over time.

4.2.8 CIDD display software

The Cartesian Interactive Data Display (CIDD) is the main user display for the radar system. The images showing the merged radar product (see section 4.2.5) were all produced by CIDD. Although CIDD cannot show storm track data with the same detail as Rview, it is a more versatile display that allows the user to overlay products such as aircraft tracks, surface station data and lightning data on top of radar grids (Figure 4.18). CIDD also has the ability to show high-resolution Range-Height-Indicator (RHI) displays of radar data taken by scanning vertically through a storm rather than the more normal horizontal scanning mode (Figure 4.19).

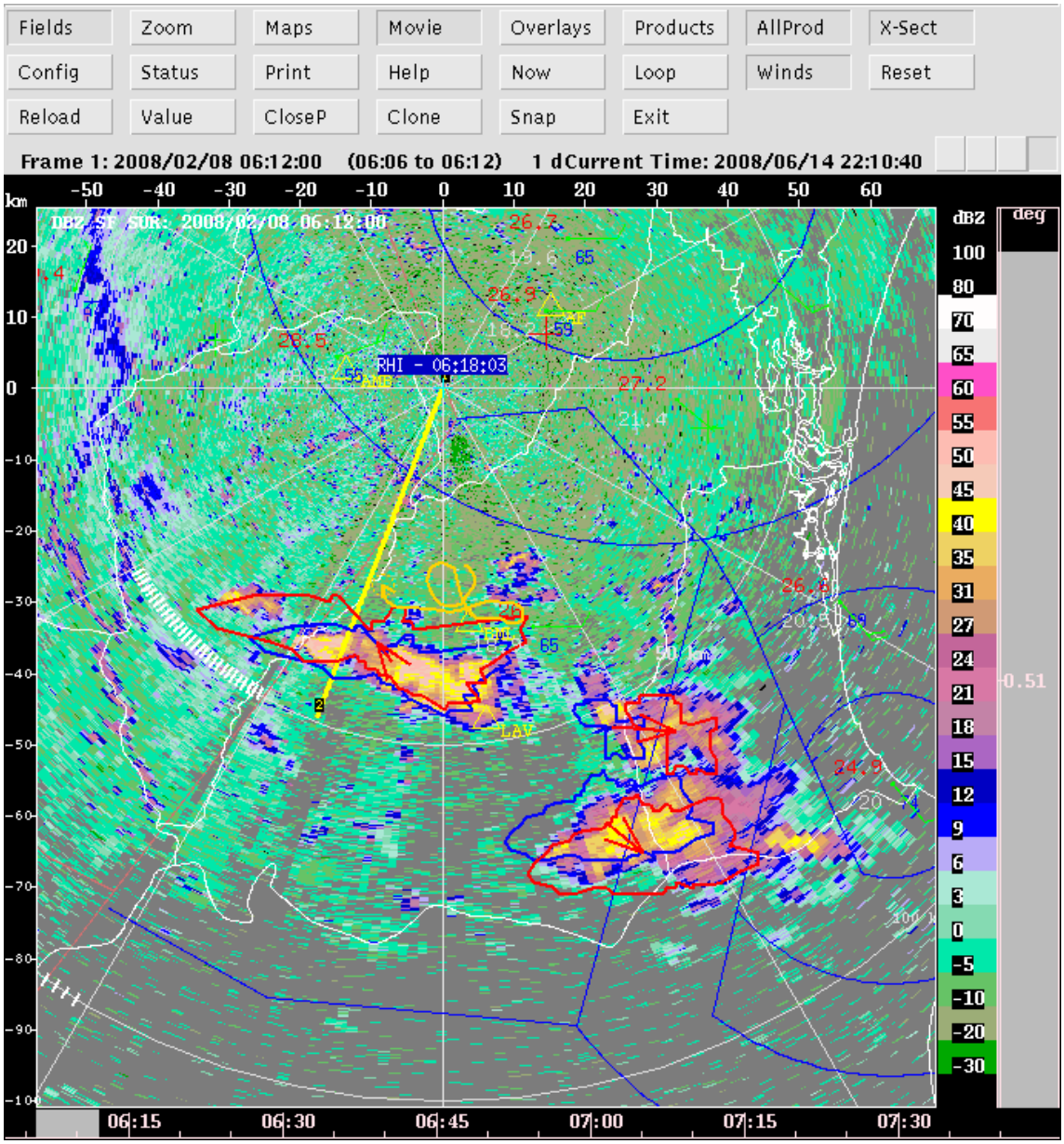

Figure 4.18. CIDD-generated image showing various products overlaid on the radar data: aircraft track (orange line), surface temperature and dewpoint (red/gray text), surface wind (green winds barbs), segment along which a vertical cross section or RHI is being displayed (thick yellow line), and location of RHI scans (white tick marks).

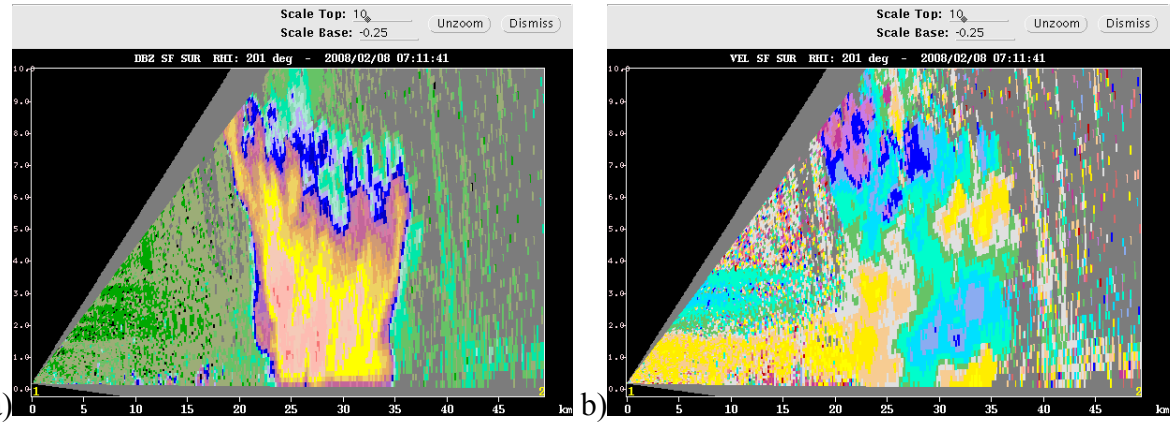

Figure 4.19. CIDD-generated Range-Height-Indicator (RHI) display showing a detailed vertical slice through a storm: (a) reflectivity and (b) Doppler radial velocity.

4.2.9 Data quality

The CP2 radar data has undergone preliminary quality checks (see Appendix, section 12.1). Overall, the data appears to be in good condition, and compares well with calculations from the video disdrometer (see section 12.1.4). Regular vertically pointing radar scans were performed which also helped to calibrate the radar data (see sections 12.1.7-12.1.8).

Also, in analyzing the precipitation estimates from the various radars, it was found that the calibration of the Mt. Stapylton radar results in reflectivity values which are somewhat higher than those from the surrounding radars, by perhaps 2 dB. This will be investigated further and the data corrected as appropriate for future analyses.

4.3 SURFACE INSTRUMENTATION

4.3.1 Disdrometer

A two-dimensional video disdrometer, manufactured by Joanneum Research at the Institute of Applied System Technology in Graz, Austria, was installed at the Willawong Animal Shelter in the community of Willawong. The latitude and longitude of the site were 27º 35.998′ and 153º 00.525′, respectively. This is 62.4º and 16.4 km from the CP2 radar. Station height is estimated to be 15 m. The disdrometer consists of two horizontally-oriented line-scan cameras that are separated in the vertical by about 6 mm. Shadowed photodiodes for each camera are recorded at a frequency of 51.3 kHz. Horizontal resolution is approximately 0.15 mm. Vertical resolution depends on the drop terminal velocity and is roughly 0.1−0.2 mm. Orthogonal views of raindrops falling through a common 10 × 10 cm area are provided. Reliable information is obtained for drops with diameters greater than about 0.5 mm. The observations are being used to fine tune the CP2 hardware calibration, establish drop size distribution (DSD) characteristics of stratiform and convective rains, and to develop procedures for monitoring drop size distributions in seeded and unseeded clouds with polarimetric radar.

Figure 4.20 depicts a drop detected at 083650 UTC on 8 February 2008. The computed equivalent volume diameter D is 6.19 mm, and the terminal velocity v_t is 8.85 m s^{-1}. Other information includes various dimensions, canting angles for the two viewing angles, and an estimate of drop oblateness. Raindrops were detected on more than 50 days (see Table 4.4). Deep stratiform rain, extending well above the freezing level, was the most frequently observed

precipitation type; but shallow stratiform rain and deep and shallow convection were also observed.

One-minute disdrometer observations were fit with the gamma distribution model

$$N(D) = N_0 D^{\mu} \exp(-\Lambda D), \qquad \textbf{(1)}$$

where N_0 ($\mathrm{mm}^{-\mu-1}\ \mathrm{m}^{-3}$) is a number concentration parameter, μ is a distribution shape parameter, and Λ (mm^{-1}) is a slope term. The three governing parameters of the distribution were determined using the 2nd, 4th, and 6th moments of the observed drop distributions.

The drop median volume diameter D_0 was computed from

$$\int_{D_{\min}}^{D_0} D^3 N(D) dD = \int_{D_0}^{D_{\max}} D^3 N(D) dD, \quad \textbf{(2)}$$

where $D_{\max}$ is the diameter of the largest observed drop in the distribution and $D_{\min}$ is the smallest drop. Rain rates are given by

$$R = 6\pi \times 10^{-4} \int_{D_{\min}}^{D_{\max}} D^3 v_t(D) N(D) dD \quad . \qquad \textbf{(3)}$$

Terminal velocities were determined as in Brandes et al. (2002).

An example of a 1-min drop size distribution for 0842 UTC on 8 February is given in Figure 4.21. A fitted curve for the truncated gamma DSD model is overlaid. The fit for a truncated exponential DSD model [Eq.(1) with $\mu = 0$], using the 3rd and 6th moments, is presented for comparison. In this case the drop distribution is close to exponential, which is typical of heavier rain rates. The number concentration turns down slightly at the smallest drop size (0.2 mm). This is probably an instrumentation problem. An example of drop terminal velocities is illustrated in Figure 4.22. Overall, fall speeds are slightly less than wind tunnel values (the plotted curve). While there is some evidence that large drop terminal velocities in the free atmosphere are less than those found in the laboratory, measured fall speeds in Figure 4.22 are believed to have been reduced by light to moderate winds that are deflected upward at the disdrometer orifice. Windy conditions also increase measurement scatter. Calm wind conditions usually produce pencil-thin v_t traces.

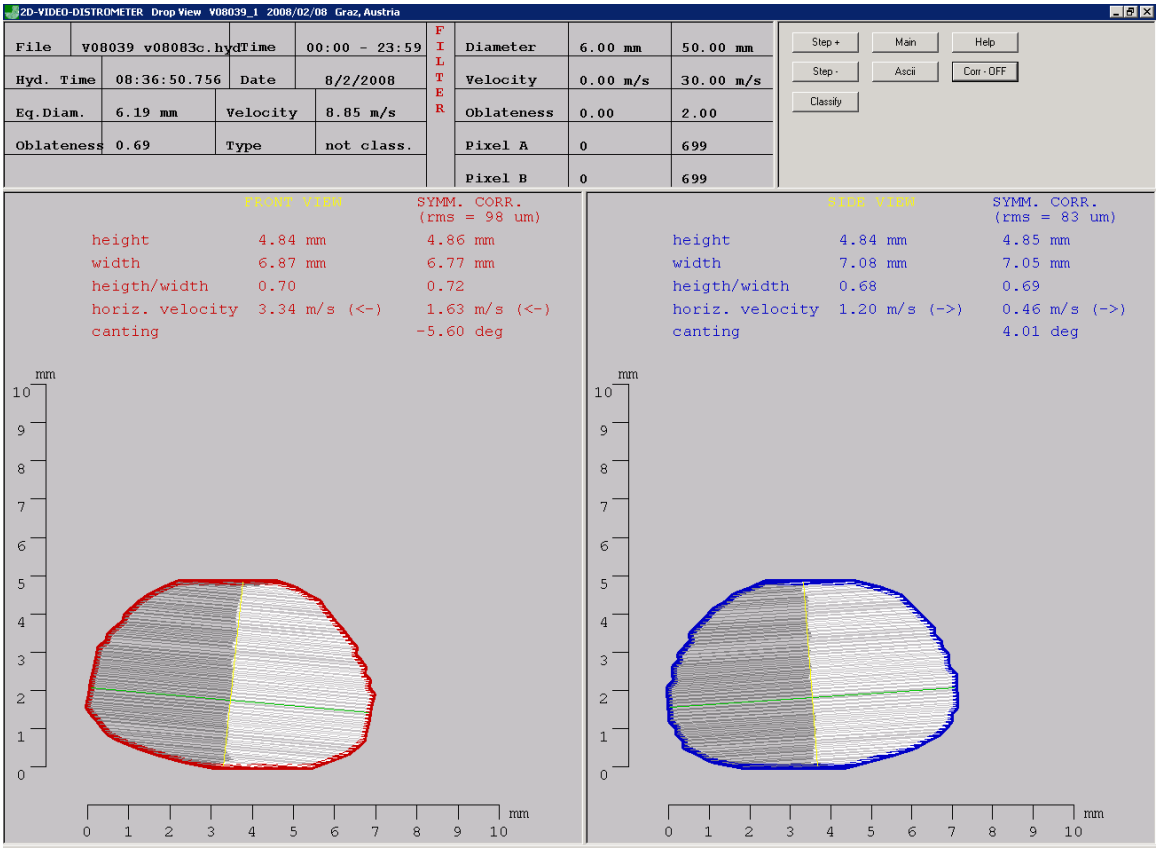

Figure 4.20. Derived attributes for a raindrop detected at 083650 UTC on 8 February 2008.

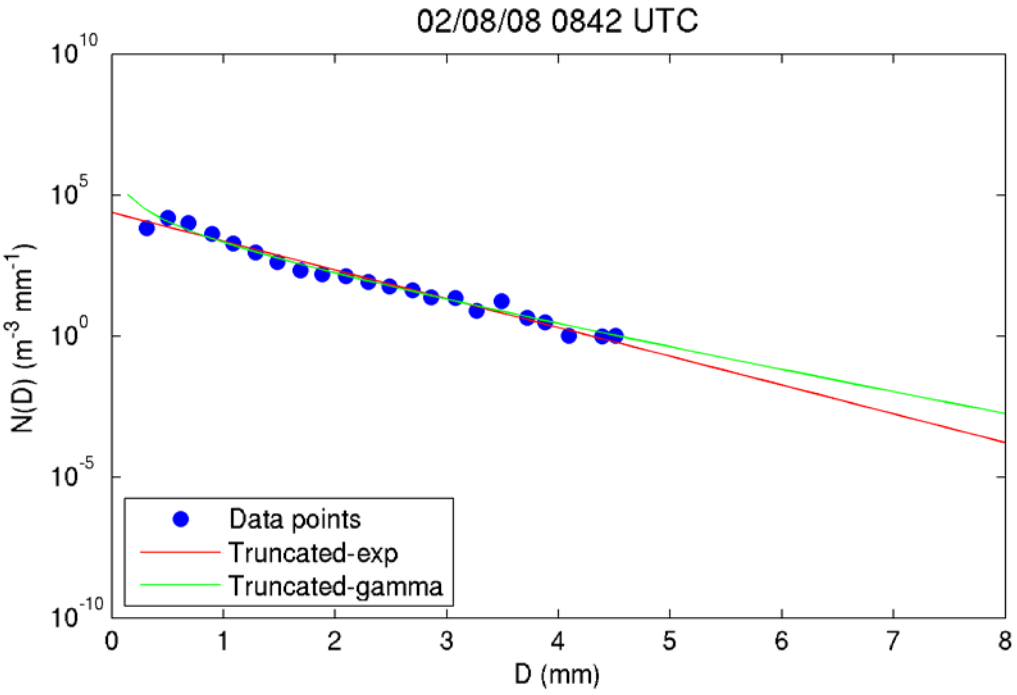

Figure 4.21. An observed drop size distribution for 0842 UTC on 8 February 2008. Fitted curves for truncated-exponential and truncated-gamma DSD models are shown. The rain rate was 44 mm h^{-1}.

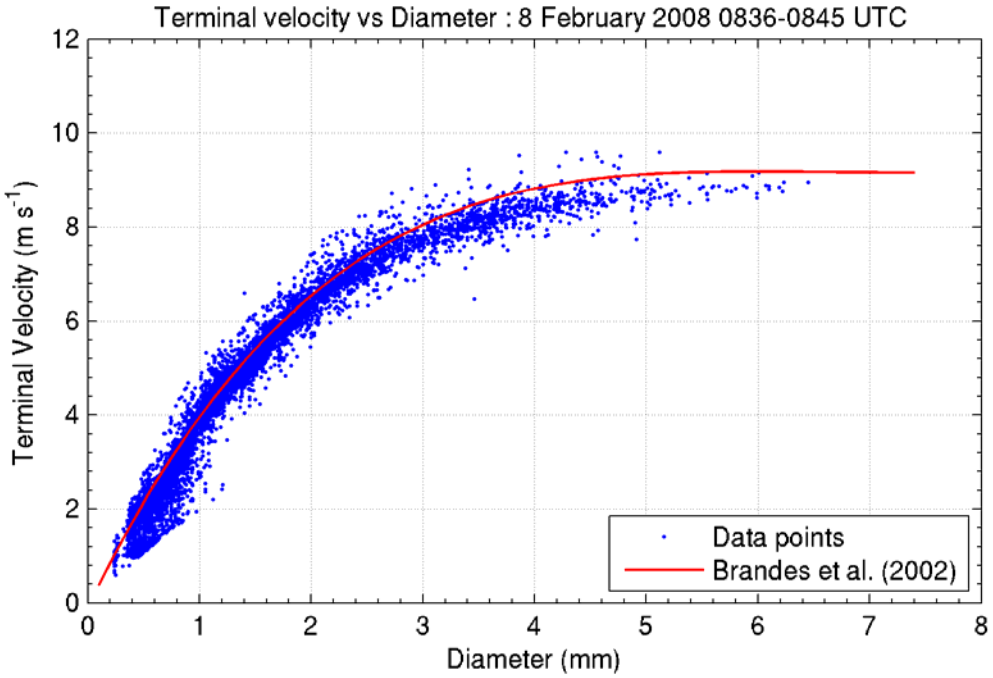

Figure 4.22. Terminal velocities for raindrops detected between 0835 and 0845 UTC on 8 February 2008 as a function of drop equivalent volume diameter. The plotted curve is a fit to wind tunnel measurements.

Table 4.4. NCAR Disdrometer table of datasets.

NCAR 2-D Video Disdrometer: Table of Datasets

Sensor location : Williwong Animal Shelter, Brisbane, QLD, AUS
Latitude/Longitude/Elevation : 27° 35.9983'/153° 00.5253'/~15 m
From CP-2 Radar : 62.36 deg / 16.36 km
Field Operations: December 2007 - March 2008

NOTE

Calibrated data and drop images are on quine.rap.ucar.edu. Please contact Kyoko (kyoko@ucar.edu; x2842) or Ed (brandes@ucar.edu; x8487) for questions regarding the data.
Calibrated drop images : /rain/kyoko/cloudseed/HYDC
Calibrated data in ascii format : /rain/kyoko/cloudseed/asc
1-min DSD data in ascii format : /rain/kyoko/cloudseed/DSD

Date (UTC)	Julian Date	Time (UTC)	Comments
Cells highlighted in light blue - disdrometer data with precipitation data	**Cells in gray - contains calibration data; Cells in yellow - incomplete data at the end of the julian day**	Time segment in UTC used for generating 1-min DSDs.	[first last] = times in UTC of the first and last raindrops in the data. This does not mean that rain continued between the two times.
12/9/2007	343	1330-1700	stratiform event. The disdrometer captured the entire event but later stopped working due to a communication loss.
12/10/2007	344		calibration dataset
12/12/2007			
1/13/2008	13	2130-2359	calibration dataset until 0400 utc. Rain after 2130 UTC. [first last] = [213154 235958]
1/14/2008	14	0000-2359	good event. [first last] = [000004 235958]
1/15/2008	15	0000-0510	good disdrometer data. No rain after 1200 UTC. [first last]= [000004 045653]
1/16/2008	16	0000-1610	intermitten precip. [first last]= 002345 155734]
1/17/2008	17	0200-1530	[first last]= 020521 150929]
1/18/2008	18	0000-2359	short event. Problem with the data at the end of the day. [first last]= [002628 234634]. Now up to 224816. error message = 'ang behind hyd'.

1/19/2008	19	0530-2359	two short events. Problem with the data at the end of the day. [first last] = [054509 235312]. Now up to 232509. error message = 'ang behind hyd'.
1/20/2008	20	0500-1945	intermitten precip. [first last] = [050530 192845]
1/21/2008	21	0100-1810	intermitten precip. [first last] = [010238 175748]
1/26/2008	26	0150-2100	a few drops. No need to process this data.
1/28/2008	28	1450-2359	intermitten precip. Problem with the data at the end of the julian day. [first last] = [145307 235957]. Now up to 231527. error message = 'ang behind hyd'.
1/29/2008	29	0000-2359	A good convective event. Problem with the data at the end of the julian day. [first last] = [000004 235613]. Now up to 231341. error message = 'ang behind hyd'.
1/30/2008	30	0000-1800	intermitten precip. [first last] = [000558 174135]
1/31/2008	31	2350-2359	very short event. [first last] = [235253 235528]
2/1/2008	32	2100-2200	very short event. [first last] = [213057 213915]
2/2/2008	33	0100-2359	A good event. [first last] = [010607 235958].
2/3/2008	34	0000-2359	A good event. [first last] = [000004 235849]
2/4/2008	35	0100-2359	Good disdrometer data. [first last] = [000037 225759]
2/5/2008	36	0600-1200	Good disdrometer data. [first last] = [060921 113103]. No rain after 1200 UTC.
2/6/2008	37	0000-1130	Drizzle early (<0045 utc). Good event after 0200 utc. [first last] = [004324 110626]
2/8/2008	39	0800-1600	Large drops associated with the first convection starting at 0830 UTC. Two short rain episodes between [first last] = [083606 155355].
2/10/2008	41	2100-2359	Light stratiform (?) rain. A very short event. [first last] = [210816-221215 and 232426-234003]
2/11/2008	42	0000-2359	A good event. [first last] = [003738 235957]
2/12/2008	43	0000-1530	Good disdrometer data. [first last] = [000004 150234]. No rain after 1502 utc.
2/13/2008	44	0400-1600	Good data. Mod rain early on. A short light rain event from 1200-1537utc. No rain after 1242 UTC. [first last] = [041405 153732].
2/14/2008	45	0000-0700	A short light rain event before 0100 utc. Then another light event from 0400 to 0627 utc. [first last] = [003214 062742].
2/15/2008	46	0230-2359	A light-mod rain between 0245 and 0800 UTC. A short drizzle event after 17 and 21 utc. [first last] = [025103 232411].
2/16/2008	47	0030-2359	A good case. Multiple short convective events (intermitten precip.). Need to fixed with V08083c. [first last] = [010151 235949]
2/17/2008	48	0000-2359	Light intermitten precipitation between [first last] = [000005 230530]
2/18/2008	49	0000-2359	Good disdrometer data. Convective. [first last] = [003739 235718]
2/19/2008	50	0000-1200	Two short light (drizzle ?) events between [first last] = [002642 112325].
2/20/2008	51	0400-0500	Very short light rain event. [first last] = [041210 043522].
2/24/2008	55	1600-2359	A good light rain case. [first last] = [164728 235638]
2/25/2008	56	0000-2359	A good stratiform event. [first last] = [002051 235958]
2/26/2008	57	0000-1730	Very good looking data. Mod-heavy rain rates. [first last] = [000004 165437]
2/27/2008	58	1630-2230	Intermitten light events between [first last] = [165751 220218].

2/28/2008	59	0500-2359	Intermitten light events between [first last] = [053955 231756].
2/29/2008	60	0300-0700	A short light rain event. [first last] = [033719 064211]
3/3/2008	63	0400-0700	Some drops between [first last] = [040826 063910].
3/5/2008	65	0200-0900	Intermitten light events between [first last] = [024742 083858].
3/6/2008	66	0000-0100	Very short event between [002736 005444].
3/8/2008	68	1000-2100	Disdrometer data ok. Mod rain between 1000-1200 UTC. Light rain after 1600-2030 UTC. [first last] = [100911 202522].
3/9/2008	69	0000-2359	Multiple episodes of light-mod rain between [first last] = [000552 230137].
3/10/2008	70	0000-0800	Light intermitten rain episodes between [first last] = [001500 072828].
3/14/2008	74	0730-2130	Two very very short events between [first last] = [173803 210742].
3/15/2008	75	0000-2300	Two very very short events between [first last] = [002003 225142].
3/19/2008	79	0000-2359	A short convection before 0200 utc. Another rain episode after 22. [first last] = [005238 235607].
3/20/2008	80	0000-0700	Light intermitten rain episodes between [first last] = 003706 063142].
3/21/2008	81	1300-2359	Ligh intermitten rain. [first last] = 130647 2359]
3/22/2008	82	0100-1600	Rain before 1530 UTC. [first last] = [010039 153036]. Sample calibration spheres were dropped after 1530utc.
3/23/2008	83	0230-1800	Calibration data before 0250 UTC but mixed with rain. Light rain around 0250utc, and more rain after 1053 utc. [first last] = [025649 171449]. DSD period should not include calibration data, so begin DSD period from 1050 utc.
3/24/2008	84	0100-1230	Intermitten rain. Heavy after 04utc. [first last] = [011719 115453].
3/26/2008	86	0900-2359	Light-mod rain. Becoming more convective after 2000 utc. [first last] = [094755 235959].
3/27/2008	87	0000-0200	Light stratiform rain. [first last] = [000004 012430].

4.3.2 Surface station data

The Bureau of Meteorology operates a network of automatic surface measurement stations, for fields such as wind speed and direction, temperature and dew point. These data are available on servers within the BOM intranet. The data were copied to the CP2 operations center servers and stored by the TITAN data system. These data were then available for display on CIDD, and for later analysis.

4.4 REAL-TIME AIRCRAFT TRACK DATA

In flight, both the instrumented aircraft and the seeding aircraft transmit their location, along with other data fields, over a data radio. A receiver was installed at the CP2 radar site and received these data, which was then read in to the TITAN data system. These data were then available for display on CIDD during real-time operations, and later for analysis purposes.

5. WEATHER AND CLIMATE

5.1 INTRODUCTION

Understanding the common weather patterns and typical climate cycles in the region is crucial to laying the foundation to understand the possible effects of cloud seeding. Which weather patterns bring the most natural rainfall, and how often do those occur? What months typically have the most rainfall, and from what types of cloud systems? After establishing this foundation of understanding, we can better assess if the cloud systems that occur in the region can be modified to enhance rainfall. This chapter discusses the preliminary weather and climate studies of the Southeast Queensland region.

5.2 ATMOSPHERIC ENVIRONMENT - A SYNOPTIC OVERVIEW

The region was often dominated by three general weather scenarios, nominally given the following descriptions: (1) trade wind cumulus; (2) northeasterly stable; (3) northeasterly unstable. Additionally, a fourth, more rare scenario is termed (4) large scale forcing.

5.2.1 Trade wind cumulus

During this scenario, the region is dominated by a high pressure cell which lies over or near southeast/eastern Australia. An example MSLP analysis for this situation is illustrated in Figure 5.1. The high forms a well-defined ridge along the eastern seaboard of Australia resulting in SE-E winds and the advection of relatively cool and moist air from southern latitudes. The heat low and associated trough located over western/central QLD does not significantly influence the Southeast Queensland region.

A sounding released at 2300 UTC (0900 LT) is shown in Figure 5.2. The most striking feature is the strong inversion located near 750 hPa and the dry slot located above, which is a result of large-scale subsidence. CAPE is typically low (< 100 J/KG) and the lapse rate moist adiabatic above the inversion. As a result, the prevailing clouds tend to be scattered cumulus humilis to cumulus mediocris; some of the latter precipitate readily.

The sounding is reminiscent of a maritime trade wind cumulus structure. Few studies have been conducted of trade wind cumulus clouds (and most have been conducted in the northern hemisphere Atlantic Ocean), however, one feature which does distinguish the trade wind Cu in SE QLD is the *increase* of wind speed with height below the inversion. Typically, trade wind Cu exhibit a *decrease* of wind speed with altitude resulting in clouds which “lean back” into the wind.

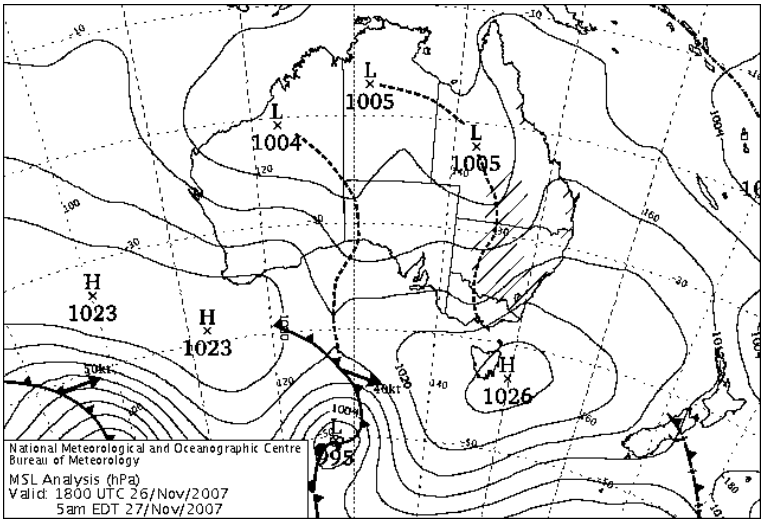

Figure 5.1. Example MSLP of the synoptic situation over SE QLD during the trade wind cumulus scenario. MSLP analysis 1800 UTC 26 November 2007. The prevailing winds are south easterlies.

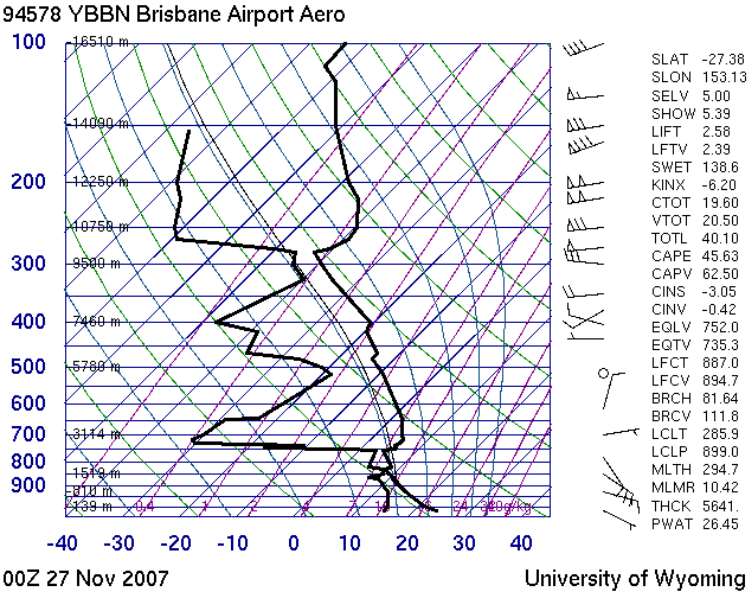

Figure 5.2. Sounding released at 2300 UTC (0900 LT) on 27 November 2007 depicting conditions encountered during the trade wind cumulus scenario. Note the strong inversion near 750 hPa and the dry slot above. Moist adiabatic conditions prevail above the inversion.

Most of the trade wind Cu clouds which form during this scenario are confined below or near the freezing level and are thus prime candidates to study the warm rain formation process and/or early ice production processes. Precipitation appears to be very efficient in these clouds, so they precipitate over the Brisbane plains region and dissipate before reaching the primary seeding catchment area located to the northwest of Brisbane. Solar heating during the day may result in some isolated storms over higher elevations near the Wivenhoe dam region, although

forecasting these will be particularly difficult and require careful monitoring of the radar to reveal their occurrence. According to the BOM forecasters, these showers are most prevalent in the morning, although the situations encountered during the project have resulted in showers throughout the day with perhaps some increased vertical development later in the afternoon.

5.2.2 Northerly stable conditions

On a synoptic scale the main feature that differentiates this situation from the trade wind Cu scenario is the movement of the high pressure system eastward due to an approaching cold front at southern latitudes. An example MSLP (0000 UTC 07/12/2007) is shown Figure 5.3. As a result, the winds are northerly/northeasterly.

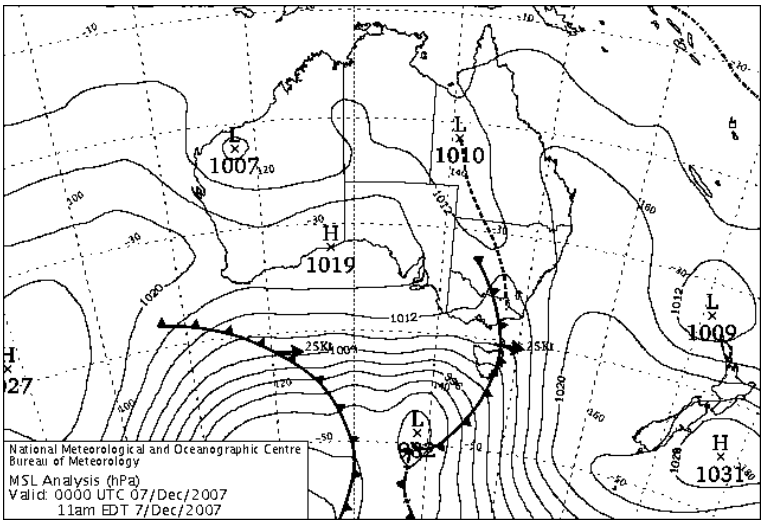

Figure 5.3: Example MSLP of the north easterly stable scenario. The high has moved east giving way to an approaching cold front.

As for the trade wind Cu case, the trough is still located over western QLD and at upper levels relatively warm air is being transported from the west resulting in a near moist adiabatic lapse above the inversion. An example sounding of this situation is shown in Figure 5.4. The dry slot present just above the inversion in the trade wind Cu scenario is absent. As a result, any clouds which penetrate the inversion will entrain moister air allowing for slightly greater vertical development and an increased likelihood of ice formation processes becoming important.

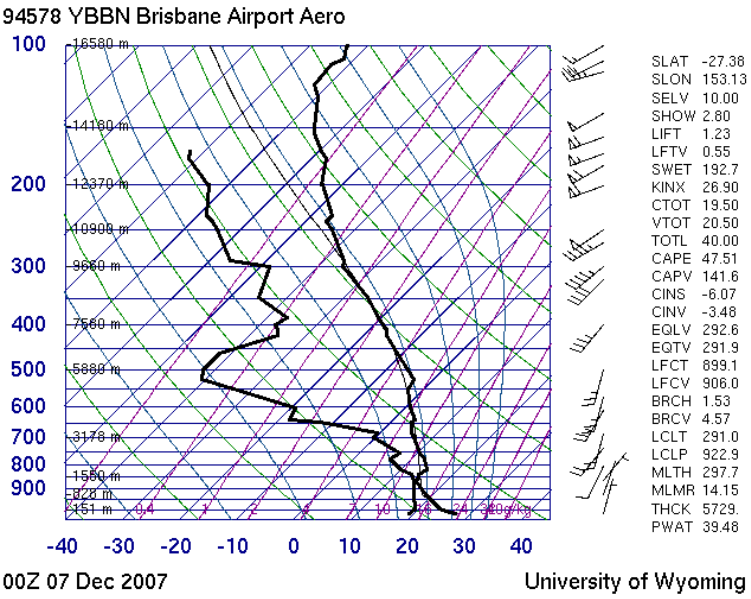

Figure 5.4: Sounding illustrating the north easterly stable scenario.

When the winds are northerly, advection of warm dry air results in significantly depressed dewpoints and few clouds; when winds are northeasterly, advection of moist air results in the development of scattered showers. Some deeper isolated storms may also develop, particularly over the ranges surrounding the Brisbane plains. The steering level of the storms is driven by the upper level flow and they tend to track from the southwest to the northeast. Since the atmosphere is stable over the Brisbane plains, the storms that form over the ranges tend to dissipate once they reach the Brisbane plains.

5.2.3 Northerly unstable

This scenario emerges as the surface trough approaches the South East Queensland region. An example MSLP (0000 UTC 06/12/2007) is shown in Figure 5.5. As the trough approaches the region, the inversion located near 800 hPa erodes slightly and the upper levels cool. An example sounding is shown in Figure 5.6.

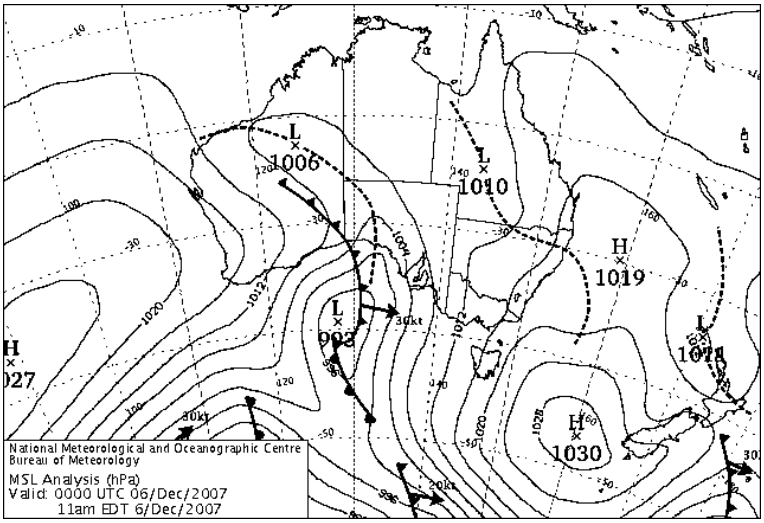

Figure 5.5: Example MSLP illustrating the northeasterly unstable scenario. Note how the surface trough has advanced closer to the Southeast Queensland region than during the northerly stable scenario.

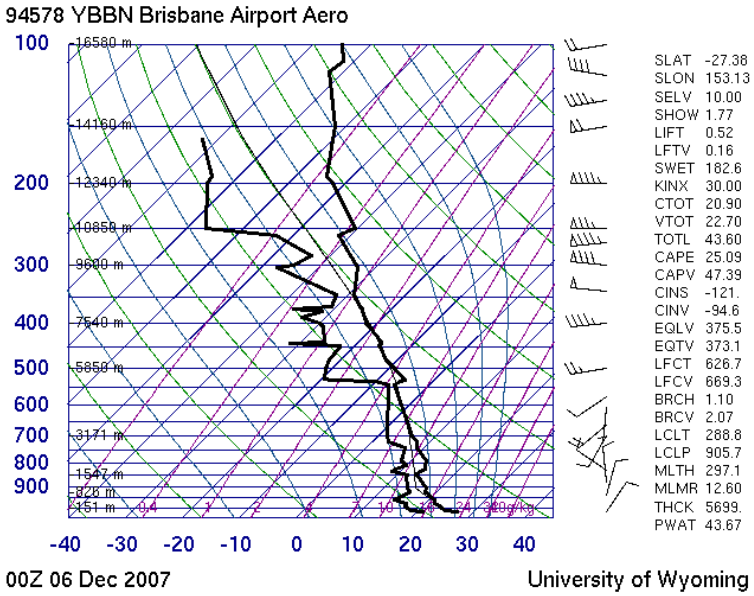

Figure 5.6: Sounding obtained at 0000Z (0900 LT) on 6 December 2007 illustrating the northeasterly unstable scenario.

This scenario can result in large isolated convective storms over the ranges and over the Brisbane plains. Additionally, rainbands containing embedded convective storms may result in widespread precipitation. The storms tend to develop before midday and persist throughout the day. If this situation develops, a takeoff after the morning (1100 LT) briefing will probably be too late to examine the early development of the droplet size distribution. As such, careful attention has to be paid to forecasting this scenario a day ahead so that an early morning take-off can be scheduled.

5.2.4 Large-scale forcing

The final scenario is due to large scale forcing by cold fronts over southern Australia which penetrate northward to the Brisbane region. **Figure 5.7**a shows a cold front that passed over the Brisbane region. Northwesterly winds associated with the warm conveyor belt ahead of the cold front converged with a northeasterly sea breeze resulting in severe storms which caused hail and wind damage. **Figure 5.7**b illustrates a slightly different case, although still due to synoptic scale, whereby thunderstorms formed ahead of a cool southeasterly cold front change.

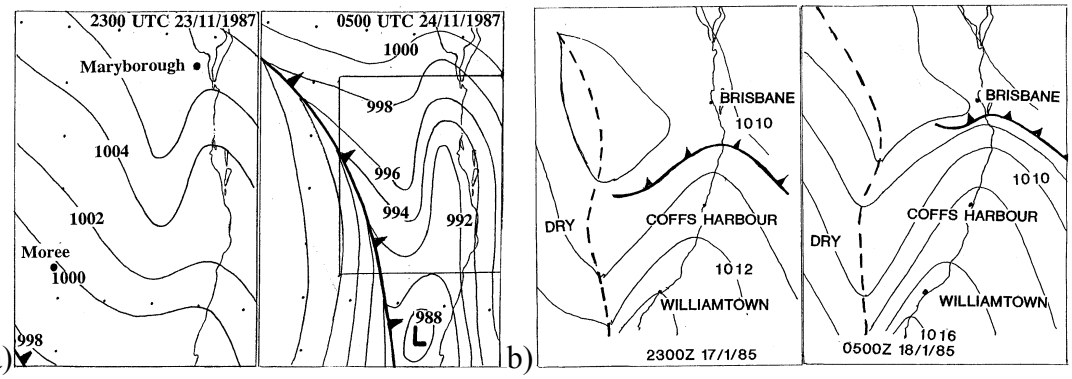

Figure 5.7: Example MSLP illustrating synoptic conditions which may result in severe thunderstorms. In particular, flying during these scenarios can be inappropriate. (Courtesy Jeff Callaghan, Brisbane BOM office)

Situations in which the weather is driven by synoptic scale weather systems tend to bring the most severe weather to the Brisbane region and, as such, are situations when flight operations may not be possible. An example of a situation similar to this scenario occurred on the evening of 7 December 2007, when the surface trough was collocated with the edge of a cold front to the south (see Figure 5.8). A squall line passed over the Brisbane region resulting in heavy downfalls; Wivenhoe dam received 20 mm of precipitation.

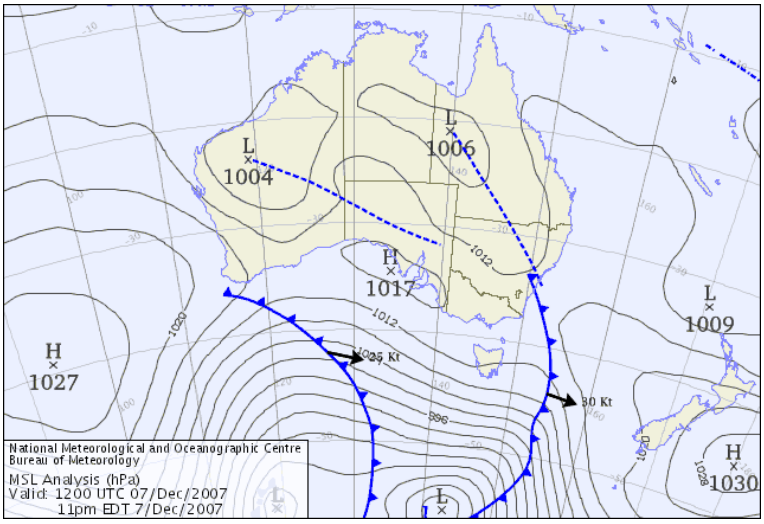

Figure 5.8: MSLP valid 1200 UTC (2200 LT). The trough over QLD extended eastward and coincided with cold front passing over southern Australia

5.3 SEASONAL PRECIPITATION CLIMATOLOGY

Using NCEP/NCAR re-analysis data[1], the seasonal variation in precipitation for the past 60 years was analyzed. Figure 5.9 shows the mean monthly precipitation rate over the Brisbane/Toowoomba region. It can be seen that the months with the highest precipitation rates are December, January, and February (DJF). Figure 5.10 shows the seasonal relationship with the concurrent and preceding Southern Oscillation Index (SOI). Positive SOI is indicative of La Nina conditions, whereas negative represent El Nino conditions. There is a slight trend for La Nina to yield a wetter DJF season for the Brisbane/Toowoomba region.

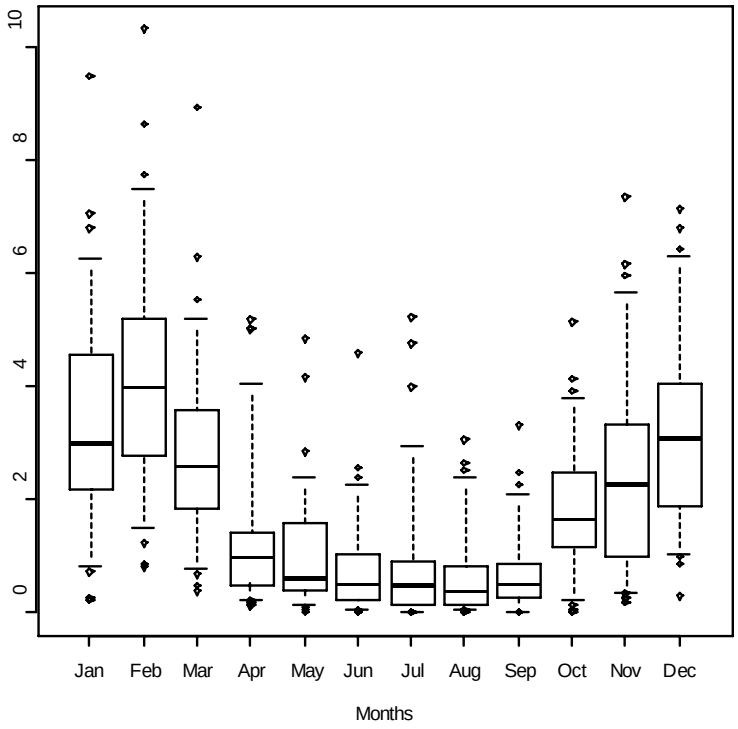

Figure 5.9. Monthly precipitation rate (mm/day) over Brisbane/Toowoomba area (Lat: -27.6; Long: 150.0 to 151.9) from 1948-2008.

[1] NCARP/NCAR re-analysis data (Kalnay et al. 1996) used for the this analysis were obtained from the NOAA-CIRES Climate Diagnostics Center (CDC) Web site (http://www.cdc.noaa.gov)

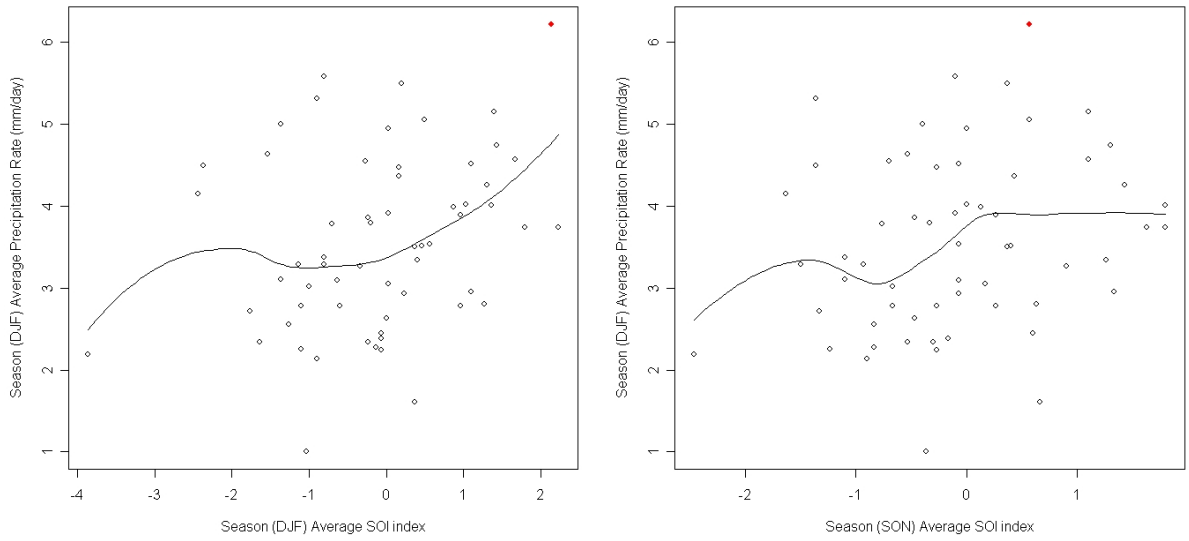

Figure 5.10 Scatterplot of 1948-2008 seasonal average DJF (left; R = 0.300) and SON (right; R=0.236) SOI versus DJF precipitation rate (mm/day). Red dot is 2008 season.

Figure 5.11 and Figure 5.12 show the relationships between the SOI index and the precipitation rate for each wet month (October through March), concurrently and with a one-month lag, respectively. Table 5.1 shows the correlation (r) values. For the 2007-2008 season, the months of DJF each had the highest precipitation rate, and also high SOI. Furthermore, it is clear that the relationship between positive SOI and higher precipitation rate is mostly valid in January and February, and not all wet months. The one-month SOI lag relationships are even less correlated.

Table 5.1. Correlation (r) values for Figure 5.11 and Figure 5.12.

	Concurrent	One-Mo Lag
Month	r	r
Oct	0.032	-0.071
Nov	0.228	0.178
Dec	0.275	0.208
Jan	0.300	0.138
Feb	0.169	0.077
Mar	0.225	0.212

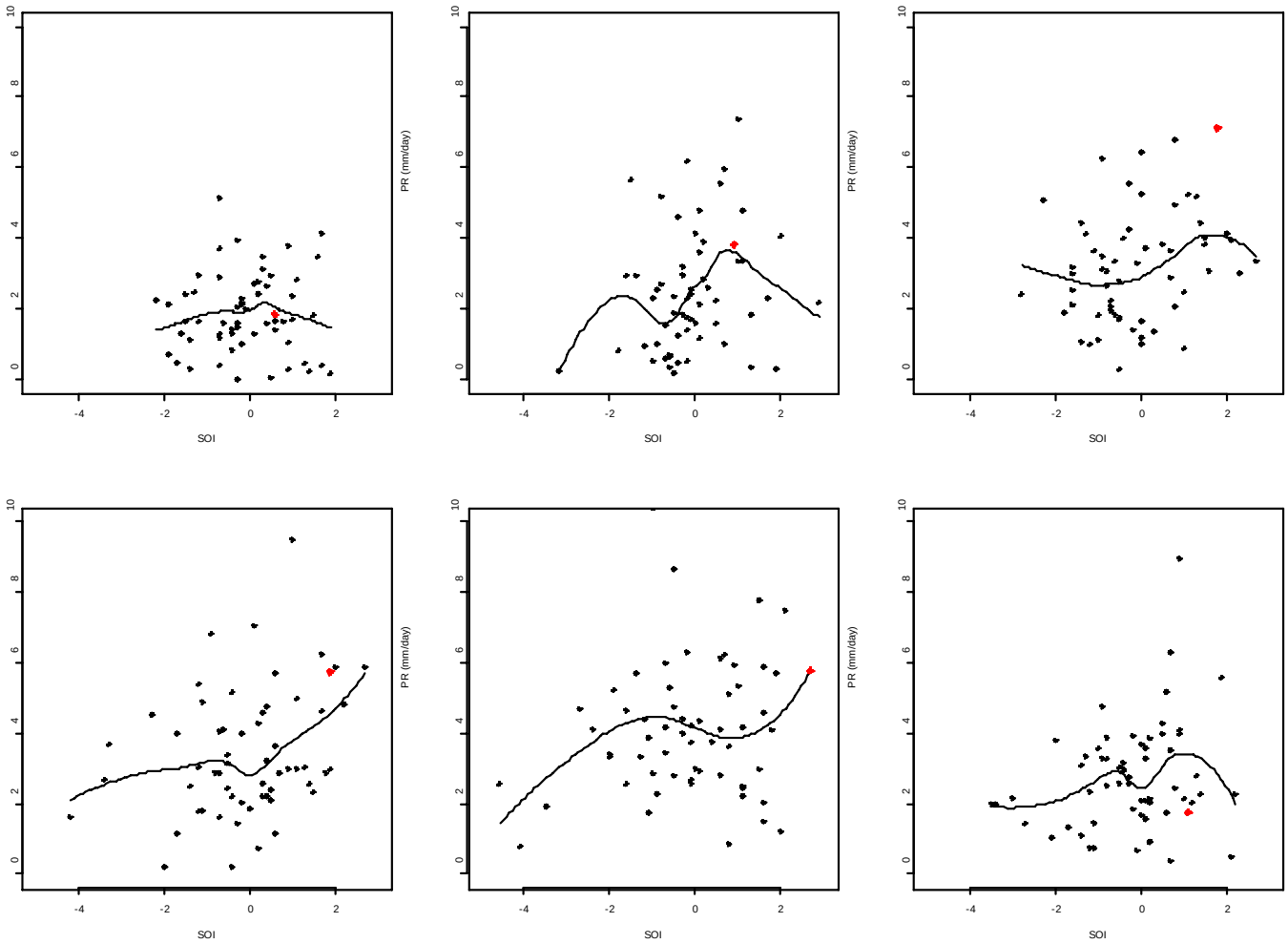

Figure 5.11 Monthly SOI versus precipitation rate (concurrent) for 1948-2008. Red dot is 2007-2008 value.

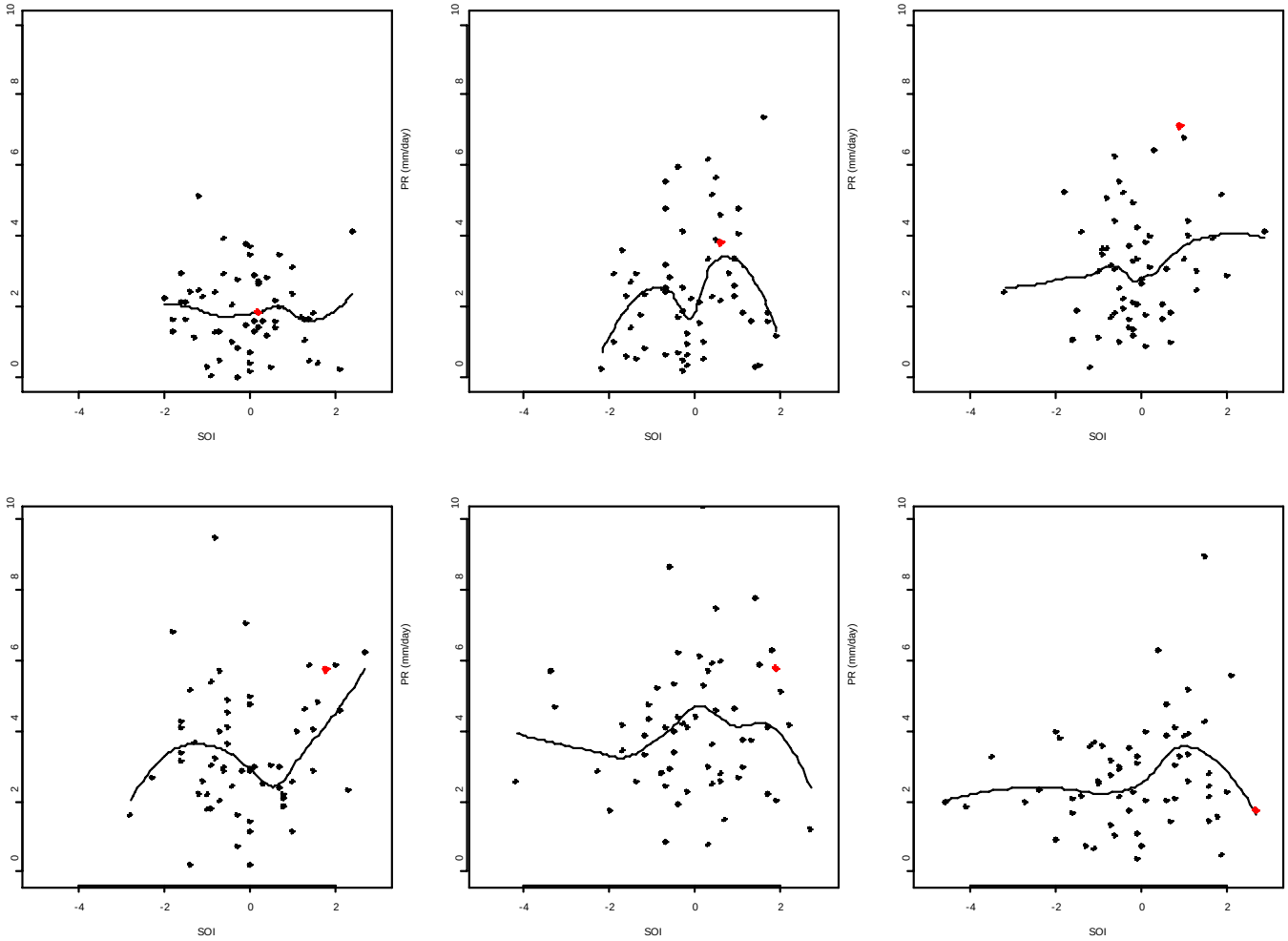

Figure 5.12 Monthly SOI versus precipitation rate (SOI lags by one month) for 1948-2008. Red dot is 2007-2008 value.

Figure 5.13 shows the relationship between precipitable water and precipitation rate for each of the monthly values of the wet season (ONDJFM). It is clear that these two variables are correlated, and thus precipitable water could be used as a proxy for precipitation rate. Figure 5.14 shows the mean monthly precipitable water available over the Brisbane/Toowoomba region. It can be seen that the months with the highest precipitable water are December, January, February, and March (DJFM).

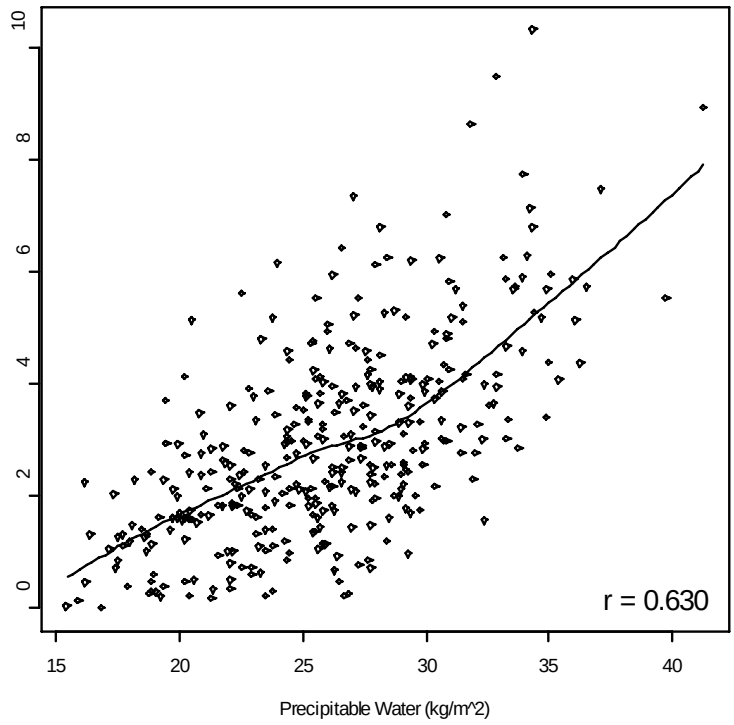

Figure 5.13 Precipitable water versus precipitation rate for each wet month (ONDJFM).

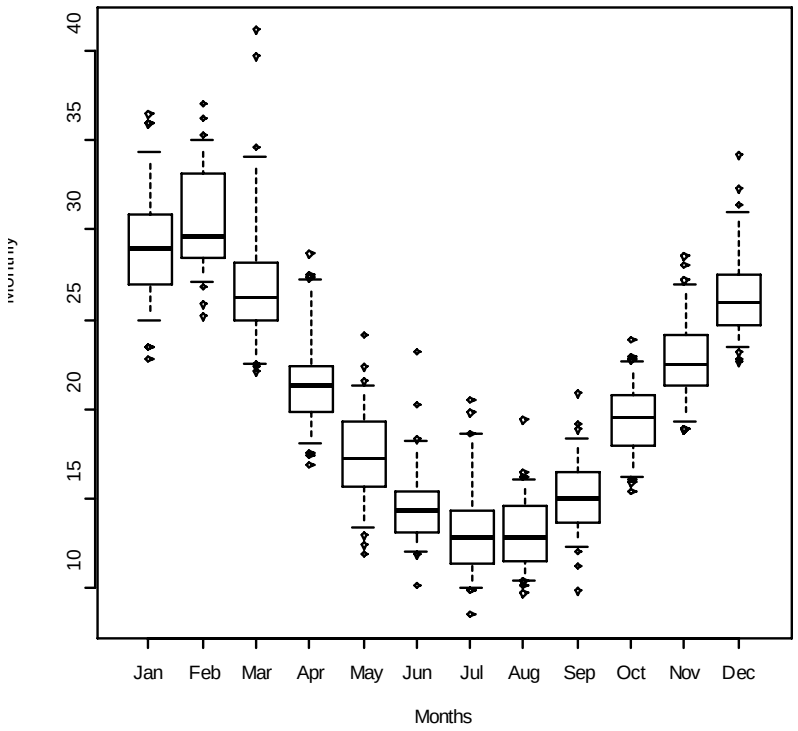

Figure 5.14 Monthly precipitable water (kg/m^2) over Brisbane/Toowoomba area (Lat: 27.5S, Lon 150.0-152.5) from 1948-2008.

Figure 5.15 shows the correlation between the average concurrent and preceding season standardized SOI index and the average DJFM precipitable water for Brisbane/Toowoomba. From the concurrent season graph, one can see that besides a few negative SOI index outliers, the relationship is strongly positive once SOI reaches zero. The correlation value (r) is 0.395. From the preceding season graph, the fitted smooth curve shows that the relationship is flat until the standardized SOI reaches about 0.5 and then becomes positive. The correlation value (r) is 0.251. As pointed out in the figure, the 2008 DJFM precipitable water was the third highest for the period of record.

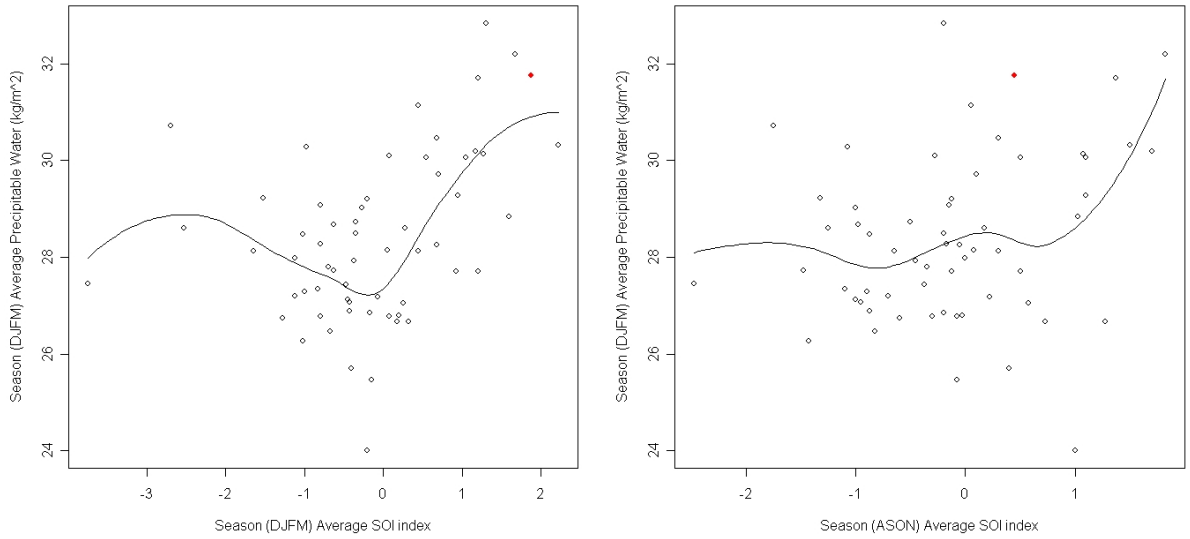

Figure 5.15 Average DJFM (left; R=0.395) and ASON (right; R=0.251) standardized SOI index versus the DJFM precipitable water from 1948 - 2008. Red dot is 2008 season.

Rather than using general climate indices such as the SOI, tailored indices can be developed to have stronger correlations with specific areas. As such, Figure 5.16 shows the correlation between preceding and concurrent sea surface temperature (SST) and the DJFM precipitable water for the Brisbane/Toowoomba area. The box with the white dashed lines shows the area of highest correlation. The plot of SST averages from each area against the precipitable water show a positive relationship (Figure 5.17).

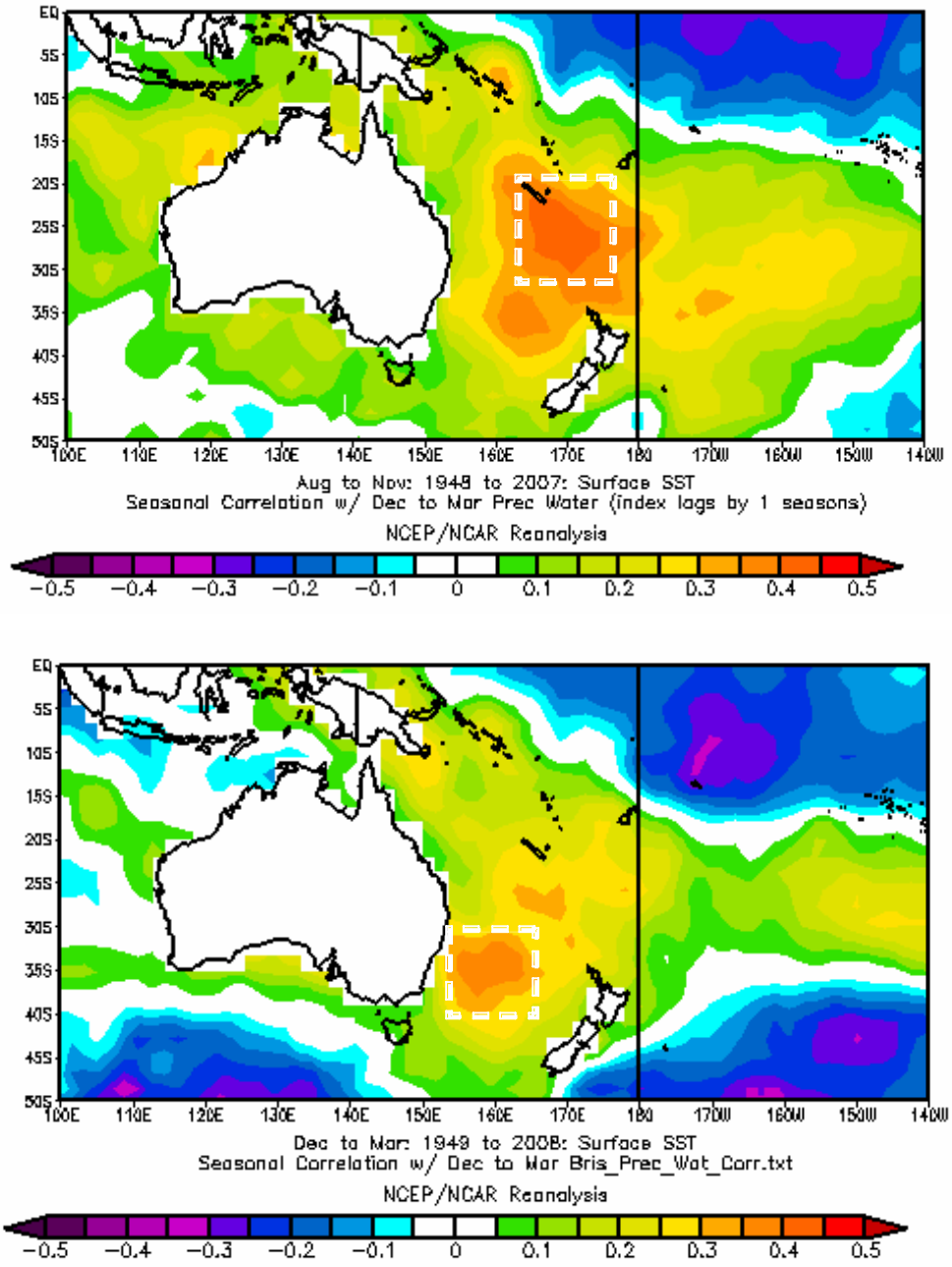

Figure 5.16 Correlation between ASON (top) and DJFM (bottom) surface SST with DJFM precipitable water. Dashed white box represents area of highest correlation (top: lat. -20.0 to -31.4, long. 163.1 to 174.4; bottom: lat. -29.5 to -41.0, long: 153.8 to 166.9).

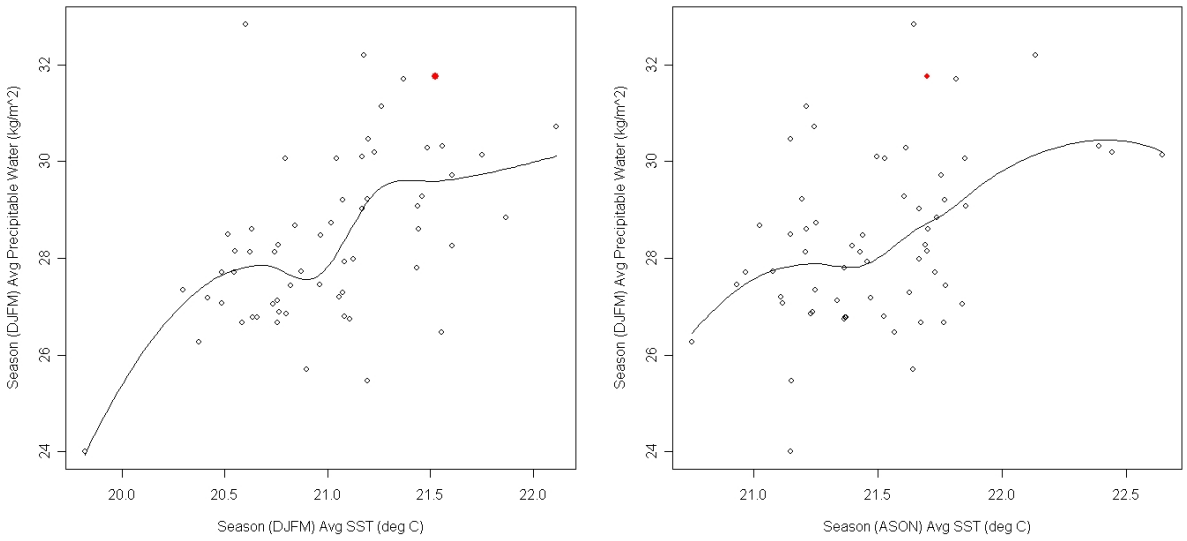

Figure 5.17 Scatterplot of average DJFM (left) and ASON (right) SST (deg C) versus DJFM precipitable water (kg/m^2). Red dot is 2008 season.

5.4 RADAR CLIMATOLOGY

5.4.1 Introduction

During the period December 2007 through the end of March 2008 a scientific study dedicated to understanding the effects of seeding of continental clouds in South East Queensland, Australia was conducted. The Cloud Seeding Research Project (CSRP) had at its disposal two aircraft; one dedicated to dispersing seeding material and a research aircraft fitted with a suite of instruments capable of measuring basic state variables, cloud droplet size distributions (DSDs), aerosol particle size distributions (ASDs) and chemical tracers (SO2, O3 and NOy). Additionally a network of five radars was employed to remotely sense the microphysical characteristics of the clouds.

This section summarizes some statistics of storms in the Brisbane region. The statistics were evaluated using measurements obtained with the Marburg S-band (10 cm wavelength) radar, which is located approximately 60 km SSW of Brisbane airport and has been measuring cloud systems on a near-continuous basis since January 2000. The statistics were derived utilizing the Thunderstorm Identification, Tracking, Analysis and Nowcasting (TITAN) software package (Dixon and Wiener 1993). TITAN defines storms as contiguous areas exceeding thresholds for reflectivity and size. In the following analysis, these thresholds have been chosen as 35 dBZ and 30 km^2 for reflectivity and size, respectively.

5.4.2 Storm initiation locations

Figure 5.18-Figure 5.24 are frequency histograms of storm initiation locations for the years 2000 to 2006 inclusive. Table 5.2 summarizes the total number of storms per year. The maximum number of storms was recorded in 2002 after which there was a steady decline with

the minimum number of storms recorded in 2006. In fact, the number of storms recorded in 2006 was roughly a quarter of the number in 2002.

Table 5.2. Number of storms registered by TITAN in a year.

Year	Number of storms (% of total)
2000	3974 (15)
2001	5068 (19)
2002	7370 (28)
2003	2500 (11)
2004	3246 (12)
2005	2208 (8)
2006	1861 (7)
Total	26227

One of the most notable features of Figure 5.18-Figure 5.24 is the preferred location for storm initiation inland. This preferred location, which extends in a north-south band between approximately 27°S and 29°S and in an east-west band between 151.5°E and 153°E corresponds spatially to the location of the Great Dividing Range, and indicates the importance of topographic forcing for storms. The formation of storms over the ranges, which may then propagate towards the coast and the more densely populated Brisbane region is well-known to local forecasters. The ability of a storm to sustain itself as it moves East is governed by the stability profile over the Brisbane plains; if conditions are stable then the storms will dissipate, however, if unstable conditions prevail then the storms which form over the ranges may intensify resulting in intense rainfall, the possibility of flash flooding and hail (Bureau of Meteorology Queensland Office 2008). Figure 5.25 is a frequency histogram for all storms in the 2000-2006 period. The region of preferred storm initiation over the ranges is particularly pronounced in this plot.

Also of interest is that the preferred location of storm initiation collocates with the position of the Wivenhoe Dam catchment region, which is one of the major water-storage supplies for the Brisbane population. Another region of enhanced storm initiation occurs south of Brisbane at 152.8°E, 28.4°S. This is near Beaudesert, a region susceptible to frequent flash flooding, and also the location of some smaller dams supplying Brisbane. For all years there is an enhanced region of storm formation near the coast. These storms are most likely trade wind cumulus, which form just off the coast of SE QLD and propagate west under the influence of the prevailing trade winds, and generally intensify just along the coast. Trade cumulus were commonly encountered during the CSRP intensive field phase of 2007/2008 (see section 8.1.2).

Brisbane is in the subtropics, resulting in the climate being dominated by two main seasons. Although, not strictly tropical the seasons can be roughly classified as a “wet” and a “dry” season. The wet season extends (approximately) from October to March, while the dry season is between April and September. Figure 5.26 and Figure 5.27 illustrate the difference in the propensity for storms to form during these seasons. The total number of storms for the summer season was 21350 and for the winter season was 4877 (i.e. there are over four times as many storms during the summer months than the winter). Besides the increased number of storms which form during the summer season, there is also an enhanced region of storm

formation over the ocean to the East of Brisbane during the summer season. These storms are trade wind cumulus and are formed by quite distinct physical mechanisms than those storms that form over the ranges.

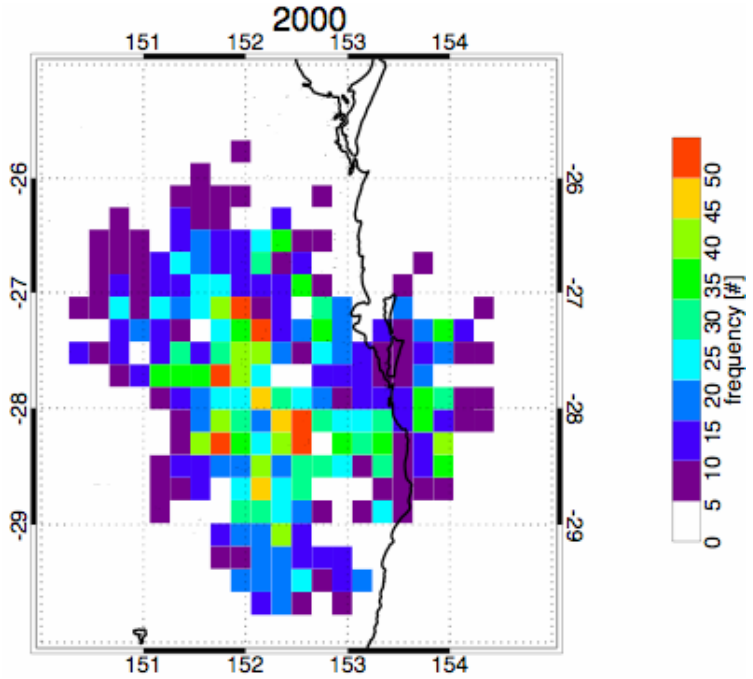

Figure 5.18. Initiation locations of TITAN derived storms for 2000. A storm was defined as a contiguous region, larger than 30 km^2 with a reflectivity greater than 35 dBz. The major catchment boundaries for the southeast Queensland region are also shown.

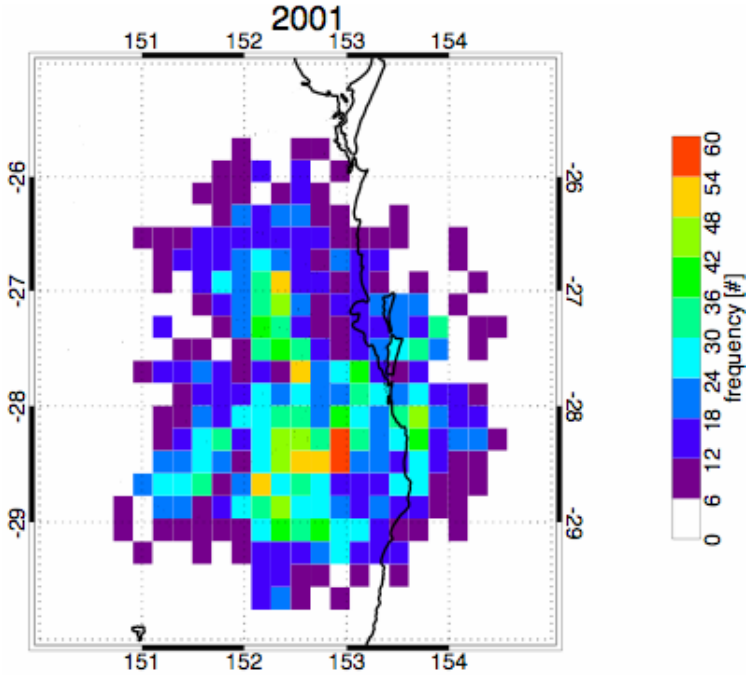

Figure 5.19. Same as Figure 5.18, except for 2001.

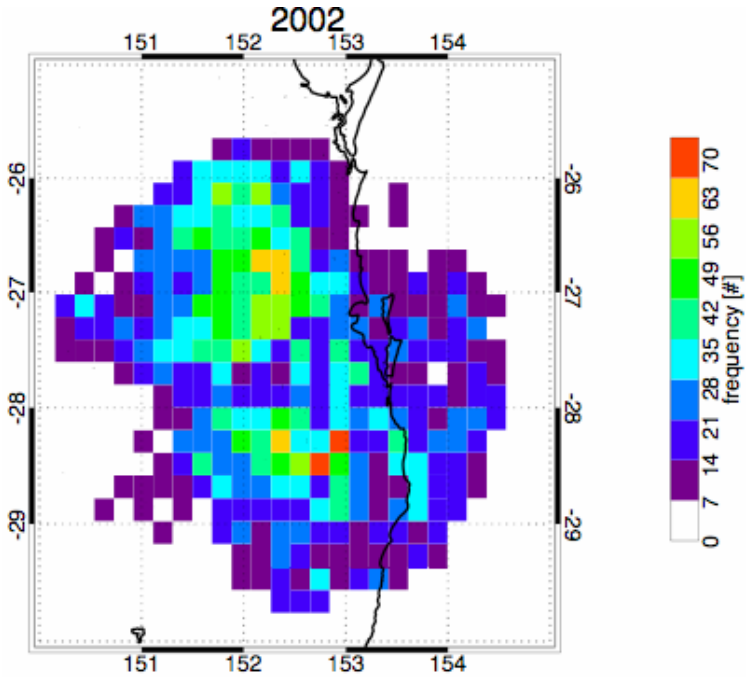

Figure 5.20. Same as Figure 5.18, except for 2002.

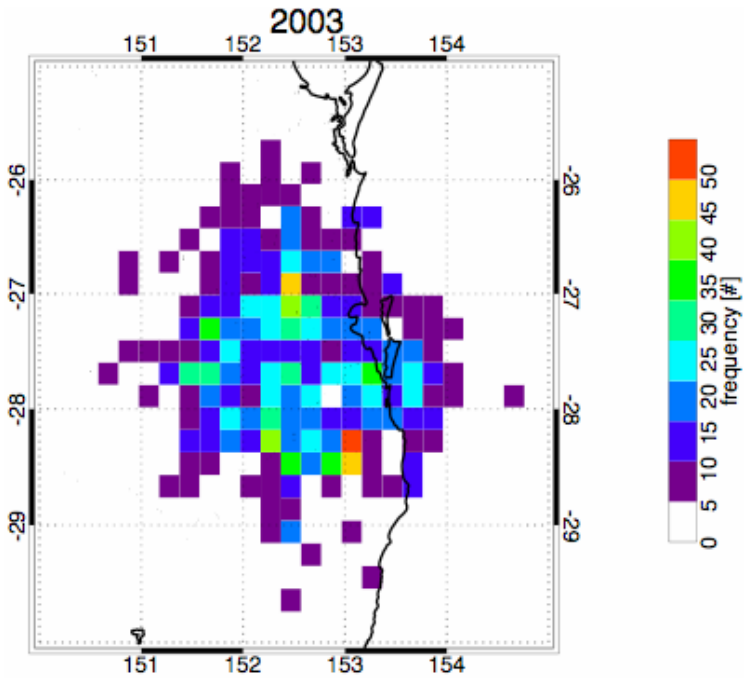

Figure 5.21. Same as Figure 5.18, except for 2003.

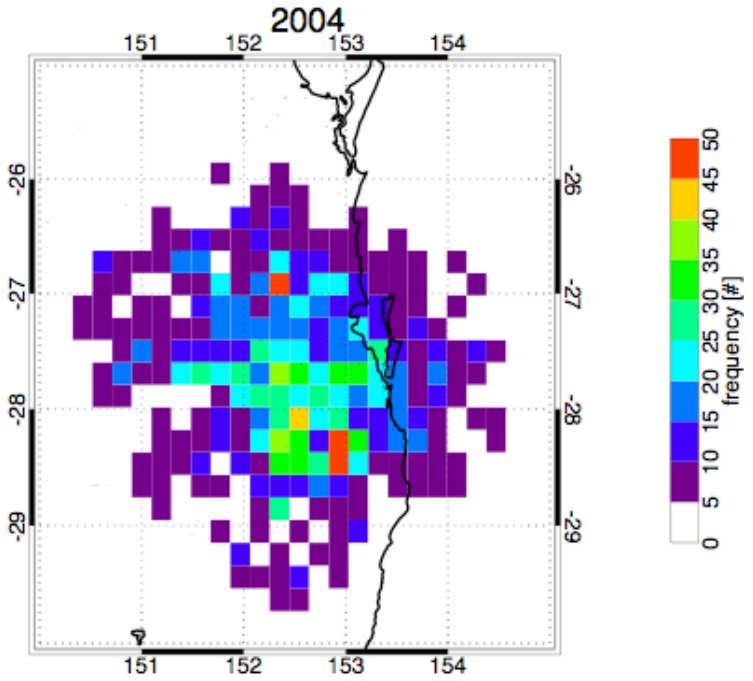

Figure 5.22. Same as Figure 5.18, except for 2004.

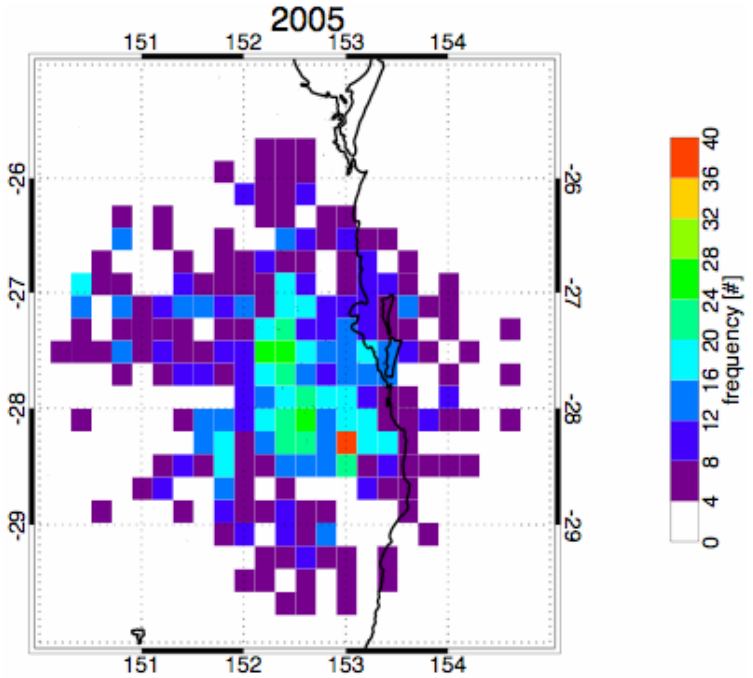

Figure 5.23. Same as Figure 5.18, except for 2005.

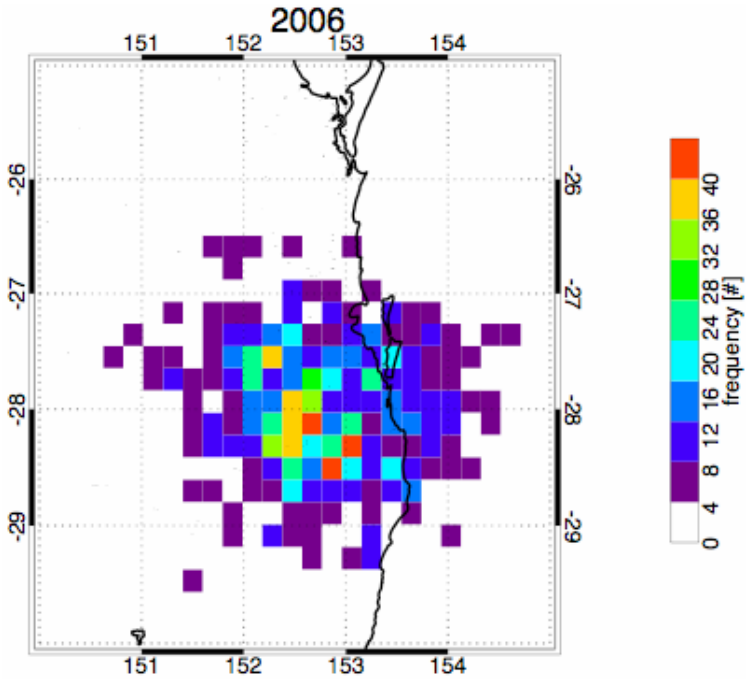

Figure 5.24. Same as Figure 5.18, except for 2006.

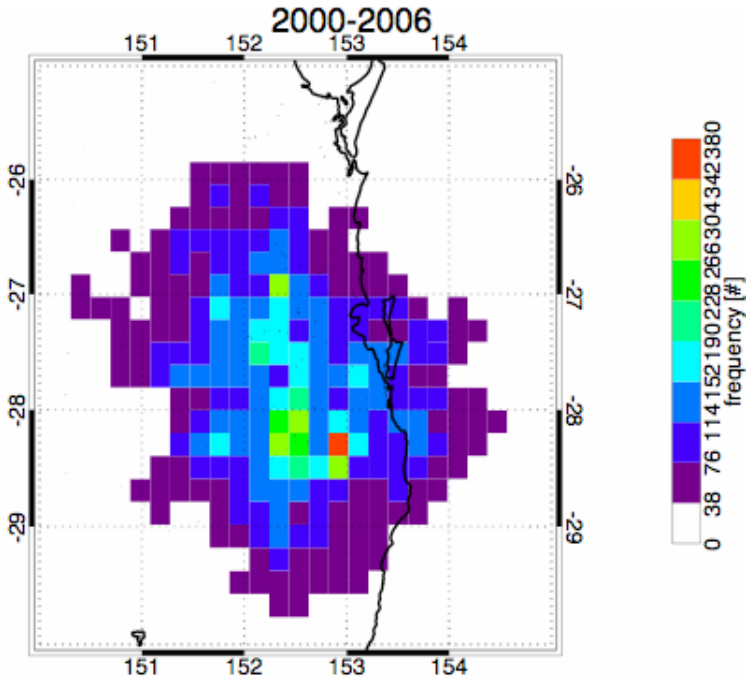

Figure 5.25. Initiation locations of TITAN-derived storms for the period 2000-2006 inclusive. Note the preferred region of storm initiation is governed by the surrounding topography. Most storms are topographically-forced by the ranges to the West of Brisbane.

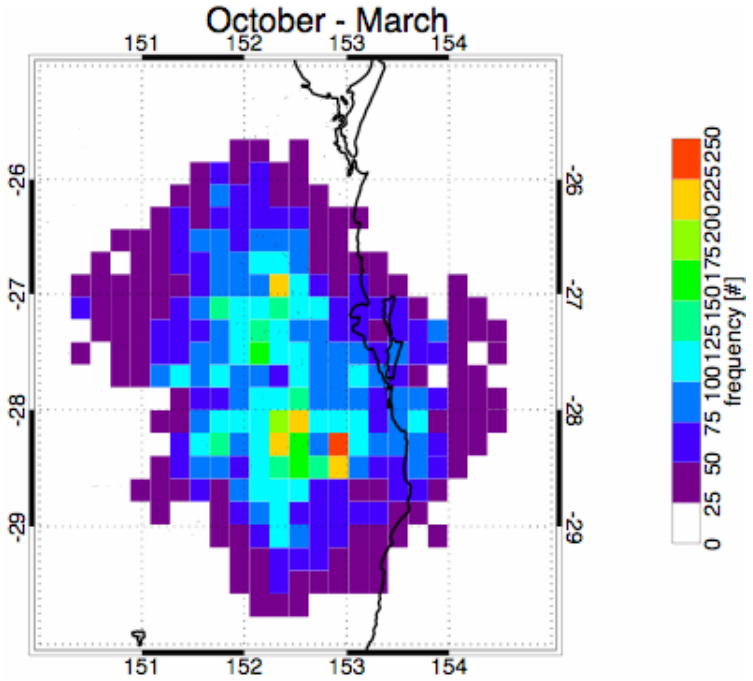

Figure 5.26. Initiation locations of TITAN-derived storms for all years (2000-2006) for the months October-March, inclusive. This period corresponds to summer months.

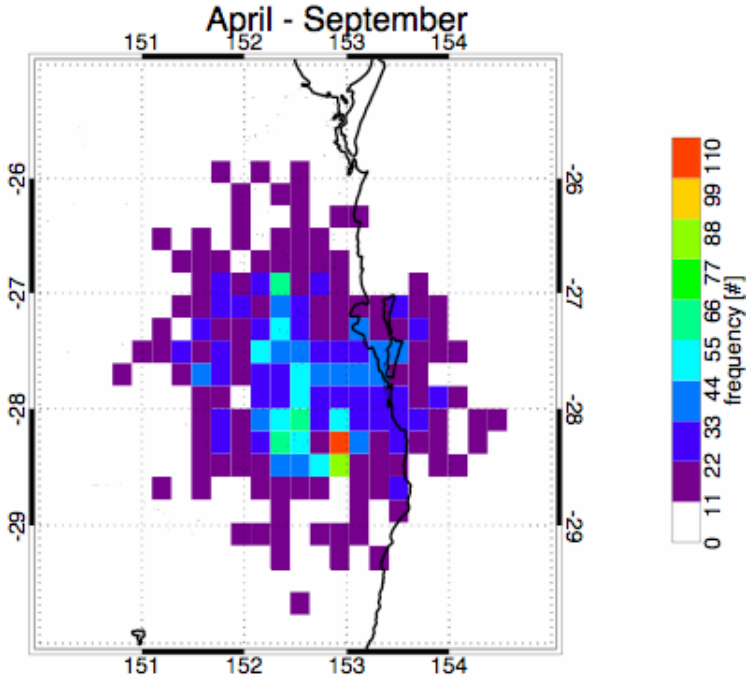

Figure 5.27. Initiation locations of TITAN-derived storms for all years (2000-2006) for the months April-September, inclusive. This period corresponds to winter months.

5.4.3 Storm top heights

Summer months

For residents of southeast Queensland (QLD), the typical forecast during the summer months is for "showers." These showers are produced by trade wind cumulus, with tops capped by the trade wind inversion which (during summer) is located at about 2500-4000 m. Additionally, the height of the trade wind inversion is nearly always below the freezing level (about 4500 m) during summer such that the warm-rain process (no ice particles involved) is an important mechanism by which precipitation is formed at this time of year. Trade wind cumulus were a prevalent cloud form encountered during CSRP, although not necessarily responsible for the most rainfall. Here we evaluate the frequency of storm top heights to determine the prevalence of trade wind cumulus and their contribution to the total precipitation in the SE QLD region.

Figure 5.28 shows a frequency histogram of the occurrence of storm-top height for the summer seasons of all years 2000-2006. The histogram indicates that the most prevalent storm-top height is about 5 km, which is very close to the approximate height of the trade wind inversion and the freezing level. Thus, the formation of rain via the warm rain process would appear to be an important mechanism for the initiation of precipitation. However, 60% of storms are below 6 km (which is well above the freezing level) indicating that both warm and ice phase processes may be responsible for the initiation of precipitation.

To gain some insight to the contribution of warm and ice-phase microphysics to the initiation of precipitation in SE QLD storms consider Figure 5.29, which is a frequency histogram of the height at which the maximum reflectivity occurs within cloud and for the same time period as Figure 5.28. It shows that most storms reach their maximum reflectivity below the height of the freezing level, which indicates that large drops are being formed below the freezing level. The prevalence of large drops below the freezing level is indicative of an effective collision-coalescence mechanism occurring within cloud and the production of precipitation-sized droplets before ice is formed. It is unclear as to how such large droplets are being formed at such low levels within cloud. This question will need to be examined in conjunction with analysis of microphysical measurements obtained on board the research aircraft employed during CSRP.

The storm-top frequency histogram decreases in what appears to be an exponential manner for storm top heights above 5 km. To examine if the distribution is exponential consider Figure 5.30. It is the same as Figure 5.28 except the ordinate has been plotted on a log scale. Most noticeable is the linear portion between 5 and 15 km, which indicates that above the height of the freezing level cloud top heights are exponentially distributed. A scale break is present at 5 km indicating the different energetics of the shallow trade wind cumulus and the deeper cumulus congestus clouds. Similar observations have been noted by Johnson et al. (1999), who suggested that glaciation of cumulus at the freezing level inhibits buoyancy and promotes detrainment.

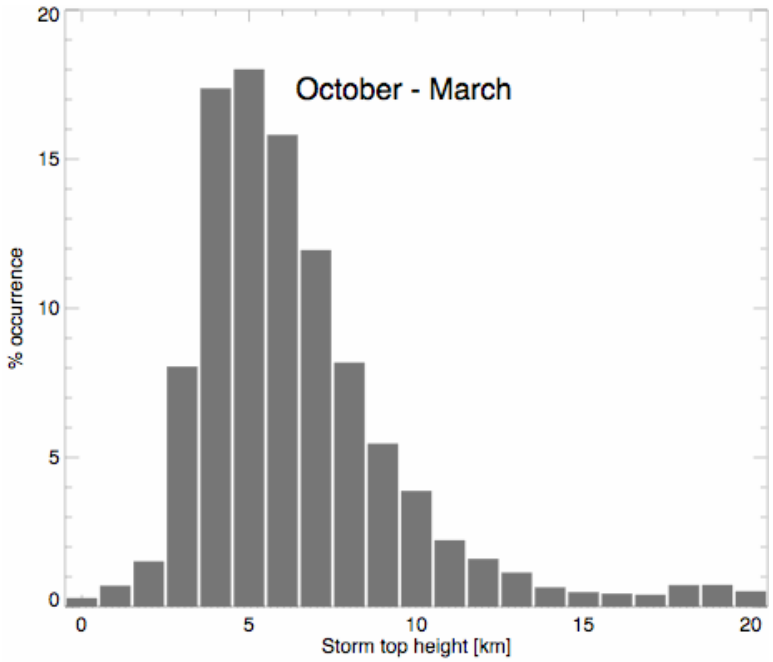

Figure 5.28. Frequency histogram of occurrence vs storm top height for the October-March season for 2001-2006. Approximately 40% of storms have tops below 5 km. The height of the freezing level for this season is about 4500 m. Therefore, both warm and cold microphysical processes may have been responsible for precipitation formation in storms during the summer months of 2000-2006.

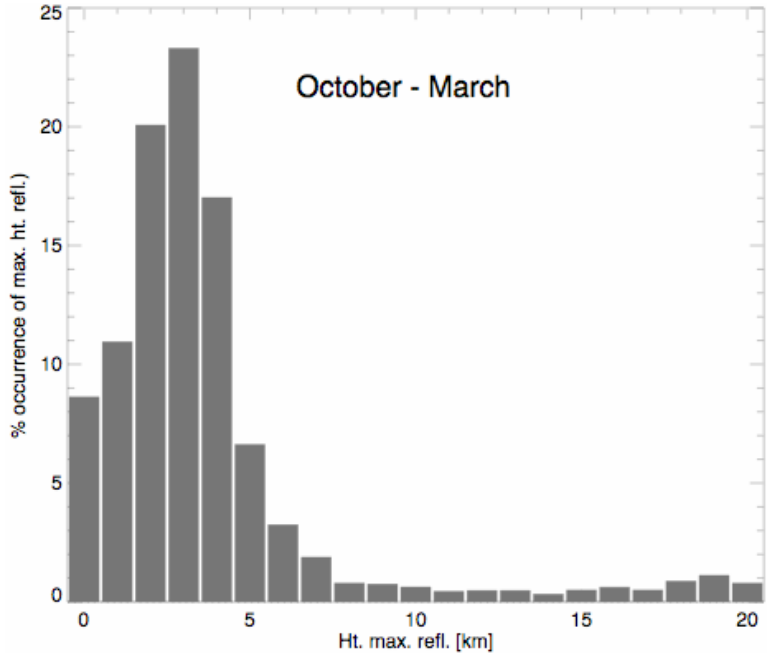

Figure 5.29. Frequency histogram of the frequency of occurrence of the maximum reflectivity vs. storm top height for the October-March period of 2000-2006. Approximately 80% of storms reach their maximum reflectivity below the freezing level suggesting that large drops are being efficiently formed by the collision-coalescence mechanism.

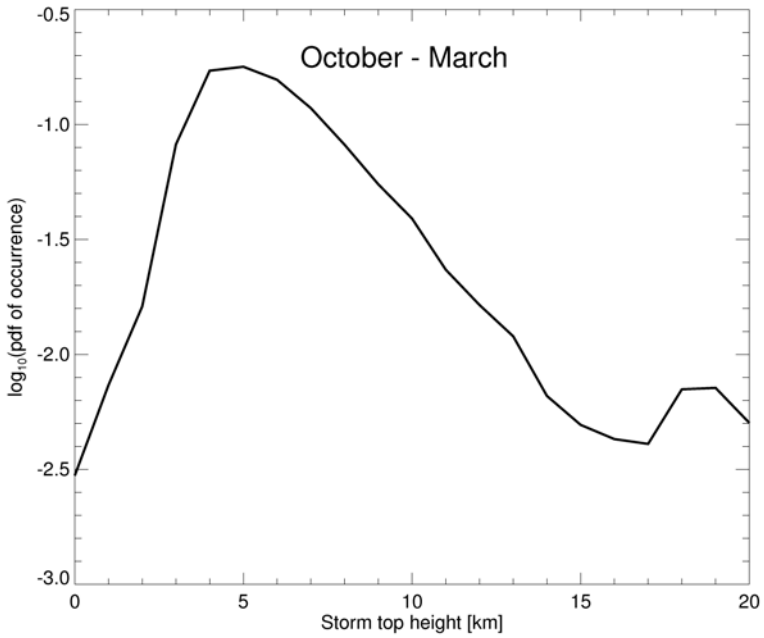

Figure 5.30. Same as Figure 5.28, however, the logarithm of the frequency of occurrence of storm-top height has been plotted on the ordinate. Storm-top heights exhibit a nearly linear relationship over the interval 5-15 km. Additionally, a scale break occurs for storm-top heights less than 5 km. This is suggestive of different physical processes controlling the height of storms above and below 5 km. Below 5 km, cloud top height is governed by the height of the trade wind inversion (which is approximately 5 km). Between 5-15 km (approximately the height of the tropopause), the storm top height can be described by an exponential relationship.

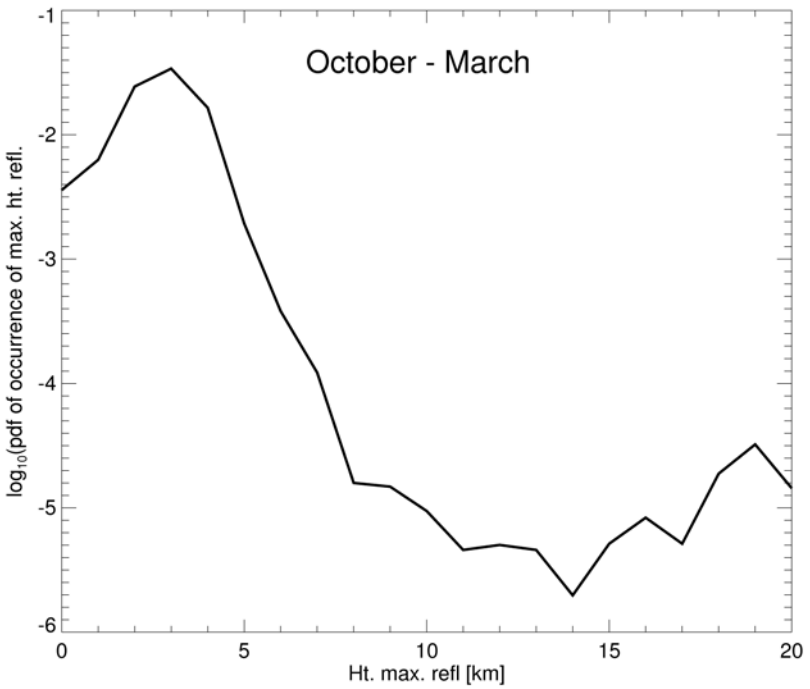

Figure 5.31. Same as Figure 5.29, however, the logarithm of the frequency of occurrence of the height of the maximum reflectivity is plotted on the ordinate. The height of the maximum reflectivity is linear over the interval 3-7 km when plotted in this manner suggesting an exponential relationship for the frequency of occurrence of the maximum reflectivity.

Winter months

The period between April and September in SE QLD is characterized by mild, clear days with limited rainfall. This is evident in the fewer number of storms initiated during the winter. Figure 5.32 shows the frequency histogram of storm-top heights for the winter months. Storms which form during this time of year are not only fewer in number but much shallower. The lower storm-top heights reached during the winter months is further illustrated in Figure 5.34. As for Figure 5.30, the ordinate has been plotted on a log scale. The linear portion of the plot (indicating an exponential relationship between storm top height and frequency) extends from 5 km (as for the summer months), however, is truncated at 10 km, whereas the linear portion for summer extended to 15 km. The truncation of the exponential relationship between storm-top height and frequency at 10 km and 15 km, for winter and summer respectively, could be due to insufficient counting statistics for larger storms, however, may also be related to the height of the tropopause. The tropopause is a stable layer which will inhibit convection and promote detrainment. During the summer months, the tropopause is at approximately 15 km, corresponding to the truncation in Figure 5.30. Further analysis of climatological soundings is required to investigate this possibility.

Despite the storms being shallower during the winter months, they still exhibit maxima in their reflectivity histograms below 5 km (see Figure 5.33 and Figure 5.35), suggesting that warm rain processes are important for the initiation of precipitation even in the winter months.

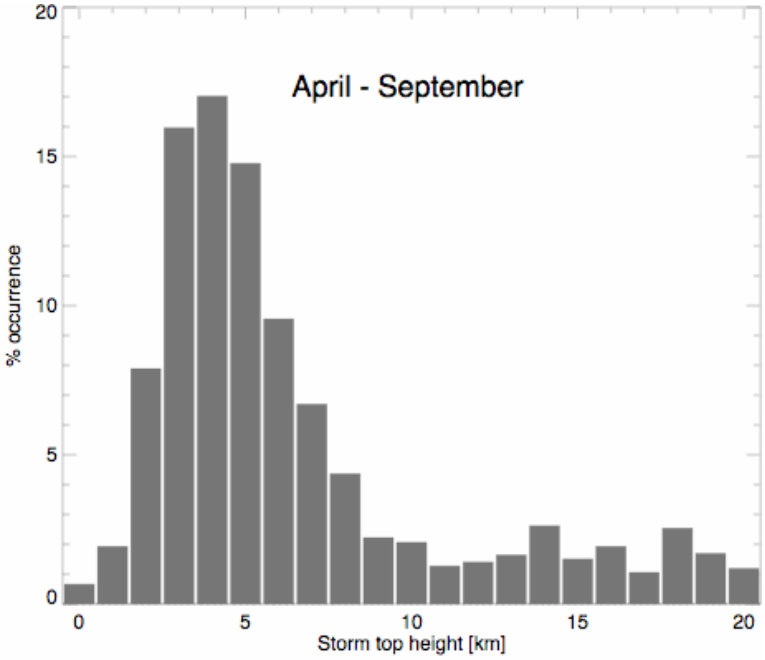

Figure 5.32. Frequency histogram of occurrence vs storm top height for the April-September season for 2001-2006.

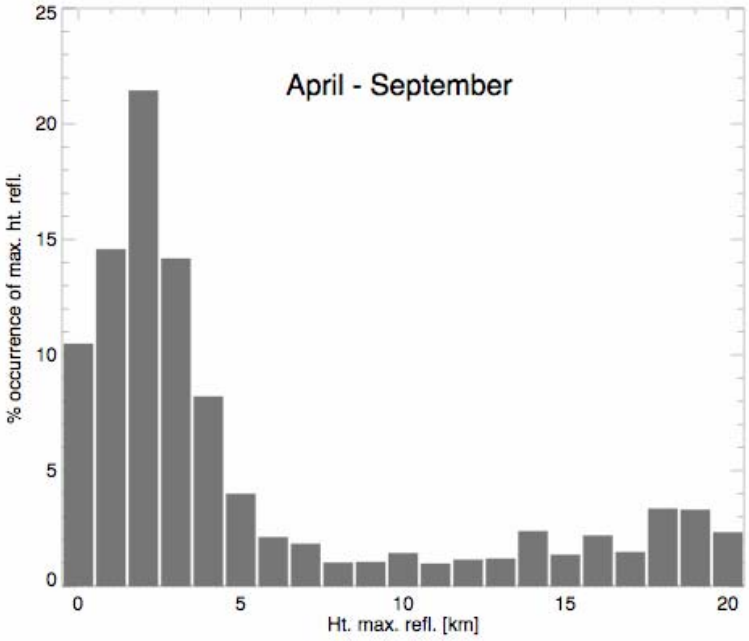

Figure 5.33. Frequency histogram of the frequency of occurrence of the maximum reflectivity vs. storm top height for the April-September period of 2000-2006.

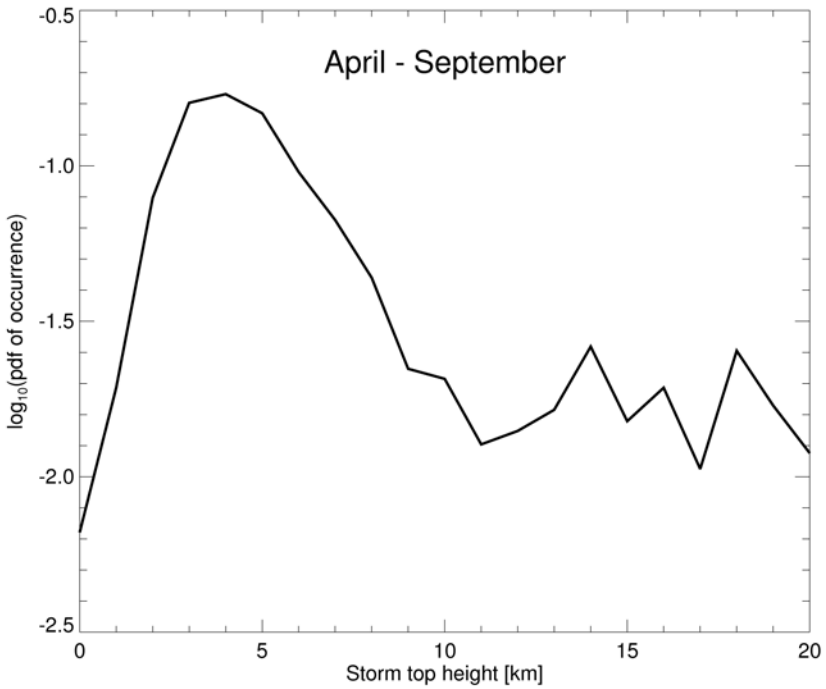

Figure 5.34. Same as Figure 5.32, however, the logarithm of the frequency of occurrence of storm-top height has been plotted on the ordinate. Storm-top heights exhibit a nearly linear relationship over the interval 5-10 km. As for Figure 5.30 a scale break occurs for storm-top heights less than 5 km. This is suggestive of different physical processes controlling the height of storms above and below 5 km. Below 5 km, cloud top height is governed by the height of the trade wind inversion (which is approximately 5 km). Between 5-10 km the storm top height can be described by an exponential fit.

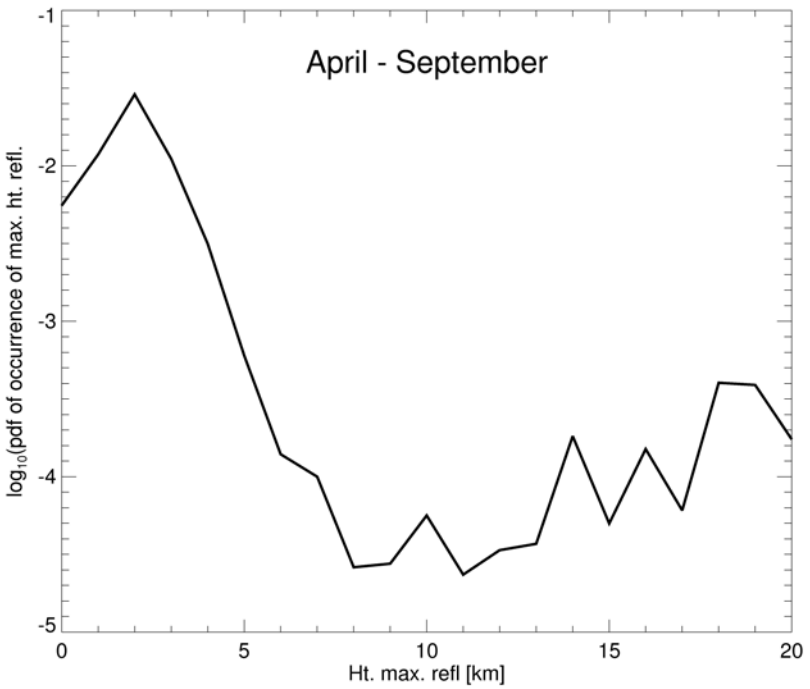

Figure 5.35. Same as Figure 5.33, however, for the winter period (April-September).

5.4.4 Summary

This section presented some statistics of storms measured by the Marburg S-band radar for the years 2000-2006. The statistics were derived using the TITAN storm tracking software which requires a minimum reflectivity threshold and storm size to identify a storm. For the present analysis, these thresholds have been specified as 35 dBZ and 30 km^2 for reflectivity and size, respectively.

Storm initiation locations were obtained for all years, both separately and for the entire period for 2000-2006. In all instances a well-defined band of storm initiation was collocated with elevated terrain to the west of Brisbane showing that topography has a strong influence on storm initiation. The Wivenhoe catchment region was also shown to be in an area conducive to storm initiation. It was also shown that the total number of storms decreased dramatically during the period 2003-2006 compared with the 2000-2002 period; 2002, in particular had a very high number of storms with nearly 30% of the total storm count being recorded in that year alone.

Storm initiation locations were also evaluated for the summer (October-March) and winter (April-September) months. Again, a well-defined region of storm initiation locations was collocated with elevated topography. Over 80% of storms occur during the summer pointing to the importance of this season in replenishing Brisbane's water supplies.

An analysis of the frequency distribution of storm top heights was made for the summer and winter seasons. It was found, for both the summer and winter seasons, that nearly 40% of storms were trade wind cumulus that had tops below or near the freezing level (about 4500 m). Additionally, nearly 80% of storms reached their maximum reflectivity below the freezing level showing that the initiation of precipitation by the warm rain process is an important process for rainfall production in southeast Queensland. A scale break in the distribution of storm top

heights was also found to occur near the freezing level. Above the freezing level, the frequency of occurrence of storm top heights was found to be exponentially distributed. In summer the exponential distribution could describe the frequency of occurrence of storm top heights up to 15 km, while in winter it held up to 10 km. Above these heights, another scale break occurred, which may be due to noise in counting statistics or possibly related to the height of the tropopause. Further analysis of soundings from Brisbane Airport will be required to resolve this question.

5.5 MODELING STUDIES

The Regional Atmospheric Modeling System (RAMS) was used in real time during the field project to forecast convection, and aided in the forecasting and planning for subsequent days' missions. The model was run by ingesting synoptic-scale weather data and using nested grids (down to the order of a kilometer resolution) to resolve convection in the Southeast Queensland region. The model was also run with a sophisticated two-moment bulk microphysics scheme, making it a highly advanced cloud resolving forecast model.

Analysis is underway using these modeling results to assess the model's ability to simulate the weather regimes and populations of cloud systems observed in the Southeast Queensland area. Techniques for using radar data to validate the model are also being developed and employed in this analysis.

6. SUMMARY OF RESEARCH FLIGHTS AND SEEDING FLIGHTS

6.1 SUMMARY OF ALL FLIGHT OPERATIONS

During the entire project a total of 236 flight hours combined between the two aircraft were flown: 150 by SEEDA1 and 86 by WXMOD. The breakdown by number of research flights (not including test or recurrency flights) is shown in Table 6.1 for each aircraft. Table 6.2 details each flight for both aircraft, and indicates whether or not seeding was performed (if seeding was performed, the type of seeding is listed). All the flight tracks for each aircraft are mapped in Figure 6.1–Figure 6.2.

Table 6.1. Total number of research flights per month by each aircraft.

Aircraft	December	January	February	March	TOTAL
SEEDA1	3	14	13	20	**50**
WXMOD	-	6	16	17	**39**

Table 6.2. All flights for both aircraft (SEEDA1 and WXMOD). Randomized cases are indicated with the randomized case number, non-randomized seeding flights are indicated with a capital letter, and all non-seeding flights are indicated with a lowercase Roman numeral. All SEEDA1 start and end times are for flight start and end time. WXMOD start and end times for randomized cases are the decision time and end time of seeding, for all non-randomized cases are the start and end times of the flight. Seeding type is hygroscopic (H), burn-in-place glaciogenic (BG), ejectable glaciogenic (EG), or no seeding (-).

		SEEDA1		WXMOD		
Flight #	Date YYMMDD	Start UTC	End UTC	Start UTC	End UTC	Seed Type H/BG/EG
i	071215	0436	0617	-	-	-
ii	071217	0508	0733	-	-	-
iii	071218	0000	0000	-	-	-
A	081219	0340	0554	-	-	H
iv	071220	1400	1649	-	-	-
v	080112	?	?	-	-	-
vi	080114	0441	0725	-	-	-
vii	080115	0436	0617	-	-	-
viii	080117	0508	0733	-	-	-
ix	080118	0417	0639	-	-	-
x	080121	0414	0537	-	-	-
xi	080121	0708	0851	-	-	-
B	080123	0550	0620	0523	0655	H
0	080124	-	-	0350	0428	-
C	080126	0314	0600	0416	0605	H
xii	080127	0218	0322	-	-	
D	080127	0451	0655	0411	0649	H
E	080129	0400	-	0433	0600	H
F	080129	-	0736	0600	0716	H
xiv	080131	0000	0252	-	-	H
G	080131	0407	0650	0520	0624	H

H	080201	0355	0633	0505	0630	H
1	080202	-	-	0224	0229	H
2	080202	-	-	0247	0252	H
3	080202	-	-	0302	0313	H
4	080202	-	-	0322	0322	H
I	080202	0501	-	0526	-	H
J	080202	-	0729	-	0719	H
xv	080206	0038	0239	-	-	-
xvi	080206	0406	0431	-	-	-
xvii	080206	0502	0620	-	-	-
K	080207	0220	0539	0518	0525	H
xviii	080208	0352	0656	-	-	-
5	080209	0157	-	0329	0338	H
6	080209	-	0519	0405	0405	-
L	080211	0201	0549	0422	0515	BG
7	080213	-	-	0320	0329	H
8	080213	-	-	0343	0351	H
9	080213	-	-	0359	0359	-
10	080213	-	-	0429	0438	H
11	080213	-	-	0446	0446	-
12	080213	-	-	0503	0509	H
ixx	080214	0139	0311	-	-	-
M	080216	0258	0529	-	-	H
13	080220	-	-	0319	0329	H
14	080220	-	-	0338	0350	H
15	080220	-	-	0408	0421	H
16	080220	-	-	0432	0443	H
17	080220	-	-	0619	0626	H
N	080225	-	-	0137	0351	EG
xx	080227	0213	0539	-	-	-
xxi	080228	0408	0706	-	-	-
O	080229	0150	0510	0459	0545	H
xxii	080301	0107	0254	-	-	-
xxiii	080303	0055	0225	-	-	-
18	080303	-	-	0311	0320	H
19	080303	-	-	0335	0344	H
20	080303	-	-	0353	0357	H
21	080303	-	-	0646	0651	H
xxiv	080305	0006	0010	-	-	-
xxv	080305	0100	0440	-	-	-
xxvi	080305	0546	0811	-	-	-
22	080306	0100	-	0324	0336	H
23	080306	-	-	0356	0356	H
24	080306	-	0436	0416	0426	H
xxvii	080307	0245	0639	-	-	-
P	080309	0049	0139	0306	0440	H
25	080309	-	-	0448	0448	H
26	080309	-	-	0535	0535	H
27	080309	-	-	0614	0624	H
28	080310	0110	-	0210	0226	H
29	080310	-	0407	0304	0304	H
xxviii	080311	0357	0557	-	-	-
ixx	080311	0637	0832	-	-	-
xxx	080313	0128	0424	-	-	-
30	080315	0100	-	0052	0052	-
31	080315	-	-	0111	0123	H
32	080315	-	-	0134	0202	H
33	080315	-	-	0330	0330	-

34	080315	-	0431	0342	0342	-
xxxi	080316	0210	0529	-	-	-
xxxii	080318	0138	0515	-	-	-
Q	080319	0108	0507	0255	0430	H
R	080320	0147	0358	0221	0228	H
35	080322	-	-	0219	0228	H
36	080322	-	-	0239	0249	H
37	080322	-	-	0309	0319	H
38	080322	-	-	0428	0438	H
39	080322	-	-	0445	0459	H
40	080324	0307	-	0214	0220	H
41	080324	-	-	0225	0230	H
42	080324	-	-	0236	0241	H
43	080324	-	-	0246	0258	H
44	080324	-	-	0310	0315	H
45	080324	-	-	0332	0337	H
46	080324	-	-	0346	0359	H
47	080324	-	-	0406	0421	H
48	080324	-	-	0543	0548	H
49	080324	-	-	0550	0555	H
50	080324	-	-	0605	0616	H
51	080324	-	0659	0631	0636	H
52	080326	0527	-	0509	0525	H
53	080326	-	0818	0602	0618	H
54	080327	-	-	0550	0550	H
55	080327	-	-	0615	0615	H
56	080327	-	-	0641	0641	H
57	080327	-	-	0658	0712	H
58	080328	0305	-	0254	0310	H
59	080328	-	-	0326	0336	H
60	080328	-	-	0403	0407	H
61	080328	-	-	0418	0418	H
62	080328	-	0600	0435	0438	H

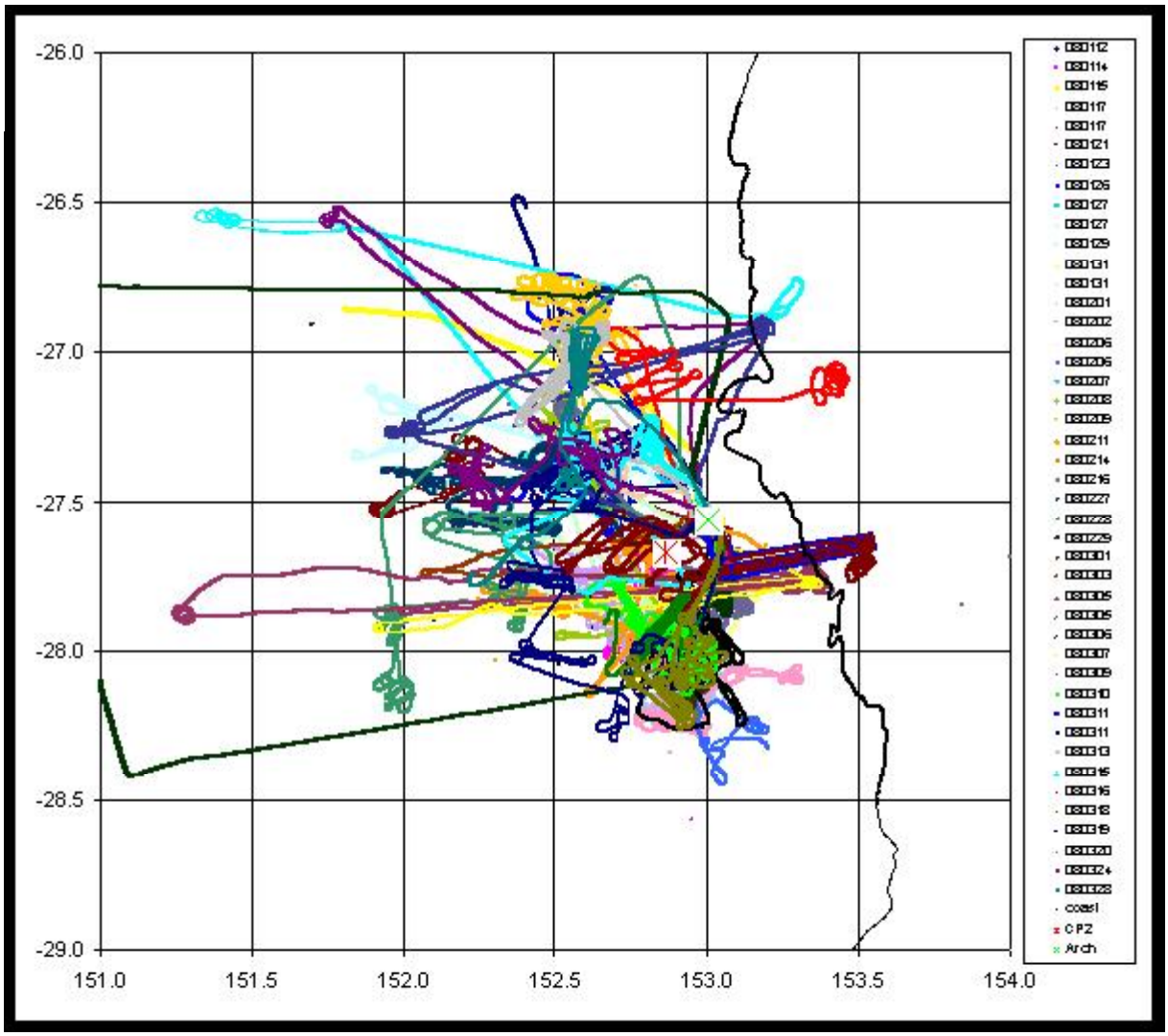

Figure 6.1. Map of all flight tracks for SEEDA1. Red asterisk indicates location of CP2 radar, and small green 'X' indicates location of Archerfield airport.

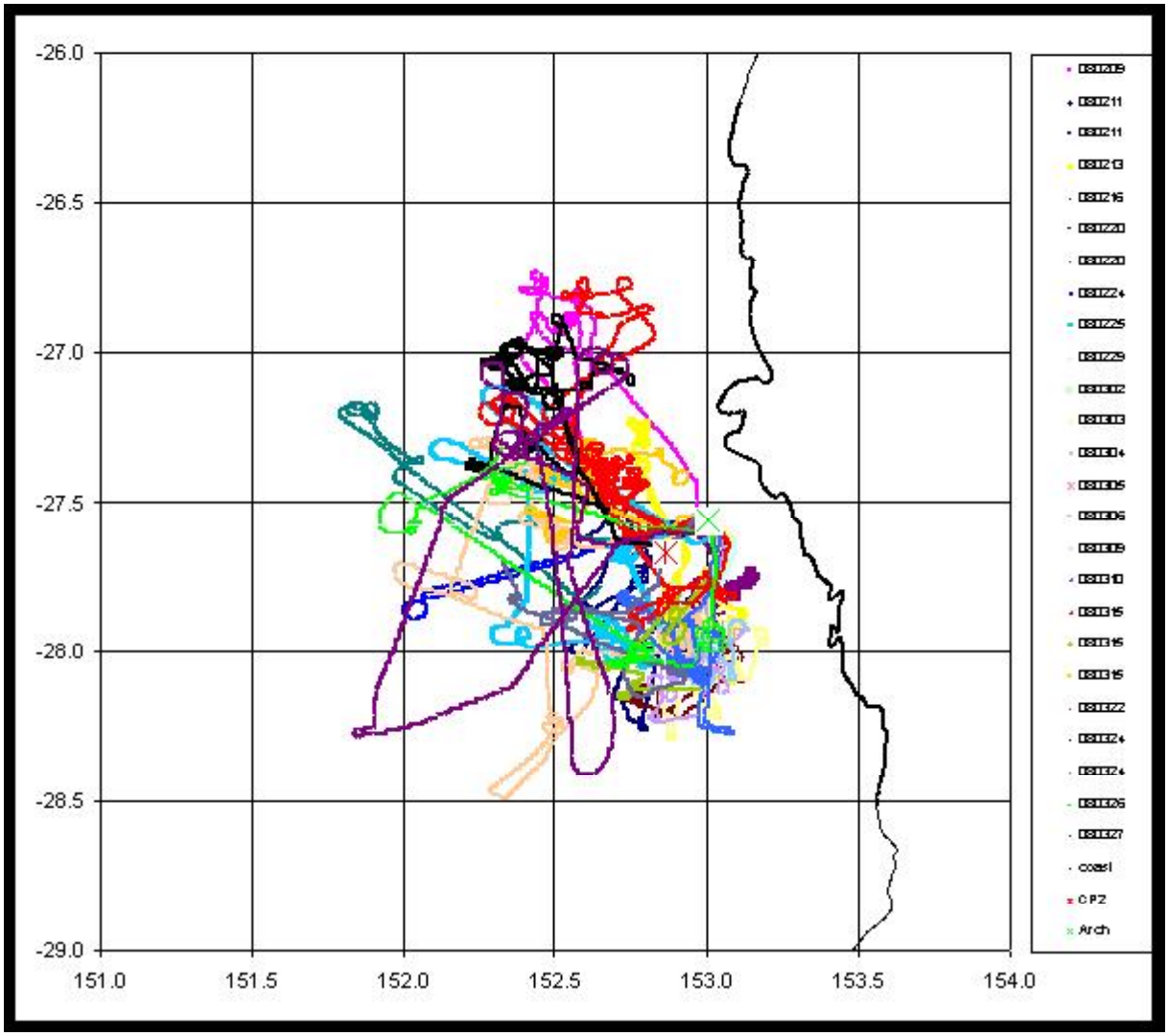

Figure 6.2. Same as Figure 6.1, except of all flight tracks for WXMOD.

6.2 SUMMARY OF ALL RANDOMIZED SEEDING FLIGHTS

During the CSRP project there were a total of 62 randomized cases declared over 14 days (see Table 6.3). All randomized cases were declared and seeded by the WXMOD aircraft. To be an eligible case for randomized seeding, the pilots had to identify a cloud with a rain-free base that appeared to be growing and had an updraft speed of at least 200 ft min^{-1}. If the updraft diminished below this threshold during seeding, the case was terminated. Typically three sets of flares were burned for each case, but this was at the discretion of the Operations Director.

During the period of February 4-9, 2008, flooding in the southeast Queensland region prevented us from performing any seeding operations, unless we could identify treatable clouds over the Wivenhoe and Somerset catchment areas only. This restriction inhibited some opportunities to include the deeper cloud systems that were in the area during this time in the randomized study (see section 8.1.2). The majority (52) of the randomized cases were shallow clouds, with tops at or below the freezing level. Figure 6.3 shows the randomized case locations.

The randomized study focused primarily on the Wivenhoe and Somerset catchments, with a secondary area of interest in the southern dual-Doppler lobe (south and southeast of CP2).

Table 6.3. All randomized cases: start time indicates decision time, end time indicates end of seeding (or for non-seed cases end time was taken as either start time or a default of start time plus 5 min). Latitude and longitude is location of WXMOD at decision time. Seeding type was always hygroscopic (H) for all randomized cases. Cloud base heights and updraft speeds were estimates reported by the pilots.

Case #	*Date* YYMMDD	*Start* UTC	*End* UTC	*LAT* deg S	*LON* deg E	*Seed* Y/N	*Type*	*Approx Cloud Base* *ft*	*Approx Updraft vel* *ft/min*
1	080202	0224	0229	27.78	153.14	Y	H	2000	200
2	080202	0247	0252	27.90	152.93	N	H	2000	200
3	080202	0302	0313	28.10	153.08	Y	H	2000	200
4	080202	0322	0322	28.06	152.80	N	H	2000	200
5	080209	0329	0338	26.90	152.52	Y	H	5000	200
6	080209	0405	0405	26.80	152.43	N	H	5000	200
7	080213	0320	0329	27.89	153.09	Y	H	3000	300
8	080213	0343	0351	28.07	153.05	Y	H	3000	200
9	080213	0359	0359	27.71	153.01	N	H	3000	400
10	080213	0429	0438	27.27	152.79	Y	H	3000	400
11	080213	0446	0446	27.57	152.86	N	H	3000	400
12	080213	0503	0509	27.96	152.96	Y	H	3000	300
13	080220	0319	0329	27.99	153.06	N	H	3000	200
14	080220	0338	0350	28.17	152.77	Y	H	3000	300
15	080220	0408	0421	27.92	153.02	Y	H	3000	300
16	080220	0432	0443	28.08	153.10	Y	H	3000	200
17	080220	0619	0626	27.17	151.80	N	H	3000	500
18	080303	0311	0320	27.94	152.98	Y	H	3000	300
19	080303	0335	0344	28.09	153.11	Y	H	3000	300
20	080303	0353	0357	28.28	152.88	N	H	3000	800
21	080303	0646	0651	27.99	152.89	N	H	3000	300
22	080306	0324	0336	28.05	152.96	Y	H	3800	400
23	080306	0356	0356	28.07	153.04	N	H	3800	400
24	080306	0416	0426	28.10	152.90	Y	H	3800	400
25	080309	0448	0448	27.32	152.25	N	H	3800	400
26	080309	0535	0535	28.22	152.52	N	H	3800	400
27	080309	0614	0624	27.89	152.94	Y	H	3800	400
28	080310	0210	0226	27.93	152.87	Y	H	6000	400
29	080310	0304	0304	28.05	152.91	N	H	6000	400
30	080315	0052	0052	27.40	152.77	N	H	3000	300
31	080315	0111	0123	27.62	152.81	Y	H	3000	500
32	080315	0134	0202	27.40	152.68	Y	H	3000	600
33	080315	0330	0330	28.15	152.73	N	H	3000	300
34	080315	0342	0342	28.04	152.59	N	H	3000	400
35	080322	0219	0228	27.92	152.72	Y	H	2500	600
36	080322	0239	0249	27.81	153.05	Y	H	2500	600

37	080322	0309	0319	27.14	152.78	Y	H	2500	200
38	080322	0428	0438	27.18	152.31	N	H	2500	200
39	080322	0445	0459	27.37	152.73	Y	H	2500	200
40	080324	0214	0220	27.14	152.47	N	H	3000	500
41	080324	0225	0230	26.98	152.38	N	H	3000	700
42	080324	0236	0241	27.00	152.50	N	H	3000	500
43	080324	0246	0258	27.19	152.38	Y	H	3000	500
44	080324	0310	0315	27.10	152.74	N	H	3000	500
45	080324	0332	0337	27.03	152.31	N	H	3000	500
46	080324	0346	0359	27.29	152.44	Y	H	3000	500
47	080324	0406	0421	27.38	152.26	Y	H	3000	500
48	080324	0543	0548	27.74	152.30	N	H	3000	400
49	080324	0550	0555	27.83	152.36	N	H	3000	500
50	080324	0605	0616	28.06	152.91	Y	H	3000	400
51	080324	0631	0636	27.88	152.56	N	H	3000	400
52	080326	0509	0525	27.47	152.29	Y	H	3000	1000
53	080326	0602	0618	28.06	152.68	Y	H	3000	500
54	080327	0550	0550	28.22	152.21	N	H	9000	800
55	080327	0615	0615	28.03	152.11	N	H	9000	500
56	080327	0641	0641	28.18	152.79	N	H	9000	200
57	080327	0658	0712	27.88	152.00	Y	H	9000	800
58	080328	0254	0310	27.65	152.03	Y	H	2000	400
59	080328	0326	0336	27.77	151.86	N	H	2000	300
60	080328	0403	0407	27.99	152.41	N	H	2000	300
61	080328	0418	0418	28.04	152.70	N	H	2000	200
62	080328	0435	0438	28.02	152.45	Y	H	2000	200

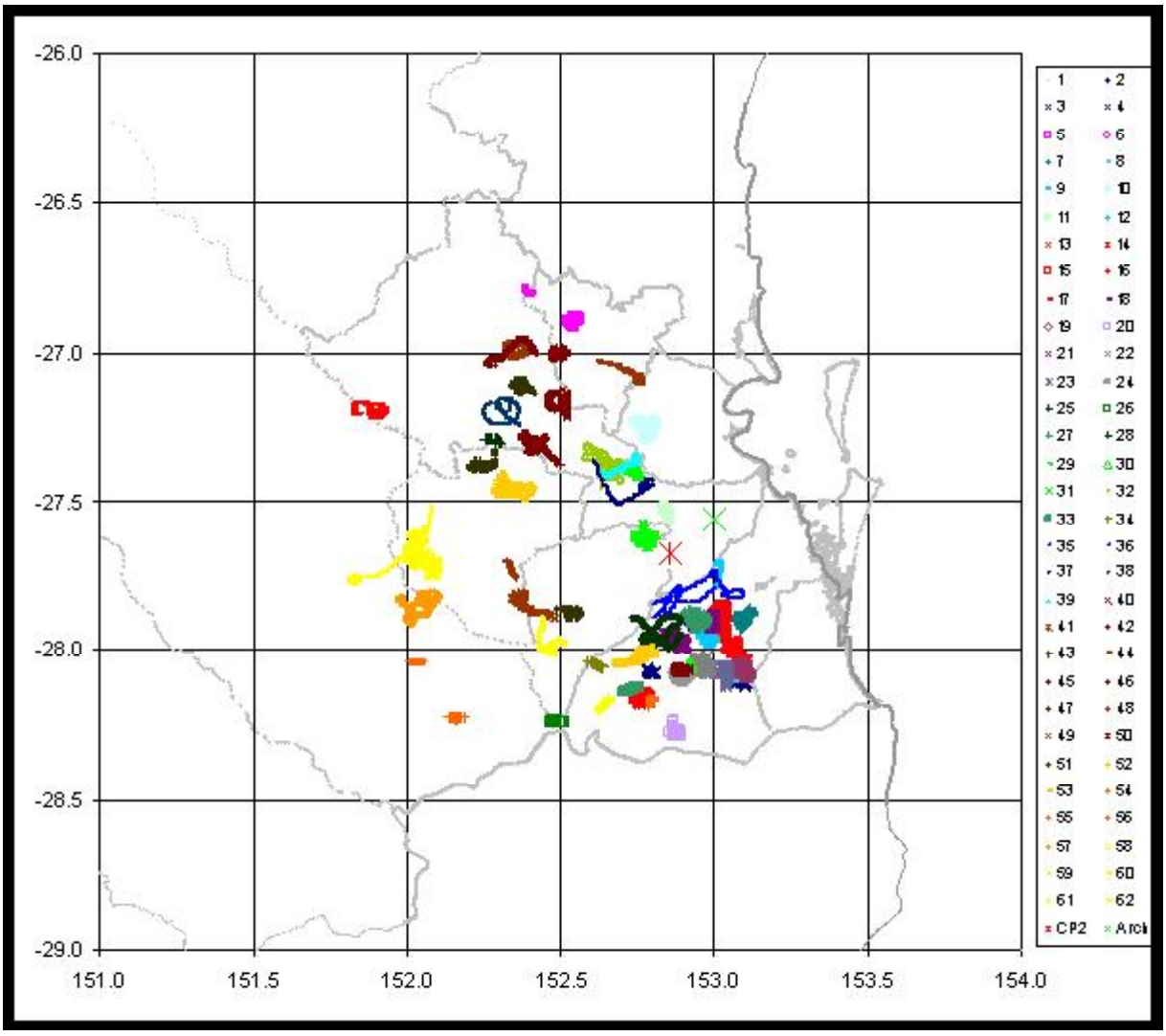

Figure 6.3. Map showing the flight locations of all randomized cases. Only flight segments during randomized case declaration are shown. CP2 is denoted by a red asterisk and Archerfield by a green X.

7. AEROSOL AND MICROPHYSICS STUDIES

7.1 MEASUREMENTS OF AEROSOLS AND CCN IN SOUTHEAST QUEENSLAND

7.1.1 14 February 2008

On 14 February 2008 the atmosphere was characterized by a moist layer up to a weak inversion at 600 hPa, above which the atmosphere was a bit drier (Figure 7.1). Winds were out of the southeast below this height and were out of the west above it. Otherwise, given the nearly moist adiabatic temperature profile, the atmosphere was fairly stable, and only shallow convection formed. Clouds that formed moved to the northwest.

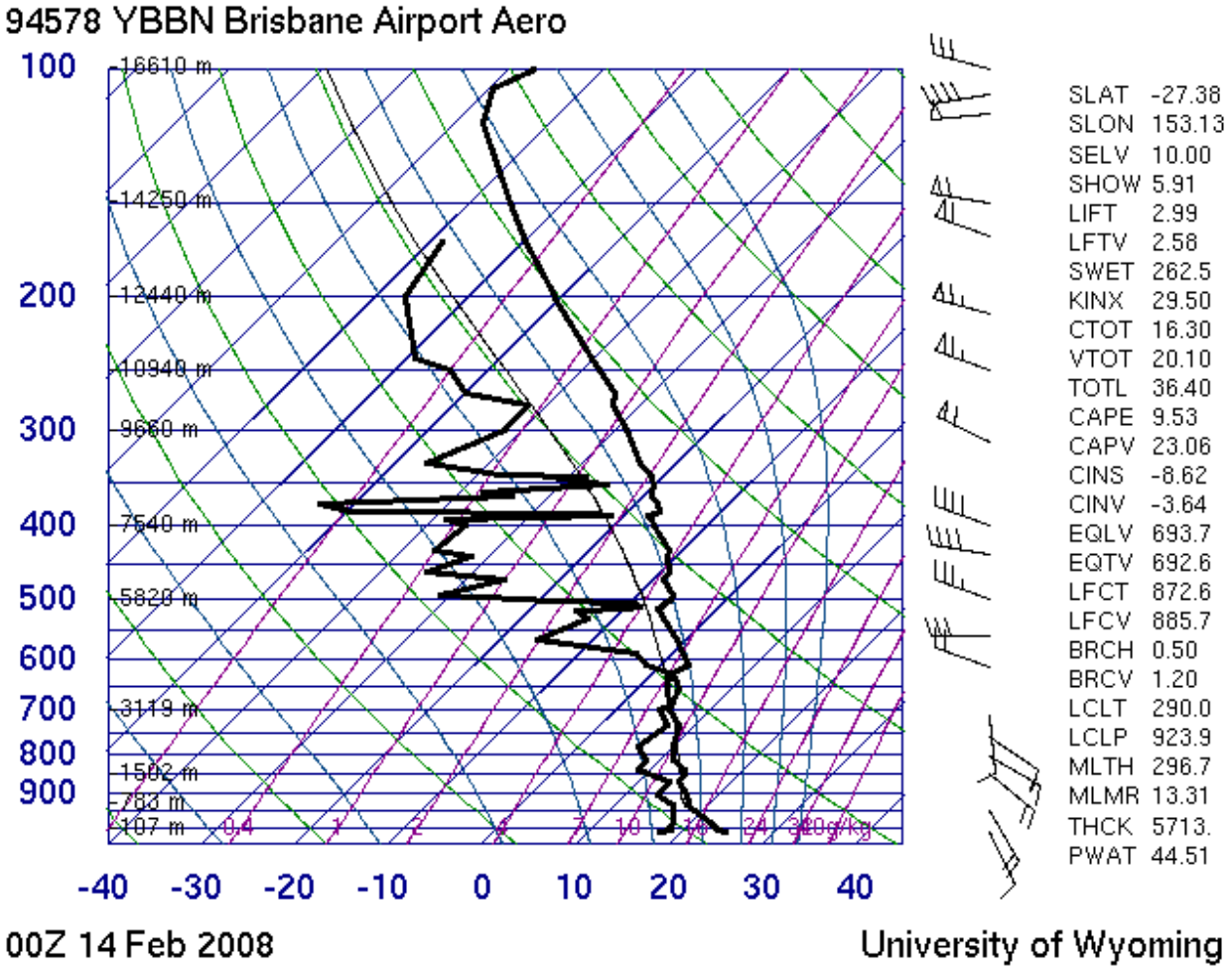

Figure 7.1. Thermodynamic sounding taken at Brisbane Airport at 00Z on 14 February 2008 (10:00am local time).

DMA measurements taken near the surface (130 m) on ascent out of Archerfield indicate a very polluted air mass, with the primary mode near .01 microns and concentrations in this mode of 1200 cm^{-3} (Figure 7.2). A secondary mode is also observed near .08 microns with concentrations over 1000 cm^{-3} also. A mode at 0.01 microns usually indicates nucleation; a process where aerosols are formed due to gas-to-particle (gtp) conversion. The mode of 0.08

microns is closer to the accumulation mode, which is usually characteristic of particle growth due to aging. The primary mode at 0.01 microns is indicative that the measurements were being conducted close to a pollution source.

DMA data can also be used to calculate CCN concentrations. Using the DMA aerosol size distribution, Köhler Theory-based relationships can be used to predict the CCN number concentrations assuming that the environmental aerosol has some soluble fraction of an organic or inorganic compound. If the size distribution and chemical composition of the ambient particles are simultaneously measured, then the measured CCN behavior can be compared to that predicted by Köhler Theory on the basis of their size and composition (Seinfeld and Pandis, 2006). Conversely, Köhler Theory can be used to predict CCN concentration for a known aerosol of known composition. In this analysis, ammonium sulfate is assumed to represent the inorganic compound and the measured DMA size distribution is used to predict the CCN number concentration at a series of fixed supersaturations. Figure 7.3 shows the DMA calculated CCN concentrations derived from the aerosol size distribution. To calculate the range in the CCN concentrations at a single supersaturation, a soluble fraction of ammonium sulfate is assumed to vary from 0.2 to 0.8. These CCN concentrations also indicate a polluted air mass, with concentrations at and greater than 1000 cm^{-3} at 1% supersaturation (Figure 7.3).

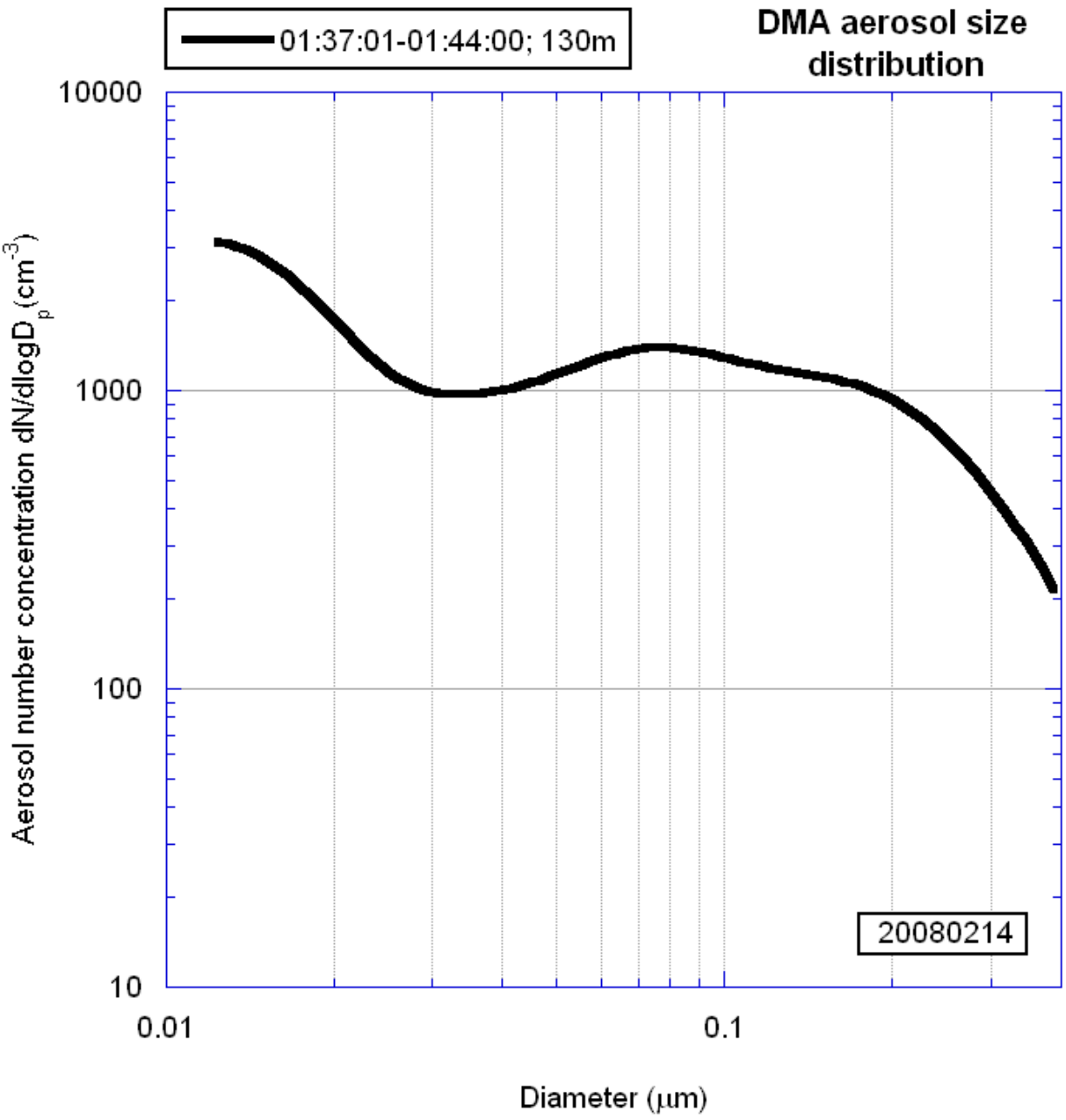

Figure 7.2. DMA fine mode aerosol size distribution on 14 February 2008 between 013701-014400UTC at 130 m altitude.

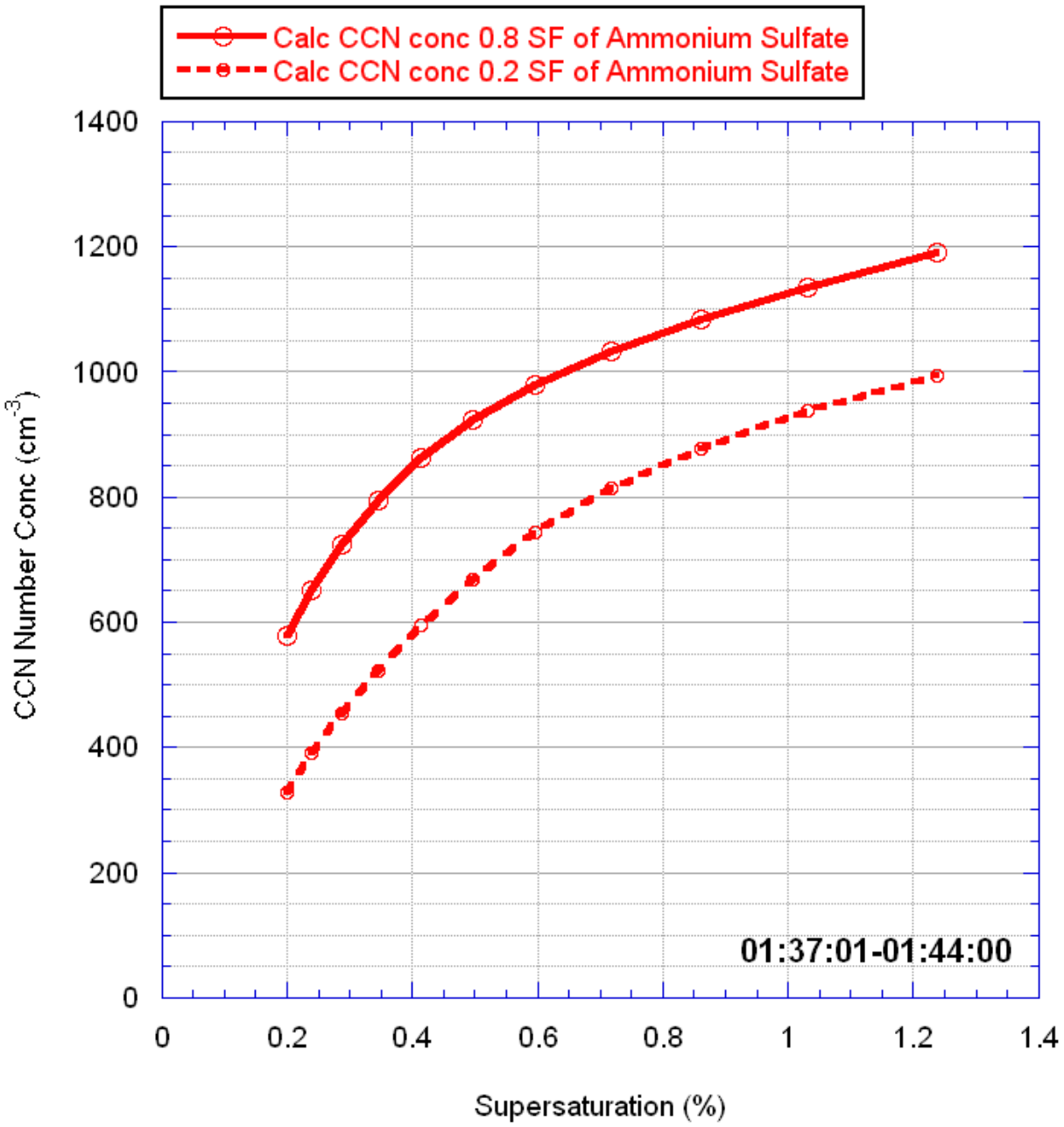

Figure 7.3. DMA-derived CCN concentration versus supersaturation on 14 February 2008 between 031701-014400 UTC at 130m altitude. Solid line indicates 0.8 solubility fraction ammonium sulfate, and dashed line for 0.2 solubility fraction ammonium sulfate.

7.1.2 16 February 2008

On 16 February 2008 the atmosphere was characterized by a moist layer up through the height of an inversion at 750 hPa (Figure 7.4). Winds were southeasterly below the inversion, and westerly above (Figure 7.4). This is typical of the trade wind cumulus regime, especially given the dryness above the inversion (see section 5.2.1). Clouds on this day were quite shallow

(bases near 3000 ft and tops just under 7000 ft) and they tracked to the northwest following the trade wind southeasterly flow.

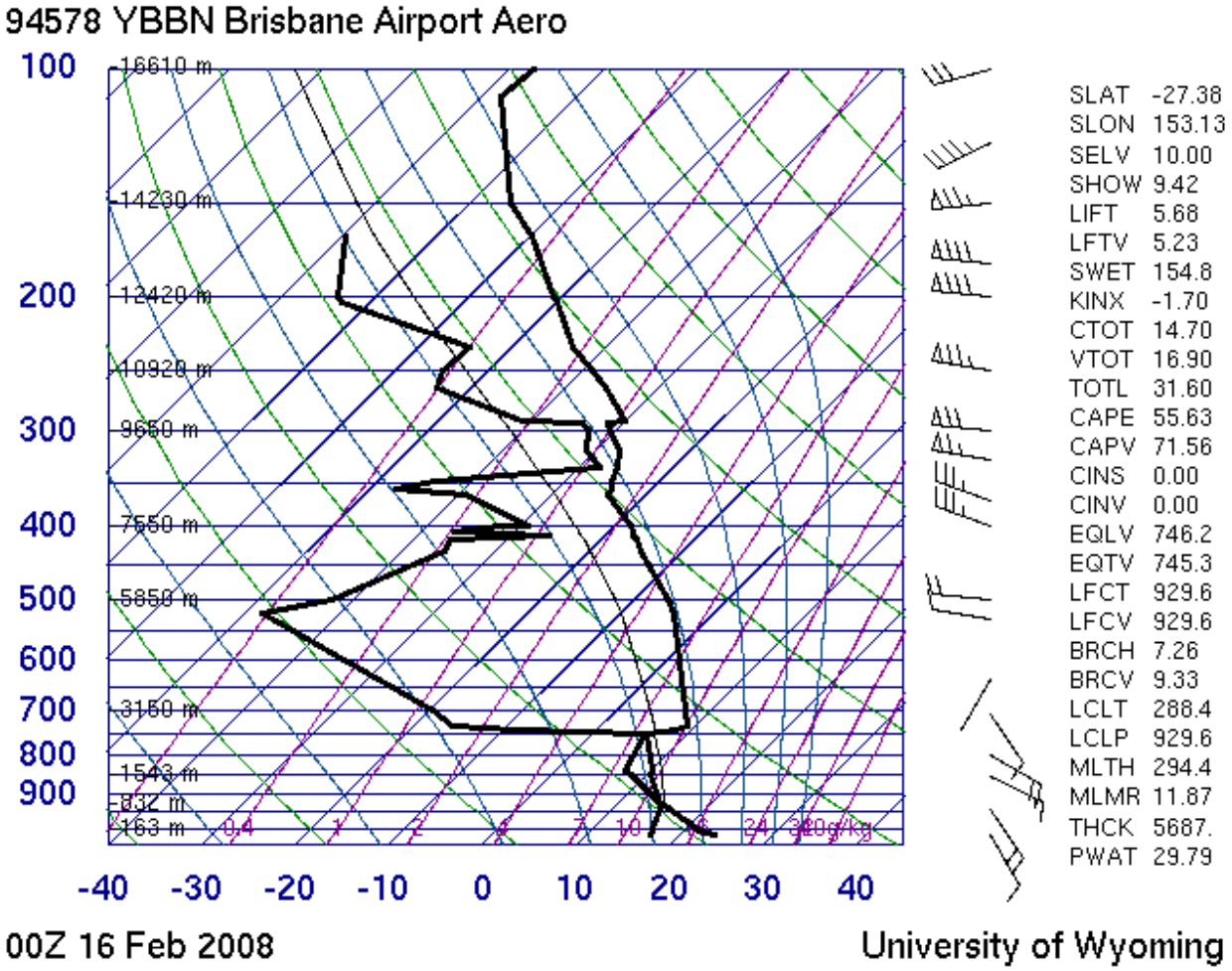

Figure 7.4. Thermodynamic sounding taken at Brisbane Airport at 00Z on 16 February 2008 (10:00am local time).

SEEDA1 conducted sub-cloud measurements and cloud penetrations south of Brisbane (near Bromelton) on this day. Thus, given the surface southeasterly winds, the air mass sampled would not be influenced by the city of Brisbane. The aircraft initially sampled at a very low altitude, near the surface, at 340 m, on its way south out of Archerfield. The air mass at this altitude was very polluted, with a single mode aerosol spectrum peaking in nucleation mode sizes at 0.02-0.03 microns, with concentrations in that mode of near 4000 cm^{-3} (Figure 7.5). Corresponding CCN concentrations at that altitude were also high, over 1000 cm^{-3} at 1% supersaturation, further indicating the polluted character of this air mass (Figure 7.6). This was a very similar distribution as observed on 14 February 2008 at low altitude near Archerfield (see section 7.1.1), also indicating enhanced gtp activity.

The next altitude sampled was just below cloud base, at 1190 m near Bromelton, and conditions at this height and location were much cleaner. DMA aerosol measurements show a

broad mode in the distribution between .04-0.2 microns, with concentrations just over 100 cm^{-3} in each size bin of this broad peak (Figure 7.5). The CCN spectra at this altitude also reflect the cleaner atmosphere, with maximum concentrations just over 100 cm^{-3} at 1% supersaturation (Figure 7.6). This discontinuity in the vertical structure of the aerosol concentration may be caused by a backing (winds turn counter-clockwise with height) in the surface winds with height. This may cause vertical layering of the aerosol, which is apparent in this case. Although this layering is observed more often in a stable sub-cloud layer, it seems that the boundary layer is not well-mixed in some cases. Observations of aerosol layering are important because cloud processing occurs immediately below cloud base and near-surface measurements may not be representative of the sub-cloud base aerosol conditions.

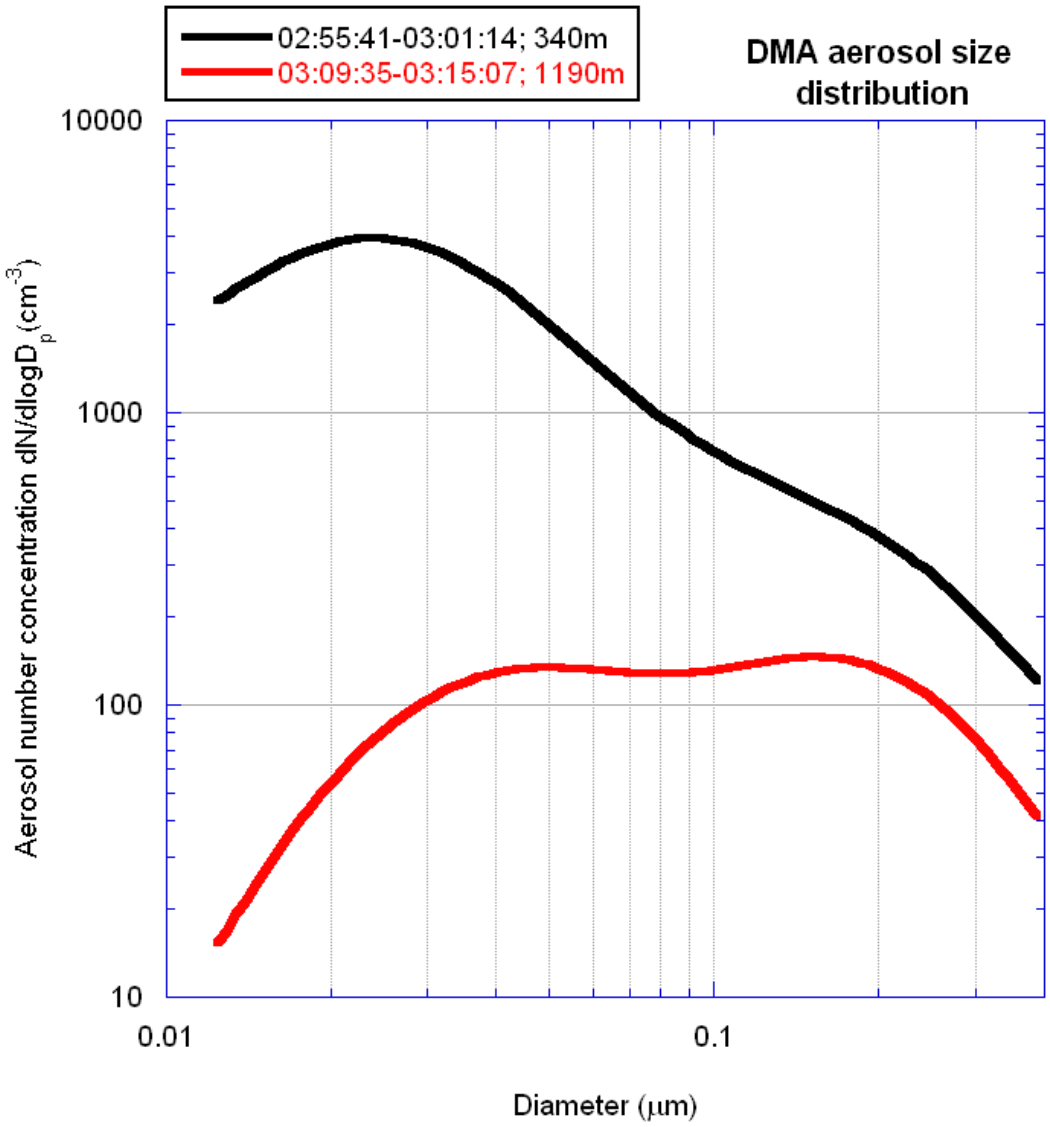

Figure 7.5. DMA fine mode aerosol size distribution on 16 February 2008 between 025541-030114 UTC (black) at 340 m altitude, and between 030935-031507 UTC (red) at 1190 m altitude (just below cloud base).

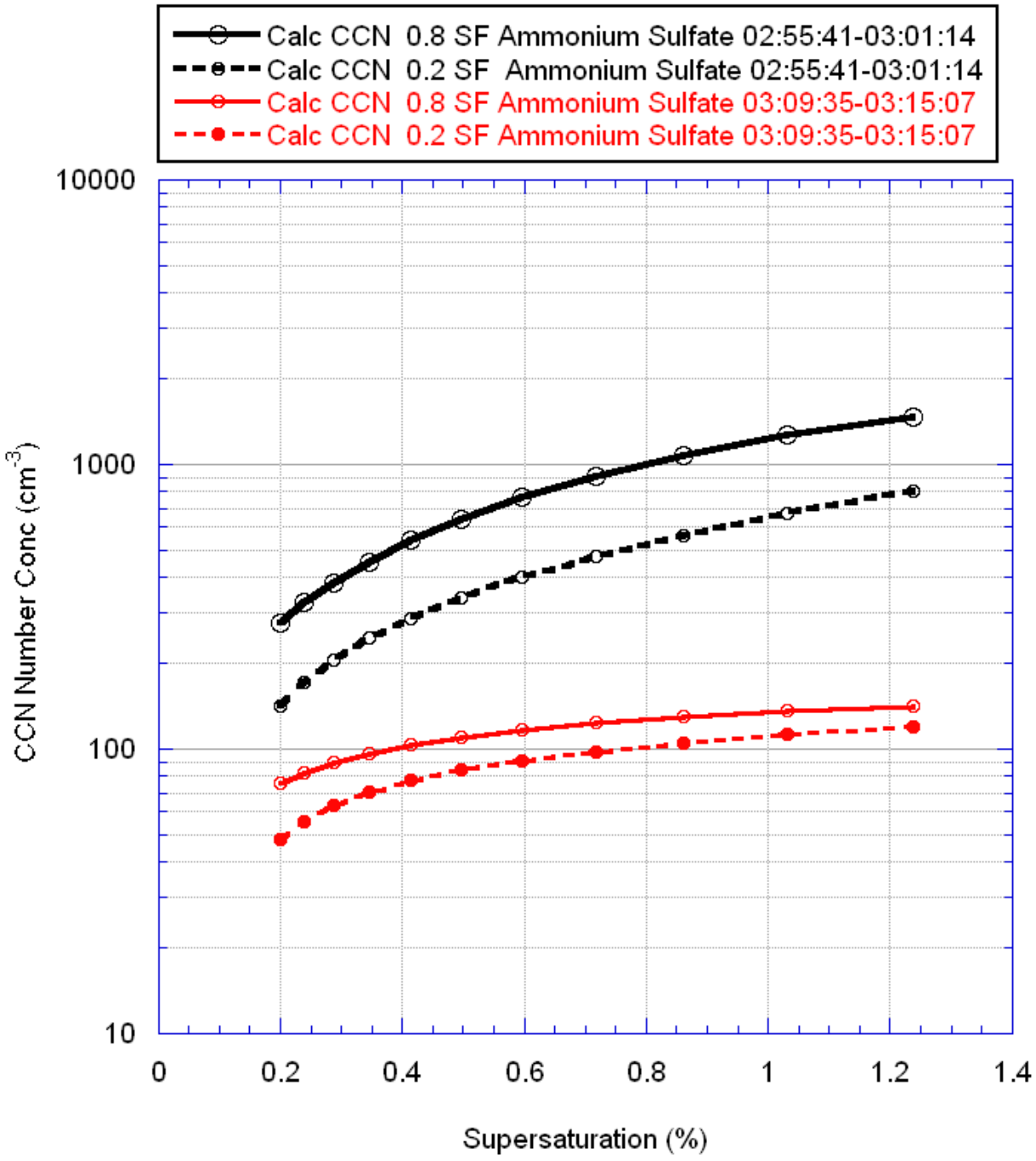

Figure 7.6. DMA-derived CCN concentration versus supersaturation on 16 February 2008 between 025541-030114 UTC (black) at 340 m altitude, and between 030935-031507 UTC (red) at 1190 m altitude (just below cloud base). Solid line indicates 0.8 solubility fraction ammonium sulfate, and dashed line for 0.2 solubility fraction ammonium sulfate.

7.1.3 28 February 2008

On 28 February 2008 the atmosphere was fairly moist up through 500 hPa, and a midlevel (600 hPa) stratiform cloud layer was present much of the day keeping most of the area overcast (Figure 7.7). There was a slight inversion at 1500 m (850 hPa), with northeasterly winds below and northwesterlies above (Figure 7.7). This capping inversion eroded during the day, allowing some weak convection to occur with tops up to 5 km (approximately -5 deg C). Clouds moved quite fast toward the southeast, given the steering flow was the midlevel northwesterlies.

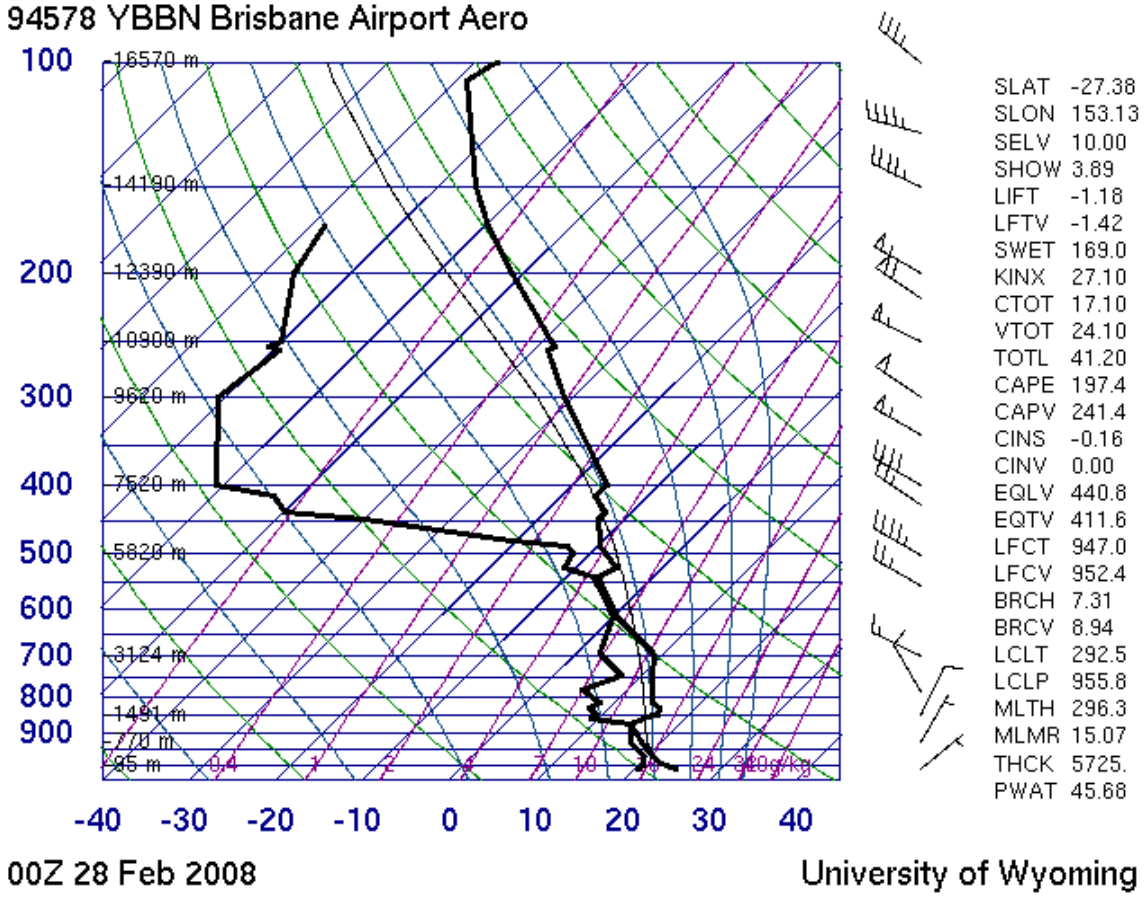

Figure 7.7. Thermodynamic sounding taken at Brisbane Airport at 00Z on 28 February 2008 (10:00am local time).

SEEDA1 conducted sub-cloud measurements and cloud penetrations west of Amberley, downwind of the city of Brisbane on this day given northeasterly surface winds. The DMA aerosol distribution measured just below cloud base (at 1250 m) is shown in Figure 7.8. Fine mode aerosol concentrations were very high (> 1400 cm^{-3}), especially in the nucleation mode size range of less than 0.05 microns. A secondary mode in the distribution, in the accumulation mode (0.05-1 microns), is present between 0.1-0.2 microns. The CCN spectra, derived from the DMA measurements, shows CCN concentrations up to 1000 cm^{-3} at 1% supersaturation, and 0.8 solubility fraction ammonium sulfate (Figure 7.9). The DMA size distribution with the high fine mode aerosol concentrations and the corresponding calculated CCN concentrations are typical of

what is measured in continental regimes. This continentality is also observed in the cloud droplet concentrations measured at cloud base (see section 7.2.2).

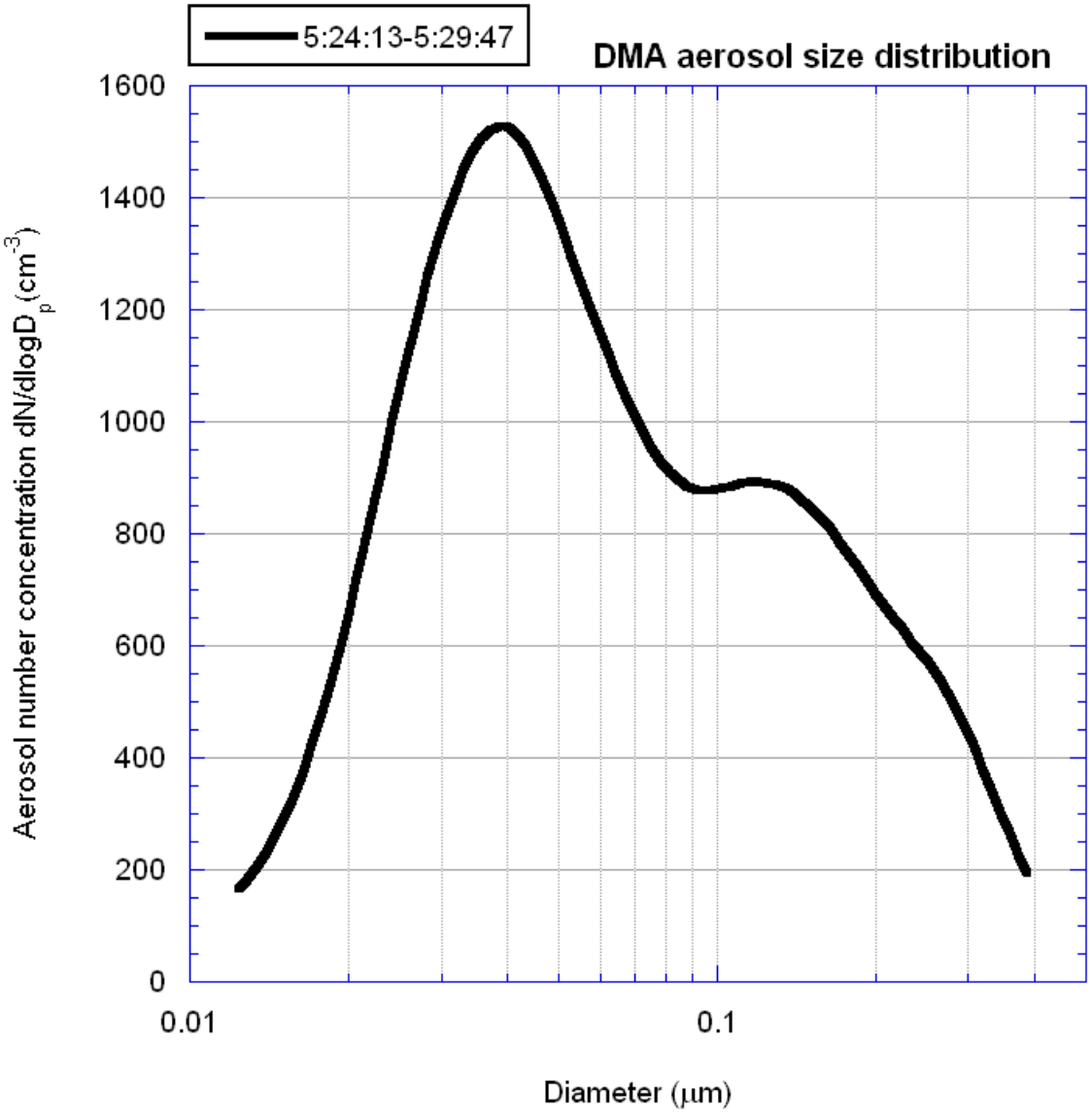

Figure 7.8. DMA fine mode aerosol size distribution on 28 February 2008 between 052413-052947 UTC.

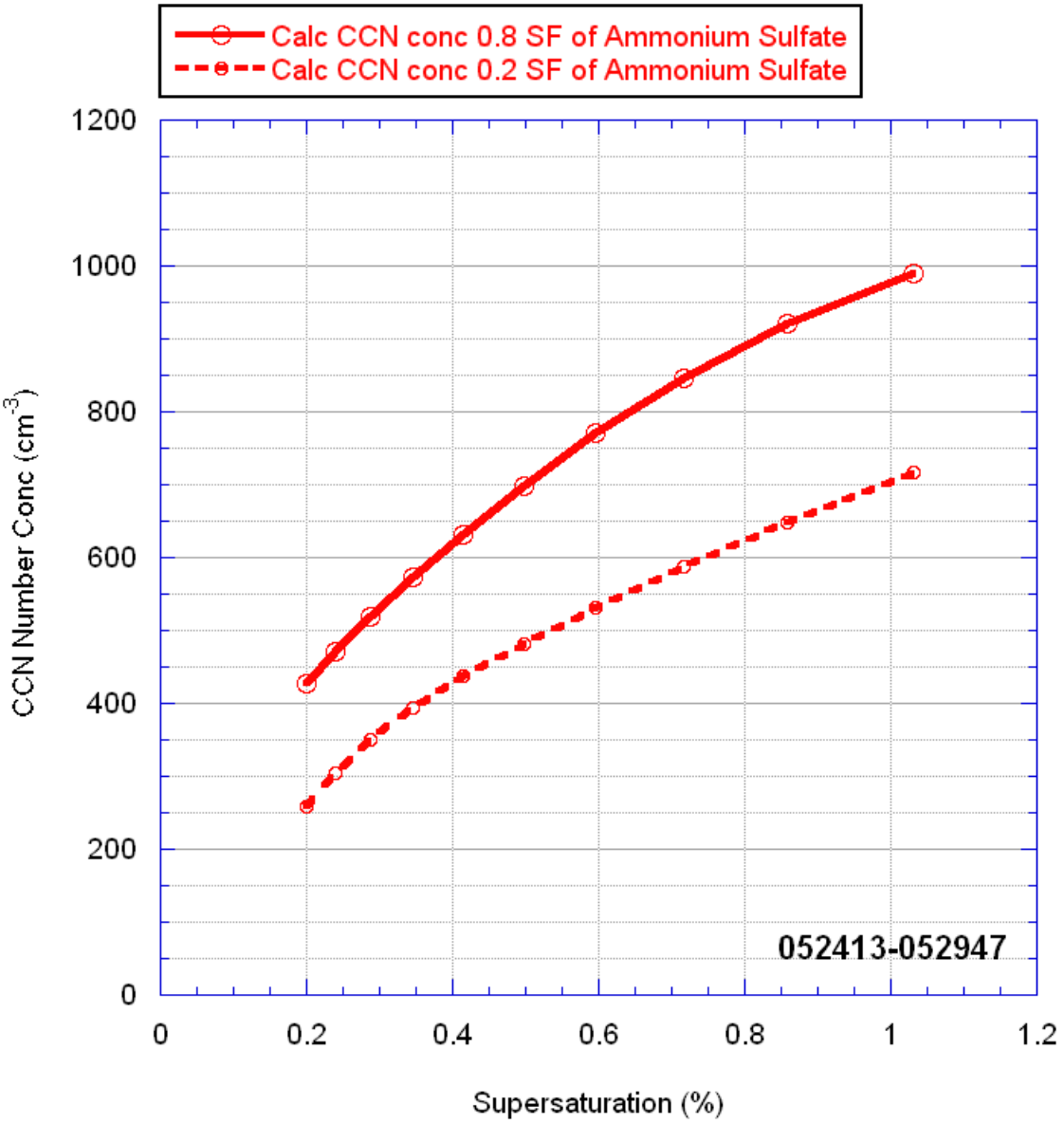

Figure 7.9. DMA-derived CCN concentration versus supersaturation on 28 February 2008 between 052413-052947 UTC. Solid line indicates 0.8 solubility fraction ammonium sulfate, and dashed line for 0.2 solubility fraction ammonium sulfate.

7.1.4 6 March 2008

On 6 March 2008 the atmosphere was characterized by a trade wind inversion at 700 hPa, with southeasterly winds below and westerlies above (Figure 7.10). This scenario is most similar to the trade wind cumulus regime described in section 5.2.1. Most clouds that formed were shallow, capped by the inversion, with tops warmer than 0 deg C. Clouds tracked toward the northwest, given the steering flow was the low-level southeasterlies.

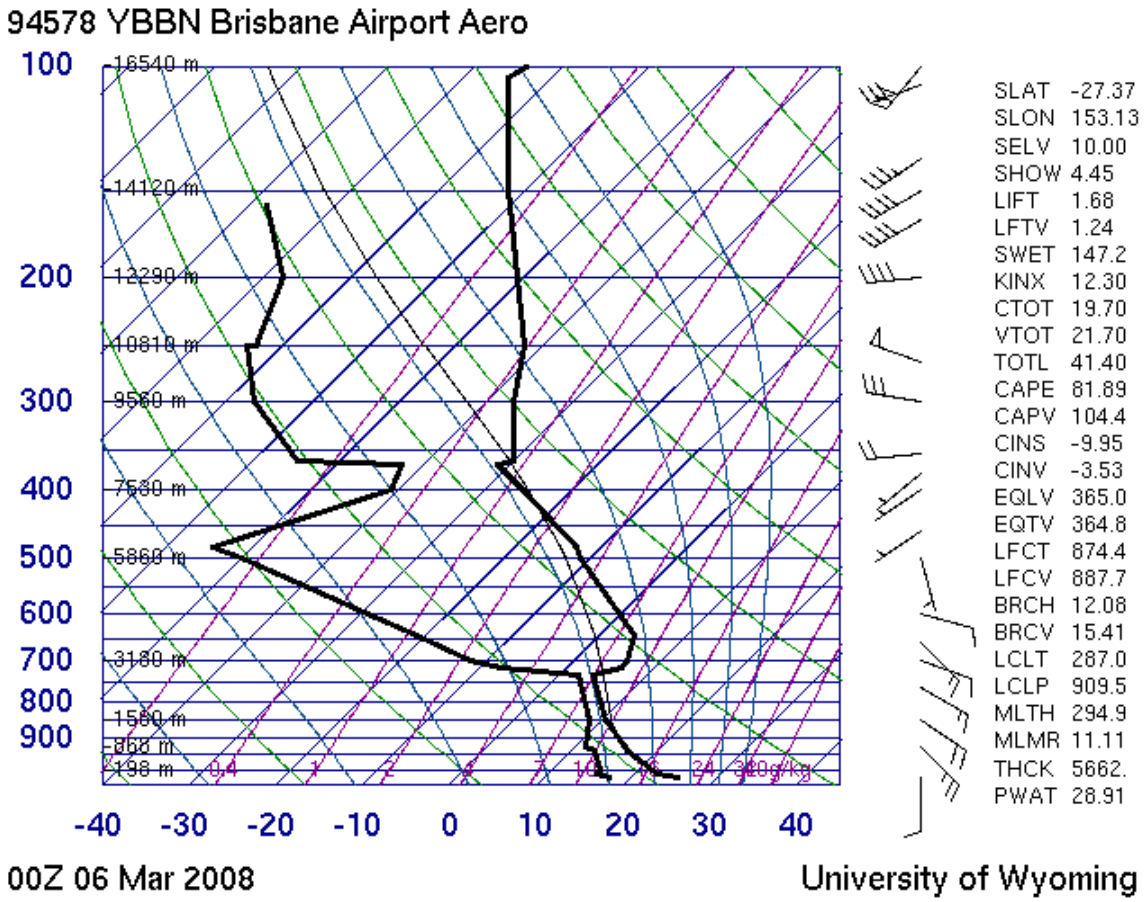

Figure 7.10. Thermodynamic sounding taken at Brisbane Airport at 00Z on 6 March 2008 (10:00 am local time).

The sub-cloud measurements on 6 March 2008 were conducted near Laravale, or south of Brisbane, at just below cloud base (1150 m). Given the surface southeasterly winds, the air mass was not affected by the city of Brisbane, but appears to be a relatively clean air mass. There was one primary mode in the accumulation mode of the aerosol spectra between 0.1-0.2 microns, with concentrations up to 600 cm^{-3} (Figure 7.11). The corresponding CCN spectra show clean conditions as well, with CCN concentrations no higher than 400 cm^{-3} at 1% supersaturation (Figure 7.12). The absence of fine mode is quite unique in this case as it represents a relatively unpolluted aerosol size distribution. The calculated CCN concentrations are from around 200-400 cm^{-3}, which shows how important fine mode aerosol is to the number concentration of aerosol and to the CCN activation properties. The relatively low CCN concentrations can be attributed to an absence of fine mode aerosol.

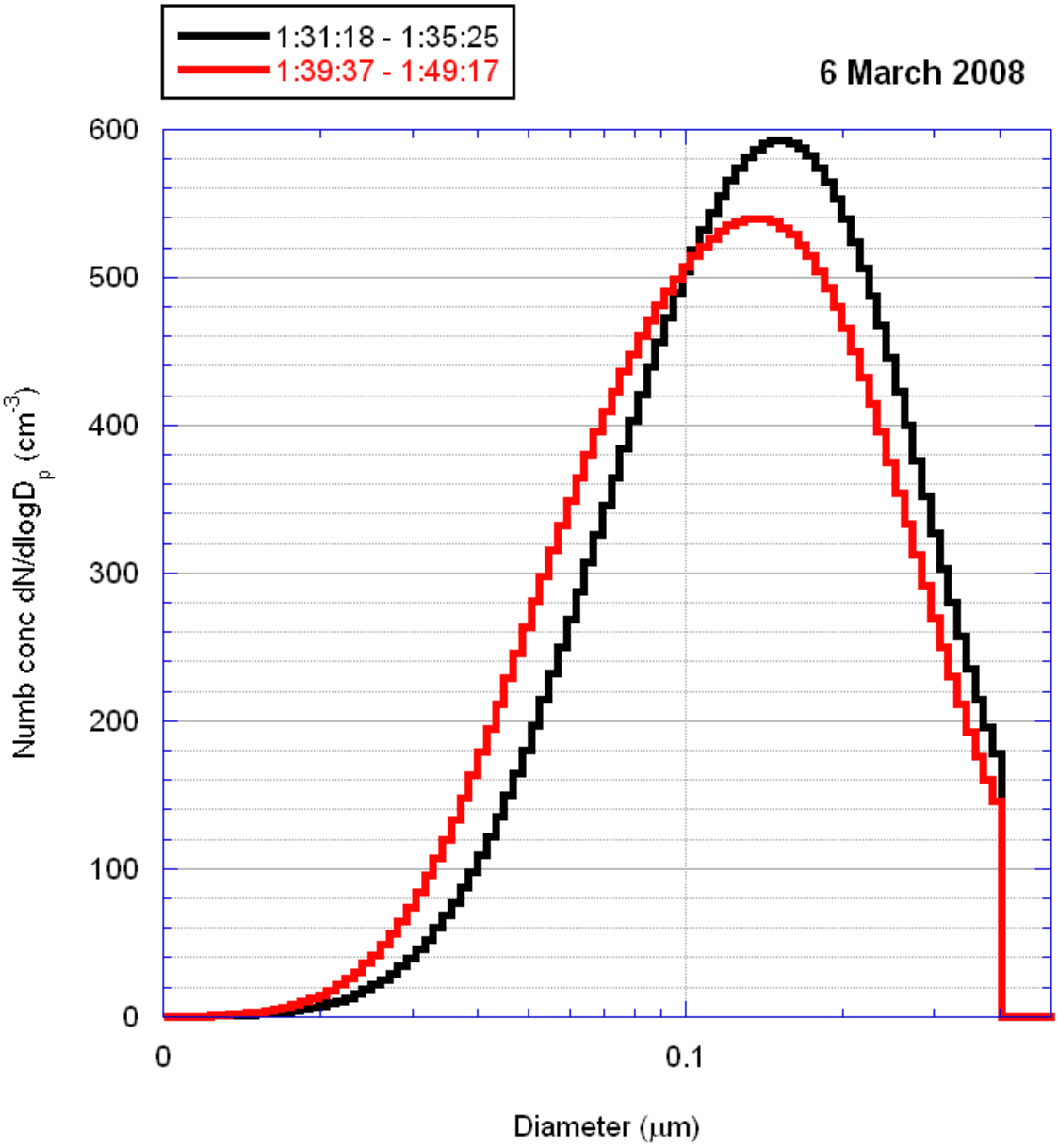

Figure 7.11. DMA fine mode aerosol size distribution on 6 March 2008 between 013118-013525 UTC (black) and 013937-014917 UTC (red).

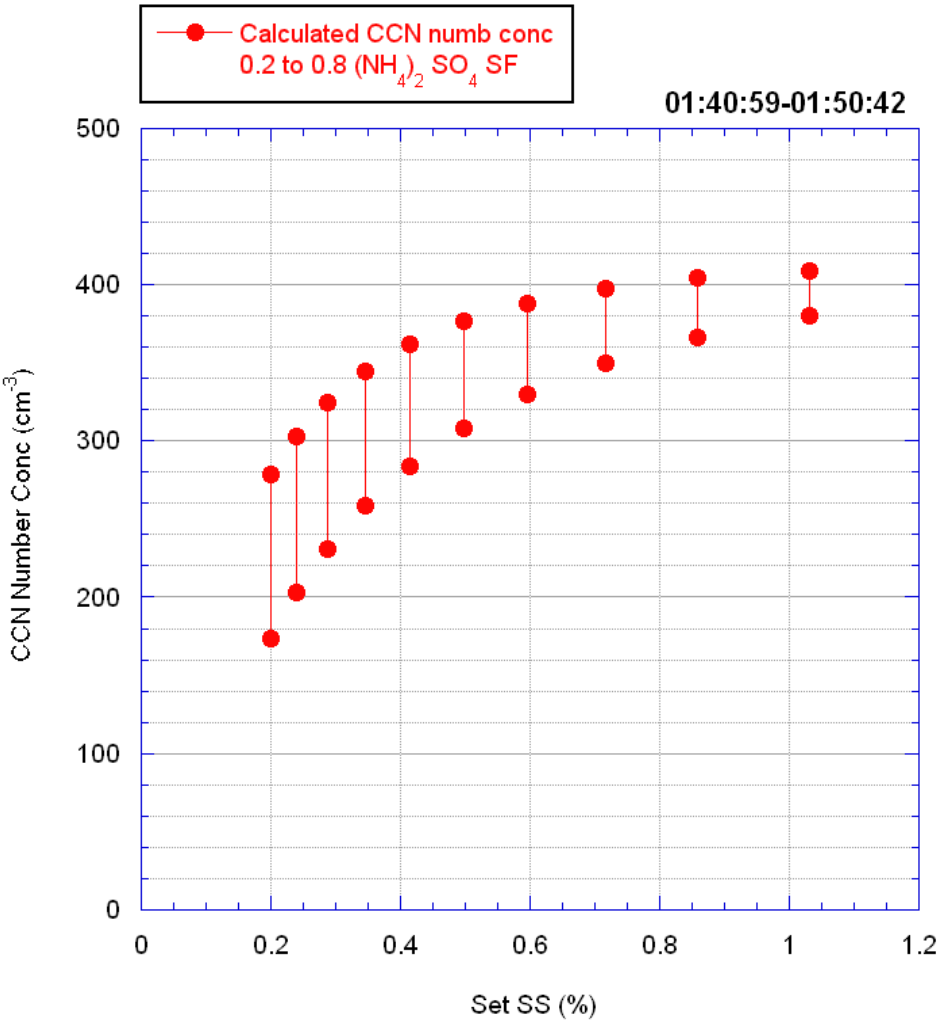

Figure 7.12. DMA-derived CCN concentration versus supersaturation for 6 March 2008 between 014059-015042 UTC. Top of range is CCN concentration for 0.8 solubility fraction ammonium sulfate, and bottom of range is for 0.2 solubility fraction ammonium sulfate.

7.1.5 Aerosol characteristics summary

Given the preliminary analysis of the four case studies presented above (the associated locations are illustrated in Figure 7.13), it has been shown that cloud base aerosol and CCN characteristics south of the Brisbane region under southeasterly trade wind scenarios exhibited quite clean conditions with the primary aerosol mode in accumulation mode sizes, and CCN concentrations were low. When the measurements were taken downwind of Brisbane, and further inland, the aerosol size distribution was characterized as being more polluted, with the primary aerosol mode in the nucleation range, with very high concentrations of aerosol and CCN. The low altitude measurements, also taken closer to the Brisbane area, were also very polluted, with high CCN concentrations and primary size mode in the nucleation mode range. It is possible that these nucleation mode aerosols originated through gas-to-particle conversion, though this will be analyzed in more detail in our future analysis. Aerosol layering is also

observed in one of the cases, which indicates that the sub-cloud aerosol layer is not always well-mixed. This observation needs to be studied further to better characterize the sub-cloud aerosol activation processes that lead to cloud droplet formation.

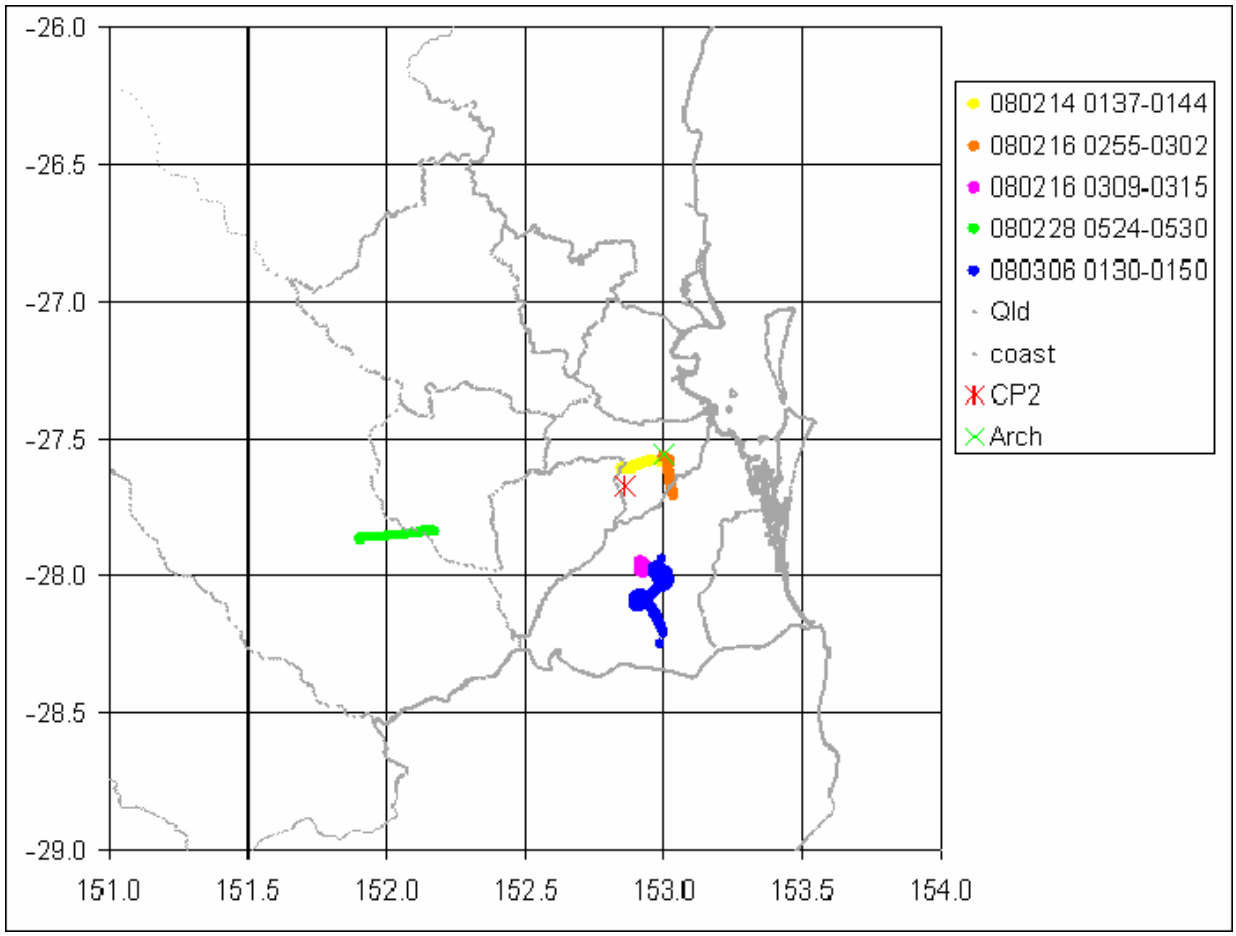

Figure 7.13. Map of flight locations for all sub-cloud aerosol measurements. The CP2 radar location is indicated by a red asterisk, and Archerfield airport is a green X.

7.2 OBSERVED CHARACTERISTICS OF CLOUDS IN SOUTHEAST QUEENSLAND

7.2.1 Cloud base characteristics

Figure 7.14 shows the typical range cloud base temperatures measured by SEEDA1 during the Jan – Mar 08 CSRP period. Temperatures were generally 17 ± 3°C for cloud bases which typically occurred at around 1000m (3000 feet), but could be as high as 20 ± 3°C for bases when they occurred as low as 500m. On one occasion however, a temperature of 0°C was recorded for a high cloud base, which was reported at 3600m.

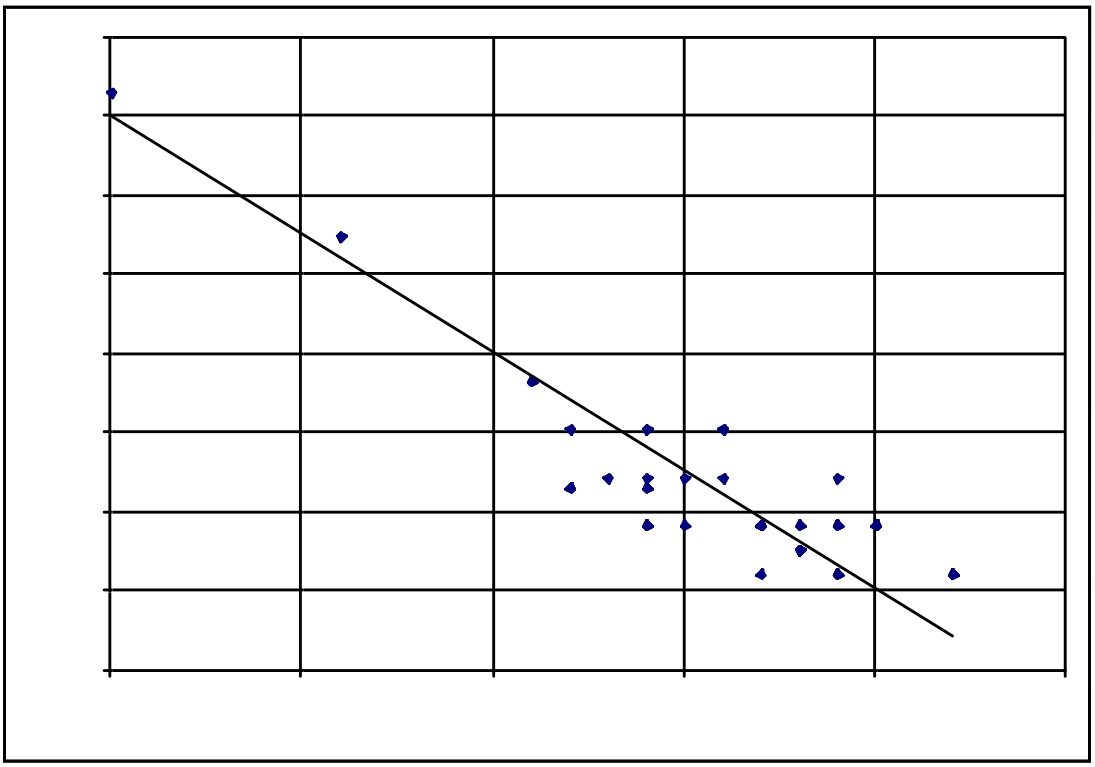

Figure 7.14. Typical range cloud base temperatures measured by SEEDA1 during the Queensland Jan – Mar 08 CSRP.

7.2.2 Cloud droplet spectra characteristics

The following case studies illustrate some cloud droplet spectra observations for non-seeded clouds. Such measurements for seeded clouds will be discussed in section 9.3.

14 February 2008

Figure 7.15 shows cloud droplet size spectra measurements recorded by the FSSP probe during a flight undertaken by SEEDA1 (ZS-JRA) on 14 Feb 2008 near the vicinity of Wivenhoe Dam, Qld (approximate lat/long coordinates -27.365, 152.568). During the part of the flight from approximately 0230 to 0300 UTC, SEEDA1 flew tight orbits and maintained a constant altitude of 1800m above a cloud base, which on this day was located at approximately 1000m (3300 feet) above sea-level (Figure 7.16).

Figure 7.15 shows cloud droplet size distributions measured at a constant altitude of 1800m. The variation in the modes of the FSSP size distributions is indicative of how variable the microphysical properties of warm clouds are in this case. Although the aircraft was flying in tight circles, it is apparent that the aircraft was flying in updraft and downdraft regions (this will be later confirmed with additional data analysis). The broad distributions with modes greater than 14 microns are likely caused by droplet shatter on the FSSP inlet shroud. This droplet breakup effect needs to be studied further and such data should be removed.

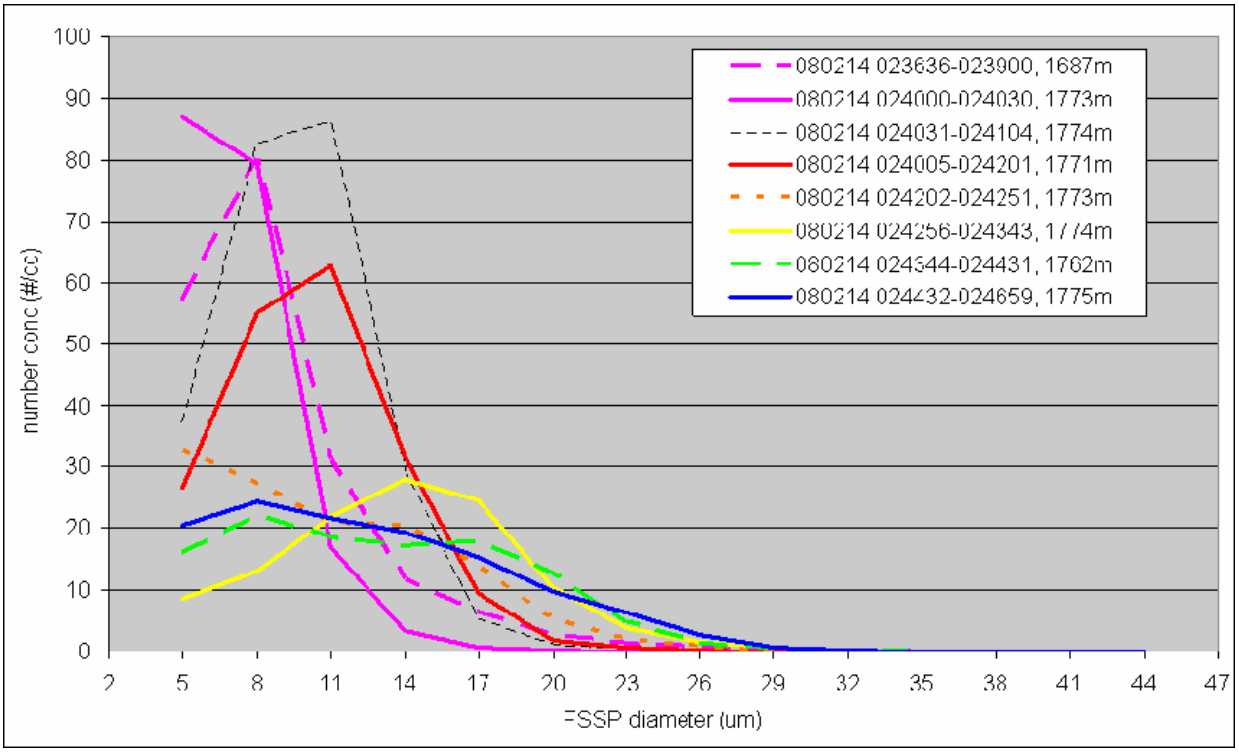

Figure 7.15. Natural coarsening of cloud droplet size measured by the FSSP probe. SEEDA1 was flying tight circles to remain in the same location above Wivenhoe Dam (-27.365, 152.568). While sampling SEEDA1 maintained a constant altitude of 1800m above a cloud base at approximately 1000m. Statistics from these distributions are listed in Table 7.1.

Table 7.1. Computed droplet distribution statistics for distributions shown in Figure 7.15.

	Mean diameter $D_{BAR}(d_{10})$	Standard deviation SD $\sigma(d_{10})$	Dispersion coefficient CV(d_{10})	Mass mean diameter MMD(d_{30})	Effective radius ER(r_{32})
080214 023636-023900	8.64	4.49	0.52	10.42	6.34
080214 024000-024030	7.04	5.34	0.76	7.82	4.36
080214 024031-024104	9.63	5.35	0.56	10.59	5.81
080214 024005-024201	10.26	4.97	0.48	11.44	6.36
080214 024202-024251	10.67	3.65	0.34	12.84	7.61
080214 024256-024343	13.86	4.70	0.34	15.49	8.59
080214 024344-024431	12.77	3.80	0.30	14.95	8.61
080214 024432-024659	12.46	3.37	0.27	14.96	8.83

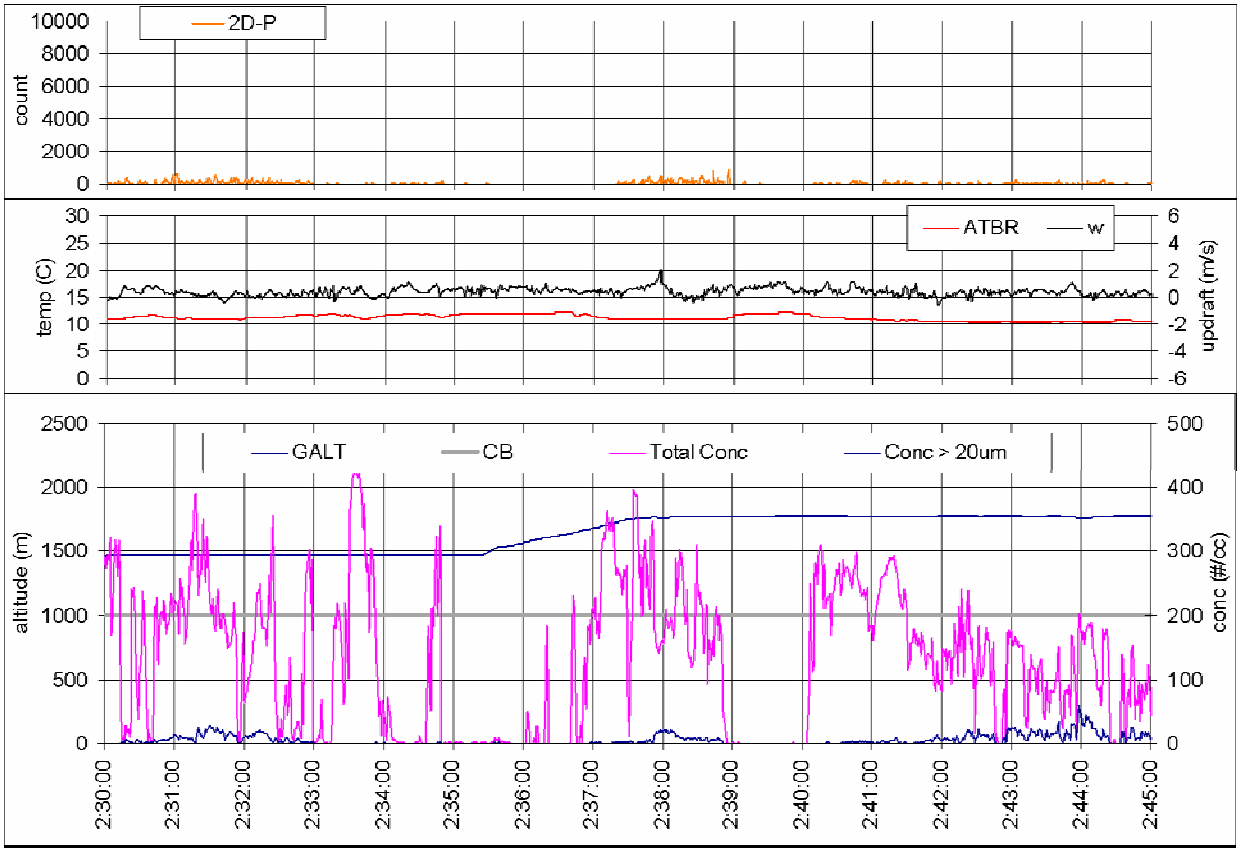

Figure 7.16. Flight chart summary details for the period of interest on 14th February 2008.

28 February 2008

Cloud penetrations on 28 February 2008 (see section 7.1.3 for weather summary on this day), showed a natural coarsening of the droplet spectra with increasing altitude (Figure 7.17-Figure 7.18). At low altitudes (or closer to cloud base), the FSSP total droplet concentrations were high (near 800 cm^{-3}), whereas total concentrations were below 600 cm^{-3} at 1300 m above cloud base (Figure 7.18). These high cloud droplet concentrations correspond well with the cloud base aerosol and CCN spectra presented in section 7.1.3. FSSP mean diameter close to cloud base was near 5 microns, and as the spectrum broadened with cloud depth increased to 13 microns.

Figure 7.17 shows a rapid widening of the drop size distribution likely caused by activation of accumulation mode aerosol in the aerosol size distribution shown in Figure 7.8. The peak cloud droplet concentration is reached at a cloud depth of around 750 m, which is indicative of a shallow diffusional growth layer. Above this cloud depth of 750 m a collision-coalescence process seems to be more active causing a rapid broadening in the size distribution.

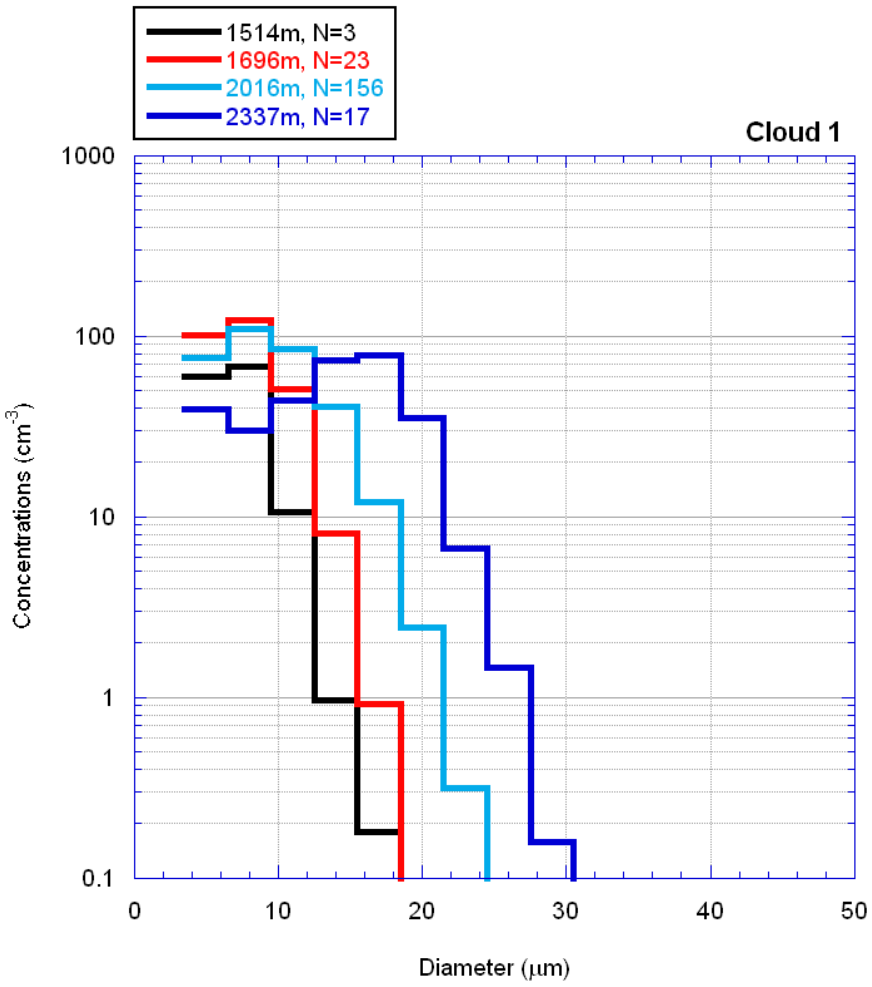

Figure 7.17. FSSP drop size distributions on 28 February 2008. Each penetration was at a new altitude (listed in the legend, along with the number of 1 Hz measurements that were included in each altitude's mean spectra).

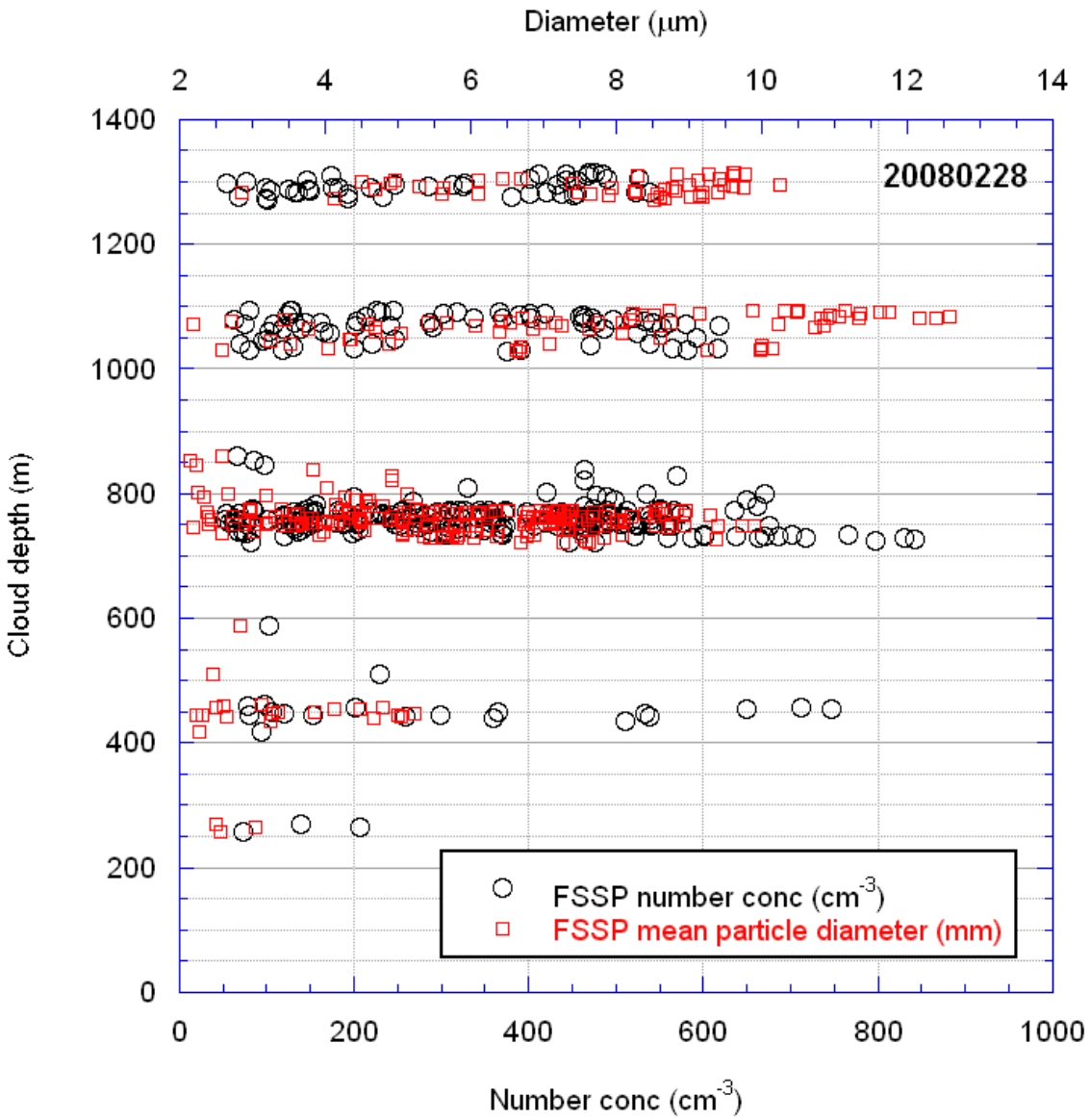

Figure 7.18. FSSP measurements versus cloud depth on 28 February 2008 with FSSP concentrations > 50 cm^{-3}: FSSP total concentrations (black, bottom axis), and FSSP mean diameter (red, top axis).

8. CLOUD AND PRECIPITATION PROCESSES

8.1 2007-2008 RADAR-BASED STORM SUMMARY

Using the merged radar product (see section 4.2.4) called BrisMerge (on a 600 km by 600 km grid) and TITAN tracking software (see section 4.2.7), storm tracks were identified for the period of 1 November 2007–30 March 2008. Storm tracks were identified for areas of reflectivity greater than 25 dBZ, and thus statistics on these tracks are also dependent on this chosen threshold (i.e. storm top height is the maximum height of the threshold reflectivity value in the identified storm volume, and so forth for cloud base). The minimum storm volume for a track to be identified in this analysis was 10 km^3. Note that the use of the term "storm" here soley represents a feature on radar that met the aforementioned criteria for tracking, thus all tracked "storms" are not thunderstorms.

8.1.1 Monthly distributions

Figure 8.1 shows a time series histogram of the daily storm count over the 5-month period. It is clear that there were numerous storms on a nearly daily basis at least somewhere in the BrisMerge coverage area, though the months of Jan-Feb had the most days with storm counts greater than both 500 and 1000 storms. The high number of storms could be attributed to the large coverage area of the BrisMerge domain (see section 4.2.4), as well as to how each storm track is counted even if the storm only last one or two radar volume scans (i.e. very short lifetime). Storm track duration is illustrated in Figure 8.6, and the mean storm duration was one hour or less. A few of the days with zero storm counts are due to missing data (Jan 4-6 and Mar 25).

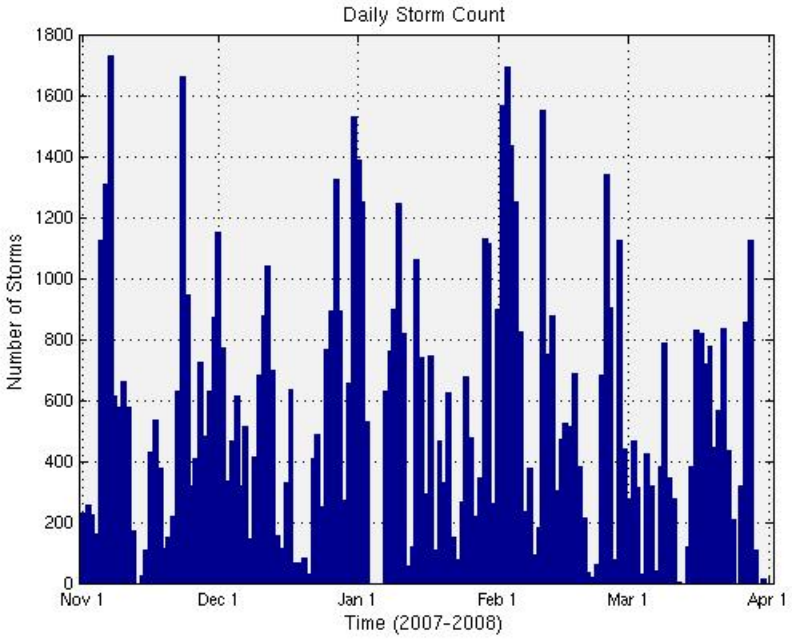

Figure 8.1. Time series of daily storm count for the CSRP study period.

Figure 8.2 illustrates the daily variation in storm precipitation flux during the CSRP period. There were several cycles of higher precipitation flux (> 100 $m^3 s^{-1}$) through this period, with the most notable being in early November, early December, and early February. A few days between late January and early February yielded very high precipitation fluxes (> 250 $m^3 s^{-1}$), and flooding was reported in many regions of Southeast Queensland during this time. A convective surge near the end of March, associated with the MJO can also be seen as a short spike of very high precipitation flux near the end of the CSRP period.

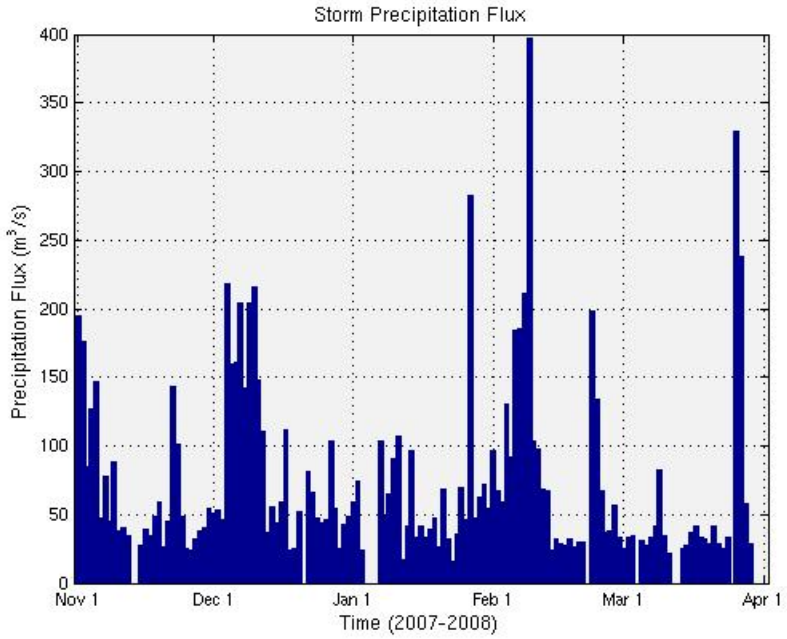

Figure 8.2. Same as Figure 8.1, except for daily average of storm maximum precipitation flux.

The average storm area is shown in Figure 8.3, and was typically around 50 km^3 or less. During the periods of higher precipitation flux discussed above, there also tends to be some storm cells with larger areas of greater than 500 km^3. However, during January, the daily storm precipitation flux was typically less than 100 $m^3 s^{-1}$, yet there were still several storms with large (> 500 km^3) coverage areas. The larger storm systems observed in January tended to have lower maximum reflectivity than those in the other months, contributing to a lower precipitation flux.

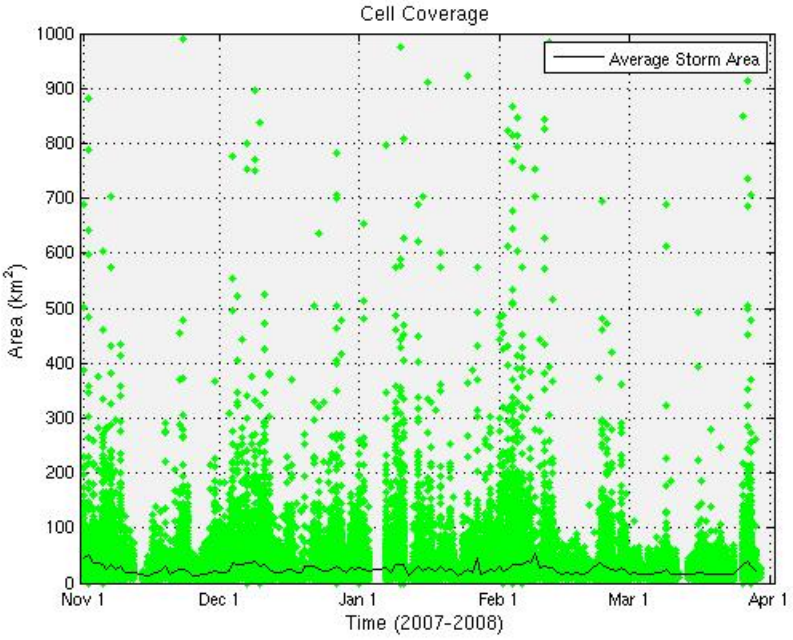

Figure 8.3. Time series of storm coverage area for the CSRP study period. The green symbols indicate the mean storm area of individual cells whereas the black line gives the daily average storm area.

Throughout the entire CSRP period there was considerable variation in the maximum radar reflectivity that each storm achieved during its lifetime (Figure 8.4). The daily average maximum reflectivity was variable, with a seasonal mean of about 38 dBZ. The trend in the daily average reflectivity was fairly steady as well over the 5-month period.

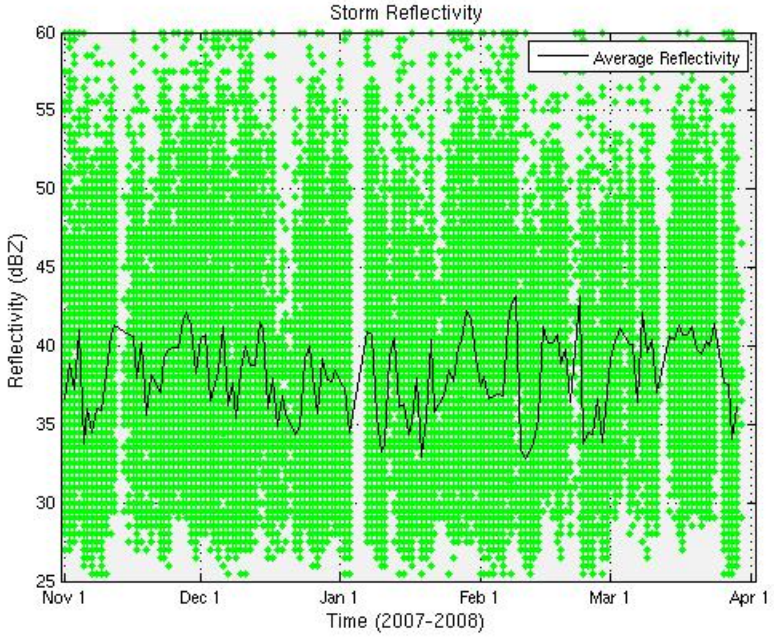

Figure 8.4. Same as Figure 8.3, except for maximum storm reflectivity.

Figure 8.5 shows the scatter in storm top heights during the CSRP period, and it is clear that during periods when higher precipitation fluxes were observed, early December and early February in particular, several storm tops were often higher than 12 km. The average storm top height was variable, but also tended to be higher (up to 6km) in the early December and February periods. The freezing level on most days was roughly 4 km, and thus storm top heights at or less than 4 km, typically were indicative of warm clouds. Average storm top heights as low as 4 km were common in November, January, and late February into March. The overall mean storm top height was about 5 km.

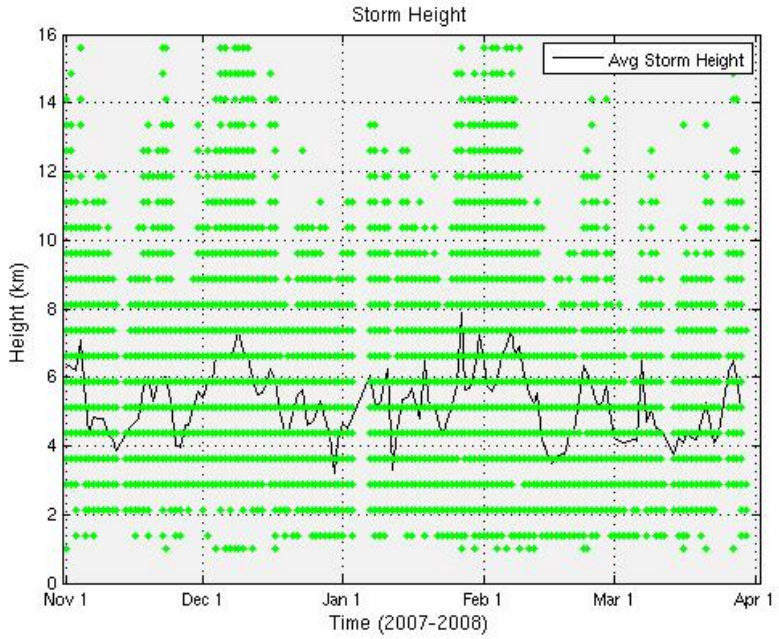

Figure 8.5. Same as Figure 8.3, except for maximum storm height.

The average life cycle of storms in the Brisbane area was on the order of one hour or less (Figure 8.6). The average storm duration was fairly uniform throughout the 5-month period. There were a few storm tracks observed to last for nearly 24 hours, but the majority of storm tracks lasted less than 5 hours.

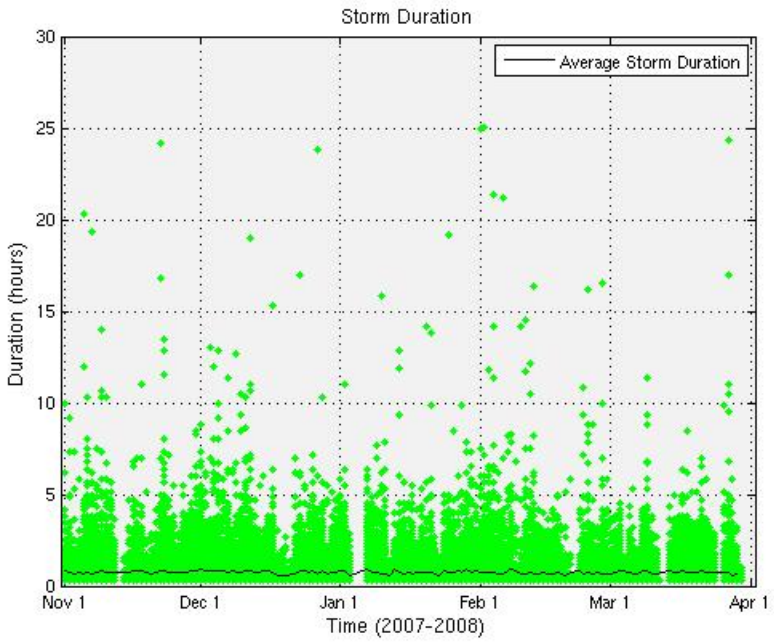

Figure 8.6. Same as Figure 8.3, except for storm duration.

Storms observed in the Brisbane area exhibited a wide range in storm speed and direction (Figure 8.7-Figure 8.8). Storm speeds were observed as high as 80 km h^{-1} during a few periods in early November and late December. Average storm speeds over the whole period were 20 km h^{-1}, and were fairly uniform during the CSRP period aside from the two periods of faster storm motion in November and December. Storms typically moved in two general directions, toward the west and northwest (270-315 deg) or toward the southeast (120-140 deg), though all directions of motion were observed. The northwestward motion was common under trade wind (southeasterly) regime, and was the dominant storm motion for this convective season. The periods of highest precipitation flux (in November, December, and February) occurred during northwesterly regimes, where the storm motion was toward the east-southeast (Figure 8.9).

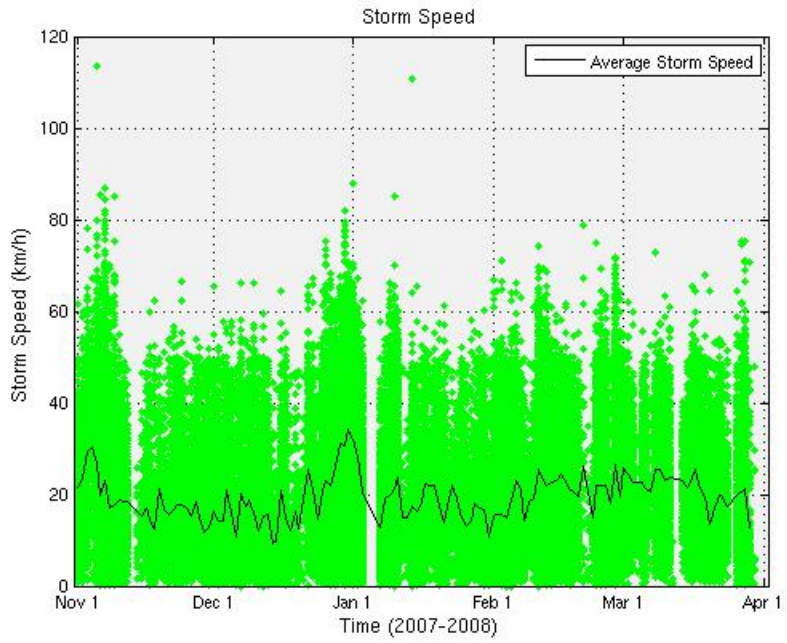

Figure 8.7. Same as Figure 8.3, except for mean storm speed.

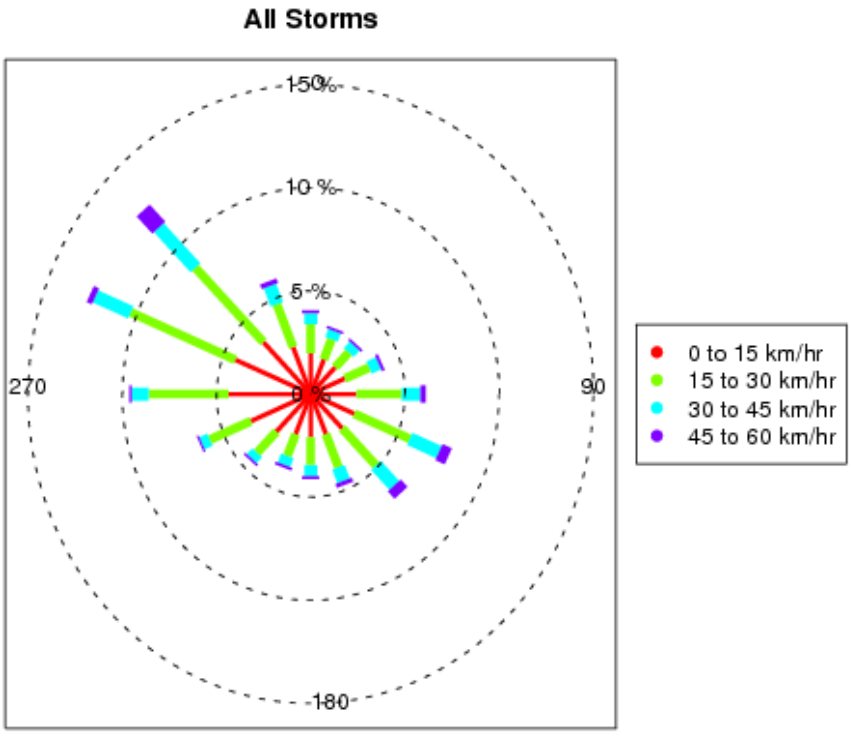

Figure 8.8. Wind rose showing the distribution of mean storm direction of movement. Mean storm speed is color-coded, and the percent of storms included in each petal of the wind rose is indicated by the petal length using the dashed ellipses as the scale.

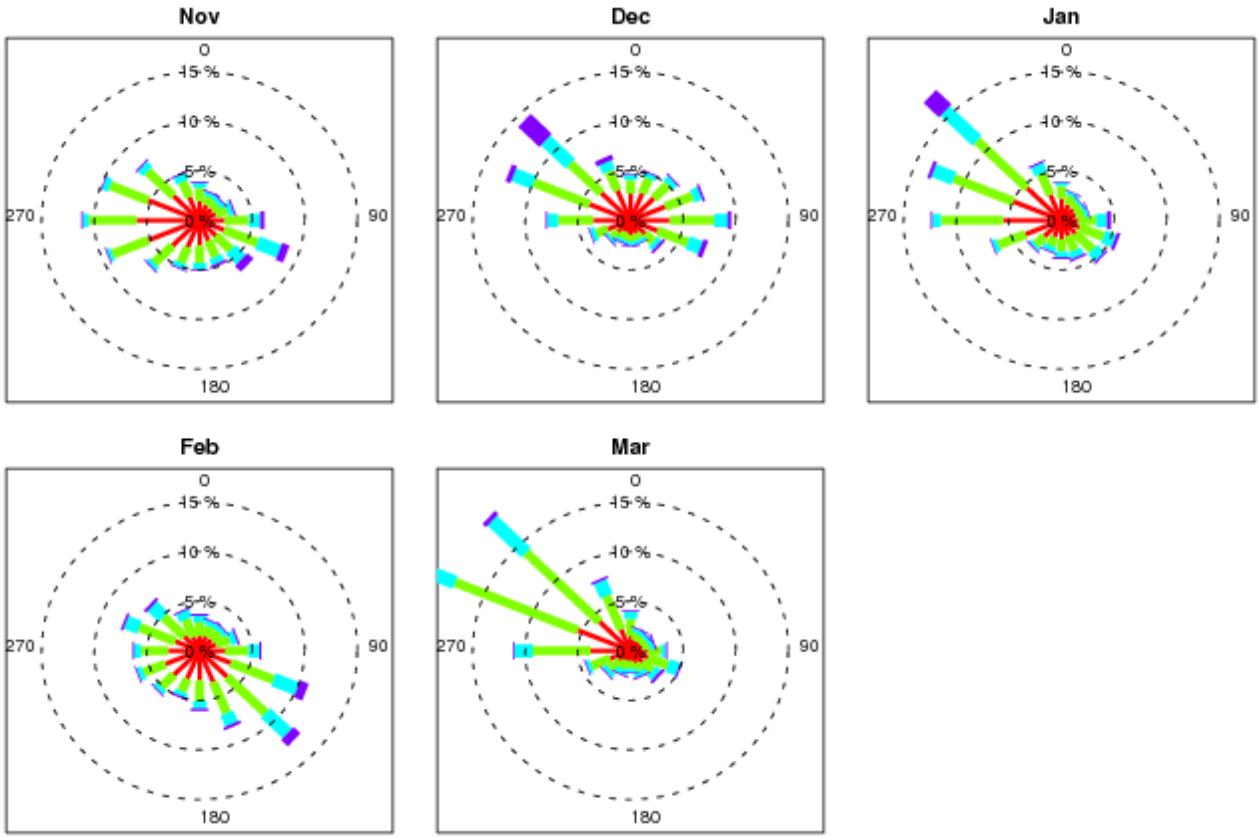

Figure 8.9. Wind rose showing the distribution of mean storm direction of movement, by month. Legend same as Figure 8.8.

8.1.2 Deep versus shallow convection

A noteworthy fraction of the convection observed during the 2007-2008 season appeared to be shallow in nature, having very little ice phase precipitation processes due to low storm tops that were close to or below the freezing level. To quantify this, we have stratified the 2007-2008 radar summary into deep versus shallow clouds based on maximum track storm top height. Figure 8.10 illustrates the importance of how deep and shallow are defined. Using a threshold of 4 km, nearly 75% of the cases are described as deep formations, whereas with a threshold of 6 km this value decreases to approximately 30%. We chose to use 6 km as the threshold to define deep versus shallow storms, given that on most days this height was at or warmer than -10 deg C.

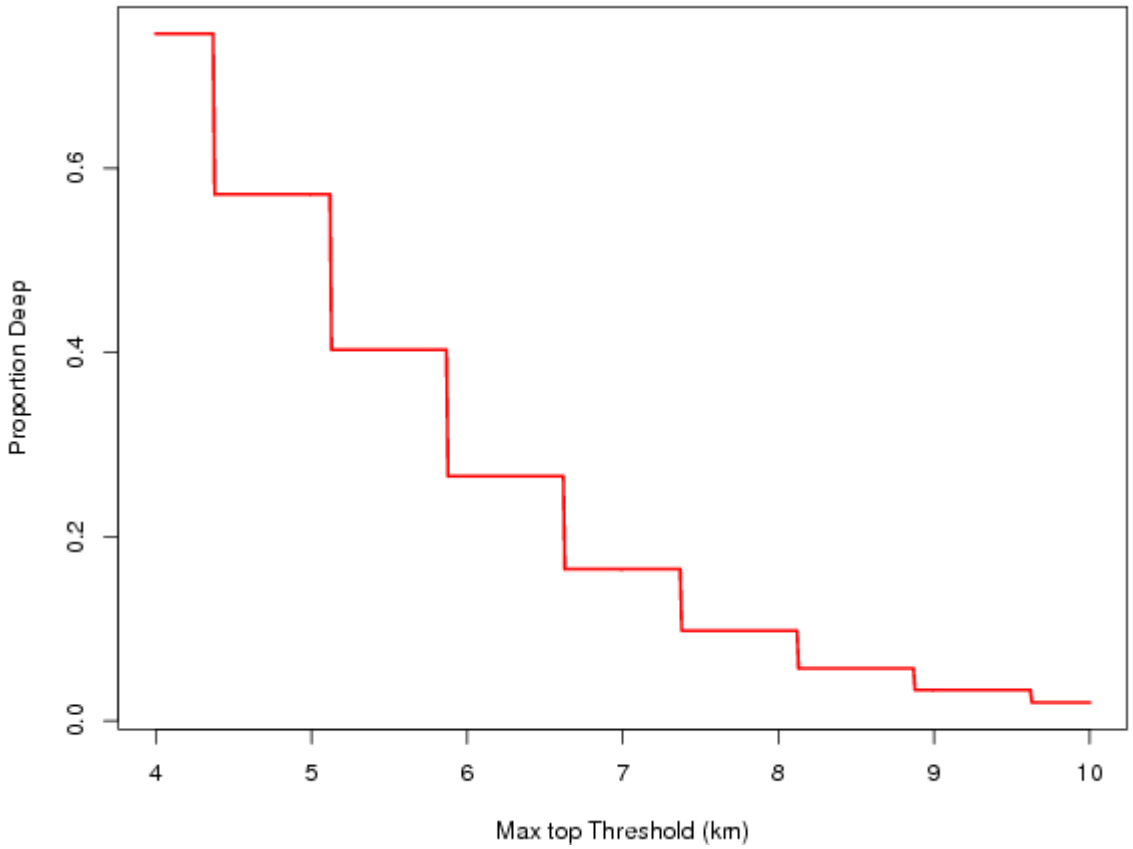

Figure 8.10. Proportion of deep formations as a function of threshold used to classify deep and shallow events.

Figure 8.11 illustrates that the proportion of formations which are deep (tops > 6 km) do not seem to have a strong seasonal pattern, though in February they were more common, in addition to a few periods in November and December as well. Total counts of formations (both deep and shallow) vary greatly on a daily basis (Figure 8.12). The maximum number of deep formations slightly exceeds 500. The maximum number of shallow events slightly exceeds 1500.

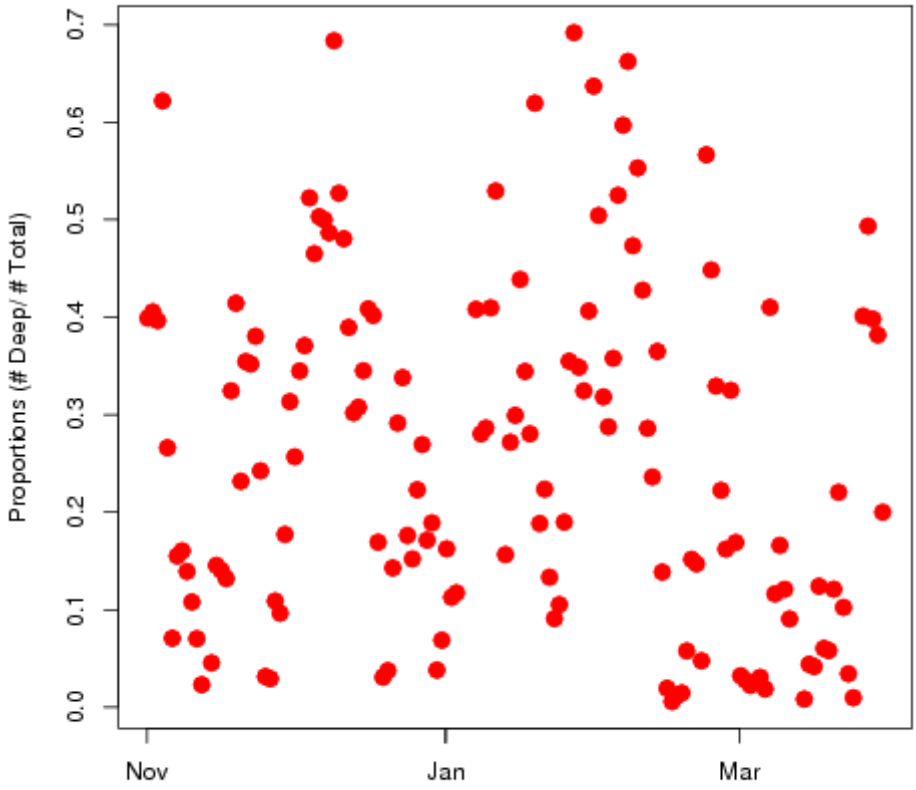

Figure 8.11. Daily proportion of deep events compared to total number of events.

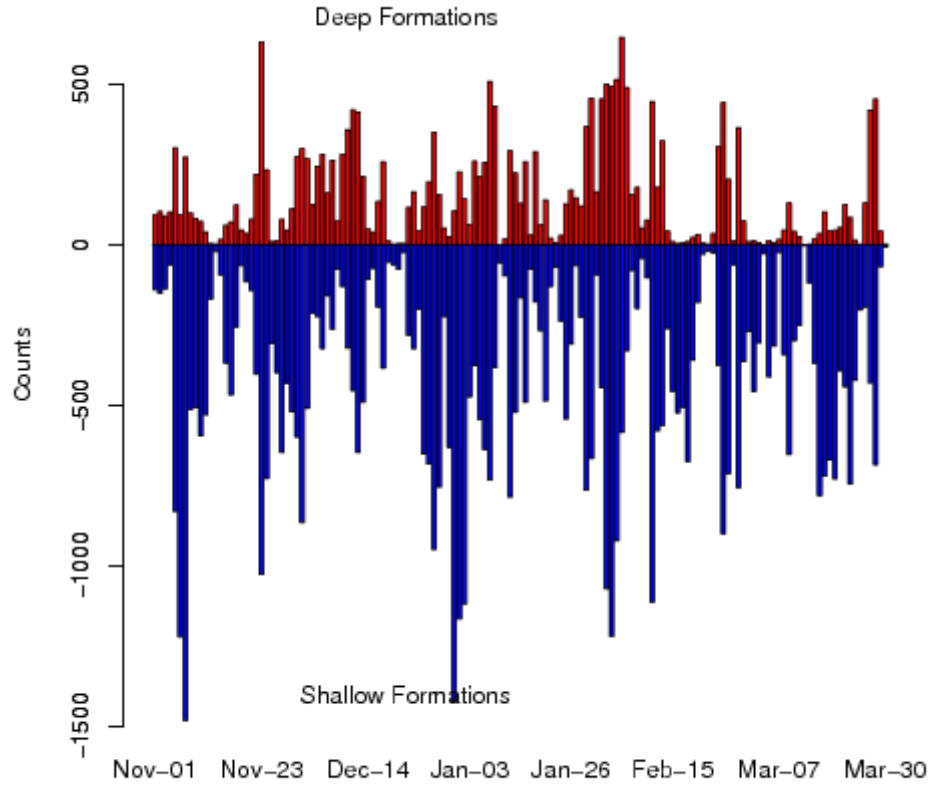

Figure 8.12. Daily counts of deep (red) and shallow (blue) storm tracks.

However, summing the number of deep and shallow events by month (Figure 8.13) shows March with a distinctly smaller number of deep events. February had distinctly a much higher number of deep storms and yet still had a high number of shallow as well. Note that between months, the range of the numbers of shallow events (from ~10,000 to 13,000) varies relatively less than deep events (from ~2,000 to ~6,000).

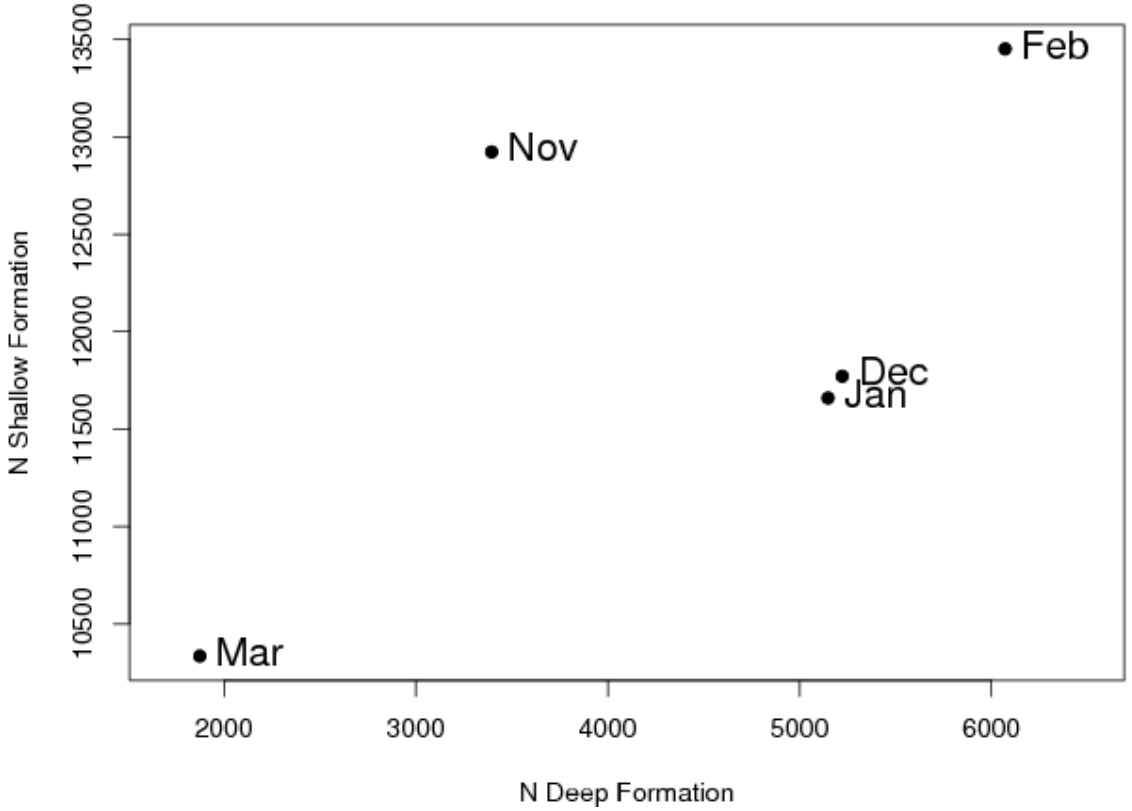

Figure 8.13. Relative numbers of deep and shallow events by month.

By month, comparisons between the distributions of mean precipitation flux values for shallow and deep events remains relatively consistent (Figure 8.14). Deep events have a higher amount of flux and greater variability. The values have been transformed using the log function, so that this distribution is more heavy-tailed than it appears.

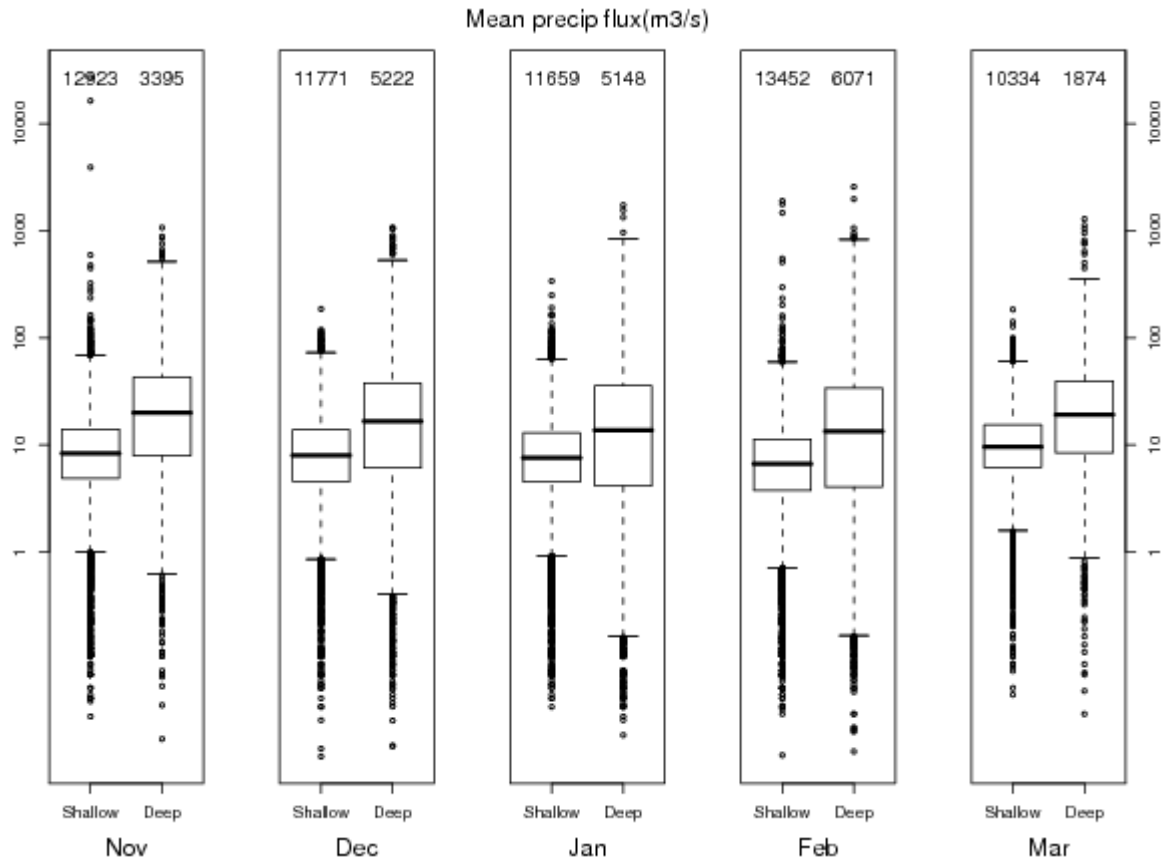

Figure 8.14. Boxplot of mean precipitation flux by month. Note the log scale.

Comparing total precipitation output, deep storms more often produce more precipitation (Figure 8.15-Figure 8.16). However, on several days, the ratio of precipitation output in deep to shallow clouds was less than or equal to unity (Figure 8.16). Figure 8.17 shows this as a function of number of deep and number of shallow storms included in the ratio. This indicates that when the ratio is smaller, then there were fewer deep storms. Higher ratios occur either when there were more deep storms, at any range in number of shallow storms. For an equal number of storms between deep and shallow, the ratio was often in the range of 10-1000. Therefore, given an equal number of deep and shallow storms, the deep clouds produce 10-1000 times more precipitation.

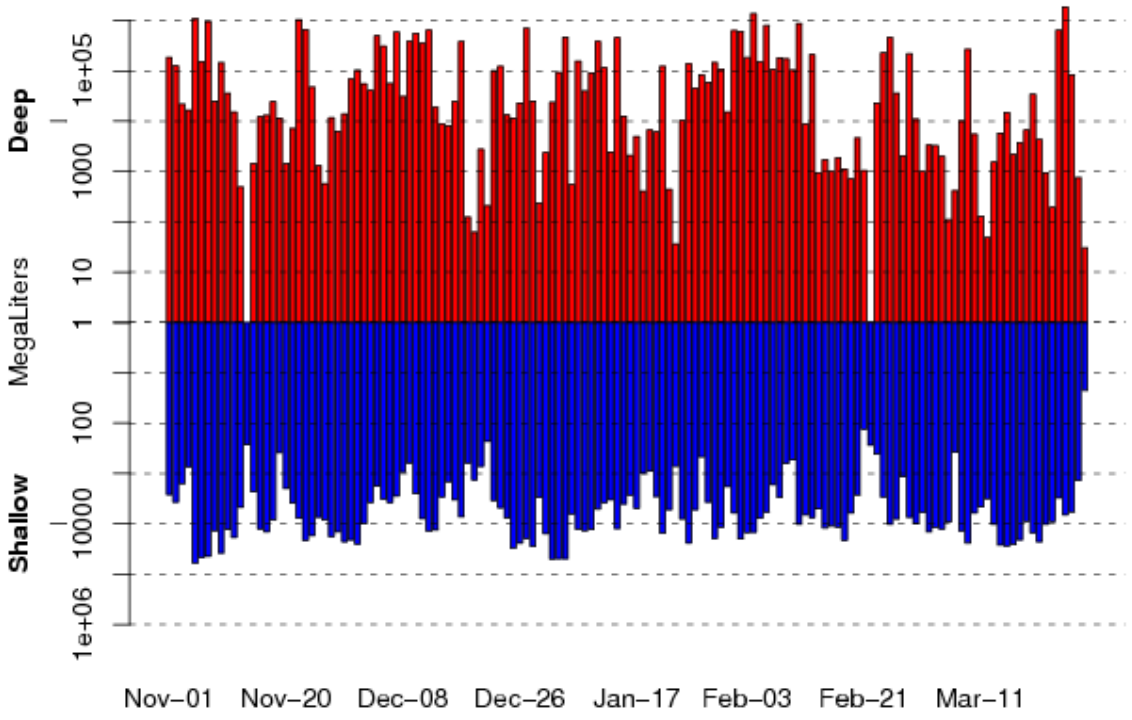

Figure 8.15. Comparison of TITAN-estimated precipitation between shallow and deep storms. Note the log scales.

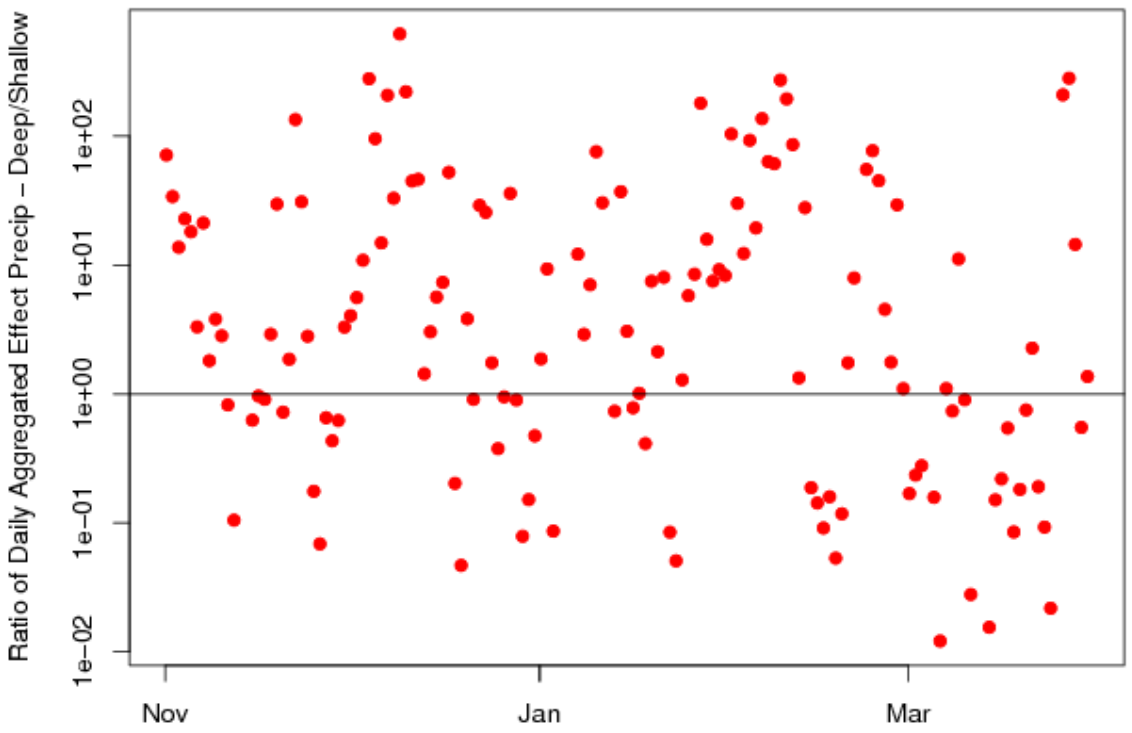

Figure 8.16. Ratio of aggregated effective precipitation between deep and shallow formations. A value of 1 indicates equal amounts.

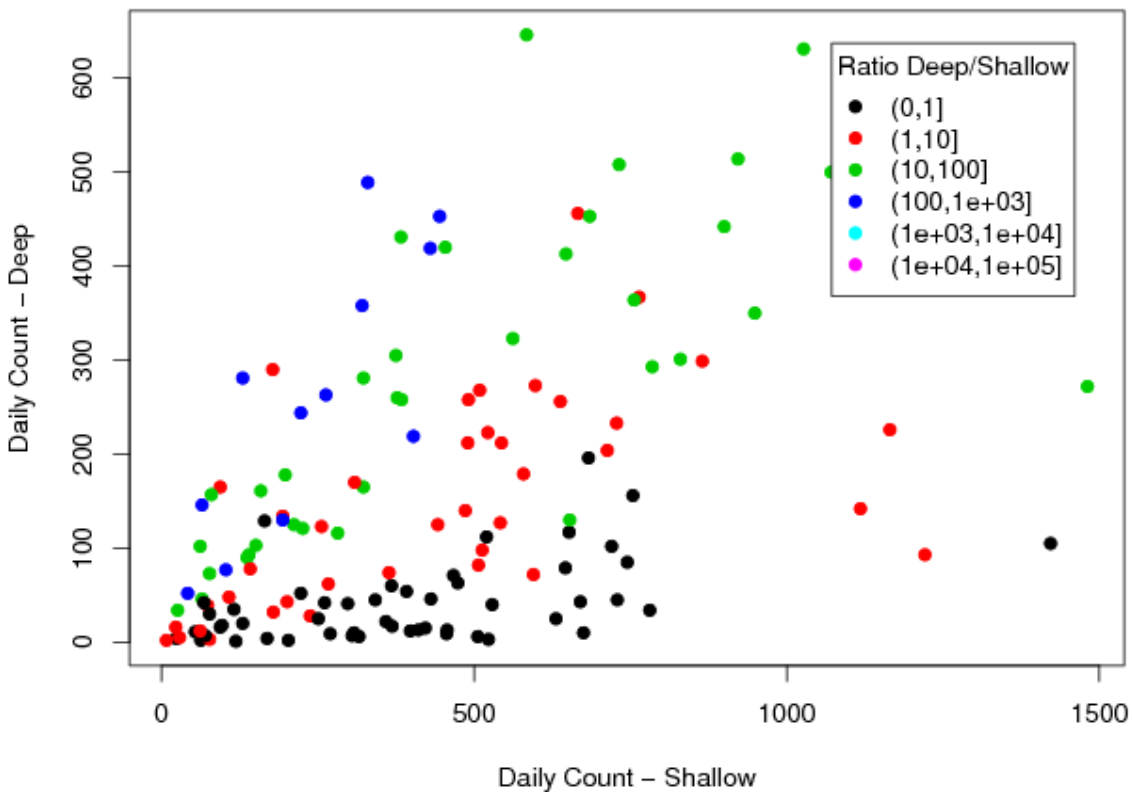

Figure 8.17 Daily counts of shallow and deep formation events. Points colors indicate the ratio of daily accumulative effective precipitation for deep/ shallow formations.

Figure 8.18 describes the mean wind directions and speed for deep and shallow storm tracks. Overall, storm directions of all tracks are bi-modals, with most events coming from the northwest or southeast (see Figure 8.8). Shallow events predominantly travel to the northwest, while deep events have two common directions: to the northwest and the southeast (Figure 8.18). The predominant shallow storm motion is consistent with trade wind cumulus storm motion (see section 5.2.1). Figure 8.19 illustrates the mean storm direction versus mean daily precipitation flux. It is clear that the most intense rainfalls, and thus higher precipitation fluxes, occurred in storms that moved in an eastward direction (approximately 20-120 deg), though lower precipitation fluxes were most common and observed in storms moving in all directions.

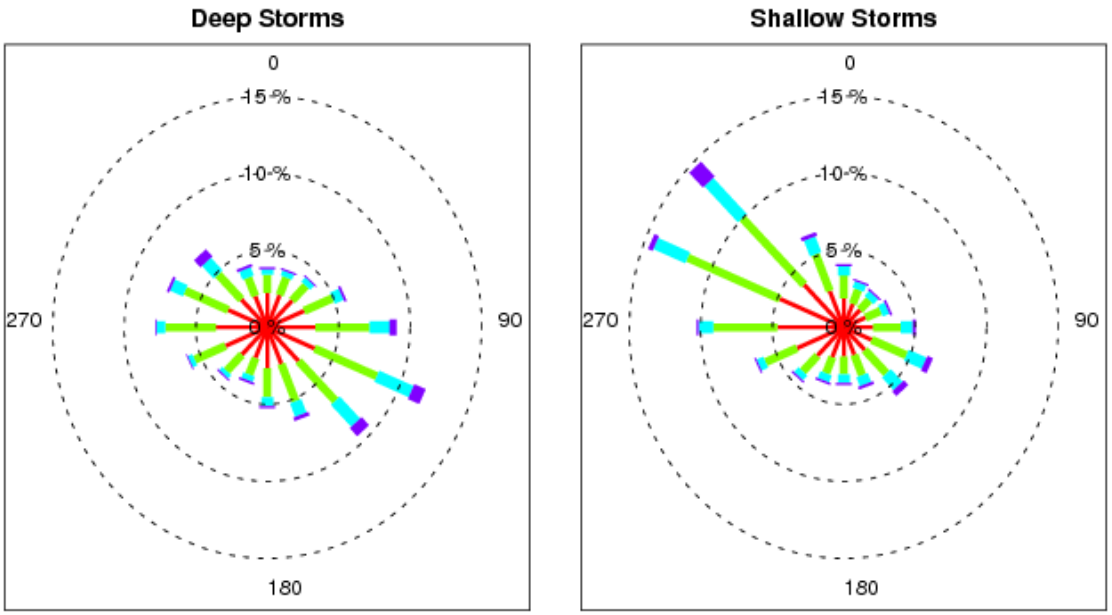

Figure 8.18 Wind roses for deep and shallow events. Legend same as Figure 8.8.

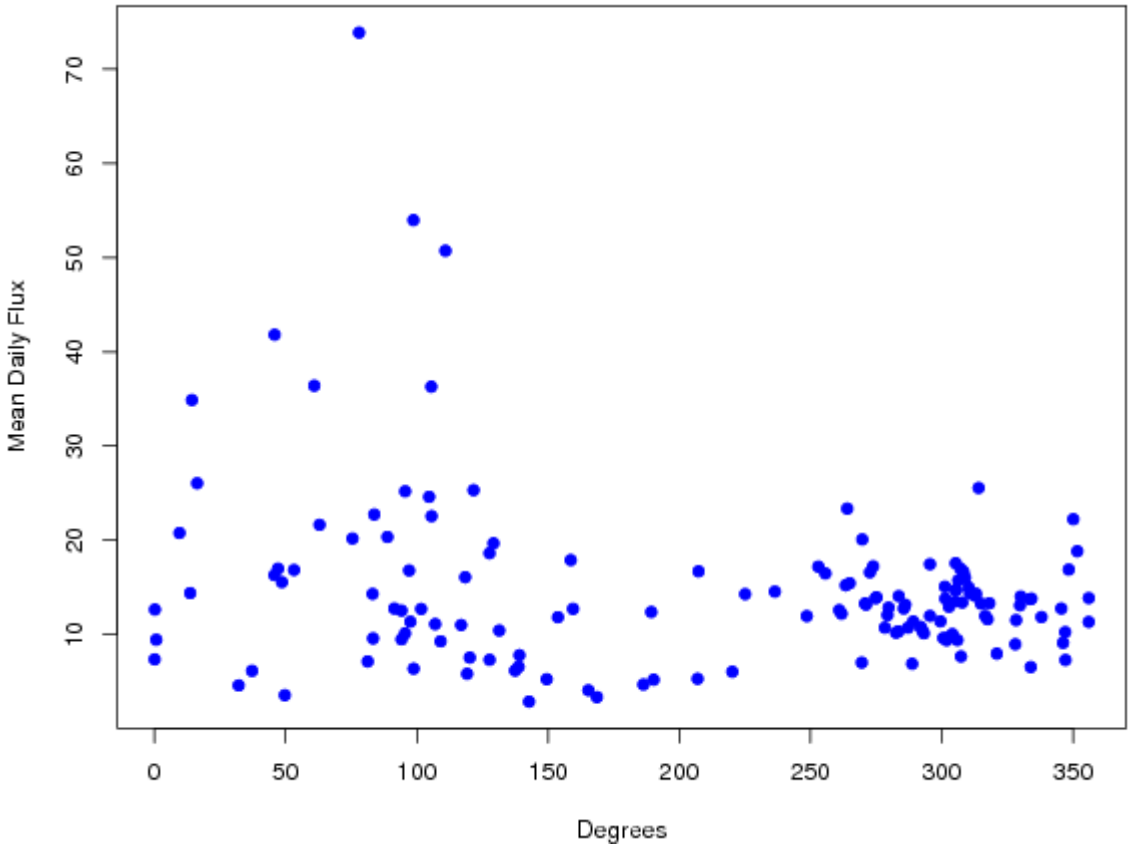

Figure 8.19 Mean daily formation direction versus mean daily mean precipitation flux.

8.2 TITAN-BASED SPATIAL CLIMATOLOGY

TITAN was used to compute and plot the spatial variability of storm characteristics for the 2007-2008 season. This was done on a month-by-month basis to show the change in storm behavior over the course of the experimental period.

8.2.1 TITAN-derived storm motion distribution

Figure 8.20 shows the mean storm motion by month, as derived from TITAN, distributed over the merged radar area. The vector lengths are scaled to represent average storm speed. A 30 km hr^{-1} vector is shown at the top of each image, for reference. The vectors are overlain on the terrain map. In December, January, and March the storm tracks over the ocean tend to be more toward land (to the northwest), while in November and February tracks over the ocean are toward the southeast. Over the land, the storm motion tends to be out of the west and northwest for all months.

a)

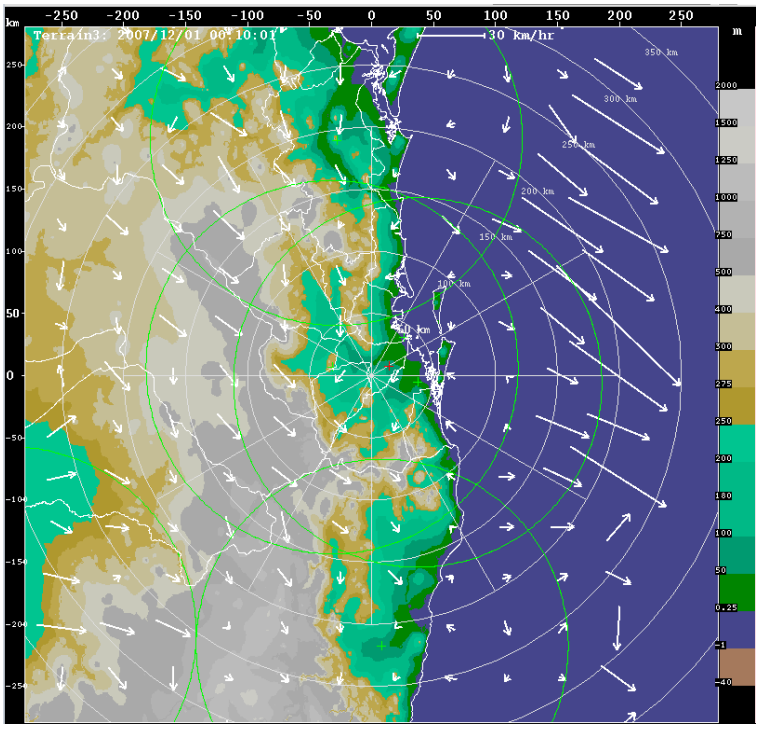

b)

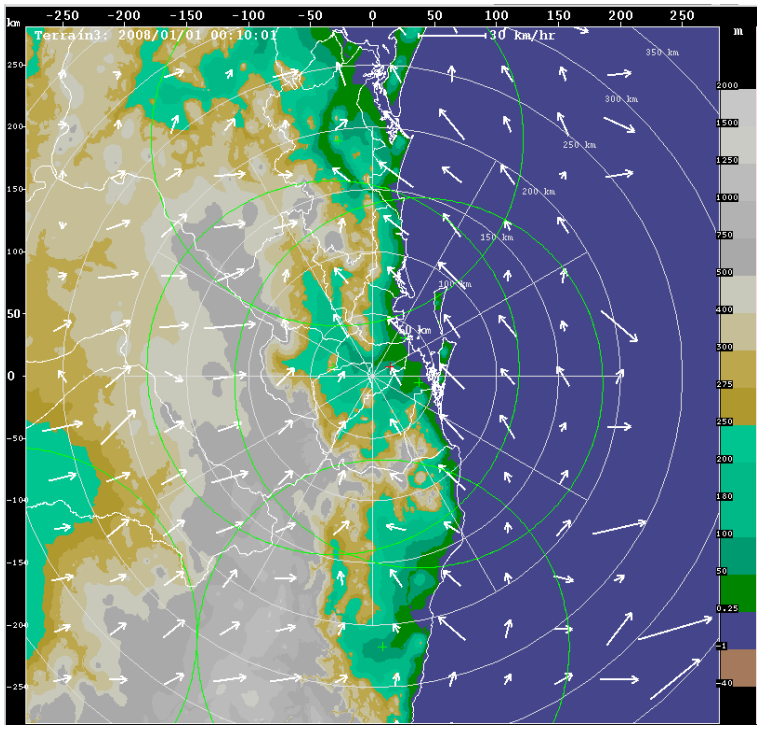
Terrain3: 2008/01/01 00:10:01
30 km/hr

c)

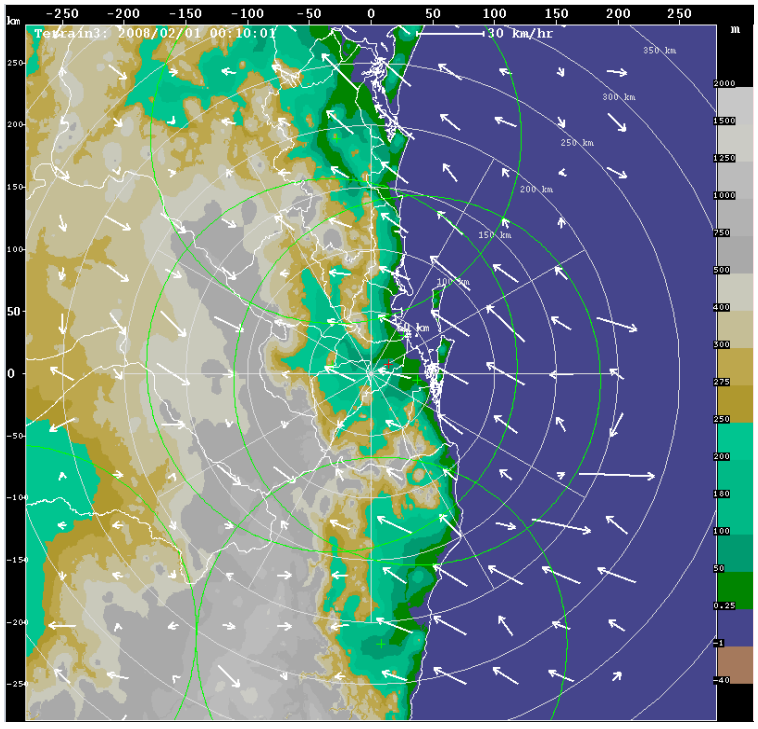
Terrain3: 2008/02/01 00:10:01
30 km/hr

d)

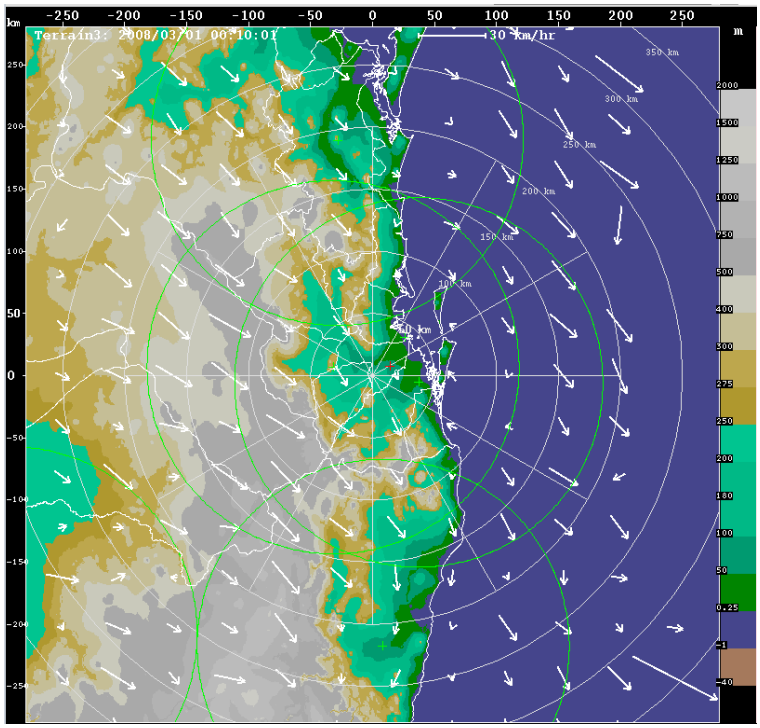

e)

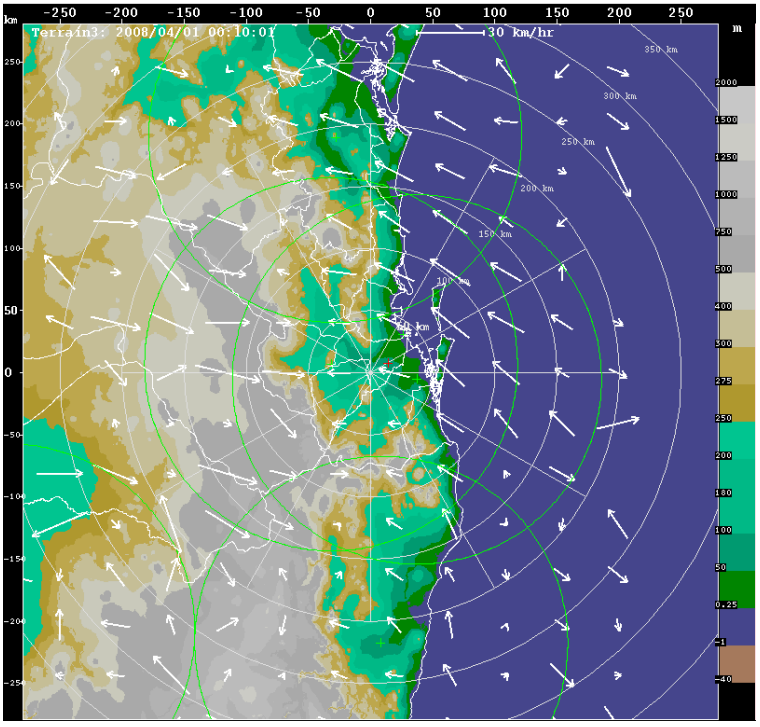

Figure 8.20. TITAN-derived storm motion distributions: (a) November 2007, (b) December 2007, (c) January 2008, (d) February 2008, (e) March 2008.

8.2.2 Storm initiation locations

Figure 8.21 shows the geographical distribution of the storm initiation locations by month, as derived from TITAN. The units are in number of storms initiated per square kilometer per month. Storm initiations were common in all months off the coast and also along higher terrain south and southeast of the CP2 radar (at a range of 50-100 km; see Figure 8.20). February exhibited the most diverse spatial distribution of initiation locations, especially frequent along the coastline, but also over a wide area in the northern portion of the merged radar domain. The higher terrain west of CP2 appears to be less influential for storm initiation in this region, however it may also be an artifact of radar coverage being less optimal in this higher terrain region (especially the dearth of initiation in each month to the southwest of CP2).

a)

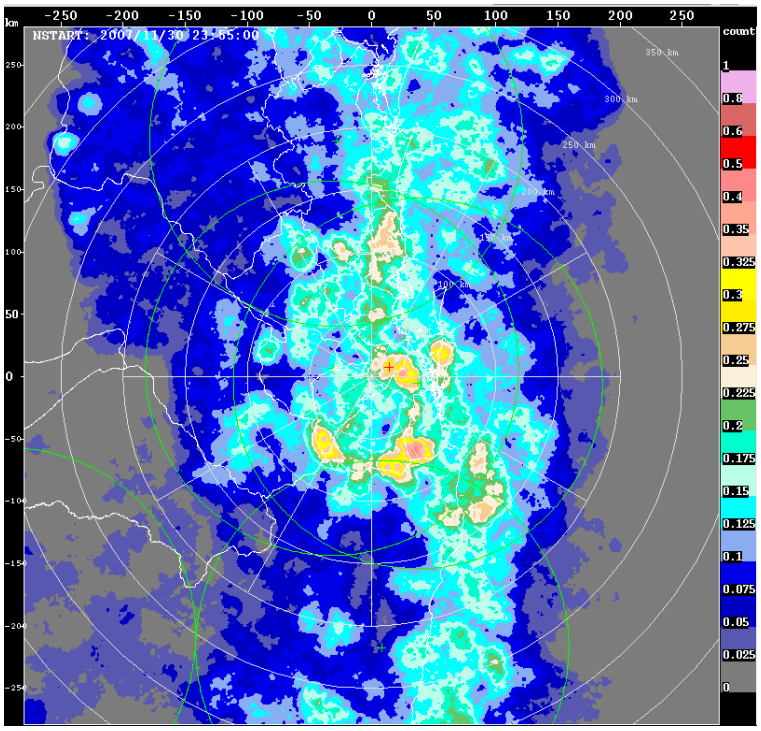

b)

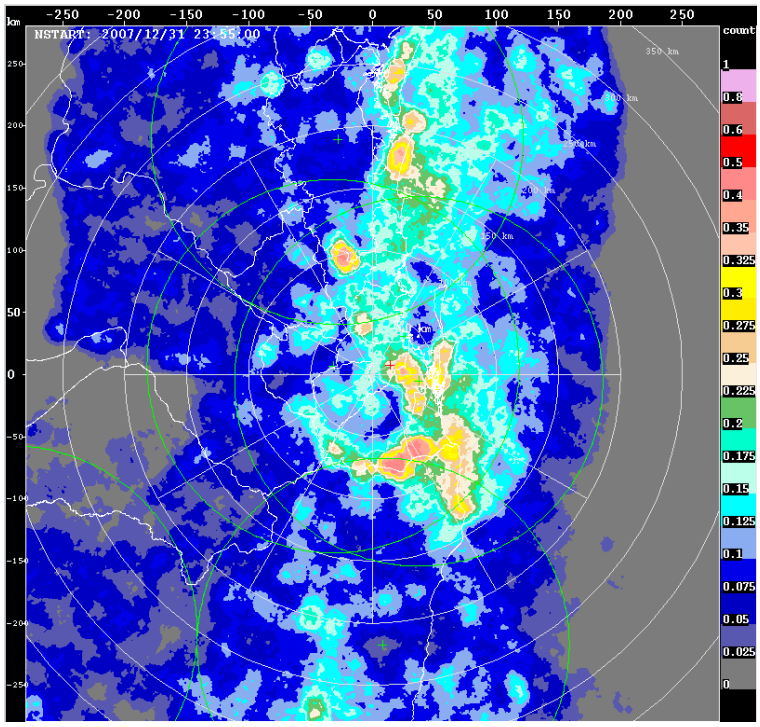
-250 -200 -150 -100 -50 0 50 100 150 200 250
km
NSTART: 2007/12/31 23:55:00
count
1
0.8
0.6
0.5
0.4
0.35
0.325
0.3
0.275
0.25
0.225
0.2
0.175
0.15
0.125
0.1
0.075
0.05
0.025
0

c)

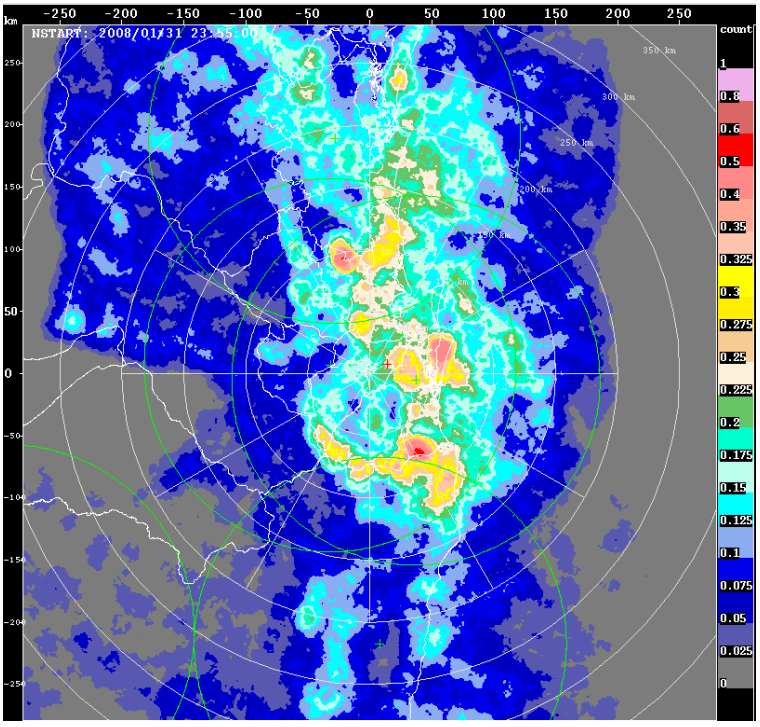
-250 -200 -150 -100 -50 0 50 100 150 200 250
km
NSTART: 2008/01/31 23:55:00
count
1
0.8
0.6
0.5
0.4
0.35
0.325
0.3
0.275
0.25
0.225
0.2
0.175
0.15
0.125
0.1
0.075
0.05
0.025
0

d)

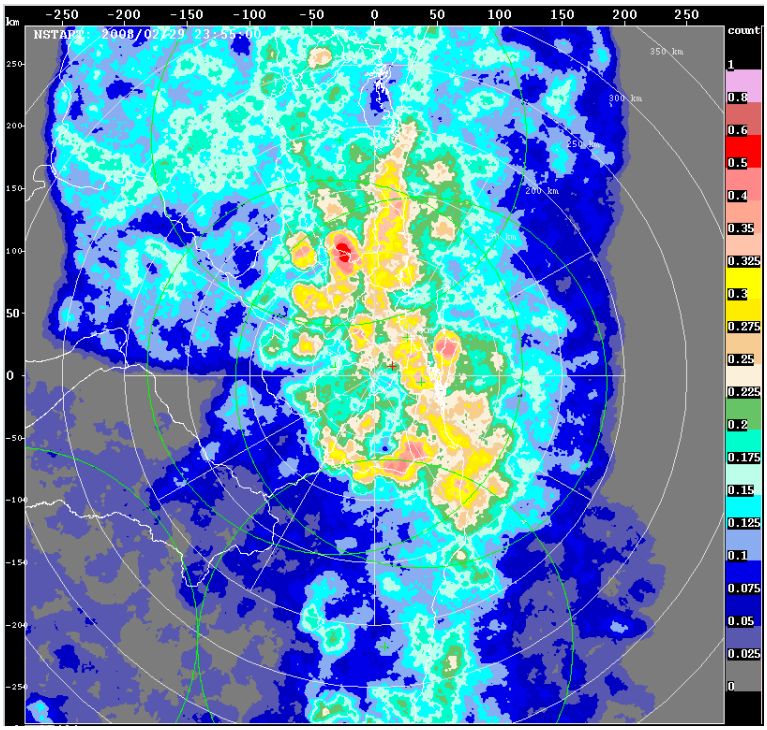

e)

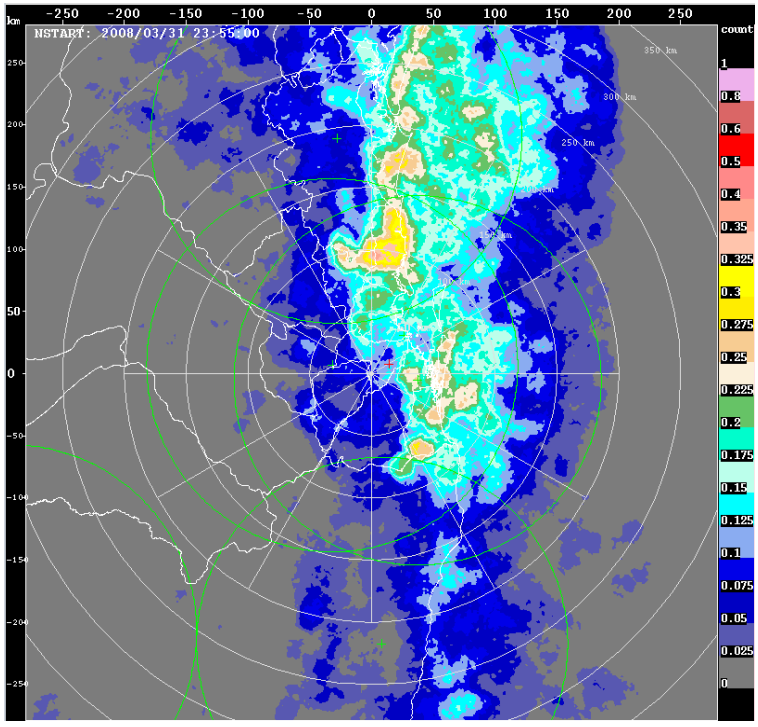

Figure 8.21. TITAN-derived storm initiation locations: (a) November 2007, (b) December 2007, (c) January 2008, (d) February 2008, (e) March 2008.

8.2.3 TITAN-derived precipitation

Figure 8.22 shows the radar-estimated precipitation depth for each month of the experiment. Since the radars used to compute the merged radar grid are not dual-polarization capable, the precipitation estimate is based on a simple Z-R relationship:

$$Z = 200\ R^{1.455} \qquad (4)$$

For this study, the precipitation was computed for the plane height of 1.75 km MSL. This was chosen because it is well below the melting layer, and is the lowest height at which full radar coverage is achieved over the merged domain.

It is clear that February was the wettest month (also shown in Figure 8.2), and precipitation was distributed over the larger Brisbane area, with maxima over the Wivenhoe Dam catchment and within 50-100 km southeast-southwest of CP2. November and December also had notable precipitation, most of which fell west and northwest of CP2 (also including the Wivenhoe Dam catchment). January and March were drier months, though most precipitation in January fell inland, while a noteworthy fraction of the precipitation in March fell just off the coast.

A data quality issue (see section 4.2.9) that is noticeable in these plots is that the Mt. Stapylton radar reflectivity tends to be a bit higher than the surrounding radars (thus possibly biasing too much precipitation in its domain). This is a radar calibration issue, which will be further investigated. This bias is most obvious in Figure 8.22d, as the domain-dependent ring of higher precipitation.

a) 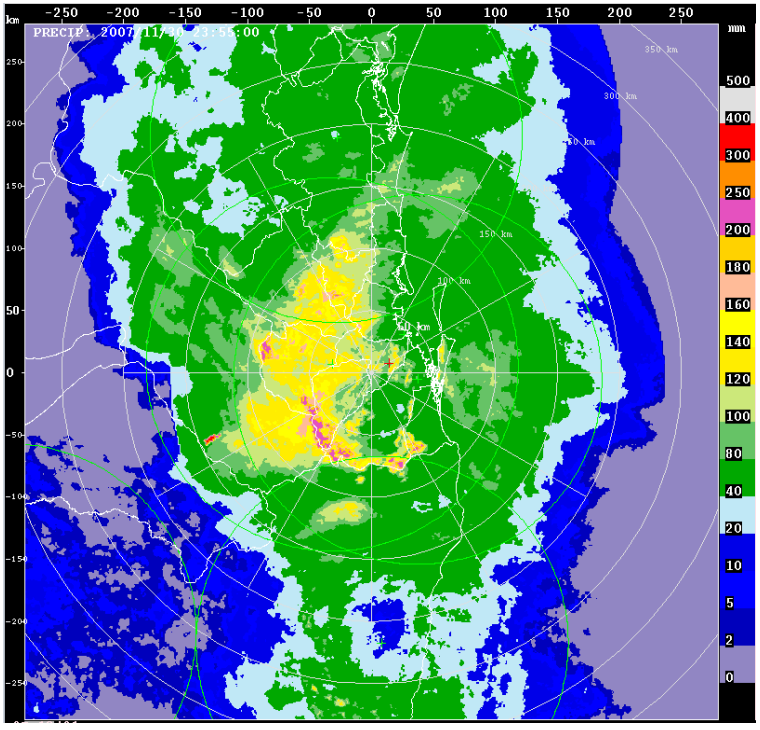

b)

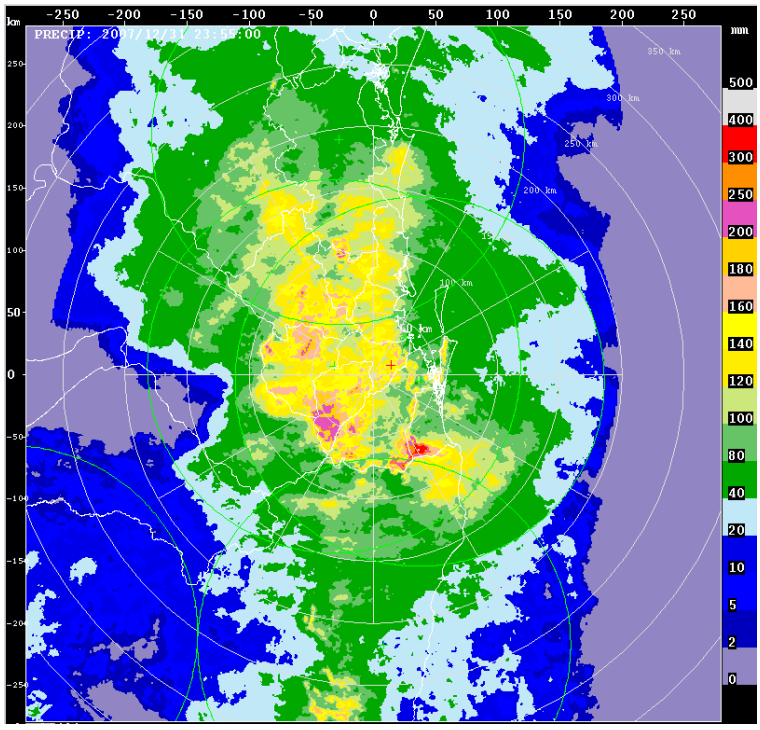
-250 -200 -150 -100 -50 0 50 100 150 200 250
km
mm
500
400
300
250
200
180
160
140
120
100
80
40
20
10
5
2
0

c)

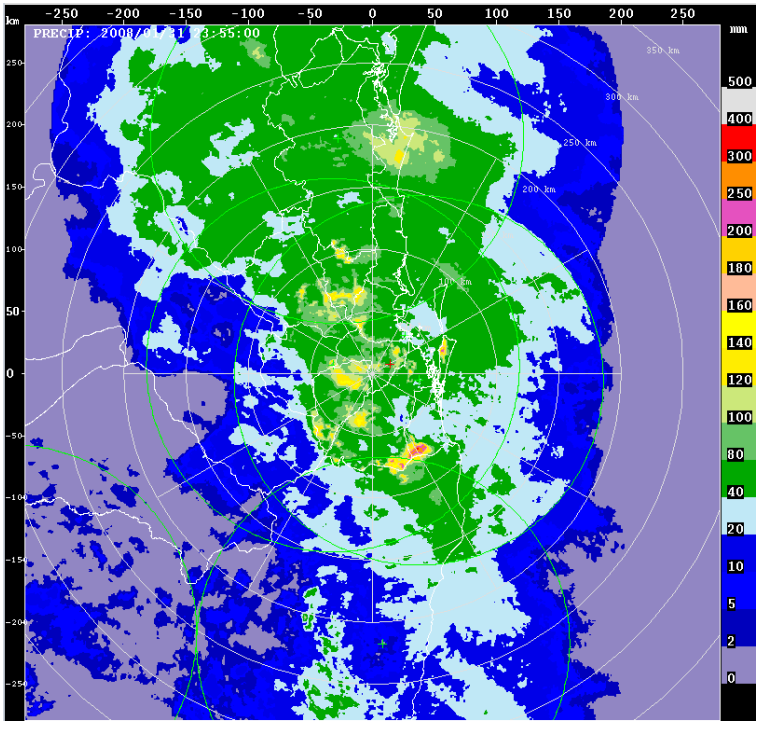
-250 -200 -150 -100 -50 0 50 100 150 200 250
km
mm
500
400
300
250
200
180
160
140
120
100
80
40
20
10
5
2
0

d)

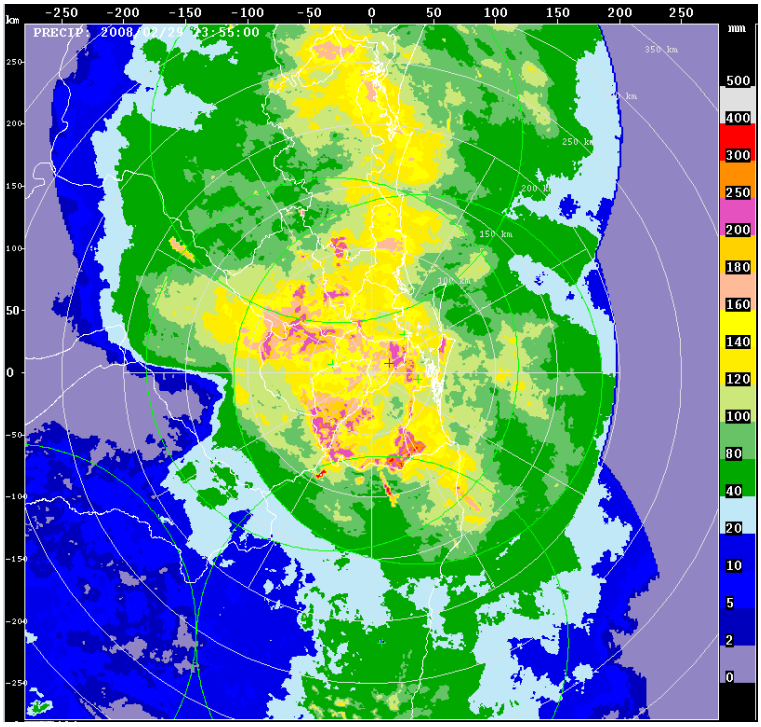

e)

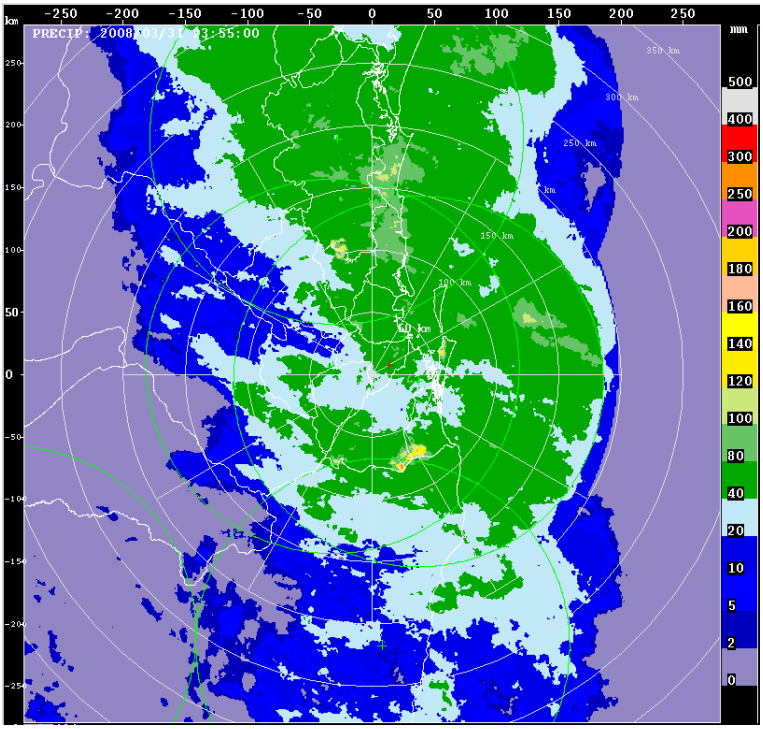

Figure 8.22. TITAN-derived precipitation maps: (a) November 2007, (b) December 2007, (c) January 2008, (d) February 2008, (e) March 2008.

8.3 RADAR ECHO EVOLUTION FROM FIRST ECHO

A unique research opportunity occurred on 8 Feb 2008 when a hailstorm with large hail occurred in the southern dual-Doppler lobe. While the storm was not seeded or sampled by the project airplanes it does provide what is believed the first ever opportunity to use a polarimetric radar to monitor the evolution of the rain and hail within a storm while at the same time retrieving from the dual-Doppler analysis the three-dimensional wind field within the storm. Figure 8.23 is a vertical scan through the storm, which shows a horizontal vortex; it is believed this mechanism allows for continued recycling of precipitation, which can lead to the growth of large hail. The 3-dimensional wind fields together with the microphysical information should provide understanding of the processes involved in producing large hail.

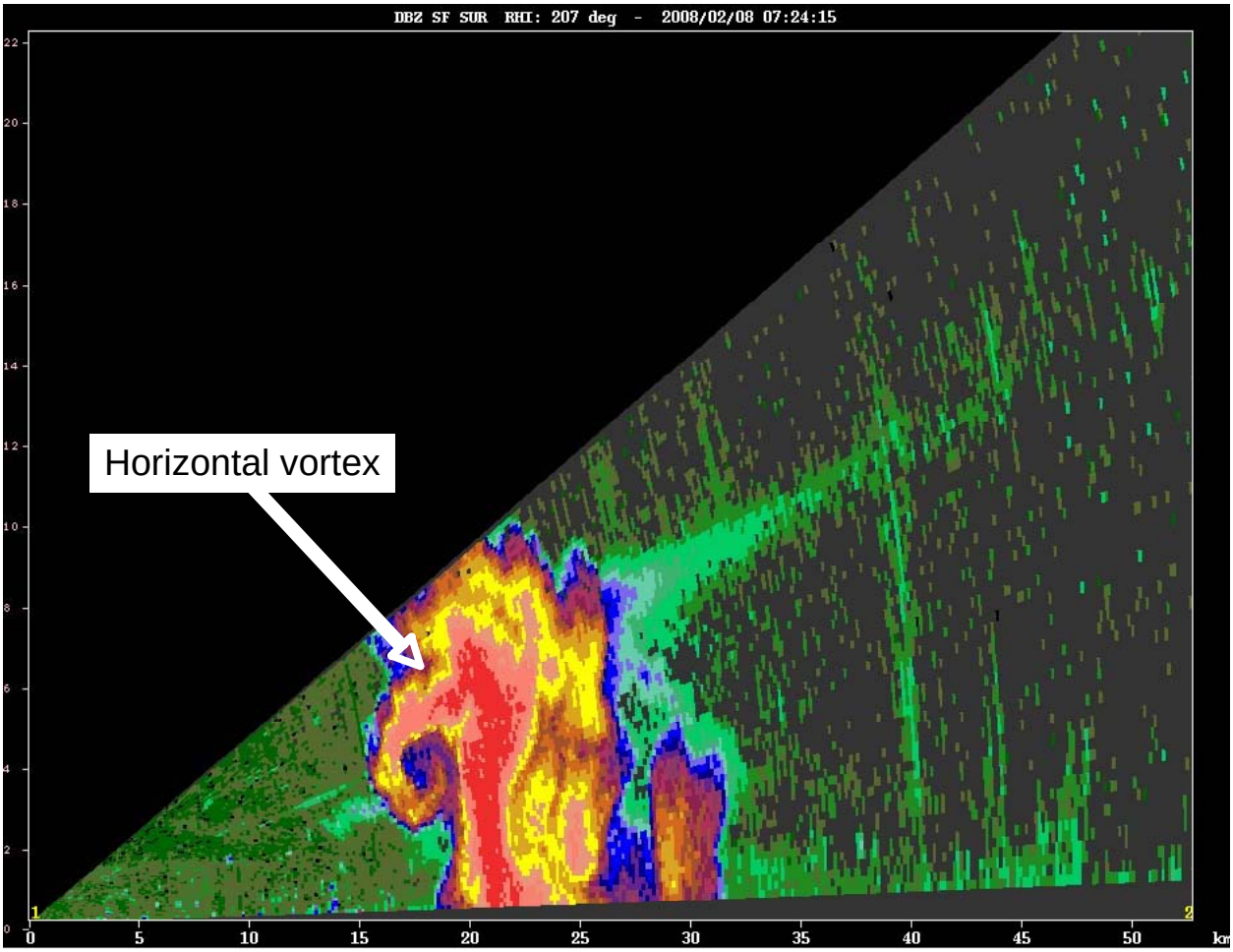

Figure 8.23. Radar reflectivity vertical scan through a hail storm on 8 Feb 2008 in the southern dual-Doppler lobe. The red reflectivities (>55 dBZ) are mostly associated with hail. It is suspected that precipitation is recycled in the horizontal vortex leading to the production of large hail.

8.4 DISDROMETER RAINDROP SIZE DISTRIBUTIONS

Rain storms were classified subjectively as convective, stratiform, and mixed. Figure 8.24 presents some drop size distribution (DSD) attributes for convective precipitation. Rain rates greater than 100 mm h^{-1} were computed. There is considerable scatter which is common for convective precipitation. The DSD slope and shape parameters tend to be small for heavy rains, i.e., the distributions are relatively broad (flat) and close to exponential. Both μ and Λ increase for light rainfall rates which generally have more mono-dispersed (peaked) DSDs. However, instrumentation issues with small drops also contribute to this result.

Drop size distribution characteristics for stratiform rains are shown in Figure 8.25. Maximum rain rates are 10−15 mm h^{-1}. While measurement error contributes to the relationship between N_0 and μ [see, for example, Chandrasekar and Bringi (1987)], the slope of the distribution differs from that of the slope for stratiform rains. Larger N_0s for convective events at a specific μ is akin to the N_0 jump found by Waldvogel (1974) for exponential DSDs. The relation between Λ and μ has proven to be useful for retrieving drop size distributions from polarimetric radar measurements (Zhang et al. 2001, 2004; Brandes et al. 2004). Examination of Figure 8.24Figure 8.25 reveals that, for a specific slope, the DSD tends to be more peaked for stratiform precipitation. Fitted relations to the measurements are (for convection)

$$\Lambda = 2.648 + 1.302\mu + 0.1261\mu^2 - 0.006366\mu^3 \qquad (5)$$

and (for stratiform rain)

$$\Lambda = 2.448 + 0.9836\mu + 0.05676\mu^2 - 0.002329\mu^3 \quad . \qquad (6)$$

Values of Λ larger than ~8 mm^{-1} often associate with small drops and small number concentrations; hence; they should be treated cautiously.

Using the disdrometer observations, polarimetric rainfall estimators were developed for convective and stratiform rains. Relations for convective storms are

$$R(Z_H) = 0.0396 Z_H^{0.679} \qquad (7)$$

$$R(Z_H, Z_{DR}) = 2.06 \times 10^{-2} Z_H^{0.867} Z_{DR}^{-5.00} \qquad (8)$$

$$R(K_{DP}) = sign(K_{DP}) 53.3 \left|K_{DP}\right|^{0.669} \qquad (9)$$

$$R(K_{DP}, Z_{DR}) = sign(K_{DP}) 192 \left|K_{DP}\right|^{0.927} Z_{DR}^{-1.48} \quad , \qquad (10)$$

where Z_H is the radar reflectivity at horizontal polarization, Z_{DR} is the differential reflectivity, and K_{DP} is the specific differential phase. All units are linear. Relations (6) and (7) are based on a sample of 605 data points. Relations (9) and (10) are based on a subset of the data (349 observations with $K_{DP} > 0^o$ km^{-1}).

Rain rate relations for stratiform storms are:

$$R(Z_H) = 0.0190 Z_H^{0.678} \tag{11}$$

$$R(Z_H, Z_{DR}) = 1.13 \times 10^{-2} Z_H^{0.903} Z_{DR}^{-6.31} \quad . \tag{12}$$

The latter expressions, based on 2347 1-min disdrometer samples, are valid for rain rates as large as 10−15 mm h^{-1}. Corresponding relations using the specific differential phase parameter have not been constructed because the signal at S-band is weak for stratiform rain and the standard error in the K_{DP} calculation is large (roughly 0.10° km^{-1} or 10 mm h^{-1}).

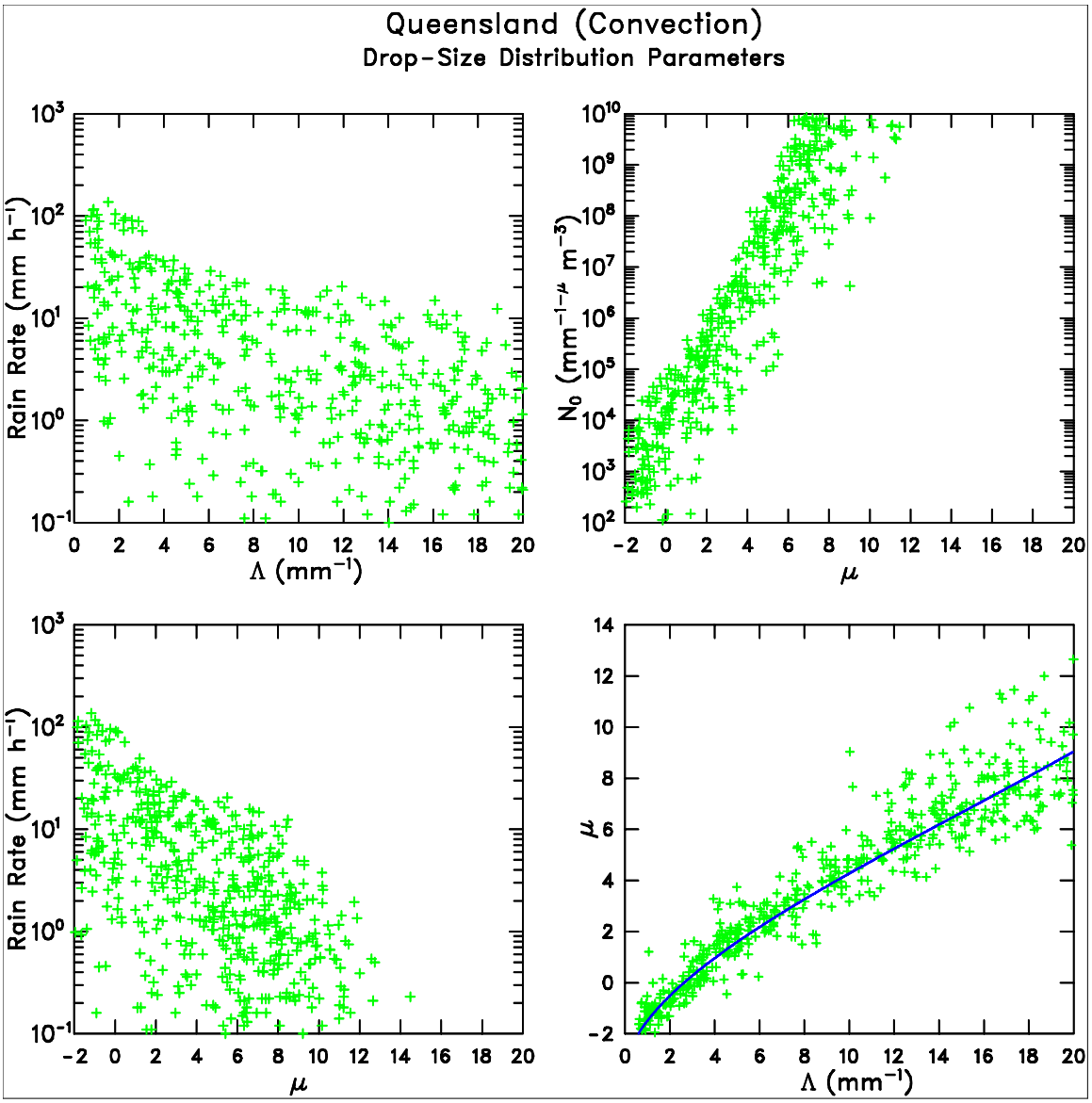

Figure 8.24. Drop size distribution attributes of convective rain storms.

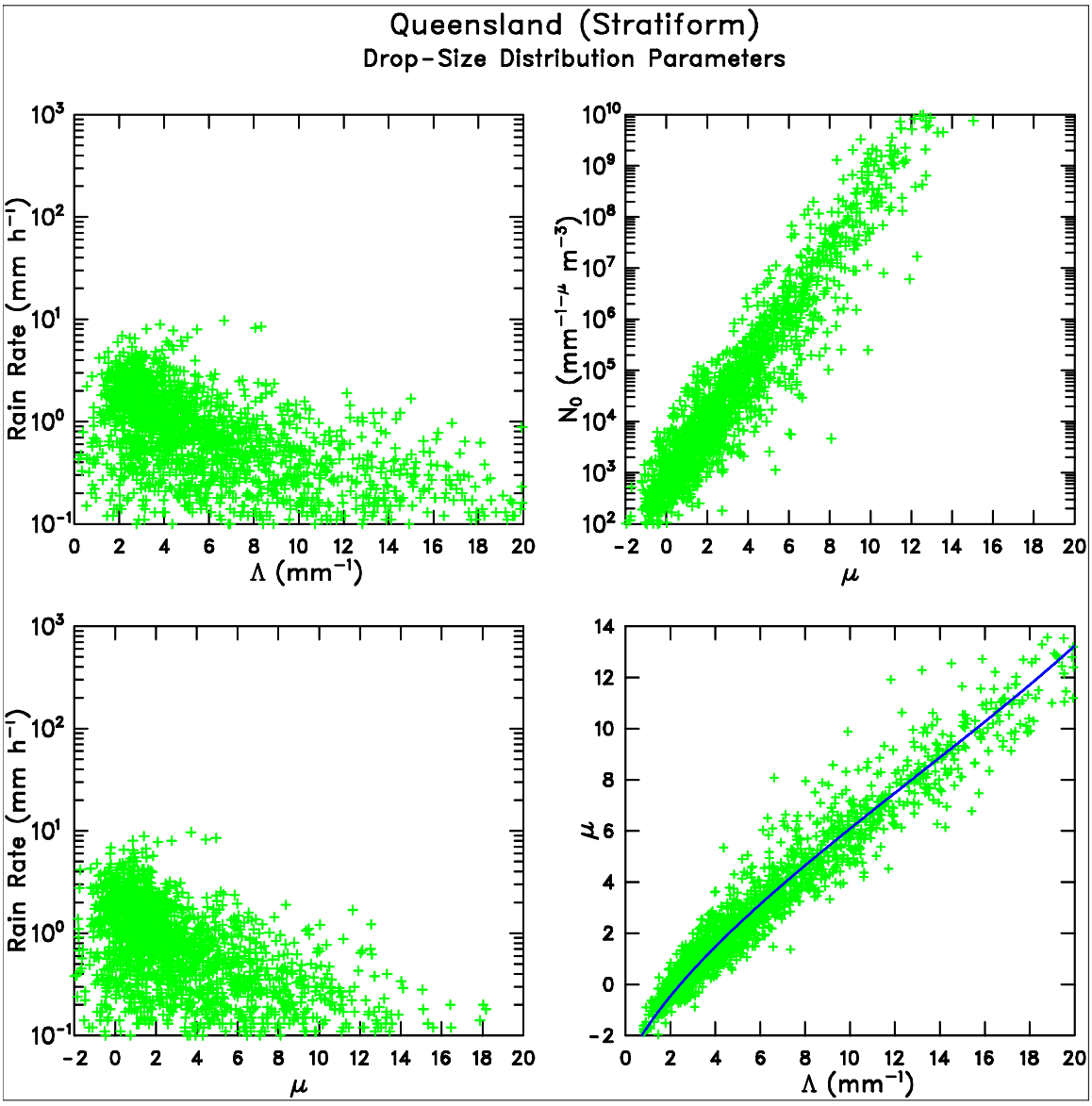

Figure 8.25. As in Figure 8.24, except for stratiform rain storms.

9. CLOUD SEEDING STUDIES AND ASSESSMENT

9.1 FLARE PARTICLE CHARACTERIZATION

On 13 March 2008, SEEDA1 flew tight orbits while firing two sets of hygroscopic flares. The purpose of this flight was to sample the flare plume to characterize the aerosol size distribution of the flare material. The background aerosol on this day compared to that measured within the flare plume is illustrated in Figure 9.1. The additional coarser mode (near 0.2 microns) in the aerosol size distribution is apparent of the flare plume, and at very high concentrations (near 3000 cm^{-3}). When the background aerosol distribution is removed from that with the flare plume measurements, the peak at 0.2 microns with a concentration of 3000 cm^{-3} is the primary mode of the flare distribution (Figure 9.2).

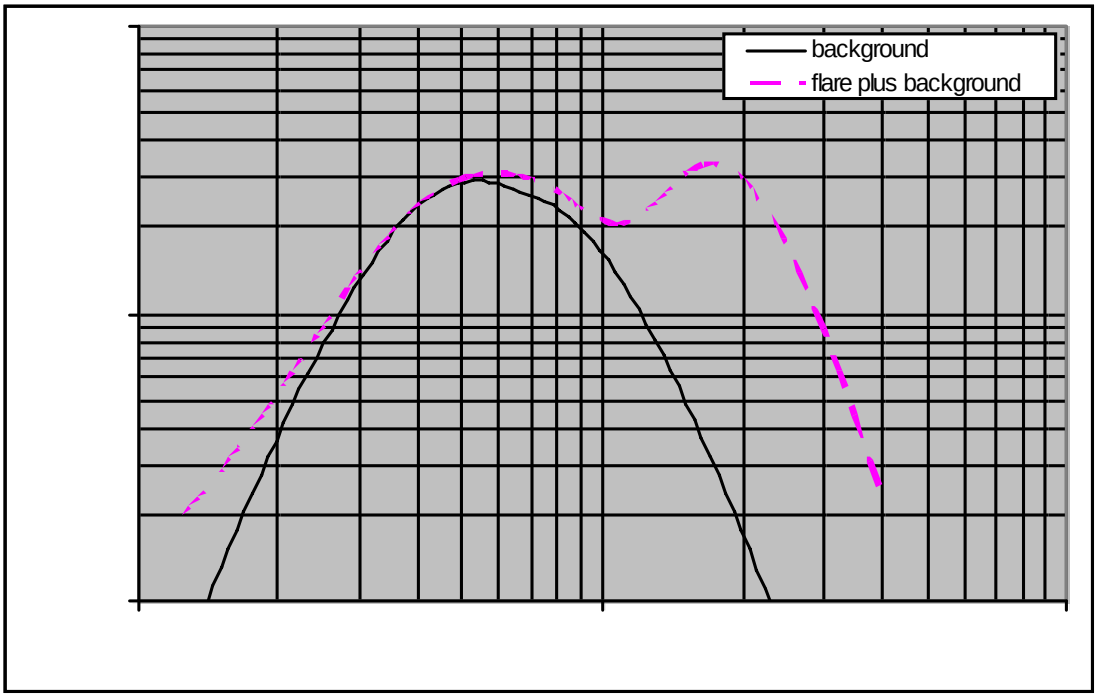

Figure 9.1. On 13 March 2008 at UTC 03:58:47, ZS-JRA sampled its own flare product released a few minutes earlier while flying tight orbits. The background aerosol distribution in non-seeded air (average of UTC 03:55:35 and 03:56:00 DMA readings) is depicted by the thin black line. The flare product particle size distribution (plus background) is depicted by the pink dashed line.

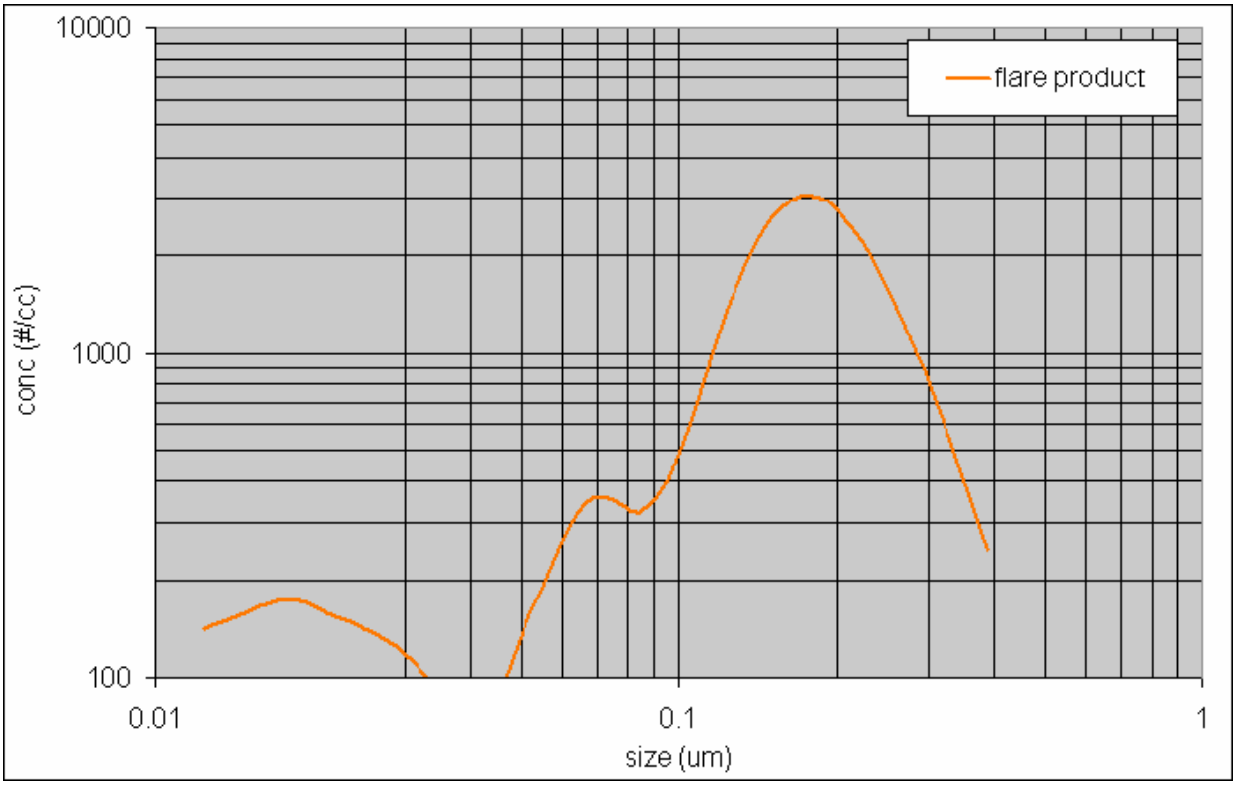

Figure 9.2. Removal of the background air from the flare plus background DMA curve has revealed the airborne particle size distribution of hygroscopic flare material released by ZS-JRA on 13 March 2008.

9.2 SEEDING HYPOTHESIS AND VALIDATION

Atmospheric water in the form of precipitation is one of the primary sources of fresh water in the world. However, a large amount of water present in clouds is never transformed into precipitation on the ground given the complex processes of precipitation development (see section 12.2.5). This has prompted the exploration of augmenting water supplies by means of artificial cloud seeding. The theories behind cloud seeding as a potential method to enhance rainfall are outlined in the Appendix (sections 12.2.6-12.2.10).

Hygroscopic seeding was the primary type of seeding conducted during the 2007-2008 Queensland CSRP. The hypothesis behind hygroscopic seeding techniques and the results of previous studies utilizing such techniques are presented in section 12.2.8.

9.3 OPERATIONAL SEEDING TRIAL CASE STUDIES

9.3.1 February 16, 2008

Figure 9.3 shows cloud droplet size spectra measurements recorded by the FSSP probe during a flight undertaken by SEEDA1 (ZS-JRA) on 16 Feb 2008 approximately 10 km northeast of Bromelton (approximate lat/long coordinates -27.800, 153.080). During the part of the flight from approximately 0330 to 0400 UTC, SEEDA1 flew repeated penetrations through a

cloud seeded by WXMOD. SEEDA1 maintained a constant altitude of 1800m above a cloud base, which on this day was located at approximately 1300m (4000 feet) above sea-level (Figure 9.4).

Figure 9.3 shows a sudden coarsening of the cloud droplet size (from around 20 to 25 microns mean droplet size). The instrumented aircraft (SEEDA1) was flying consistently 2000 feet above the WXMOD seeding aircraft, which had been continuously seeding the cloud since 0336 UTC. It is possible that the spectrum coarsening at 0341 UTC may have been facilitated by hygroscopic particles introduced into the cloud by WXMOD approximately five minutes earlier. In five minutes, the particles would have risen 2000 feet in the cloud, as the approximate updraft velocity reported by WXMOD was 400 feet per minute. Furthermore, total FSSP droplet concentrations were measured at and above 200 cm^{-3} (Figure 9.4), which is slightly higher than might have been expected given the cloud base aerosol and CCN measurements of near 100 cm^{-3} at maximum (1%) supersaturation (see section 7.1.2). This can be explained in two ways: first, the flare particles could have caused a broadening in the drop size distribution, and secondly the aerosol concentration could be composed of large CCN (CCN > 1 micron). These aerosols are not measured by the DMA. The DMA measures aerosols from 0.01-0.38 microns. When the CCN are calculated, the DMA distribution is used, meaning that the calculated CCN concentration is dependent on the DMA size distributions. It is observed from Figure 7.6 that the CCN concentration reaches just slightly over 100 cm^{-3} at 1% supersaturation. As mentioned above, the FSSP peak concentration reaches 200 cm^{-3}, which is greater than the calculated CCN concentration. A more detailed look at the FSSP drop size distributions (Figure 9.3) show that droplets larger than 20 microns are present at 500 m above cloud base. Since the FSSP concentration are larger than the CCN concentration calculated using the DMA size distribution, then it is likely that aerosols greater than 0.38 microns were acting as CCN, which can explain the discrepancy between the calculated CCN concentration and the measured FSSP cloud droplet concentration. Furthermore, precipitation-sized drops were detected in high numbers (see 2DP shadow counts in Figure 9.4), and thus droplet shatter on the FSSP inlet could have increased FSSP total concentrations. All of these possible effects on the FSSP measurements need to be studied further.

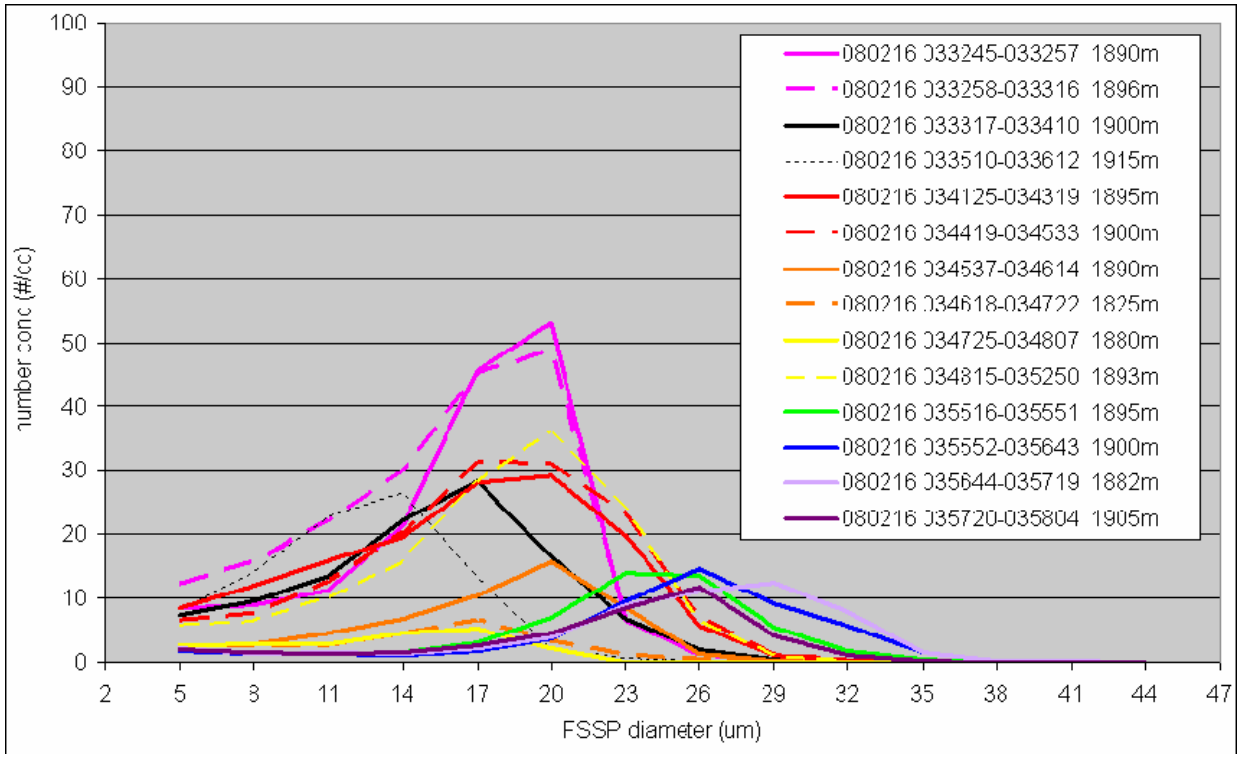

Figure 9.3. Cloud droplet size distributions measured by the FSSP probe. ZS-JRA was flying repeated penetrations through a cloud seeded by WxMOD northeast of Bromelton (-27.800, 153.080). Whilst sampling ZS-JRA maintained a constant altitude of 1800m above a cloud base at approximately 1300m. Statistics from these distributions are outlined in Table 9.1.

Table 9.1. Droplet spectra statistics relevant to the spectra shown in Figure 9.3.

	Mean diameter $D_{BAR}(d_{10})$	Standard deviation SD $\sigma(d_{10})$	Dispersion coefficient $CV(d_{10})$	Mass mean diameter $MMD(d_{30})$	Effective radius $ER(r_{32})$
080216 033245-033257	16.36	6.97	0.43	17.47	9.23
080216 033258-033316	15.26	5.95	0.39	16.61	8.93
080216 033317-033410	15.05	5.02	0.33	16.59	9.04
080216 033510-033612	12.10	5.28	0.44	13.26	7.21
080216 034125-034319	16.37	4.86	0.30	18.10	9.87
080216 034419-034533	17.21	5.24	0.30	18.71	10.06
080216 034537-034614	17.19	6.00	0.35	18.53	9.88
080216 034618-034722	14.41	4.91	0.34	16.30	9.09
080216 034725-034807	13.12	5.26	0.40	14.60	8.00
080216 034815-035250	17.67	5.71	0.32	19.08	10.19
080216 035516-035551	22.39	6.50	0.29	23.89	12.60
080216 035552-035643	24.47	6.35	0.26	26.06	13.72
080216 035644-035719	24.72	6.17	0.25	26.42	13.95
080216 035720-035804	21.99	6.57	0.30	23.72	12.61

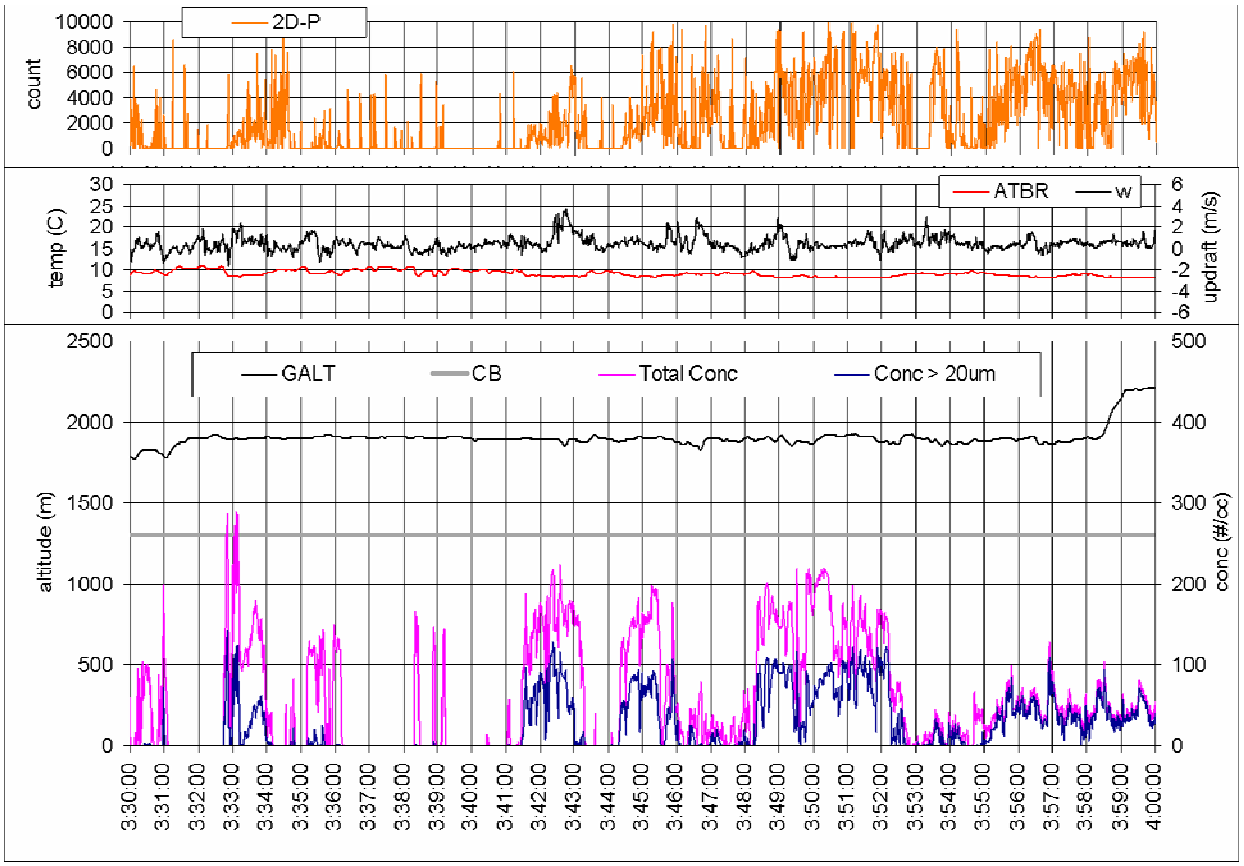

Figure 9.4. Flight chart summary details for the period of interest on 16th February, 2008. There is an apparent droplet spectrum coarsening as revealed by the FSSP instrument which may have been the result of hygroscopic seeding of the cloud by WXMOD.

9.3.2 March 6, 2008

Three randomized cases were conducted on this day in shallow cumulus clouds (see Table 6.3), all with clouds bases around 3800 ft (1150 m) and reported updrafts of 400 ft min^{-1} (~2 m s^{-1}). Randomized case #22 (seeded) was targeted by SEEDA1 for research measurements at 0327 UTC, and seeding occurred between 0324-0336 UTC at cloud base by WXMOD. For a summary of the weather conditions on this day, see section 7.1.4.

Individual cloud penetrations were defined as time periods when the FSSP total concentration was > 50 cm^{-3} for at least three seconds (at an average aircraft speed of 80 m s^{-1} this yields clouds of at least 240 m width). Penetrations were analyzed beginning when SEEDA1 targeted case #22 at 1550 m (400 m, or approximately 1500 ft, above cloud base) at 032700 UTC (Table 9.2). SEEDA1 initially penetrated this cloud at 400 m (approximately 1500 ft) above cloud base, then ascended to 700 m (2300 ft), 1350 m (4500 ft), and 1950 m (6400 ft) above cloud base for further penetrations. As the cloud began to dissipate, SEEDA1 descended back to 1650 m (5500 ft) above cloud base for a final penetration. As can be seen in Figure 9.5, the seeding was conducted between two weak echoes, one slightly north-northwest of the other. Given the storm motion to the northwest, it is assumed in this analysis that either the seeding was being conducted in a new updraft and separate turret not yet seen on radar in between these two

echoes, or the seeding was conducted on the updraft of the existing echo to the south (since over time this echo was repeatedly targeted by SEEDA1). Regardless, without a tracer in the seeding material, determining exactly where the seeding material went is ambiguous, thus the notes in Table 9.2 describe where the penetration was relative to the seeding activity and location of WXMOD and not the exact cloud penetrated. However, as time passed, only one echo remained (possibly still the original southern echo) and final penetrations by SEEDA1 were targeted through this echo, referred to then as the primary cloud (Figure 9.12, Figure 9.15).

Table 9.2. List of selected cloud penetrations by SEEDA1 of and near seeded cloud (randomized case #22). Penetration number is relative to when SEEDA1 targeted this cloud (at 032700 UTC) , but otherwise is somewhat arbitrary. Time is in UTC (HHMMSS), altitude is in meters.

Pen #	Time	Altitude	Direction	Notes
6	033034-033047	1550	NE to SW	south of seeding
7	033056-033110	1550	NE to SW	south of seeding
8	033118-033129	1550	NE to SW	west of seeding
9	033140-033147	1550	NE to SW	west of seeding
10	033149-033158	1550	NE to SW	west of seeding
11	033210-033214	1550	NE to SW	west of seeding
12	033446-033508	1850	SW to NE	north of seeding
14	033700-033719	1850	SE to NW	south of seeding
15	033804-033806	1850	SE to NW	south of seeding
16	033827-033838	1850	SE to NW	north of seeding
17	033904-033912	1850	SE to NW	north of seeding
20	034111-034136	2500	W to E	over seeding
21	034139-034157	2500	W to E	over seeding
24	034357-034402	2500	S to N	primary cloud
25	034411-034415	2500	S to N	primary cloud
26	034749-034822	2500	N to S	primary cloud
31	035036-035118	3100	E to W	primary cloud
33	035316-035345	2800	NW to SE	primary cloud

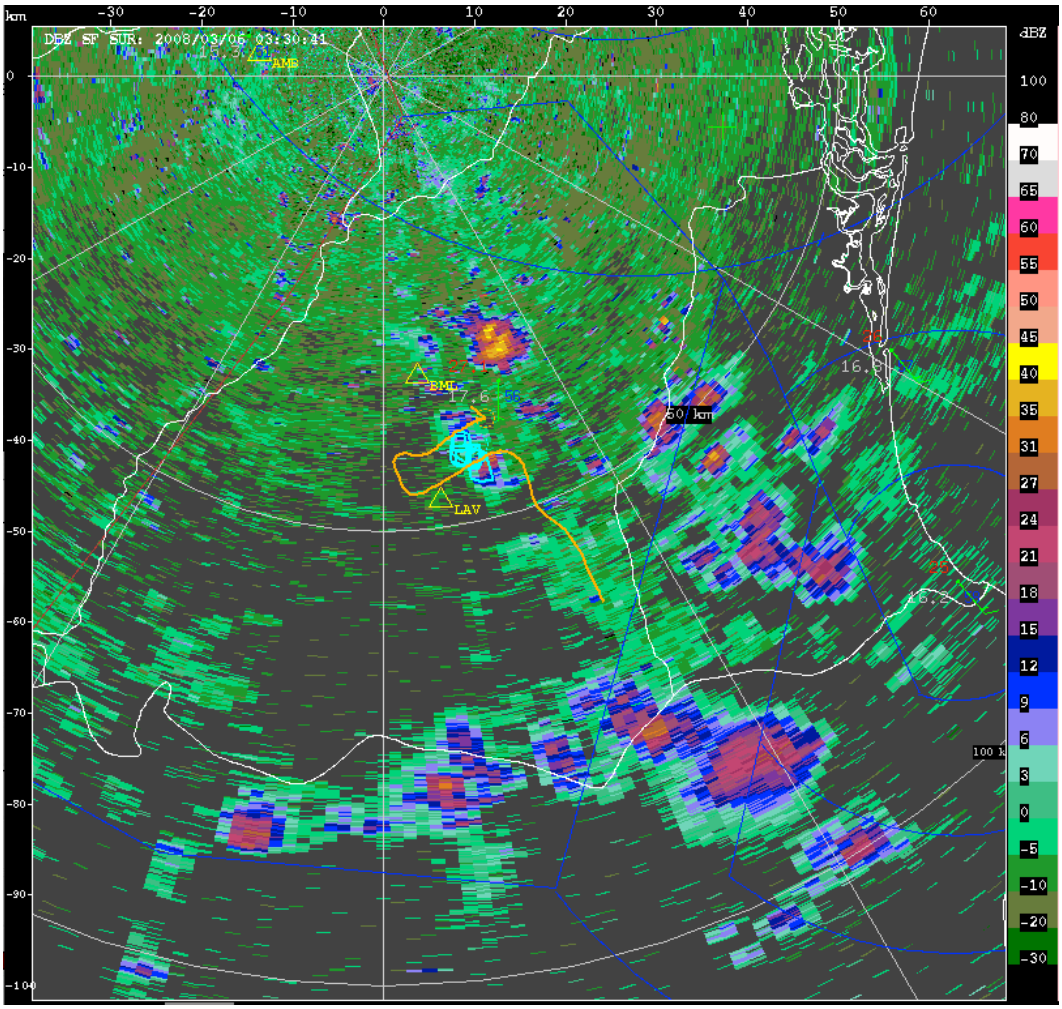

Figure 9.5. CP2 radar reflectivity PPI (.98 deg) scan at 033041 UTC on 6 March 2008. WXMOD is seeding at this time (cyan track), and SEEDA1 is beginning penetrations of the seeded cloud (orange track). Aircraft tracks encompass the time interval from 032600 to 033600 UTC.

In an attempt to simplify the analysis, the flight segments have been broken into segments at constant altitude (Figure 9.6, Figure 9.8, Figure 9.11, Figure 9.14). The first segment illustrates the time period when SEEDA1 conducted penetrations at 400 m above cloud base (Figure 9.6). The aircraft track during this time is shown in Figure 9.5, as the northeast to southwest portion of the SEEDA1 track that was south of the seeding location. Several cloud penetrations were defined along this track, even though not all were evident on radar. Based on the timing of the track relative to the radar echo, the earlier penetrations along this segment were more likely in the targeted cloud, while the later penetrations were well southwest of the targeted cloud. The drop size distributions (DSDs) from each of these penetrations are shown in Figure 9.7. Penetrations #6-8 had similar DSD shapes, with mean particle diameters of 9-10 microns. Penetration #8, however, had high 2DP shadow counts (> 2000 s^{-1}) indicating precipitation-sized drops were present, and may have enhanced the FSSP concentrations at that time due to drop shattering. Penetrations #9-10 had similar DSD shapes as well, with slightly larger mean

diameters of 10-11 microns. The last penetration (#11), however, had a much smaller mean diameter of 6 microns and narrower DSD shape. All penetrations except #11 also had total concentrations near 400 cm^{-3}, while penetration #11 had lower total drop concentrations of 300 cm^{-3}. These total cloud droplet concentrations were consistent with the calculated CCN activation using the DMA aerosol size distribution on this day (Figure 7.12).

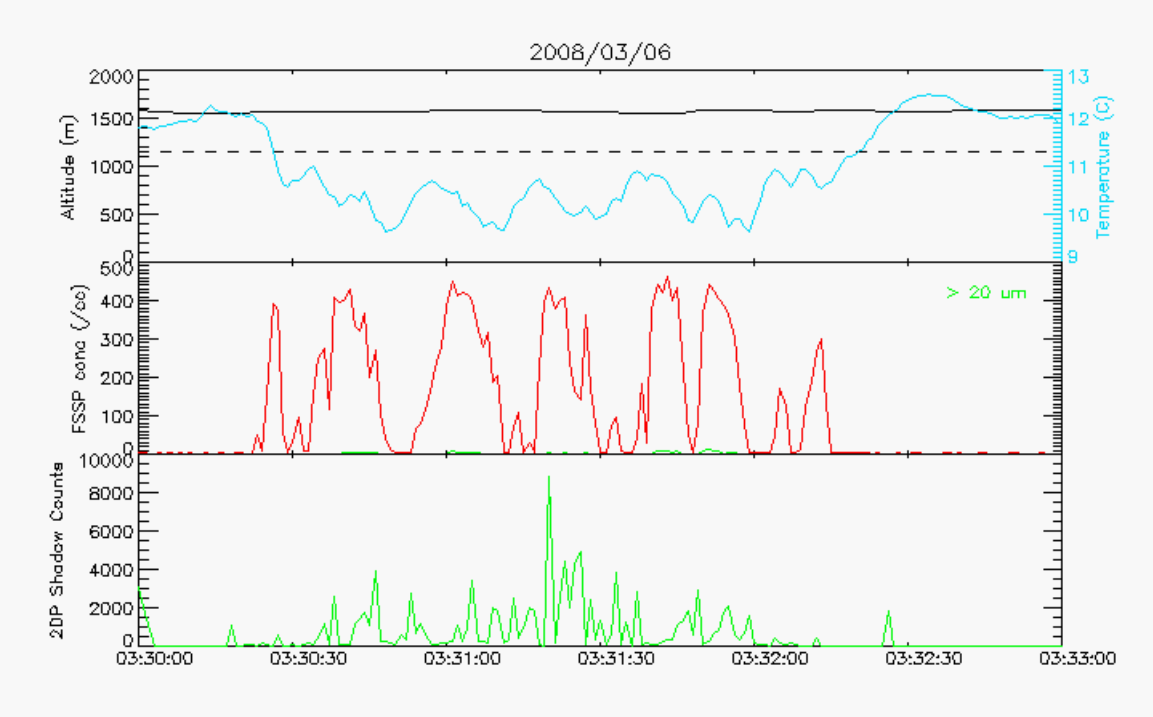

Figure 9.6. Time series of data from SEEDA1 between 033000-033300 UTC on 6 March 2008. Upper panel shows aircraft altitude (black solid), cloud base height (black dashed), and temperature (cyan; right axis). Middle panel shows FSSP total concentration (red), and FSSP concentration > 20 microns (green). Lower panel shows 2DP total shadow counts (green).

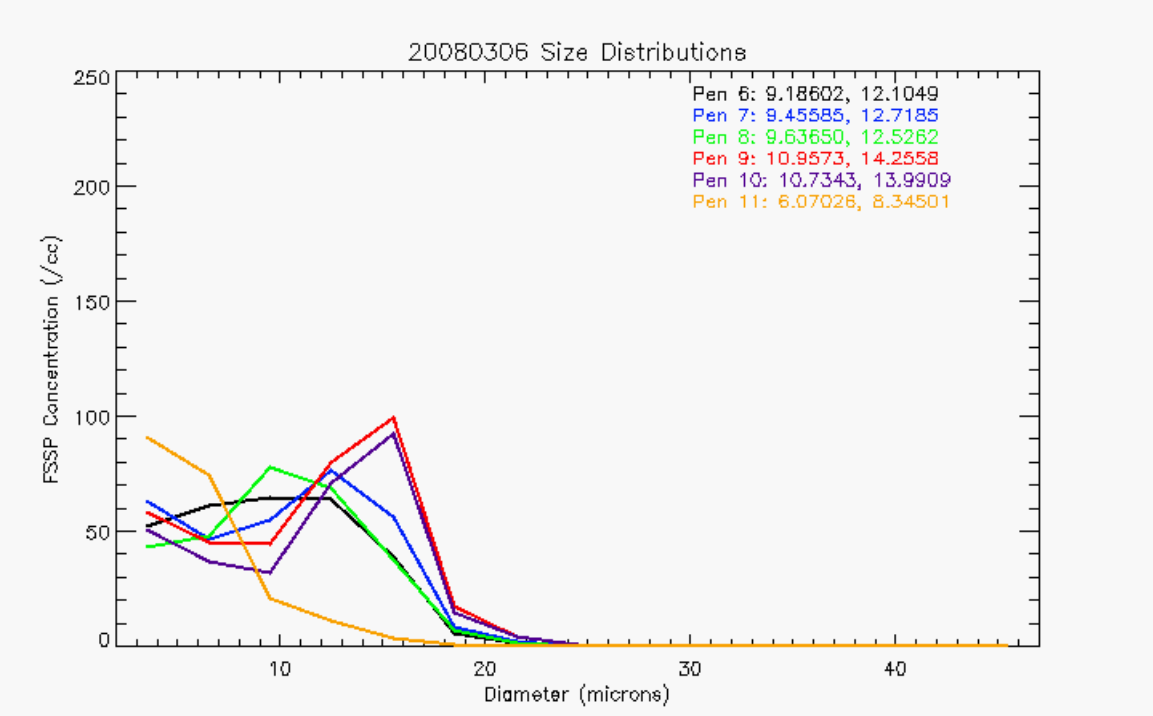

Figure 9.7. FSSP drop size distributions averaged over the penetration time (see Table 9.2) for penetrations 6-11. The penetration number listed in the legend gives the mean particle diameter (microns) and effective mean diameter (microns), respectively, for each penetration. The color of the penetration in the legend corresponds to the color of the DSD.

The second segment (shown in Figure 9.8) includes the time that SEEDA1 was conducting penetrations at 700 m above cloud base. During this segment, the aircraft first penetrated cloud north of the seeding activity from southwest to northeast (see end of flight track in Figure 9.5), and then penetrated across the seeding activity from southeast to northwest such that at the beginning of this period of penetrations the aircraft was south of the seeding and then moved north of the seeding activity (Figure 9.9). The first penetration in this segment (#12) had a mean diameter of 9 microns and a total drop concentration of 600 cm^{-3} (Figure 9.10). The latter portion of this penetration had higher 2DP shadow counts (> 1000 s^{-1}), and thus some influence of precipitation-sized drops, yet the FSSP DSD for the first portion of the segment has similar shape and mean particle diameter as the whole segment, other than slightly higher concentrations of drops in the 10-18 micron range (not shown). The next two penetrations (#14-15) had similar DSD shapes, both very narrow, with mean particle diameters of 6.5 microns and total concentrations of 450-600 cm^{-3}. These penetrations were likely through newly growing turrets, given the narrow shape and high concentrations. Penetration #16 had a mean diameter of 8 microns and total concentration of 450 cm^{-3}, while #17 had a mean diameter of 11 microns and total concentrations of 650 cm^{-3} (see Figure 9.11). The DSD shapes from penetration #17 were very similar to #12, which would be expected as both penetrations were in the same area (using radar as guidance), and both of which were north of the seeding location. Penetration #16, however, was along the same flight track as #14-17, and was possibly closest to the seeding location of any of the penetrations. Interestingly enough, this penetration had a slightly dual

mode to its DSD shape, with its primary peak in the 6 micron range, but a secondary peak near 16 microns. One could speculate that this could be a potential seeding signature defined by the broader distribution.

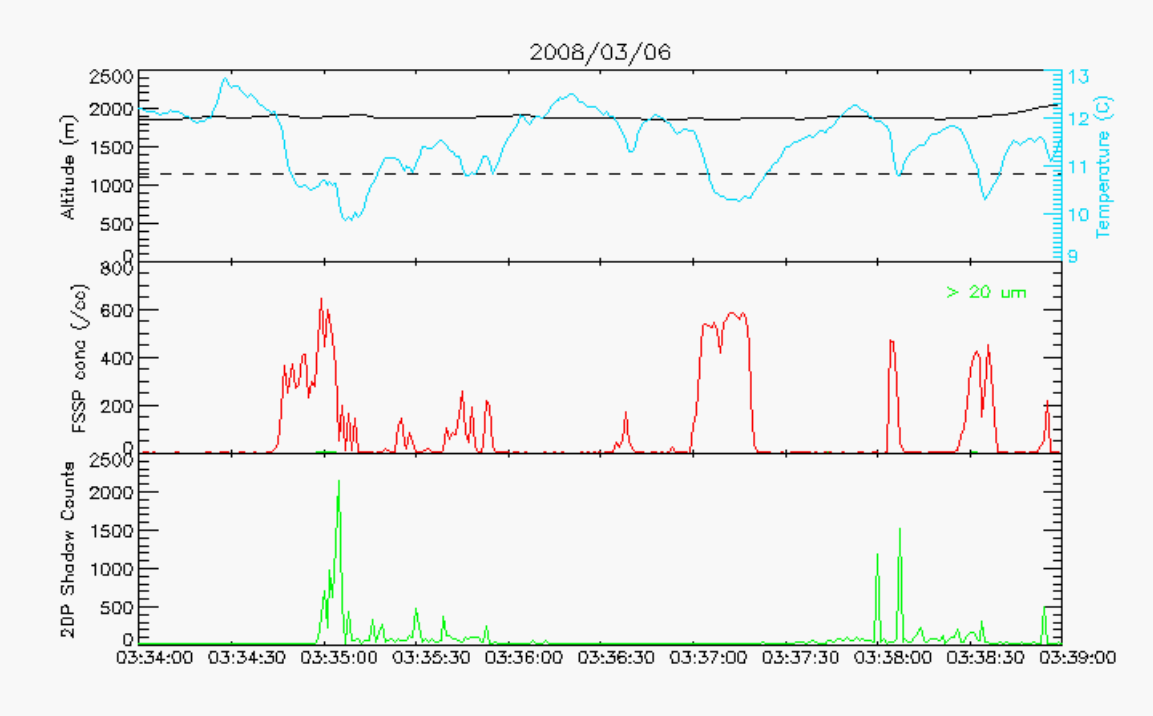

Figure 9.8. Same as Figure 9.6, except for 033400-033900 UTC.

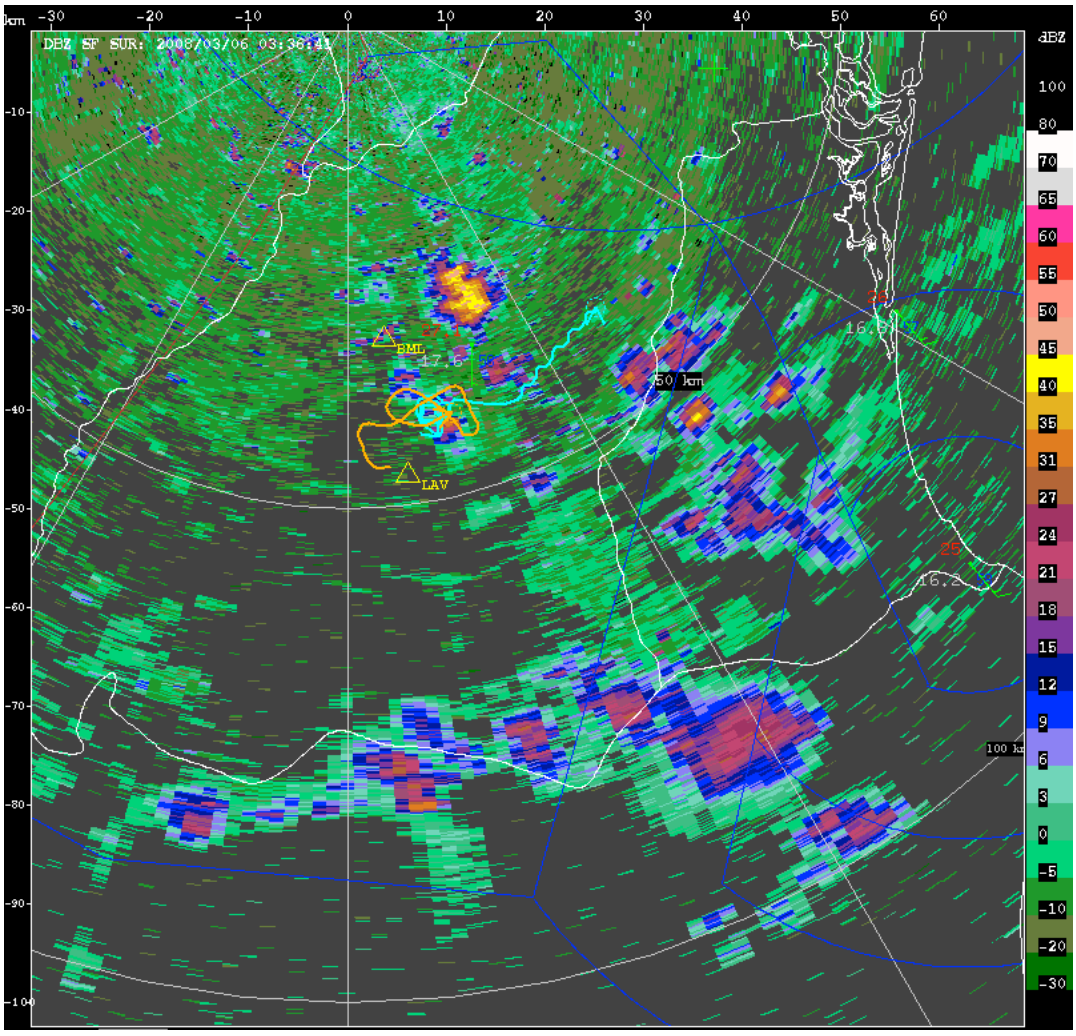

Figure 9.9. Same as Figure 9.5, except at 0336 UTC. Aircraft tracks encompass 033200-034200 UTC.

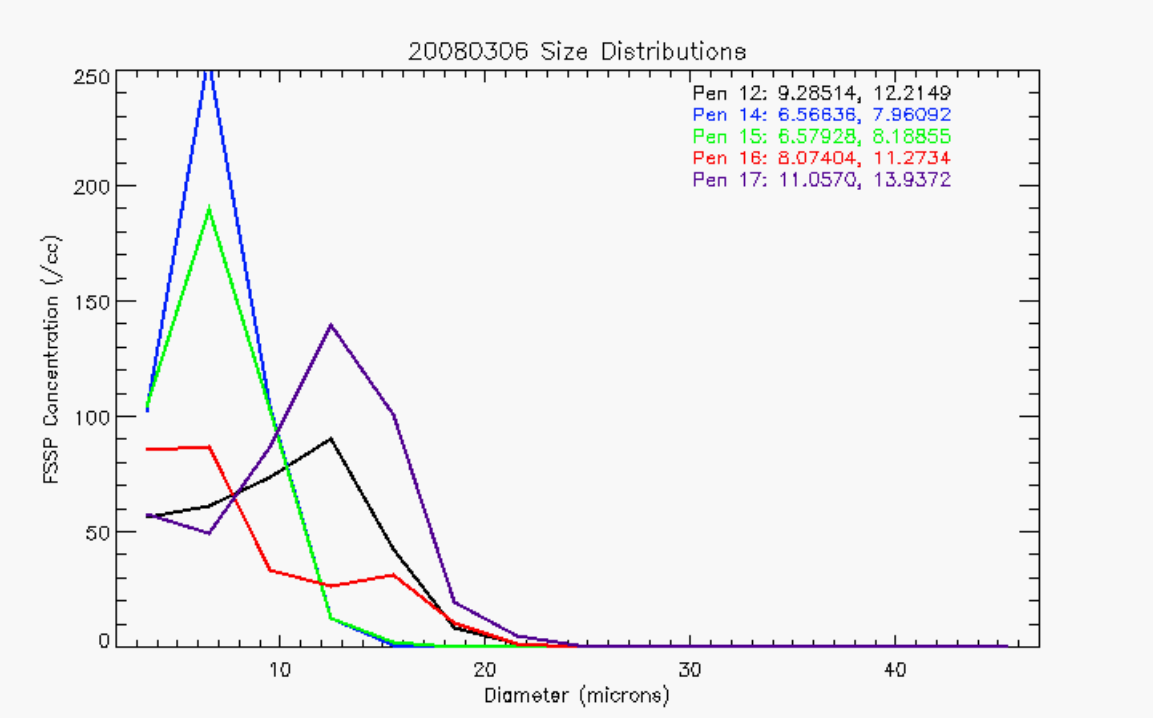

Figure 9.10. Same as Figure 9.7, except for penetrations 12 and 14-17.

After penetration #17 (discussed above), SEEDA1 ascended to 1350 m above cloud base (Figure 9.11) and conducted two penetrations from west to east over the seeding activity (#20-21; shown as end of SEEDA1 track in Figure 9.9), then turned south and approached the target from south to north (two cloud penetrations, #24-25, were observed on FSSP during this period), and then turned around and penetrated the target from north to south (#26; see SEEDA1 track in Figure 9.12). Penetrations #20-21 both have similar DSD shape, though #20 has a bit larger mean particle diameter (Figure 9.13). Both also have similar total drop concentrations of 400 cm^{-3} (Figure 9.11). Penetrations #24-25, however, have very different DSD shapes and mean diameters, even though they were flown in the same direction one after another and both have similar total drop concentrations of 300 cm^{-3}. This indicates two very different clouds at this time, either due to seeding or due to different growth stage of the two clouds. Penetration #24 has a broad DSD with a mean diameter of 11 microns, while #25 is narrower and has a smaller mean diameter of 7 microns (Figure 9.13). All penetrations at this altitude had higher 2DP shadow counts (> 1000 s^{-1}), except penetrations #24-25. Both of these penetrations had shadow counts well below 500 s^{-1} during the penetration time period, thus neither was notably affected by precipitation-sized drops, therefore, reaffirming that their FSSP DSDs were markedly different, and not likely due to precipitation contamination. Penetration #26 was broad again, similar in shape to #24, with a mean diameter of 11 microns. Penetration #26, though, was also the first to have a noticeably higher concentration of drops > 20 microns (~100 cm^{-3}), indicating the extent to which the DSD had broadened compared to earlier penetrations. Penetration #26 also had very high (> 2000 s^{-1}) 2DP shadow counts, thus precipitation-sized drops were prevalent in this penetration and could affect the FSSP measurements.

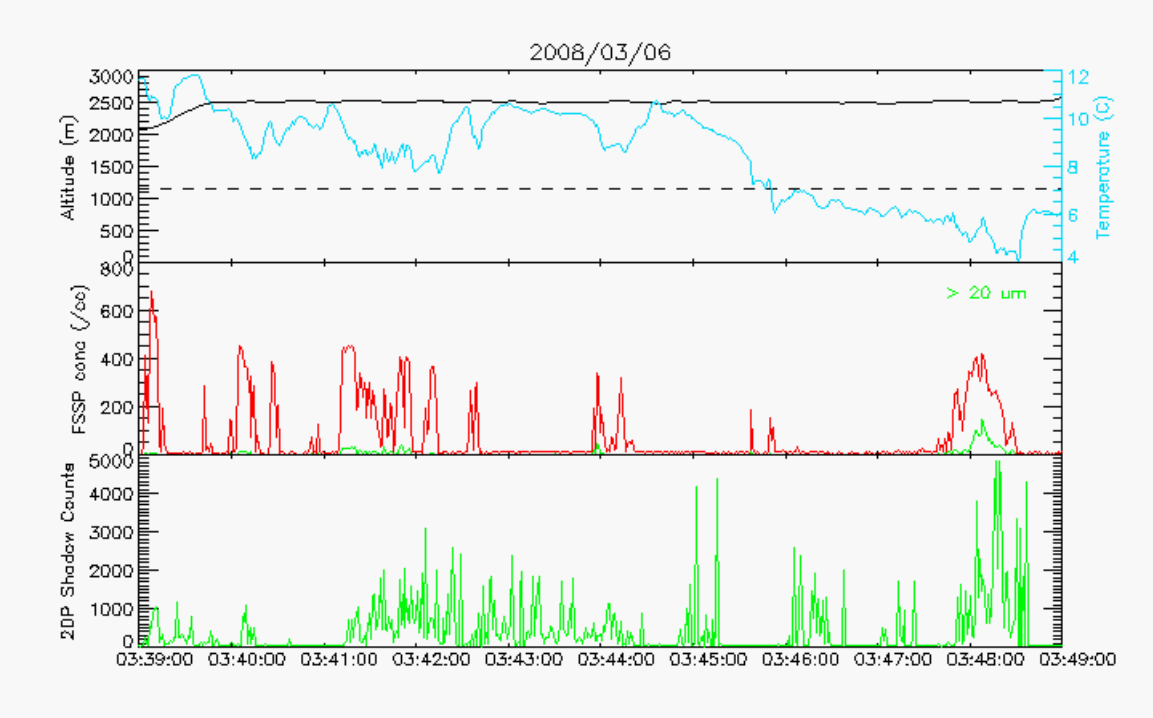

Figure 9.11. Same as Figure 9.6, except for 033900-034900 UTC.

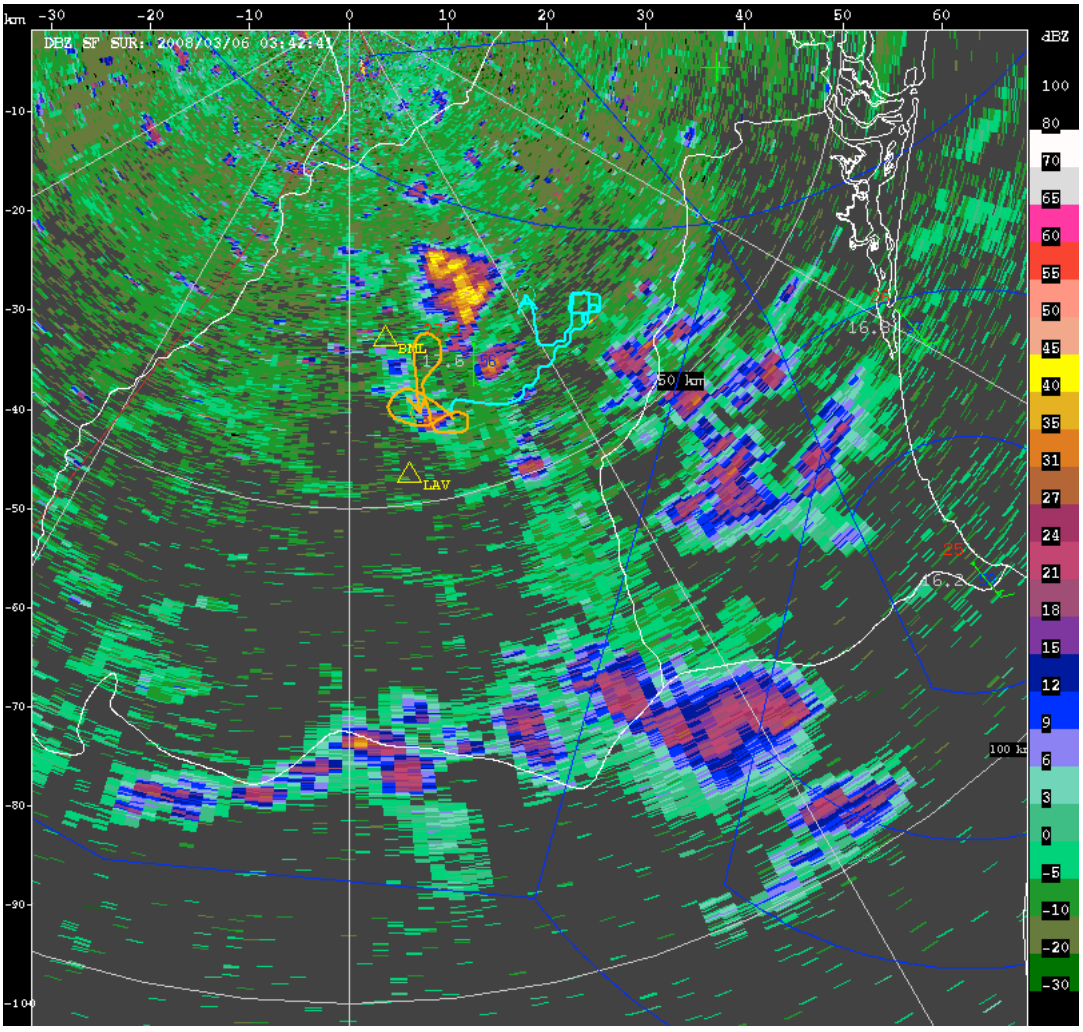

Figure 9.12. Same as Figure 9.5, except for at 0342 UTC. Aircraft tracks encompass 033800-034800 UTC.

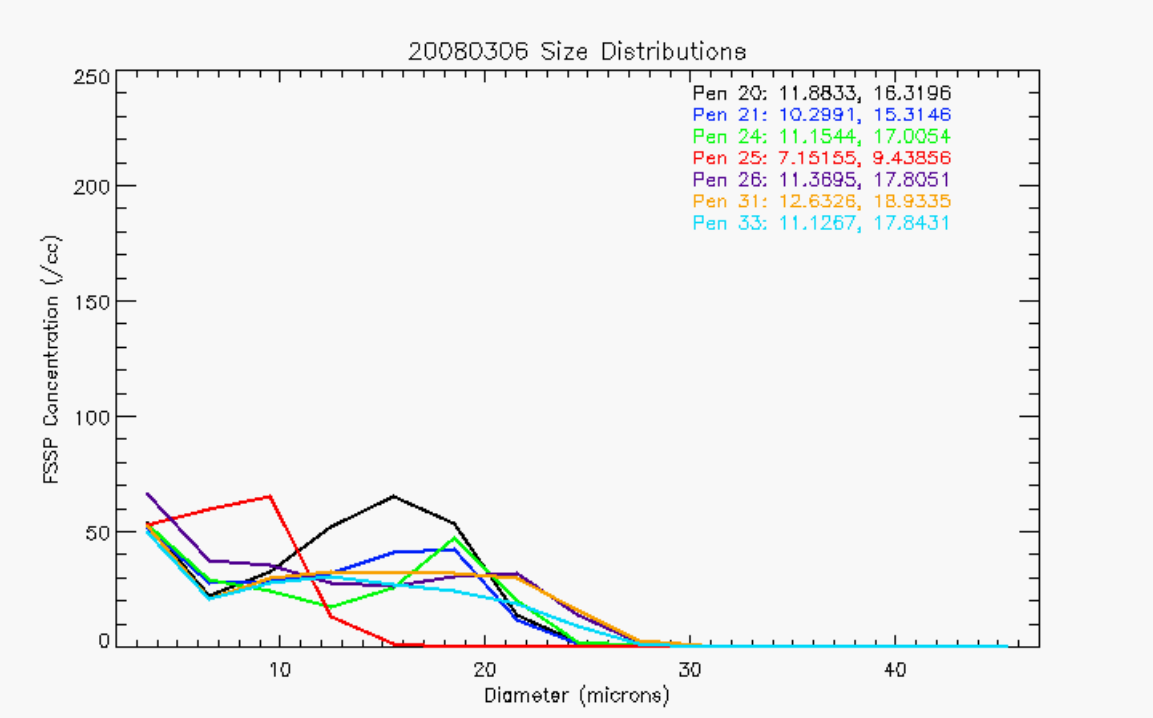

Figure 9.13. Same as Figure 9.7, except for penetrations 20-21, 24-26, 31, and 33.

The final segment (Figure 9.14) covers the last ten minutes that SEEDA1 targeted randomized case #22. Initially SEEDA1 ascended to 1950 m above cloud base, and conducted one penetration (#31) from east to west in the targeted cloud. Then, as the cloud dissipated, SEEDA1 descended to 1650 m above cloud base for a final penetration (from northwest to southeast through the targeted cloud) before directing its efforts on a new target (see end of SEEDA1 track in Figure 9.15). Both penetrations #31 and #33 have broad DSD shapes, with mean diameters of 12.6 and 11 microns, respectively (Figure 9.13). FSSP total concentrations in these two penetrations were near 400 cm^{-3}, but they also had noticeable concentrations of drops > 20 microns (as did penetration #26) of 50-75 cm^{-3}. 2DP shadow counts are also very high (2000-4000 s^{-1}) in both penetrations, and thus precipitation was clearly present at this time in the penetrated cloud.

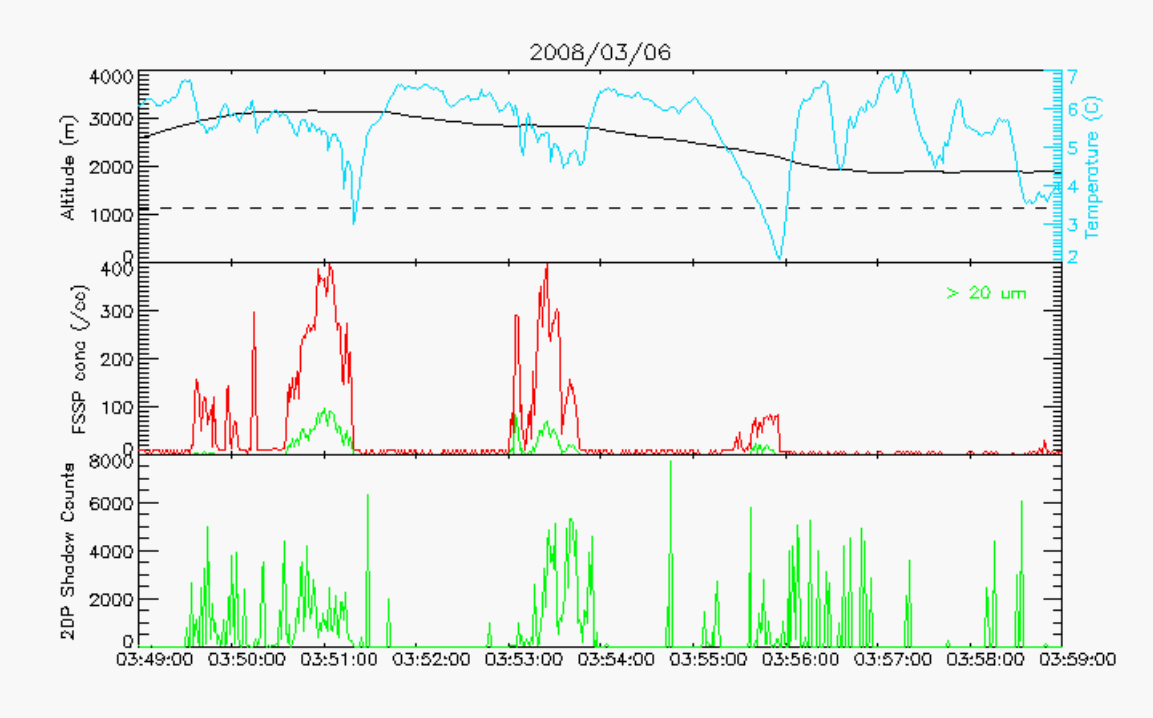

Figure 9.14. Same as Figure 9.6, except for 034900-035900 UTC.

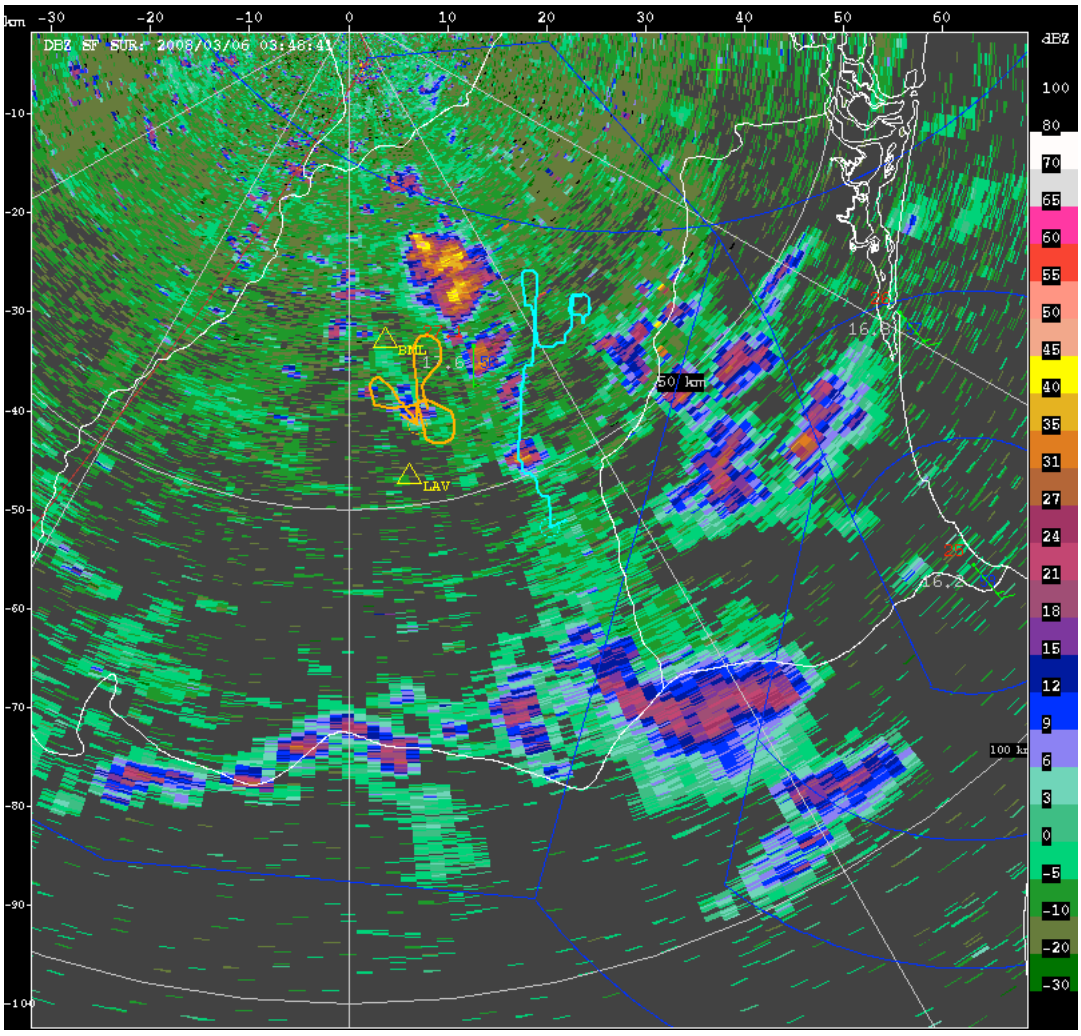

Figure 9.15. Same as Figure 9.5, except at 0348 UTC. Aircraft tracks encompass 034400-035400 UTC.

A summary of all FSSP measurements taken during the time period that SEEDA1 targeted this case is illustrated in Figure 9.16. It is clear that the mean diameters increased with altitude while total concentrations decreased, as would be expected from collision and coalescence growth processes. It is also observed that the diffusional growth depth is limited to cloud base due to the rapid broadening of the DSDs and the cloud droplet concentrations peaking immediately above cloud base. This suggests that the collision-coalescence process is initiated by giant or large CCN as the diffusional growth process is quite shallow. Furthermore, 2DP shadow counts increased over the course of these penetrations, as the aircraft ascended to higher altitudes, confirming the growth of precipitation-sized drops.

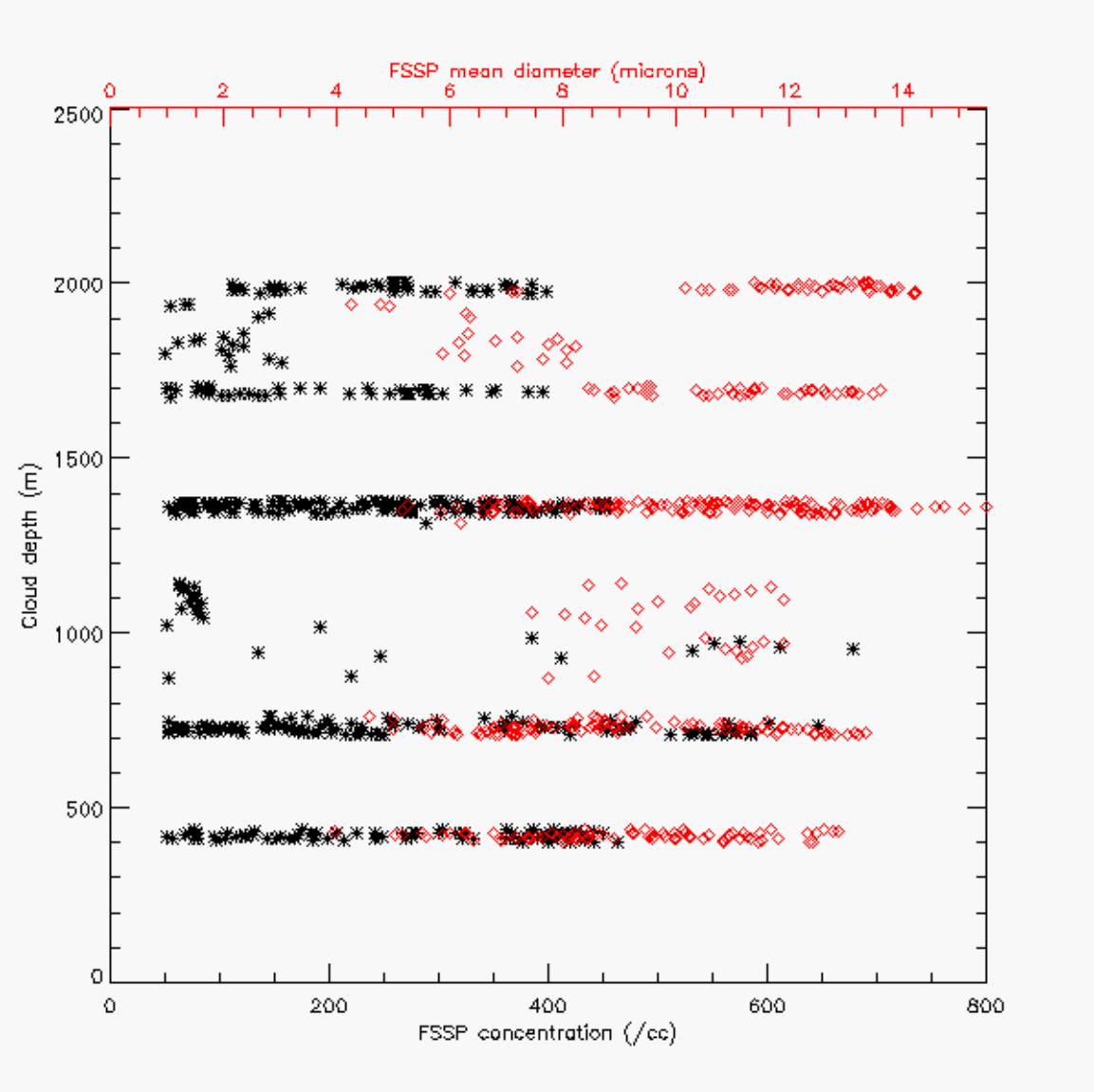

Figure 9.16. FSSP measurements versus cloud depth for all times between 0330-0400 UTC with FSSP concentrations > 50 cm^{-3}: FSSP total concentrations (black, bottom axis), and FSSP mean diameter (red, top axis).

9.3.3 Planned dual-Doppler analysis

In addition to utilizing CP2 for studying rainfall and storm characteristics (intensity, size, lifetime) between seeded and unseeded convective clouds it will be used to examine any changes in storm dynamics. We wish to examine the question: does hygroscopic seeding of clouds act to modify the dynamics within the seeded storms by modifying the precipitation microphysics thus changing the storm updraft and downdraft intensities? Second if stronger and colder downdrafts result from seeded storms, does this lead to a greater likelihood for secondary convection to initiate? Secondary convection refers to the initiation of new storms by the outflows (gust fronts) from the original storm. A stronger downdraft may generate a more intense gust front that will increase the likelihood of secondary storms.

Specifically we will examine a) changes in precipitation type and size distribution as inferred from CP2 polarimetric variables, b) magnitudes of updraft and downdraft velocities as determined from dual-Doppler analysis derived from CP2 and Mt. Stapylton radars and c) near surface outflow strengths and any subsequent initiation by these outflows (secondary initiation).

A rich data set was obtained for this purpose during the field phase. In order to obtain high quality vertical and horizontal winds from the dual-Doppler data the seeding needed to take place where the subtended angle between the radars to the seeding location was 30 deg or more (see Figure 9.17). This we call "within the dual-Doppler lobes." The great majority of the seeding was carried out in these lobes particularly the southern dual lobe where permission to fly was more easily obtained.

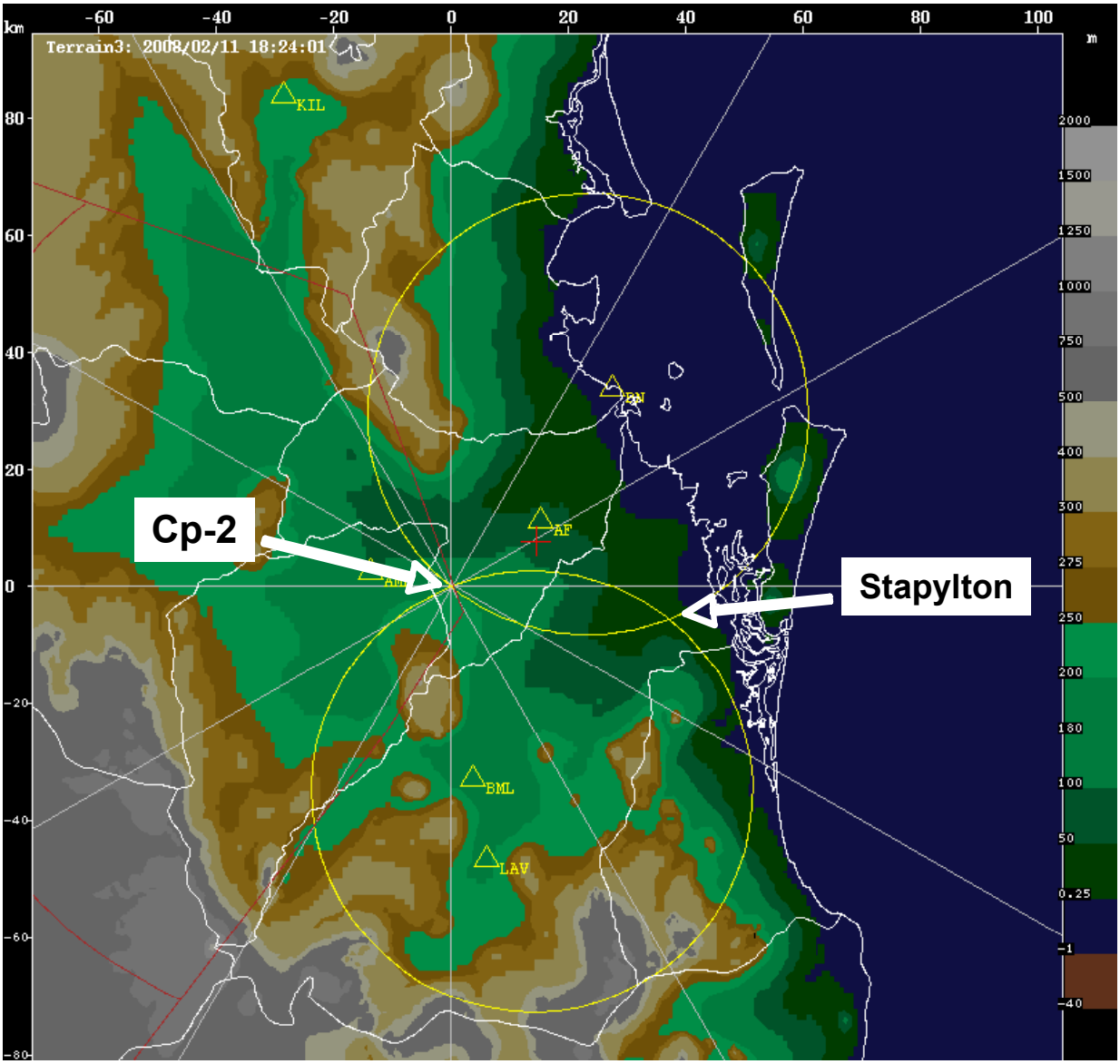

Figure 9.17. Thirty degree dual-Doppler lobes (yellow circles) between CP2 and Stapylton radars. The background colors represent the height of the terrain.

We have noted several cases where seeding was conducted in one cloud and later there was initiation or intensification of nearby storms; these will be good candidates for examining what we called "above secondary initiation." Two examples are shown in Figure 9.18-Figure 9.19. Figure 9.18 is from February 2, 2008 where a nearby echo intensified and Figure 9.19 is from January 31, 2008 where both intensification of the seeded cell and new initiation occurred on the western side of the seeded cloud. At this time it is unknown if the seeding played any role in the initiation or intensification of these example. Insight will be obtained from further analysis over the next few months.

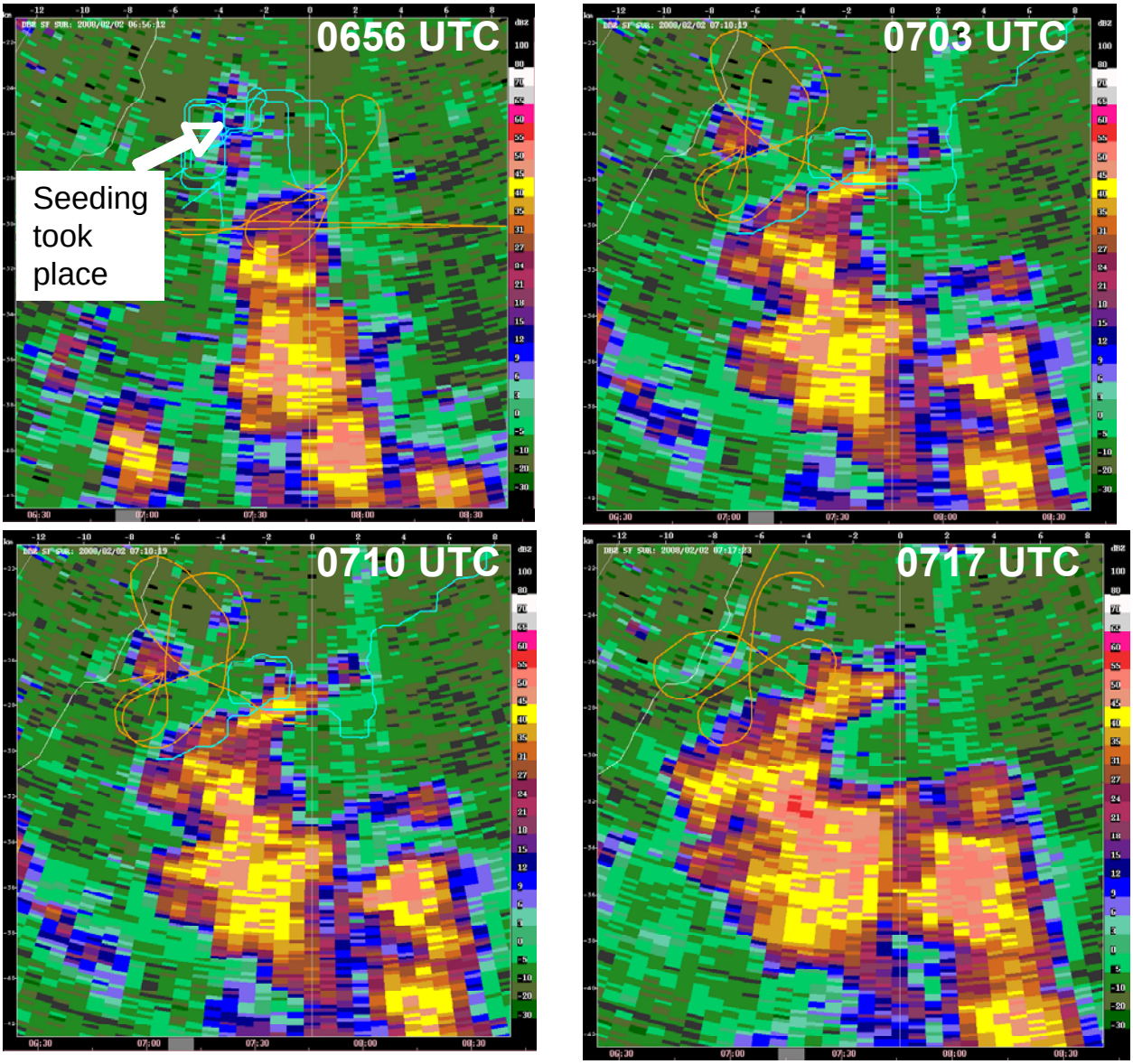

Figure 9.18. Example from 2 Feb 2008 of the intensification of a storm following the seeding of a nearby cloud. The colors represent radar reflectivity given by the scale on the right. The blue line in the image for 0656 UTC is the track of the seeding plane.

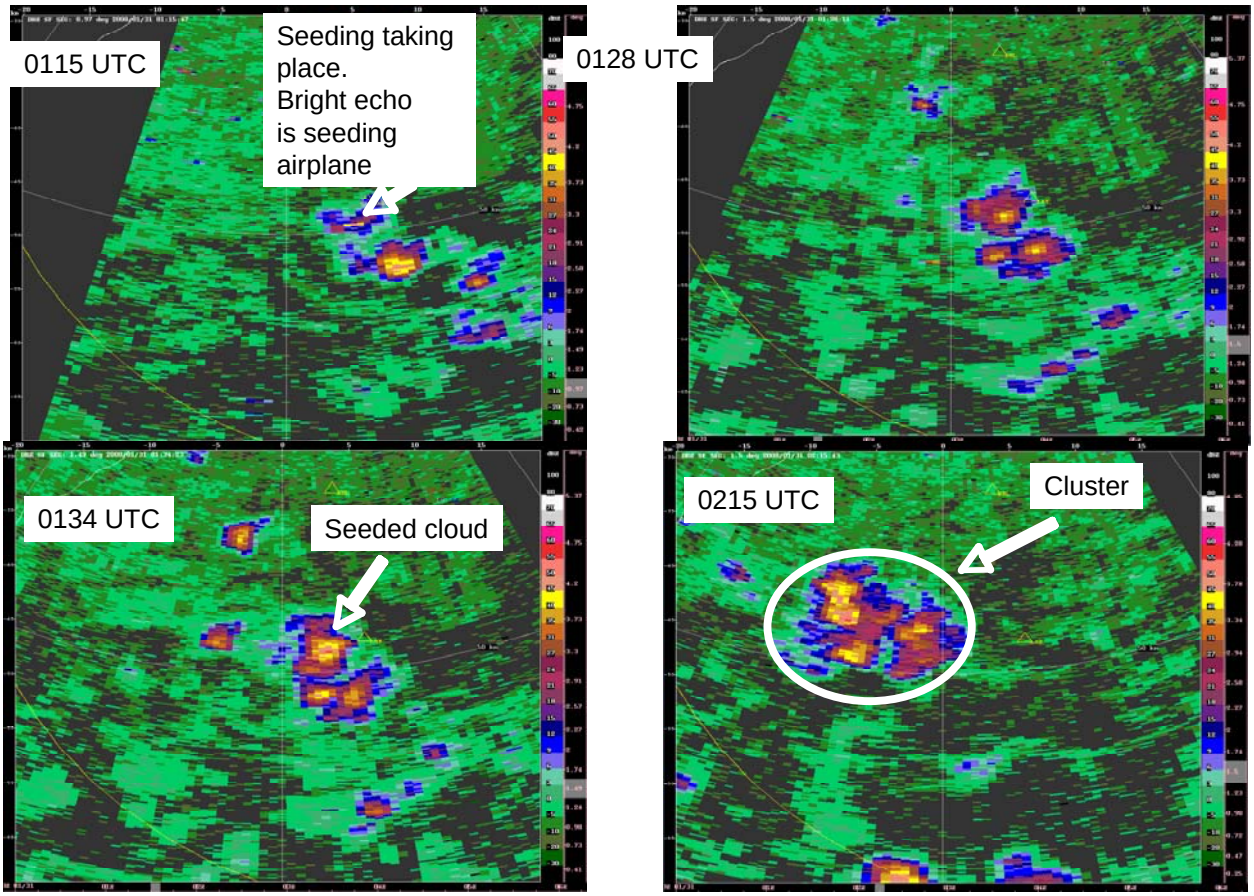

Figure 9.19. Radar reflectivity from 31 Jan 2008 of the formation of a cluster of showers that followed the seeding of the initial cloud.

Radar data collected on 6 seeded and non-seeded clouds on 13 February 2008 are currently being processed to retrieve the 3-D wind field. This is a unique case as all storms were triggered by the same feature, a sea breeze front moving through the northern and southern dual-Doppler lobes (see Figure 9.20). It should prove an excellent case to determine the quality of the vertical wind motions that can be obtained and how well low-level outflows from these showers can be retrieved. Since all the showers are being initiated by the sea breeze it serves as an excellent opportunity for studying seeded versus non-seeded cases because of the similarity in the cloud forcing mechanism and hopefully the primary difference between the showers is whether they have been seeded or not.

Figure 9.21 shows the early cumulus clouds that developed above the sea breeze that were targeted for the randomized seeding experiments. Fortunately the CP2 radar is able to observe early cumulus clouds prior to the presence of precipitation. The radar receives scattering from gradients in water vapor along the edges of the cumulus clouds; this is called Bragg scattering.

Radar data format converters, radar editing and display tools (SOLO, CIDD), Cartesian radar interpolation and wind synthesis packages (REORDER, CEDRIC) have been installed on NCAR machines to process the CSRP data and produce the dual-Doppler wind fields and particle trajectories. Figure 9.22 shows the CP2 reflectivity fields at two time periods: 0332 UTC, ~5-7 min after first cloud was seeded, and 0342 UTC, 20 min after seeding on the first

cloud began (and the start of seeding of a second cloud further to the south). The domain for dual-Doppler analyses is shown by the red box which includes both seeded and non-seeded cloud areas, providing an ideal opportunity to compare the differences in storm dynamics and precipitation intensities. Preliminary REORDER and CEDRIC syntheses are currently being run.

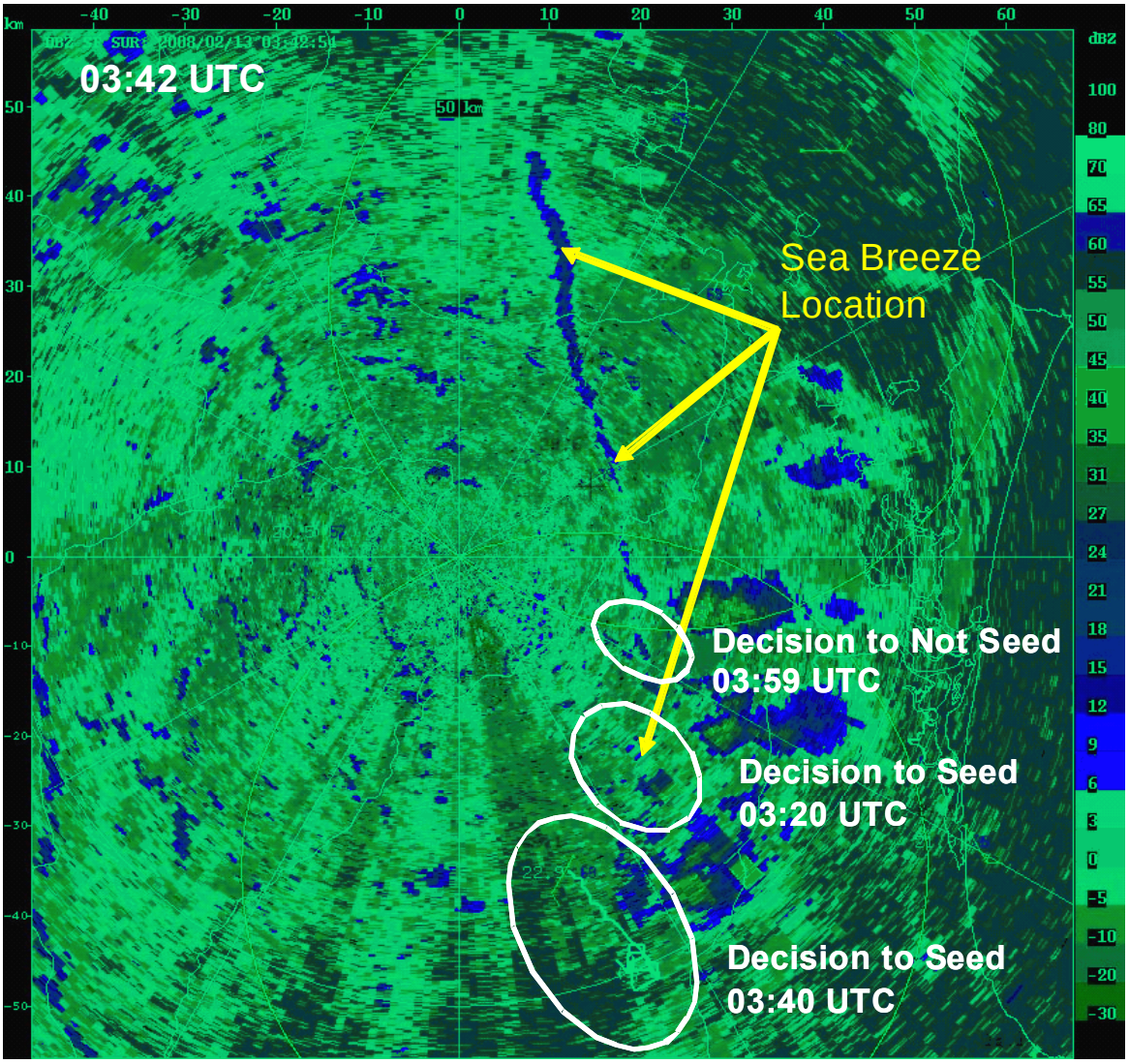

Figure 9.20. Westward moving sea breeze and storms on 13 February 2008 within the dual-Doppler lobes (yellow circles). White ovals represent approximate locations of randomized seeding tests. The north-south enhanced thin line of reflectivity is the sea breeze front.

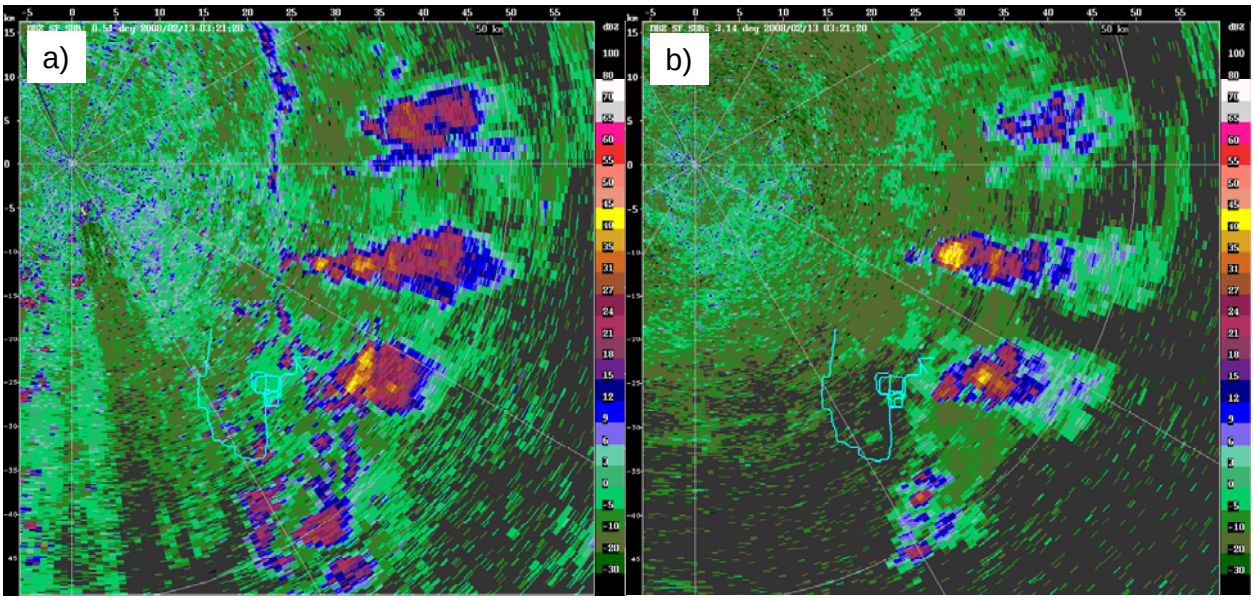

Figure 9.21. Sea breeze triggered storms observed by CP2 radar on 13 February at 0332. WxMOD aircraft tracks (cyan) overlaid. a) Reflectivity image at 0.5 deg elevation. The thin N-S line of 15-20 dBZ reflectivities indicates the location of the sea breeze front. b) Reflectivity image at 3.1 deg elevation. Early cumulus cloud development above the sea breeze is indicated by N-S line circular type Bragg scatter echoes (< -3 to -15 dBZ).

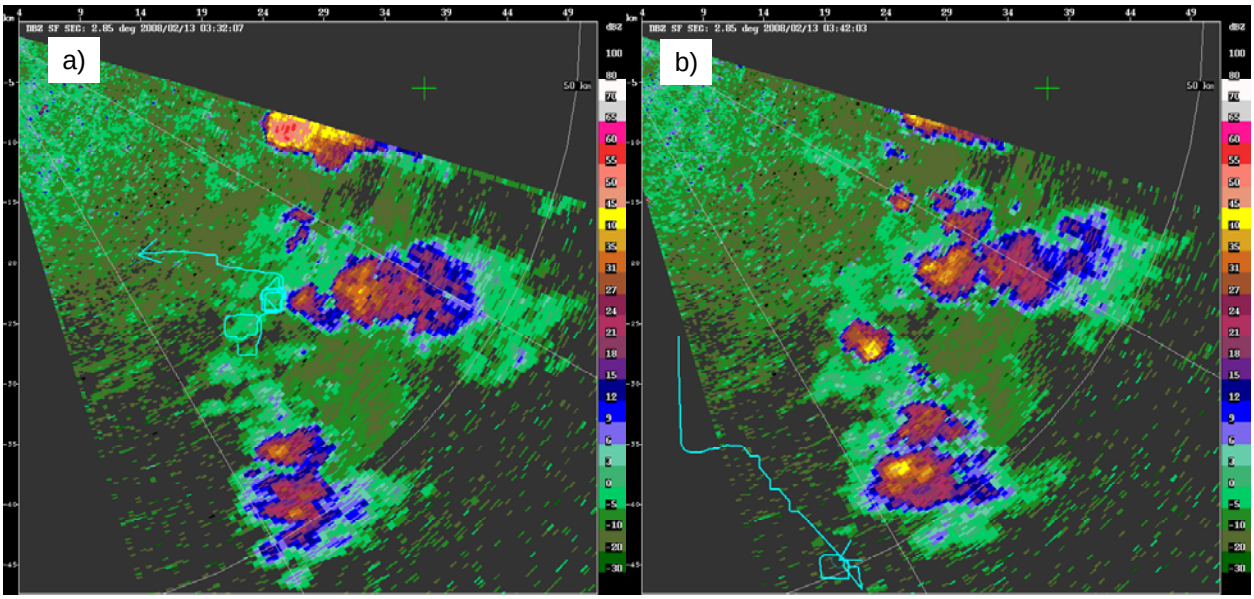

Figure 9.22. CP2 reflectivity at 2.85 deg elevation at a) 0332 and b) 0342 UTC. The domain for dual-Doppler analyses is within the region defined by the red box. WxMOD aircraft tracks (cyan) are overlaid.

9.4 RANDOMIZED SEEDING EXPERIMENT

9.4.1 Analyzing the seeding cases using TITAN

Analysis of the randomized seeding cases was restricted to isolated warm-rain cases. Since many of the selected storms were reasonably small, the TITAN storm detection threshold was set to 20 dBZ, and the minimum storm volume was set to 4 km^3. 20 dBZ is a low threshold value, since the storms were generally weak. By contrast, storms in the South Africa and Mexican experiments were identified using a threshold of 30 dBZ.

The Mount Stapylton radar data was determined to be the most suitable for tracking the storms in the randomized experiment, because the radar operates on a regular 6-minute surveillance scan which is ideal for TITAN. It was found that there was one period of missing data for Mt. Stapylton, from around 0400 UTC on 2008/04/24 to around 1400 UTC on 2008/04/26. It is believed that there was a problem with the data-gathering for the operational BOM radars at that time, because all of the operational radar data is missing for that period. The CP2 data was used to fill in this gap. CP2 is not ideal for this purpose, however, because the scan strategy is less regular than for the other radars. Nevertheless, data from CP2 was suitable for filling in some of the data gap.

Of the 62 storms in the randomized seeding table (Table 6.3), 27 were found to be suitable for statistical analysis. The rest of the cases were discarded because either (a) TITAN did not identify and track the case or (b) the chosen storm was part of a very large storm complex and the resulting track was too large to be included in the analysis.

9.4.2 TITAN tracks for randomized seeding cases

Table 9.3 shows the TITAN tracks for the randomized cases considered suitable for statistical analysis.

Table 9.3. TITAN cases for randomized experiment

Case number	Seed?	Number of flares	Date	Decision time	TITAN complex track num	TITAN simple track num
03	Y	06	2008/02/02	03:02:00	1130	1130
07	Y	06	2008/02/13	03:20:00	148	148
10	Y	06	2008/02/13	04:29:00	29	343
11	N	00	2008/02/13	04:46:00	543	543
12	Y	05	2008/02/13	05:03:00	443	536
17	N	00	2008/02/20	06:19:00	491	491
20	N	00	2008/03/03	03:53:00	322	322
21	N	00	2008/03/03	06:46:00	738	738
22	Y	06	2008/03/06	03:24:00	375	375
26	N	00	2008/03/09	05:35:00	912	1040
32	Y	16	2008/03/15	01:34:00	105	105
35	Y	06	2008/03/22	02:19:00	426	514
36	Y	08	2008/03/22	02:39:00	568	568
37	Y	08	2008/03/22	03:09:00	608	608
38	N	00	2008/03/22	04:28:00	735	735
39	Y	10	2008/03/22	04:45:00	683	851
41	N	00	2008/03/24	02:25:00	560	560
42	N	00	2008/03/24	02:36:00	699	699

Case number	Seed?	Number of flares	Date	Decision time	TITAN complex track num	TITAN simple track num
43	Y	08	2008/03/24	02:46:00	710	710
45	N	00	2008/03/24	03:32:00	826	826
47	Y	08	2008/03/24	04:06:00	941	941
48	N	00	2008/03/24	05:43:00	999	999
58	Y	08	2008/03/28	02:54:00	1224	1224
59	N	00	2008/03/28	03:26:00	1429	1429
60	N	00	2008/03/28	04:03:00	1415	1415
61	N	00	2008/03/28	04:18:00	1542	1542
62	Y	08	2008/03/28	04:35:00	1599	1599

9.4.3 Overview of analysis of randomized cases

This section focuses on the analysis of randomized cases. The key reason to conduct randomized cases is to permit fair comparisons between seeded and unseeded targets. Randomization was introduced to the field of weather modification in order to address biases found in early studies. Without randomization, trying to make inferences about the effectiveness of seeding is difficult. In operational (non-randomized) seeding experiments, promising clouds were seeded, while the remaining clouds were treated as un-seeded cases. Obviously, this inflated the apparent effectiveness of seeding. Other studies compared years during which seeding programs were active with years without seeding. The variability of annual precipitation made it difficult at best to detect differences.

During the 2008 field season from February 2nd to March 28th, 62 cases where conducted in a randomized fashion. Of this group only 27 produced features that could be characterized using TITAN. Some observations from an initial analysis of the randomized experiments, which will be discussed below, are summarized here:

- Maximum precipitation flux, mass and volume of targets are highly correlated
- There is no distinction between the maximum flux measured in the seeded and unseeded targets.
- There is no distinction between seeded and un-seeded targets in the growth of targets following the decision time (DT).
- The duration of seeded and unseeded cases is approximately the same.

9.4.4 Statistical Issues

Analyzing data from weather modification has provided many statistical challenges. The following paragraphs discuss some of these issues and their consequences for this analysis. Due to the small number of cases, most of the following observations and comments are qualitative in nature. With more data, more formal statistical inferences can be made by testing the observed patterns against randomness.

The Queensland experiment was proposed and is being conducted as an exploratory experiment. There are significant differences between exploratory data analysis and a confirmatory experiment. In an exploratory context, after the data has been collected the analyst looks for relations between measured variables that allow scientific theories about the experiment to be developed, supported and often modified. Comparisons between seeded and

un-seeded conditions are made using a variety of statistical methods. One of the most important results from exploratory data analysis is to suggest a confirmatory experiment. No matter how strong the evidence is from an exploratory experiment, it cannot be used to prove a concept.

In a confirmatory experiment, before the experiment begins, a plan for analysis is created that describes specifically the concept or theory, which is to be tested. Often this concept is suggested by an earlier exploratory experiment. Data collection methods and statistical analysis procedures are described in detail. At the conclusion of the experiment, data is then analyzed according to the proposed methods.

Multiplicity

One of the problems with exploratory data analysis is that of multiplicity. Increasing the number of comparisons one makes increases the chance that one will incorrectly reach a significant conclusion. There are ways to compensate for the issue of making multiple comparisons. They typically require higher significance levels for each test and ultimately require more data.

9.4.5 Variables

Key target characteristics described by TITAN include precipitation flux, rain mass, volume and area. A pairs plot (Figure 9.23) shows the relation between these variables. Pairs plots illustrate relations between multiple variables. By row, the named variable is represented on the y-axis. By column, the named variable is represented by the x-axis. For example, the plot in the upper right corner shows flux on the y axis and storm area on the x-axis. Not surprisingly most of these variables are highly correlated. High values of flux generally correspond to high mass and volume measurements. Target area (km^2) shows the weakest relation with the other variables. For this reason and for the sake of clarity, only mean precipitation flux will be analyzed in subsequent sections. One would be surprised to see that comparisons between seeded and unseeded flux values differ from comparisons of volume or mass estimates.

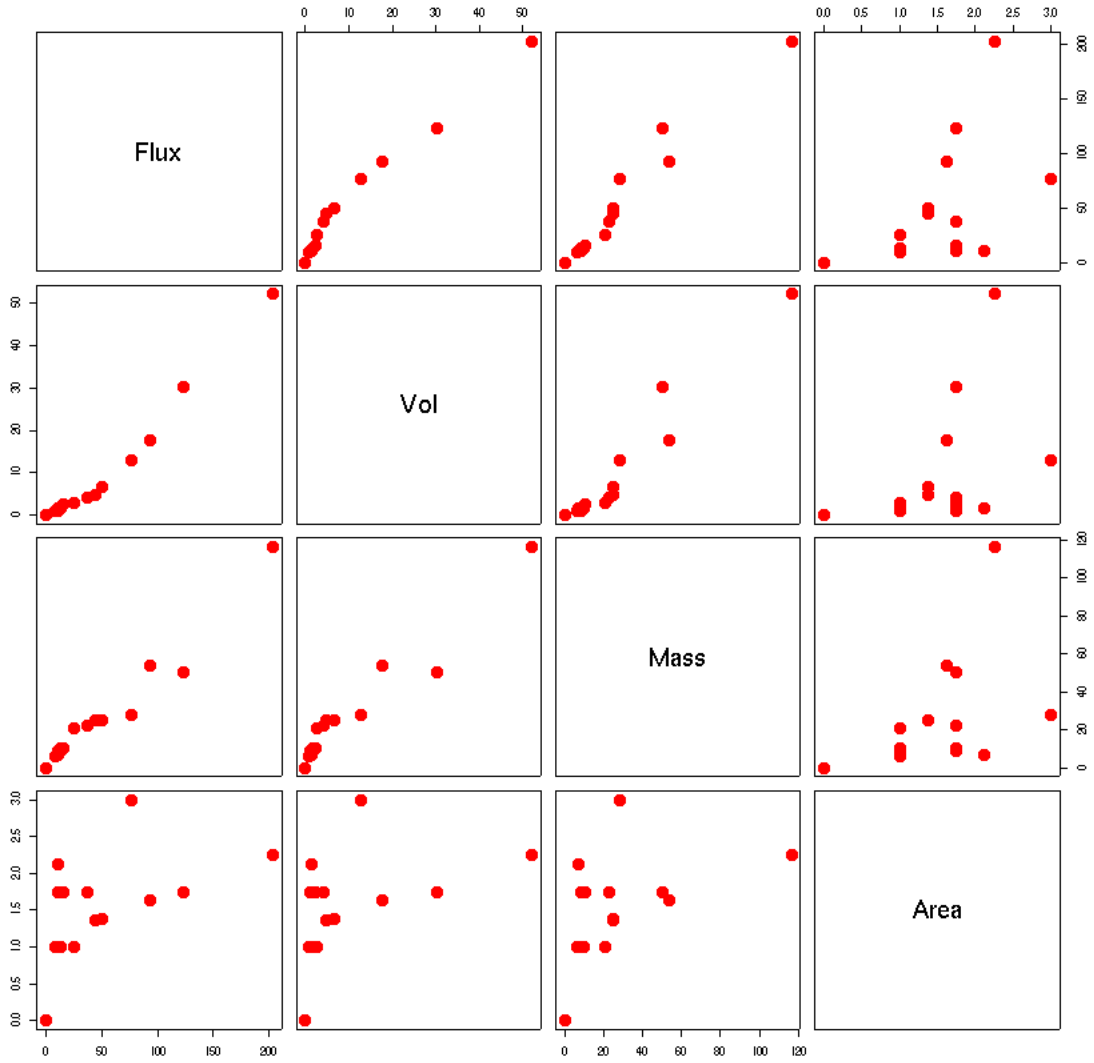

Figure 9.23. Pairs plot displaying the relation between the maximum values measured 15 to 55 minutes following DT.

Describing the dynamics of targets

Clouds, whether seeded or not, have continuously changing features. They go through an initiation, growth, decay and termination phases. To describe these dynamics, several aspects of target tracks have been summarized in the following manner. Figure 9.24 provides a schematic example of mean precipitation flux measurements through the life cycle of a storm. The difference between the flux measurement at DT and 10 minutes prior to DT describes changes prior to seeding action. For targets without a TITAN signal at this point, this change is 0. Targets in decline have a negative value of change. These changes are independent of any effect from the seeding action.

The earliest one might expect to detect an effect from seeding is assumed to be 10 minutes after the DT. This definition is based on the following assumption: at 10 minutes after the decision time, the effects of the seeding activity are minimal and the dynamics of the targets up until this point are independent of the seeding action and part of the natural variability of the target. The effects of seeding should be observable, at the earliest, 15 minutes after the DT. This is based on pilot reports that most of the randomized clouds had updrafts of around 500 ft min^{-1} (some as low as 200 ft min^{-1} and as high as 1000 ft min^{-1} though). Thus at 500 ft min^{-1} the flare material would take at least 10 minutes to rise 5000 ft in the cloud, and longer to go even higher. Depending on how much enhancement to collision and coalescence processes occurs will affect the time and depth of the cloud that the flare material will ascend to, and that plus the time it takes for the rain to reach the surface would take at least 10 min if not closer to 20 min.

The maximum value of flux occurs between 10 and 55 minutes after DT is calculated. Flux growth has been defined by the change in flux measured at 10 minutes and the maximum flux value occurring between 10 and 55 minutes after DT. Storms growing suddenly after the DT will have larger growth rates than more slowly developing storms. For this reason, growth rate could be the wrong measure to quantify a more slowly developing effect. For this hypothesis, the direction of the change is still a useful piece of information.

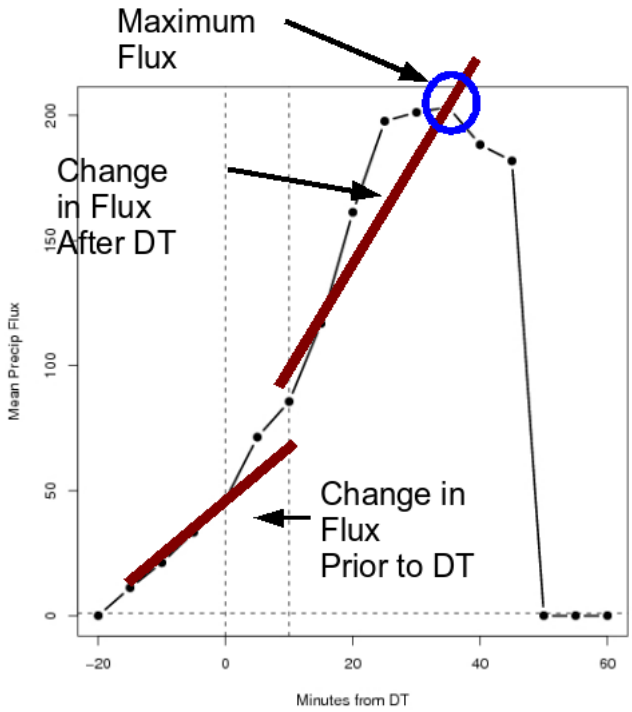

Figure 9.24 Schematic example of storm precipitation flux characteristics with time.

Conditions prior to decision time

Before evaluating changes which occur after the seeding action, it is important to exam initial conditions to determine whether the groupings are biased. With biased groupings, the

seeded and unseeded targets would be notably different prior to DT. This makes it more difficult to attribute differences after DT to the seeding action. Figure 9.25 shows that for both seeded and unseeded cases, prior to DT, both groups mostly have similarly small changes in precipitation flux (i.e. the slope of change in flux prior to DT in Figure 9.24). Histograms are used to compare differences in the two groups. With larger sample sizes, box-plots would be appropriate with this type of data, however, with so few data points, box-plots can be deceptive and create a false sense of confidence. Mean flux in many targets are slightly declining. One unseeded case experienced rapid decline, while the greatest growth was being experienced by a seeded case. With such a small sample size, it is difficult to see it these differences are statistically significant, but qualitatively one does not detect a great bias in initial conditions.

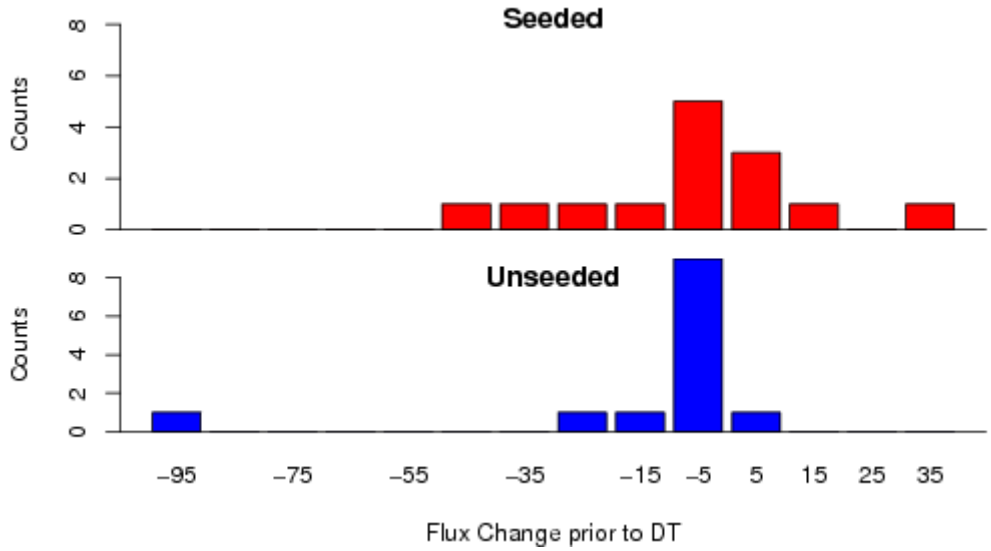

Figure 9.25 Change in precipitation flux in 10 minute period prior to DT.

Maximum Flux after decision time

To succinctly describe conditions after the decision time, the maximum flux value measured between 10 and 55 minutes past the action time is calculated (see time to reach maximum flux illustrated in Figure 9.24). Figure 9.26 describes these differences. For both groups, the most common maximum value is zero – within this time period TITAN was no longer detecting flux. This is a feature of short-lived targets. Both seeded and unseeded cases have a similar number of values greater than 40 m3/s with the largest flux value occurring in a seeded case.

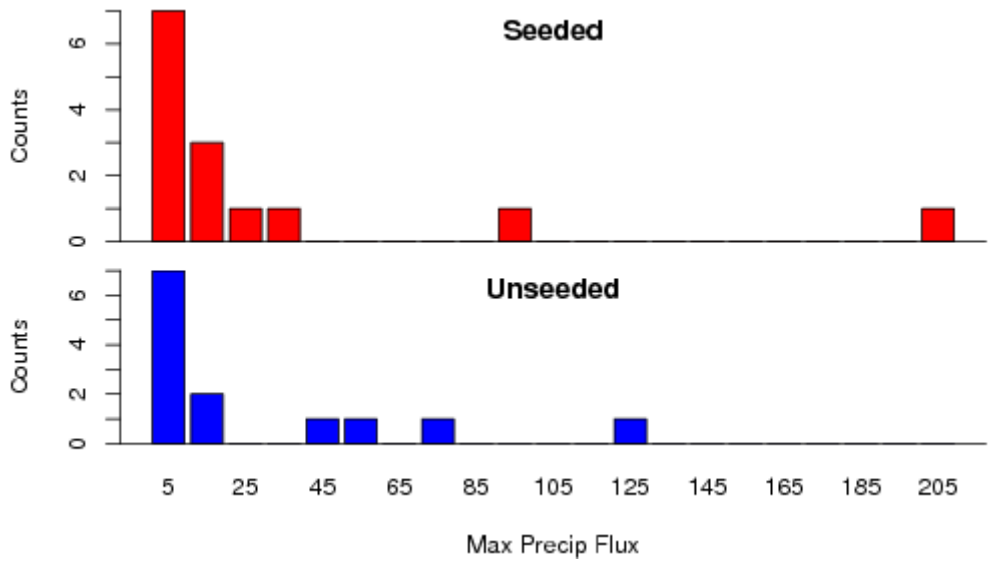

Figure 9.26. Maximum mean precipitation flux recorded between 15 and 55 minutes after DT.

Flux Growth

Flux growth is the difference in flux values from the value at 10 minutes after DT, to the maximum (if growing) or minimum if declining flux value measured between 10 and 55 minutes after DT (i.e. slope of change in flux after DT in Figure 9.24). Figure 9.27 illustrates the growth in precipitation after DT. Seeded values are shown in the top group, unseeded in the bottom. For both actions, flux values generally decrease in the 10 to 55 minute period following DT. One seeded target grew significantly after DT and two unseeded cases show a rapid decline. The remainder of the events experienced a slight decline or remained even with 0 flux values being reported.

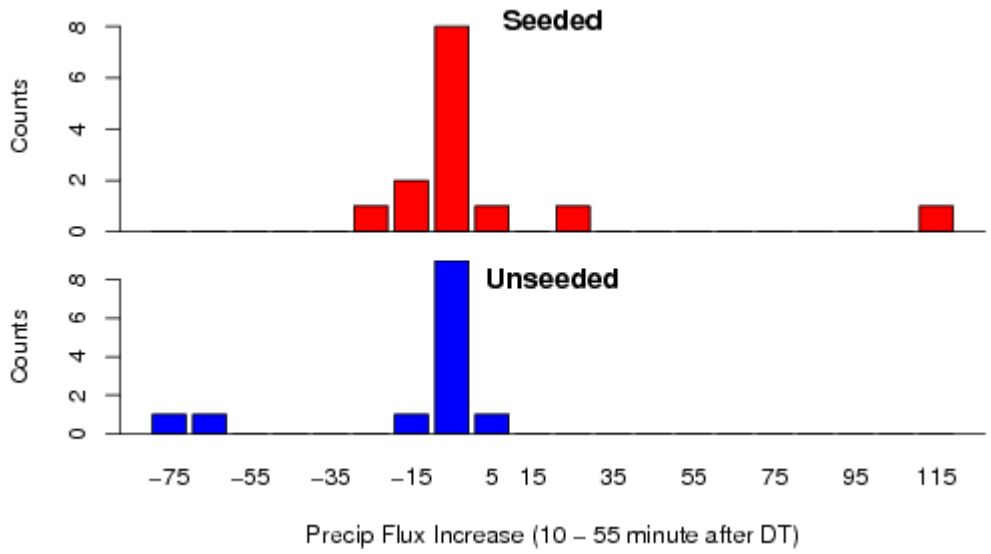

Figure 9.27. Growth of precipitation between 10 minutes after DT and the maximum value. recorded from 15 to 55 after DT.

9.4.6 Evolution of flux with respect to time

Precipitation flux varies both within the lifetime of each target as well as between targets. Some targets exist (as an object identified by TITAN) for very short periods of time (Figure 9.28). The dynamics of storms also varies greatly before the decision time. The y-axis in this figure is in logarithms and some differences between events vary over several orders of magnitude.

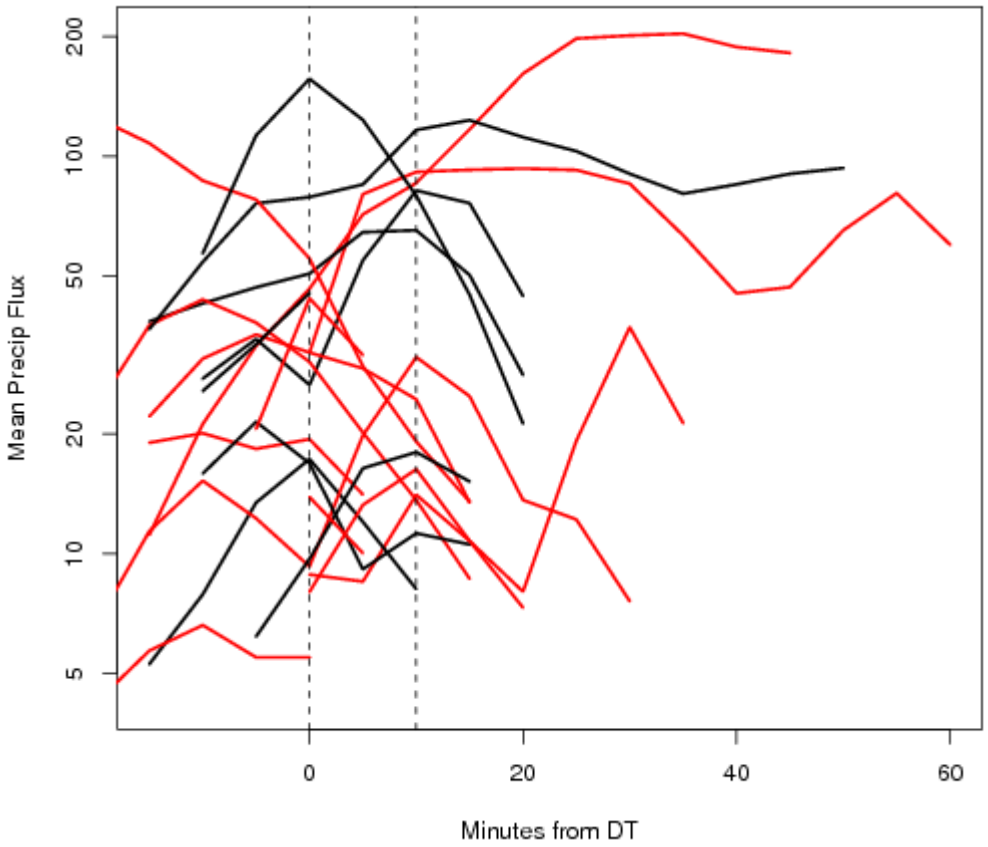

Figure 9.28 Precipitation flux as a function of time. Note that the y-axis is logarithmic. (Seeded cases are depicted with red lines, unseeded black.)

To adjust for the initial differences in the magnitude of each storm, flux values were normalized by scaling each series by the conditions at DT (Figure 9.29). Therefore, at DT all targets have a value of 1. A value of 2 indicates the flux has doubled since DT. Since flux values change over 2 orders of magnitude, this also allows all plots to be readily displayed in a single figure. Prior to DT, flux in the target storms are both decreasing and increasing. Only 4 targets have measurable flux beyond 20 minutes. This feature, combined with the concept that the effects of seeding might not be expected until possibly 20 minutes after the decision time suggest that these targets are too short lived to see results from seeding using TITAN/ radar based techniques. Three of the four long-lived targets were seeded, but this is a result that will reasonably happen by chance.

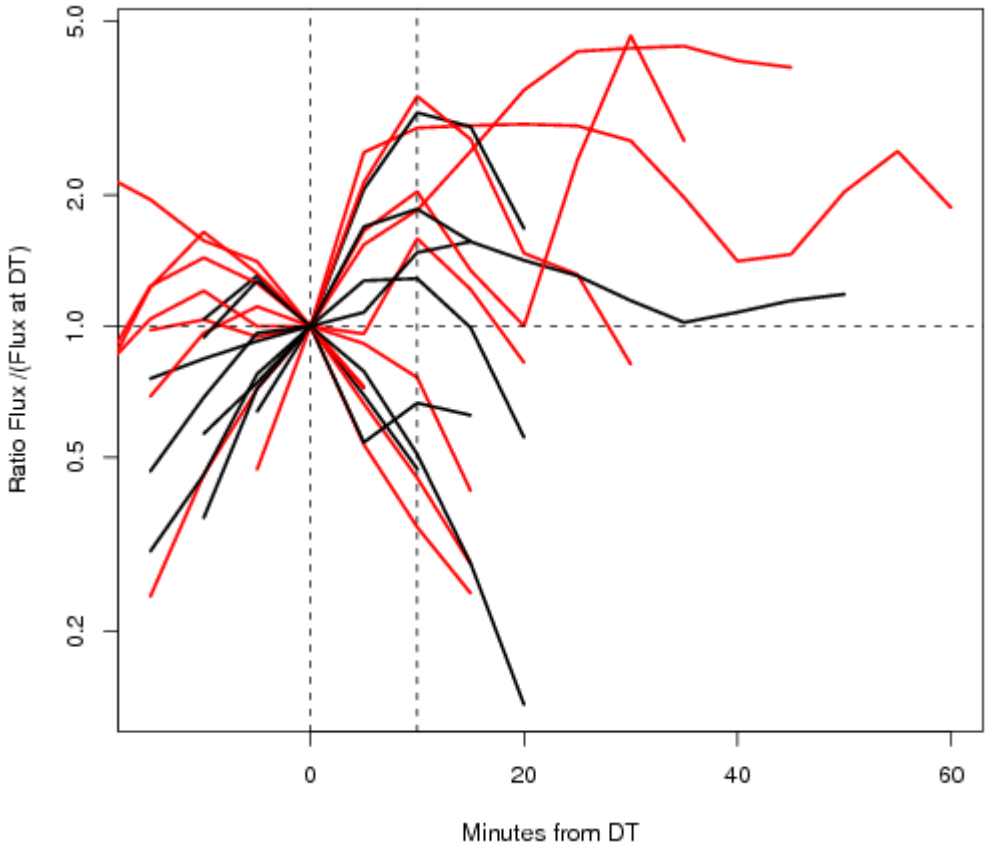

Figure 9.29. The ratio of precipitation flux to precipitation flux at DT. (Seeded cases are depicted with red lines; unseeded black.)

9.4.7 Duration

The duration of the targets after decision time was calculated (Figure 9.30). It is assumed that targets lived 5 minutes beyond the last non-zero measured value. The median duration of seeded targets was 5 minutes longer than un-seeded events, but the difference is not statistically significant. The analysis window ends 60 minutes after decision time, so the longest duration can be treated as censored data with positive flux values lasting at least 60 minutes.

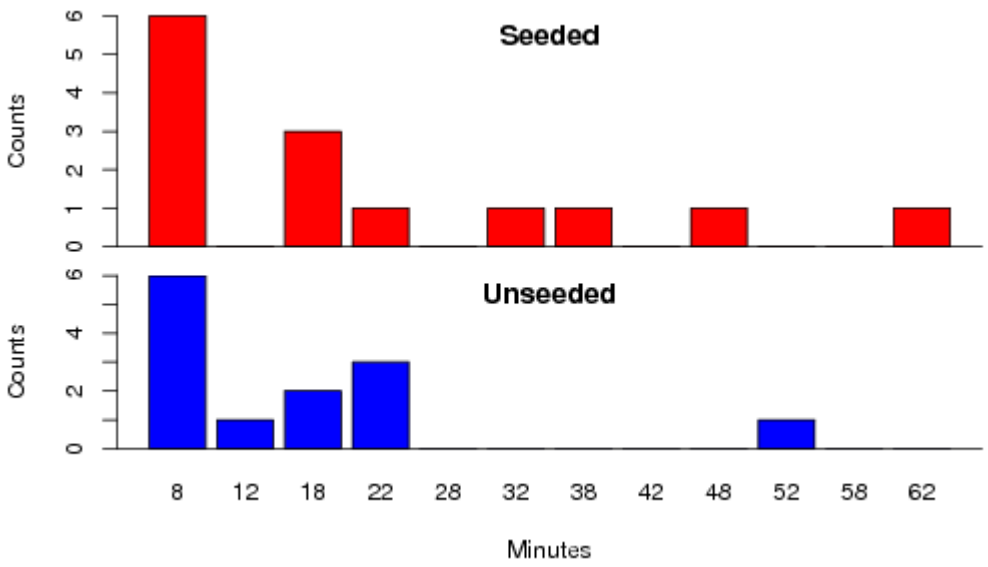

Figure 9.30. Duration of targets after DT. The duration of the target is calculated as 5 minutes beyond the last non-zero flux measurement.

10. SUMMARY AND RECOMMENDATIONS

The results summarized in the report are only preliminary at this stage because a lot more work and analyses are still ongoing and should be done to reach more final conclusions about the work. However, the results presented herein provide a first look at the data that could help guide future experimentation and decision-making. The preliminary results are summarized below.

The strong La Nina contributed to a unique year for Queensland in terms of rainfall and many parts of Queensland subjected to flooding, so much so that it was not representative of previous years. Climatological analysis presented in section 5.3 illustrated how unique this previous season was relative to the past 60 years, especially in terms of the strength of La Nina and the precipitable water observed. The trends in the climatology show that La Nina years are usually associated with abundant moisture through deep levels of the atmosphere and above normal rainfall.

The measurement season was characterized by a variety of cloud systems (deep convective, shallow convective, and deep stratiform). The shallow convective systems were the most predominant, while the deep convective and stratiform systems occurred less frequently. The radar analysis of the 2007-2008 season presented in section 8.1 showed that although the shallow convective systems occurred on more days than the deep convective and stratiform systems, the precipitation produced by the deep cloud systems overall was greater (Figure 8.15) and was 10-1000 times greater than that of shallow clouds when equal numbers of each cloud type were compared (Figure 8.17). Shallow convective showers were most associated with the southeasterly trade wind regime. Due to their higher frequency of occurrence, the shallow convective systems were more often observed by the aircraft operations than the deeper cloud systems. Due to their shallow nature, however, they were usually shorter-lived than the deep convective systems.

Aerosol measurements, as measured by the Differential Mobility Analyzer (DMA) and presented in section 7.1, seem to indicate higher concentration of aerosols than initially expected. In some cases, however, cleaner conditions were observed. This variation will need to be studied in more detail to understand the aerosol characteristics surrounding Brisbane and their relationship under varying wind regimes. These DMA aerosol measurements were in agreement with the cloud droplet concentrations that were measured in the preliminary case studies presented in sections 7.2.2 and 9.3.

Cloud droplet concentrations in clouds observed in Southeast Queensland were similar to those observed in the South African and Mexican experiments in the 1990's ranging between 400 and 600 cm^{-3}. Hygroscopic seeding randomized seeding experiments indicated positive effects of seeding on rainfall in those experiments. The South African and Mexican experiments only focused on deep convective systems. Based on these conditions and the previous results from South Africa and Mexico, deep convective systems could be amenable to hygroscopic seeding to enhance rainfall (a few occasions in December, January and February). The enhancement factor should be dependent on the cleanness of the atmosphere and may increase with more polluted air. Only a few deep convective systems were studied this past season and even fewer were seeded because of seeding restrictions in place due to flooding. We do not have sufficient data at this time to assess the seeding effects on deep convective systems.

The randomized seeding experiment, using hygroscopic seeding, was most often conducted in shallow cloud systems given their higher frequency of occurrence. Although 62

storms were selected for randomized seeding, only 27 cases were able to be analyzed as part of the statistical analyses (see section 9.4). Due to the small sample size none of the results are statistically significant and no definitive conclusions can be drawn from the results. Nonetheless, there are similar tendencies as was observed in the Mexican data after such a small sample set during its first year. These tendencies, although not statistically significant, are that more seeded storms had larger precipitation fluxes after seeding than unseeded storms, and more seeded storms tended to live longer than unseeded storms. These results provide encouragement to continue with randomized experiment.

The preliminary results presented herein have to be evaluated against the background described above. Only limited analyses of the data have been conducted to date and thus the results should be viewed as preliminary. Based on these results we would like to make the following recommendations:

1. Continue with the program from late September to Christmas (if another La Nina year is anticipated) to capture the early season, which was missed this year and indicated primarily convective systems that could be more amenable to cloud seeding.
2. Continue with a full season (October to March) if La Nina has weakened substantially and a more normal year or El Nino year is experienced.
3. Given the latest Southern Oscillation Index (SOI), as reported by the Bureau of Meteorology (http://www.bom.gov.au/climate/current/soi2.shtml), La Nina is in retreat, and the current SOI is slightly negative (see Figure 10.1).

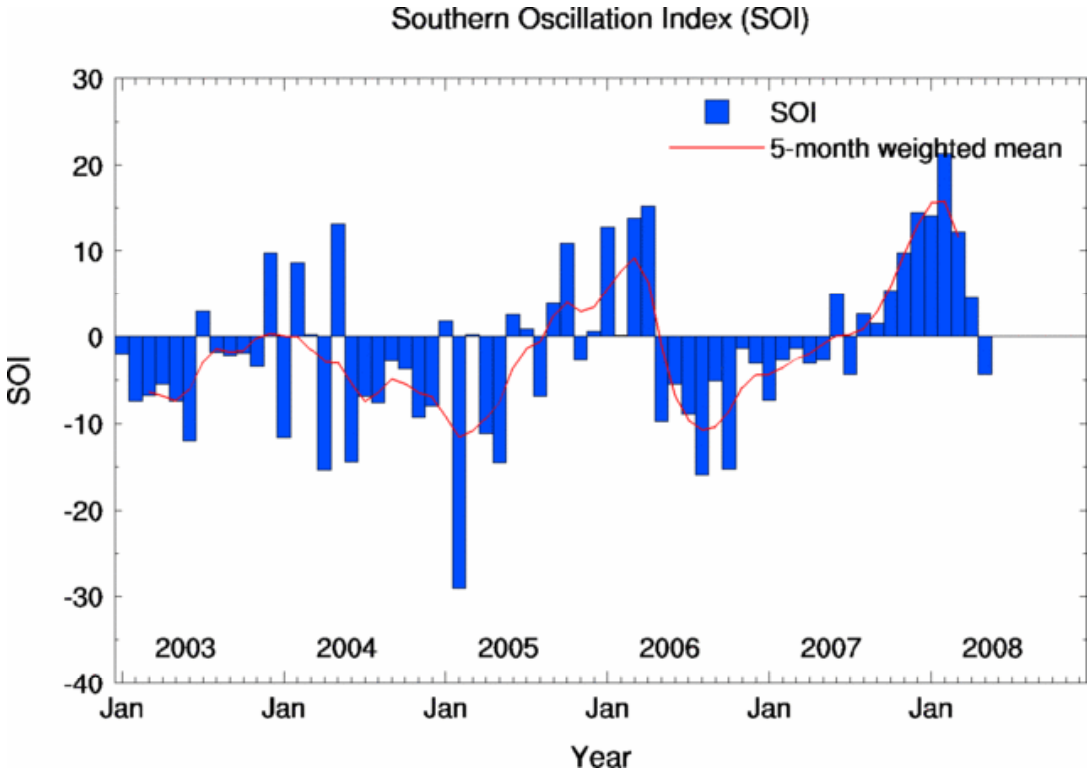

Figure 10.1. Time series of the Southern Oscillation Index (SOI), where positive values represent La Nina conditions, and negative values El Nino. (from (http://www.bom.gov.au/climate/current/soi2.shtml)

11. REFERENCES

Albrecht, B.A., 1989: Aerosols, cloud microphysics and fractional cloudiness, *Science*, **245**, 1227-1230.

Battan, L. J., and A. R. Kassander. 1967. Summary of randomized cloud seeding project in Arizona. In *Proceedings of the Fifth Berkeley Symposium on Mathematical Statistics and Probability*, pp. 29-42. Berkeley: University of California Press.

Bigg, E. K. 1997. An independent evaluation of a South African hygroscopic cloud seeding experiment, 1991-1995. *Atmos. Res.* **43**, 111-27.

Biswas, K.R., and A.S. Dennis, 1971: Formation of rain shower by salt seeding. *J. Appl. Meteor.*, **10**, 780-784.

Boucher, O., H. Le Treut and M.B. Baker, 1995: Precipitation and radiation modelling in a general circulation model: introduction of cloud microphysical processes, *J. Geophys. Res.*, **100**, D8, 16395-16414.

Bowen, E. G. 1952. A new method of stimulating convective clouds to produce rain and hail. *Q. J. Roy. Meteorol. Soc.* 78:37-45.

Braham, R.R. Jr, 1952: The water and energy budgets of the thunderstorm and their relation to thunderstorm development. *J. Meteor.,* **9**, 227–242.

Braham, R. R. 1964. What is the role of ice in summer rain showers? *J. Atmos. Sci.* **21**, 640-45.

Braham, Jr., R. R. 1979. Field experimentation in weather modification. *J. Am. Stat. Assoc.* **74**, 57-68.

Brandes, E. A., G. Zhang, and J. Vivekanandan, 2002: Experiments in rainfall estimation with a polarimetric radar in a subtropical environment. *J. Appl. Meteor.,* **41,** 674–685.

Brandes, E.A., G. Zhang, and J. Vivekanandan, 2004: Drop size distribution retrieval with polarimetric radar: Model and application. *J. Appl. Meteor.,* **43,** 461–475.

Bringi, V.N. and A. Hendry, 1990: Technology of Polarisation Diversity Radars for Meteorology, Chapter 19A, *Radar in Meteorology*, Edited, D. Atlas, American Meteorological Society, 806pp.

Bruintjes, R. T, 1999: A review of cloud seeding experiments to enhance precipitation and some new prospects. *Bull. Amer. Meteor. Soc.*, **80**, 805-820.

Bruintjes, R.T., Heymsfield, A.J., Krauss, T.W., 1987. An examination of double-plate ice crystals and the initiation of precipitation in continental cumulus clouds. *J. Atmos. Sci*. 44 (9), 1331 – 1349.

Bureau of Meteorology Queensland Regional Office, 2008: Qld forecasting digest. Technical report, Bureau of Meteorology, 51.

Chandrasekar, V., and V. N. Bringi, 1987: Simulation of radar reflectivity and surface measurements of rainfall. *J. Atmos. Oceanic Technol.,* **4,** 464–478.

Charlson, R.J., J. Langer and H. Rodhe, 1990: Sulfate aerosol and climate, *Nature*, **326**, 655-661.

Charlson R.J., S.E. Schwartz, J.M. Hales, R.D. Cess, J.A. Coakley, J.E. Hansen and D.J. Hofmann, 1992: Climate forcing by anthropogenic aerosols, *Science*, **255**, 422-430.

Cotton, W. R., 1972: Numerical simulation of precipitation development in supercooled cumuli. Part II. *Mon. Weather Rev.,* **11**, 764-84.

Cotton, W. R., 1982: The modification of warm clouds—a review. *Bull. Amer. Meteor. Soc.*, **63**, 146-160.

Cotton, W. R., and R.A. Anthes, 1989: *Storm and Cloud Dynamics*. Academic Press, San Diego, CA. International Geophysics Series, vol. 44.

Cruz, C. N. and S. N. Pandis, 1997: A study of the ability of pure secondary organic aerosol to act as cloud condensation nuclei. *Atmos. Environ*., **31**, 2205-2214.

Cruz, C. and S. Pandis, 1998: The effect of organic coatings on the cloud condensation nuclei activation of inorganic atmospheric aerosol. *J. Geophys. Res.,* **103**, 13,111-13,123.

Dennis, A. S., 1980: *Weather Modification by Cloud Seeding.* Academic Press, NY, 145.

Deshler, T., D. W. Reynolds, and A. W. Huggins, 1990: Physical Response of Winter Orographic Clouds over the Sierra Nevada to Airborne Seeding Using Dry Ice or Silver Iodide. *J. Appl. Meteor.*, **29**, 288-330.

Dixon, M., and G. Wiener, 1993: TITAN: Thunderstorm Identification, Tracking, Analysis, and Nowcasting—A radar-based methodology. *J. Atmos. Oceanic Technol*., **10**, 785-797.

Facchini, M. C., M. Mircea, S. Fuzzi, and R. J. Charlson, 1999: Cloud albedo enhancement by surface-active organic solutes in growing droplets, *Nature*, **401**, 257-259.

Farley, R. D., and C. S. Chen, 1975: A detailed microphysical simulation of hygroscopic seeding on the warm rain process. *J. Appl. Meteor.*, **14**, 718-733.

Gabriel, K. R., and Rosenfeld, D., 1990: The second Israeli rainfall stimulation experiment: analysis of precipitation on both targets. *J. Appl. Meteor.*, **29**, 1055-1067.

Gagin, A., D. Rosenfeld, W. C. Woodley, and R. E. Lopez, 1986: Results of seeding for dynamic effects on rain-cell properties in FACE-2. *J. Climate Appl. Meteor.,* **25,** 1–12.

Garvey, D.M., 1975: Testing of cloud seeding materials at the Cloud Simulation and Aerosol Laboratory, 1971-1973. *J. Appl. Meteor*., **14**, 883-890.

Goddard, J.W.F., J. Tan, and M. Thurai, 1994: Technique for calibration of meteorological radars using differential phase. *Electronics Letters*, **30**, 166-167.

Grant, L. O., and P. W. Mielke, Jr. 1967. Cloud seeding experiment at Climax, Colorado. 1960-65. In *Proceedings of the Fifth Berkeley Symposium on Mathematical Statistics and Probability*, vol. 5, pp. 115-31. Berkeley: University of California Press.

Guerzoni, S., and R. Chester, 1996: *The impact of desert dust across the Mediterranean*, Kluwer, Dordrecht.

Hallet, J., and S. C. Mossop. 1974. Production of secondary ice particles during the riming process. *Nature* **104**, 26-28.

Houze, R.A. Jr., 1993: *Cloud Dynamics*, Academic Press, Inc., Orlando, FL, 573 pp.

Hudson, J.G., 1991: Observations of anthropogenic cloud condensation nuclei, *Atmos. Environ.*, 25A, **11**, 2449-2455.

Jaenicke, R., 1998: Atmospheric aerosol size distribution, in R.M. Harrison and R.E. van Grieken (eds), *Atmospheric Particles*, IUPAC series on analytical and physical chemistry of environmental systems, Volume 5, John Wiley and Sons, New York.

Johnson, D.B., 1987. On the relative efficiency of coalescence and riming. *J. Atmos. Sci*. 44, 1671 – 1680.

Johnson, R., T. Rickenbach, S. Rutledge, P. Ciesielski, and W. Schubert, 1999: Trimodal characteristics of tropical convection. *J. Climate*, **12**, 2397-2418.

Kalnay, E., [et al.], 1996: The NCEP/NCAR 40-year reanalysis project, *Bull. Am. Meteorol. Soc*., **77**, 437–471.

Keeler, R.J., P.H. Herzegh and C.L. Frush, 1984: Measurements of CP2 copolar and cross-polar antenna illumination functions at S and X-Band. Preprints, *22nd Radar Meteorology Conf.,* Zurich, Amer. Meteor. Soc., 287-291

Keeler, R.J., B.W. Lewis and G.R. Gray, 1989: Description of NCAR/FOF CP-2 Meteorological Doppler Radar. Preprints, *24th Radar Meteorology Conf.,* Tallahassee, Florida, Amer. Meteor. Soc., 589-592.

Koenig, L. R., and F. W. Murray. 1976. Ice-bearing cumulus cloud evolution: Numerical simulation and general comparison against observations. *J. Appl. Meteor.* **7**, 747-62.

Krauss, T.W., Bruintjes, R.T., Verlinde, J., Kahn, A., 1987. Microphysical and radar observations of seeded and non-seeded continental cumulus clouds. *J. Clim. Appl. Meteorol*. 26, 585 – 606.

Levi Y., and D. Rosenfeld. 1996. On ice nuclei, rainwater chemical composition and static cloud seeding effects in Israel. *J. Appl Meteorol.* **35**, 1494-1501.

Liu, P. S. K., W. R. Leaich, C. M. Banic, and S. M. Li, 1996: Aerosol observations at Chebogue Point during the 1993 North Atlantic Regional Experiment: Relationships among cloud condensation nuclei, size distribution and chemistry, *J. Geophys. Res*., **101**, 28,971-28,990.

Marwitz, J. D., A. H. Auer, Jr. and D. L. Veal, 1972: Locating the organized updraft on severe thunderstorms. *J. Appl. Meteor.,* **11**, 236–238.

Mather, G. K., D. E. Terblanche, F. E. Steffens, and L. Fletcher, 1997: Results of the South African cloud-seeding experiments using hygroscopic flares. *J. Appl. Meteor.*, **36**, 1433-1447.

Menon, S., and V.K. Saxena, 1998: Role of sulphates in regional cloud-climate interaction, *Atmos. Res.*, **47-48**, 299-315.

Mielke, Jr., P. W., G. W. Brier, L. O. Grant, G. J. Mulvey, and P. N. Rosensweig. 1981. A statistical reanalysis of the replicated Climax I and II wintertime orographic cloud seeding experiments. *J. Appl. Meteorol.* **20**, 643-60.

Mooney, M. L., and G. W. Lunn, 1969: The area of maximum effect resulting from the Lake Almanor randomized cloud seeding experiment. *J. Appl. Meteor.*, **8**, 68–74.

Murty, A.S.R., A.M. Selvam, P.C.S. Devara, K. Krishna, R.N. Chatterjee, B.K. Mukherjee, L.T. Kemani, G.A. Momin, R.S. Reddy, S.K. Sharma, D.B. Jadhav, R. Vijayakumar, P.E. Raj, G.K. Manohar, S.S. Kandalgaonkar, S.K. Paul, A.G. Pillai, S.S. Parasnis, C.P. Kulkarni, A.L. Londhe, C.S. Bhosale, S.B. Morwal, P.D. Safai, J.M. Pathan, K. Indira, M.S. Naik, P.S.P. Rao, P. Sikka, K.K. Dani, M.K. Kulkarni, H.K. Trimbake, P.N. Sharma, R.K. Kapoor, and M.I.R. Tinmaker, 2000: 11-year warm cloud seeding experiment in Maharashtra state, India. *J. Wea. Mod.*, **32**, 10-20.

National Academy of Sciences, 2003: Critical Issues in Weather Modification Research. The National Academy Press, M. Garstang, Ed., 123 pp.

Novakov, T. and Penner, J. E., 1993: Large contribution of organic aerosols to cloud-condensation nuclei concentrations. *Nature* **365**, 823-826.

Orville, H. D., 1996: A review of cloud modeling in weather modification. *Bull. Amer. Meteor. Soc*., **77**, 7, 1535-1555.

Penner, J.E., R.E. Dickinson and C.A. O'Neill, 1992: Effects of aerosol from biomass burning on the global radiation budget. *Science*, **256**, 1432-1434.

Penner, J.E., R.J. Charlson, J.M. Hales, N.S. Laulainen, R. Leifer, T. Novakov, J. Ogren, L.F. Radke, S.E. Schwartz and L. Travis, 1994: Quantifying and minimising uncertainty of climate forcing by anthropogenic aerosols, *Bul. Amer. Meteor. Soc.*, **75**, 375-400.

Pruppacher, H. R., and J. D. Klett, 1998: *The Microphysics of Clouds and Precipitation*, 954 pp., Kluwer Academic Press, Amsterdam, 1998.

Rangno, A. L., and P. V. Hobbs. 1995. A new look at the Israeli cloud seeding experiments. *J. Appl. Meteorol.* 34:1169-93.

Raymond T. M, Pandis S. N., 2002: Cloud activation of single-component organic aerosol particles. *J. Geophys. Res*., **107**, doi:10.1029/2002JD002159.

Reynolds, D. W., and Dennis, A. S., 1986: A review of the Sierra Cooperative Project. *Bull. Amer. Meteor. Soc.*, **67**, 513-523.

Rivera-Carpio, C. A., C. E. Corrigan, T. Novakov, J. E. Penner, C. F. Rogers, and J. C. Chow, 1996: Derivation of contributions of sulphate and carbonaceous aerosols to cloud condensation nuclei from mass size distributions. *J. Geophys. Res*., **101**, 19,483-19,493.

Rogers, R. R. 1976. *A Short Course in Cloud Physics*. New York: Pergamon.

Rokicki, M. L., and K. C. Young, 1978: The initiation of precipitation in updrafts. *J. Appl. Meteor.*, **17**, 745-754.

Rosenfeld, D., and H. Farbstein, 1992: Possible influence of desert dust on seedability of clouds in Israel. *J. Appl. Meteor.*, **31**, 722-731.

Rosenfeld, D., and R. Nirel, 1996: Seeding effectiveness—the Interaction of desert dust and the southern margins of rain cloud systems in Israel. *J. Appl. Meteor.*, **35**, 1502-1510.

Rosenfeld, D., and W. L. Woodley. 1993. Effects of cloud seeding in West Texas: Additional results and new insights. *J. Appl. Meteorol.* **32**, 1848-66.

Rosenfeld, D. and W. L. Woodley. 2000. Convective clouds with sustained highly supercooled liquid water down to -37.5°C. *Nature* **405**, 440-442.

Rosenfeld D., R. Lahav, A. P. Khain, M. Pinsky. 2002. The role of sea-spray in cleansing air pollution over ocean via cloud processes. *Science* **297**, 1667-70.

Ryan, B.F., and W.D. King, 1997: A critical review of the Australian experience in cloud seeding. *Bull. Amer. Meteor. Soc.,* **78**, 239-254.

Scott, B. C., and P. V. Hobbs. 1977. A theoretical study of the evolution of mixed-phase cumulus clouds. *J. Atmos. Sci.* 34:812-26.

SCPP (Sierra Cooperative Pilot Project). 1982. The design of SCPP-1. A randomized precipitation augmentation experiment on winter cellular convection in the central Sierra Nevada. Denver, Col.: Project Skywater. Bureau of Reclamation, Division of Atmospheric Resources Research.

Seinfeld, J. H., and S. N. Pandis, 2006: Atmospheric Chemistry and Physics: From Air Pollution to Climate Change, Wiley.

Shantz, N.C., W.R. Leaitch, and P.F. Caffrey, 2003: Effect of organics of low solubility on the growth rate of cloud droplets. *J. Geophys. Res*., **108***,* doi:10.1029/2002JD002540.

Shine, K.P., R.G. Derwent, D.J. Wuebbles and J.J. Morcettee, 1990: Radiative forcing of climate, in J.T. Houghton, G.J. Jenkins and J.J. Ephraums (eds), *Climate Change: The IPCC Scientific Assessment*, Cambridge University Press, Cambridge.

Silverman, B. A., 2000. An independent statistical reevaluation of the South African hygroscopic flare seeding experiment. *J. Appl. Meteorol.* 39(8):1373-78.

Silverman, B.A., and W. Sukarnjanaset, 2000: Results of the Thailand warm-cloud hygroscopic particle seeding experiment. *J. Appl. Meteor.*, **39**, 1160-1175.

Smith, P. L., A. S. Dennis, B. A. Silverman, A. B. Super, E. W. Holroyd, W. A. Cooper, P. W. Mielke, K. J. Berry, H. D. Orville, and J. R. Miller. 1984. HIPLEX-1: Experimental design and response variables. *J. Clim. Appl. Meteorol.* 23:497-512.

Sokolik, I., and O. Toon, 1999: Incorporation of mineralogical composition into models of the radiative properties of mineral aerosol from UV to IR wavelengths, *J. Geophys. Res*., **104**, 9423-9444.

Super, A. B., 1986: Further exploratory analysis of the Bridger Range winter cloud seeding experiment. *J. Appl. Meteor.*, **25**, 1926-1933.

Super, A. B., and J. A. Heimbach, Jr.. 1983: Evaluation of the Bridger Range winter cloud seeding experiment using control gages. *J. Appl. Meteor.*, **22**, 1989–2011.

Tegen, I., and I. Fung, 1995: Contribution to the atmospheric mineral aerosol load from land surface modification. *J. Geophys. Res.*, **100**, D9, 18707-18726.

Terblanche, D. E., F. E. Steffens, L. Fletcher, M. P. Mittermairer, and R. C. Parsons, 2000: Toward the operational application of hygroscopic flares for rainfall enhancement in South Africa. *J. Appl. Meteor*., **39**, 1811-1821.

Twomey, S., 1977: *Atmospheric Aerosols*. Elsevier Scientific, Amsterdam, 302 pp.

Vali, G., L. R. Koenig, and T. C. Yoksas, 1988: Estimate of precipitation enhancement potential for the Duero Basin of Spain. *J. Appl. Meteor.*, **27**, 827-850.

Waldvogel, A., 1974: The N_0 jump of raindrop spectra. *J. Atmos. Sci.,* **31,** 1067–1078.

Warneck, P., 1988: *Chemistry of the Natural Atmosphere*. Academic Press, Inc., San Diego, CA, 757 pp.

White, W., 1990: The contribution of fine particles scattering to total extinction, visibility: Existing and historical conditions – cause and effect, *Acid Deposition State of Science Report 24*, National Acid Assessment Program, Government Printing Office, Washington, D.C., 85-102.

WMO (World Meteorological Organization), 2000: Report on the WMO International workshop on Hygroscopic seeding: Experimental results, physical processes and research needs. Geneva: WMO.

Woodley, W., J. Jordan, and A. Barnston, 1982: Rainfall results of the Florida Area Cumulus Experiment, 1970 –76. *J. Appl. Me- teor.,* **21,** 139 –164.

Woodley, W.L., A. Barnston, J. A. Flueck, and R. Biondini, 1983: The Florida Area Cumulus Experiment's second phase (FACE-2). Part II: Replicated and confirmatory y analyses.*J. Climate Appl. Meteor.,* **22,** 1529 –1541.

Woodley, W. L., B. A. Silverman, and D. Rosenfeld, 1999: Final contract report to the Ministr y of Agriculture and Cooperatives. Woodley Weather Consultants Report, 110 pp. [Available from Woodley Weather Consultants, 11 White Fir Ct., Littleton, CO 80127; also available from Bureau of Royal Rainmaking and Agricultural Aviation, Kasetsart University Campus, Phahony- othin Rd., Chatuchak, Bangkok 10900, Thailand.]

Young, K. C., 1996; Weather modification – a theoretician's viewpoint. *Bull. Amer. Meteor. Soc.*, **77**, 2701-10.

Zhang, G., J. Vivekanandan, and E. Brandes, 2001: A method for estimating rain rate and drop size distribution from polarimetric radar measurements. *IEEE Trans. Geosci. Remote Sens.,* **39,** 830–841.

Zhang, G., J. Vivekanandan, E. Brandes, R. Menegini, and T. Kozu, 2003: The shape–slope relation in observed gamma drop size distributions: Statistical error or useful information? *J. Atmos. Oceanic Technol.,* **20,** 1106–1119.

12. APPENDIX

12.1 CP2 DATA QUALITY REPORT

12.1.1 Data-mask for meteo/non-meteo echoes

Good data mask has been previously based on criteria applied to two parameters : (1) ρ_{hv} and (2) standard deviation of Φ_{dp} , to mask out non-meteo echoes. For example, C-Pol data analysis for the Jan 2006 monsoon cases used thresholds for 10 consecutive range gates for both parameters. This was repeated for the CP2 data, but it seems that the ρ_{hv} criteria sometimes removes rain (wanted) echoes, as shown below in Figure 12.1. The left plot shows the mask superimposed with both criteria applied and the right plot shows the mask based on standard deviation of Φ_{dp} alone.

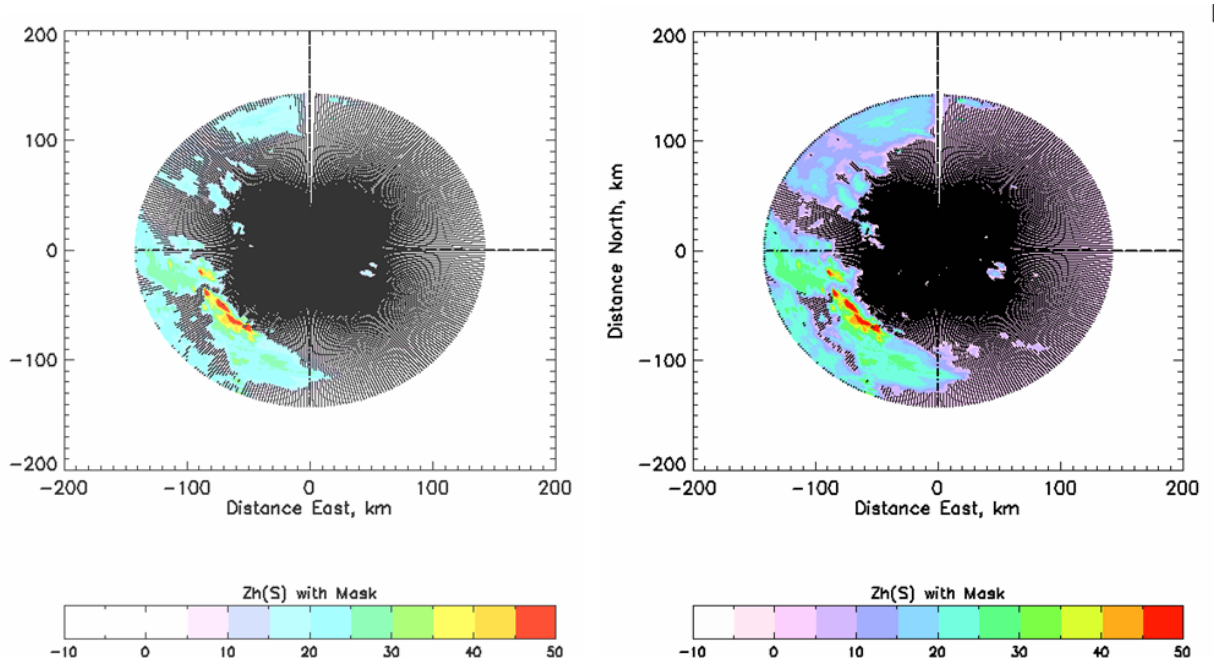

Figure 12.1: Data mask applied to 2.3 deg elevation PPI sweep on Feb 06 2008 @ 0818. Low intensity rain echoes are masked out on the left hand plot which uses both criteria.

Hence it appears that it would be better to apply only the standard deviation of Φ_{dp} criterion for the CP2 PPI sweeps. A preliminary threshold of 10 deg appears to be suitable to mask out non-meteo echoes (10 gate moving estimate of standard deviation: 1.5 km for CP2 range sampling).

12.1.2 Zdr smoothing

The S-band Z_{dr} is very noisy, i.e. very high frequency gate-to-gate fluctuations (see also section on LDR and vertically pointing data). We have attempted two types of smoothing: (1)

box-car smoothing over 2 azimuths and 2 range gates on either side (i.e. over 5 pixels) and (2) FIR range filtering. Both seem to reduce the noise and give reasonable range profiles. These are illustrated in Figure 12.2-Figure 12.3 for two different profiles using both methods (top for the first method and bottom for the second method). Notice the large variation of raw Z_{dr} in Figure 12.3 in adjacent azimuths at range 12 km and at 16-16.5 km (over the 2-D video disdrometer). Clearly, some form of smoothing is required to remove such sharp variations.

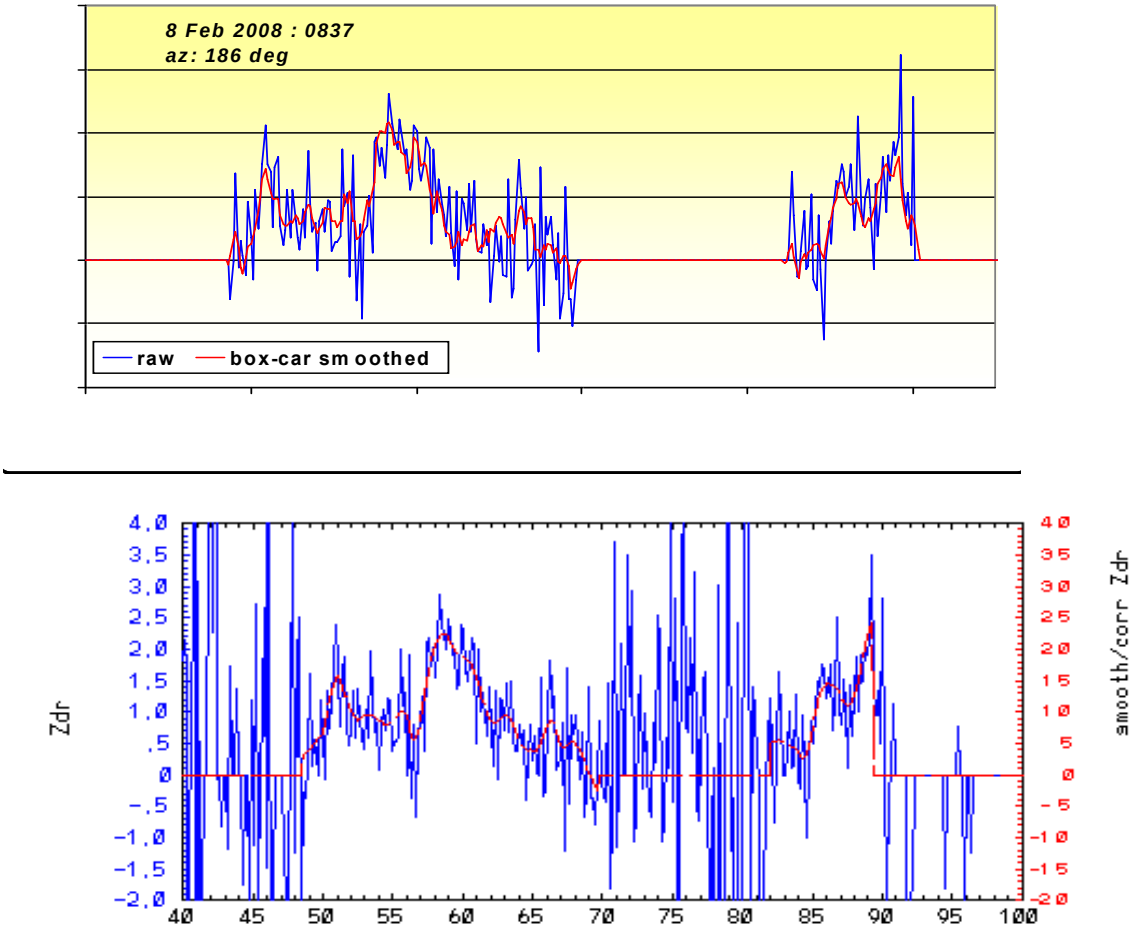

Figure 12.2. The upper panel shows the data masked raw Z_{dr} (in blue) and the box-car smoothed Z_{dr} (in red) using method (1) and the lower panel shows the unmasked raw Z_{dr} (in blue) with the range filtered Z_{dr} (in red) using method (2), for an example range profile.

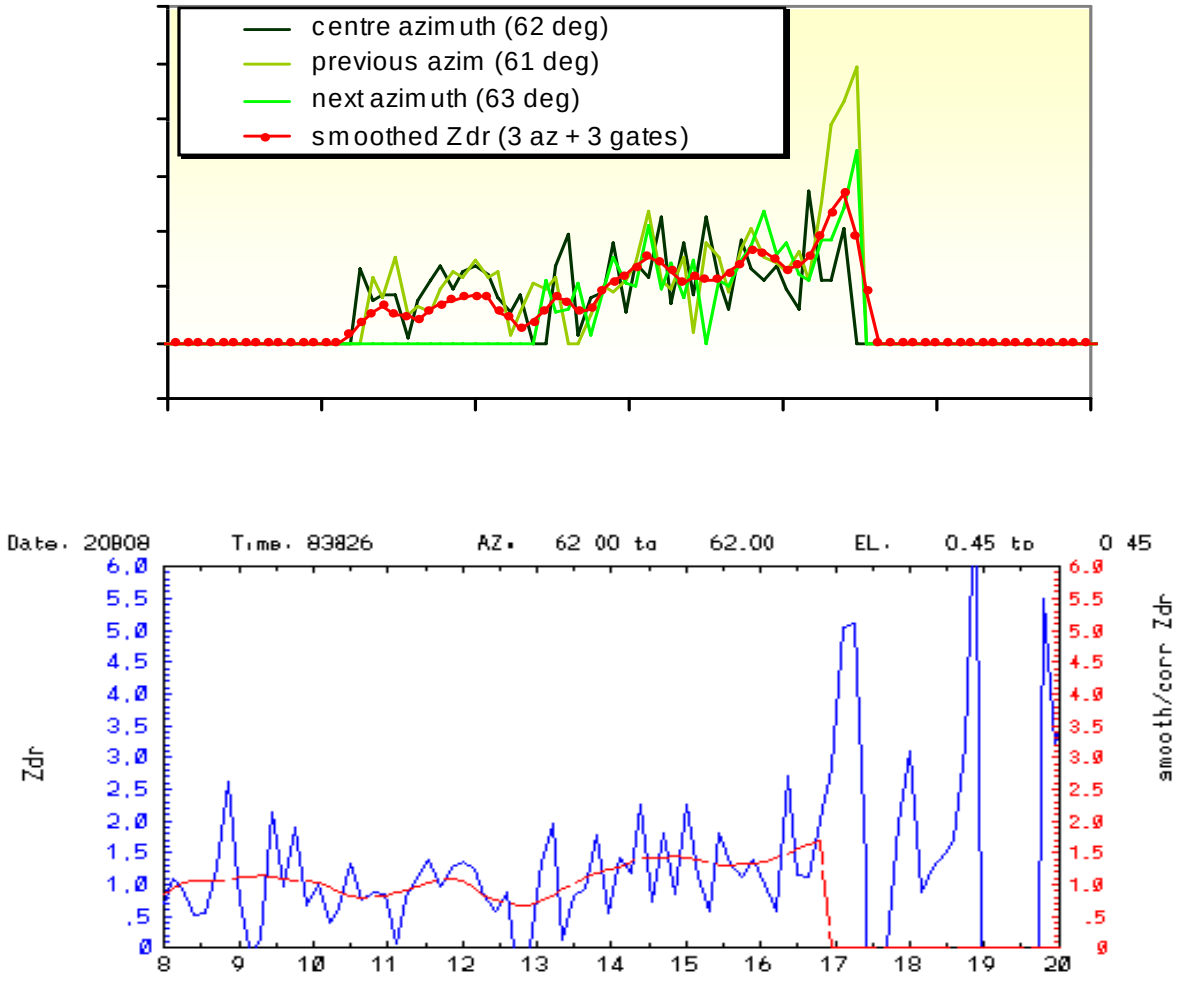

Figure 12.3. The same as Figure 12.2 but using a different example. (Note the top panel shows the azimuthal variation as well).

12.1.3 Estimated Z_h, Z_{dr} calibration from data in rain

Two methods have been used for evaluation of the absolute Z_h and Z_{dr} calibrations (also referred to here as system offsets assuming that all engineering, including solar, calibrations have been performed prior to our analyses) . The first method entails the use of color-intensity plots for the Z_h - K_{dp} variation as well as the Z_h - Z_{dr} variation, derived from the radar data. Figure 12.4 shows these variations for a PPI sweep. In both cases, the calculations using the 2D video disdrometer data are superimposed, and in both cases there seems good agreement.

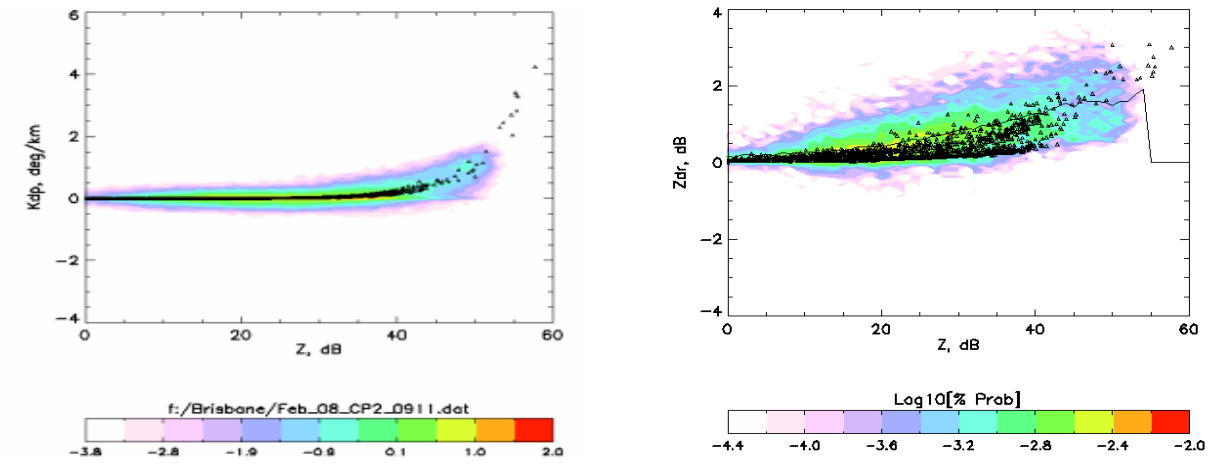

Figure 12.4. Z_h - K_{dp} variation (left) and Z_h - Z_{dr} variation (right) derived from the CP2 radar data shown as color intensity plots compared with theoretical calculations (black dots) using 2DVD DSDs. The color scale represents Log_{10} of % probability.

The second method entails Φ_{dp} consistency check along a suitable range profile using the method similar to Goddard et al. (1994): the Φ_{dp} range profile is re-constructed using Z_h and Z_{dr} values at each range gate and then compared with the measured Φ_{dp} profile. The right plot in Figure 12.5 shows these comparisons for the range profile at 225 deg azimuth from the PPI sweep shown on the left. Note the reconstructed curve is sensitive to Z_h calibration, and, to some extent, Z_{dr} calibration.

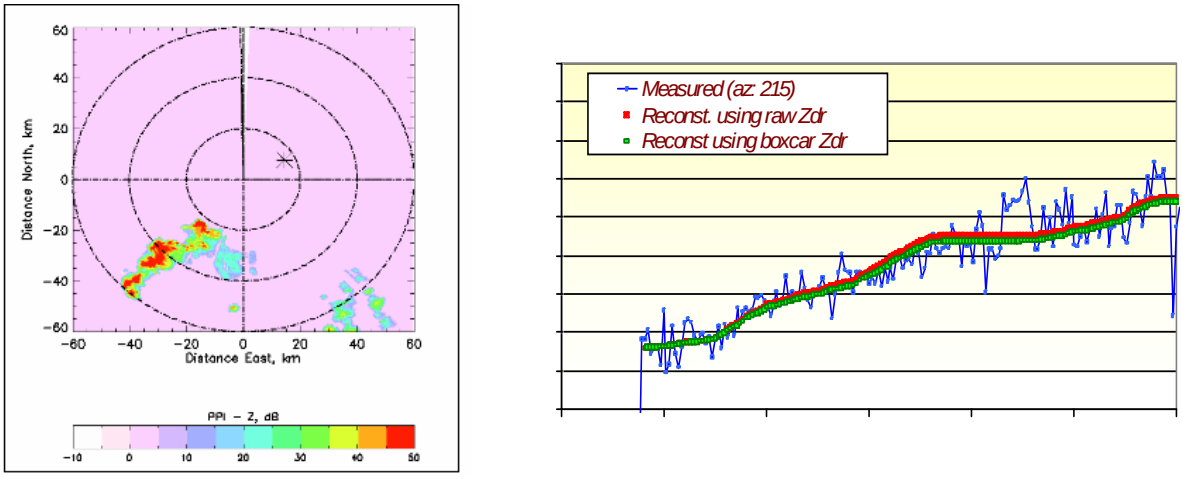

Figure 12.5. Φ_{dp} range profile (right) at 215 deg azimuth from a PPI sweep (left) used for checking Z_h calibration.

These two techniques have yielded the following adjustment shown in Table 12.1.

Table 12.1. Positive offset values meaning that the 'raw' values have to be increased by the noted amount.

Day	Z_h cal	Zdr_cal
2 Feb 2008	0	0.5 dB
4 Feb 2008	0	0.5 dB
6 Feb 2008	0	0.5 dB
8 Feb 2008	0	-0.25 dB
26 Feb 2008	0	0

The absolute calibration of the CP2 S-band reflectivity (Z_h) is considered to be excellent (i.e., no further system offset need be applied to the 'raw' values). This is confirmation of the solar calibration done by NCAR and BMRC at the beginning of the project. We note that NCAR has long history and experience with solar calibrations since the mid 1980s.

The Z_{dr} offsets in Table 12.1 (i.e. 'calibrated' Z_{dr} = 'raw' Z_{dr} + offset value) show consistency from 2-6 Feb and then become closer to 0 dB later. We have confirmed that for the 26th of Feb 2008 case, the Z_{dr} offset had already been applied to the 'raw' data prior to our analyses. Thus, our independent estimate of no Z_{dr} offset for this case (shown in the last row in the above table) agrees with this. We are not sure at this point if Z_{dr} offsets had already been applied or not for the 2-8 February datasets before being given to us for further analyses but we suspect not, at least for the 2-6 February datasets.

12.1.4 Comparison with 2D video disdrometer (2DVD) data-based calculations

The 2DVD belonging to NCAR is located at 62 deg azimuth and 16.3 km range from the CP2 radar. This has made it possible to make preliminary comparisons of Z_h and Z_{dr} between the S-band radar measurements and those derived from the 2DVD DSD data. Figure 12.6 shows one example. The DSDs derived from the 2DVD measurements* are given as time series in Figure 12.6. Notice drop sorting occurring at the beginning, i.e. the larger drops falling through the 2DVD's sensor area initially, which is followed by the (somewhat) smaller drops. The two black curves represent the mass-weighted mean diameter (upper curve) and the DSD width (lower curve), defined by the standard deviation of the mass spectrum.

* the 2DVD data need to undergo a 're-matching' process, which may alter the DSDs slightly for D< 1.5 mm.

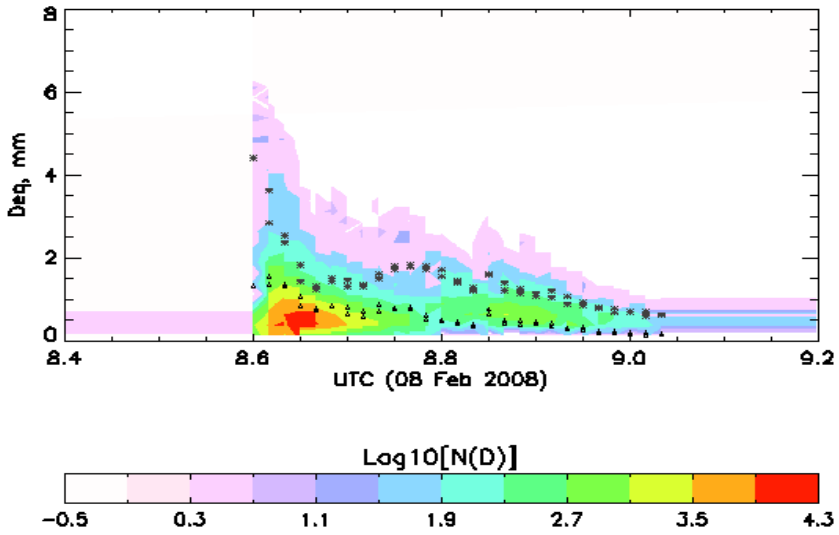

Figure 12.6. Time series of 30 second averaged DSDs from the 2DVD measurements on the 8th of Feb 2008. The color-filled values represent the N(D) in log scale while the lower series of points shows the mass-weighted mean diameter and the upper series shows the standard deviation of the mass spectrum.

PPI scans covering the NE sector were used to make the time series comparisons. The scan taken just at the beginning of the event is shown in Figure 12.7 where the 2DVD location is also marked.

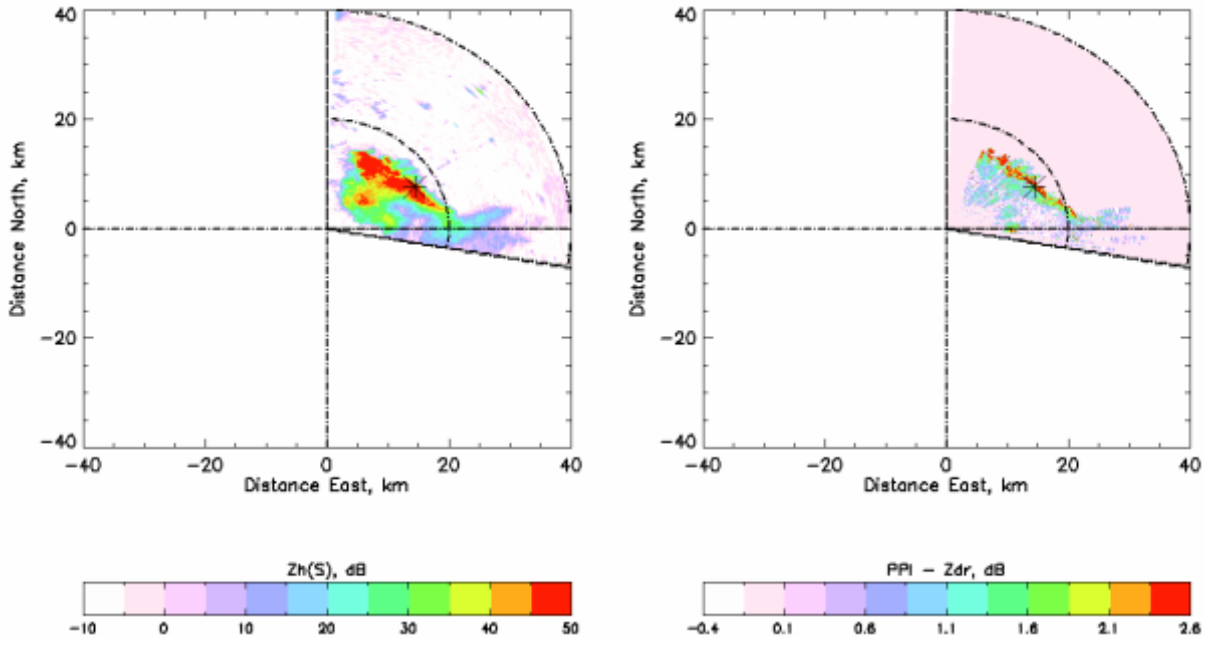

Figure 12.7. PPI sector scan taken at (0839), the beginning time of the event in Figure 12.6.

Time series of Z_h and Z_{dr} at this location were extracted from such PPI sector scans and are compared over a 40 minute time period in Figure 12.8. The green circles represent radar data at the 2DVD location and in the adjacent pixels. Overall the agreement is very good, considering the large differences in spatial and temporal resolutions. (The 2DVD sensor area is 10 cm by 10 cm and the Z_h, Z_{dr} calculations were derived from DSDs averaged over 30 seconds.)

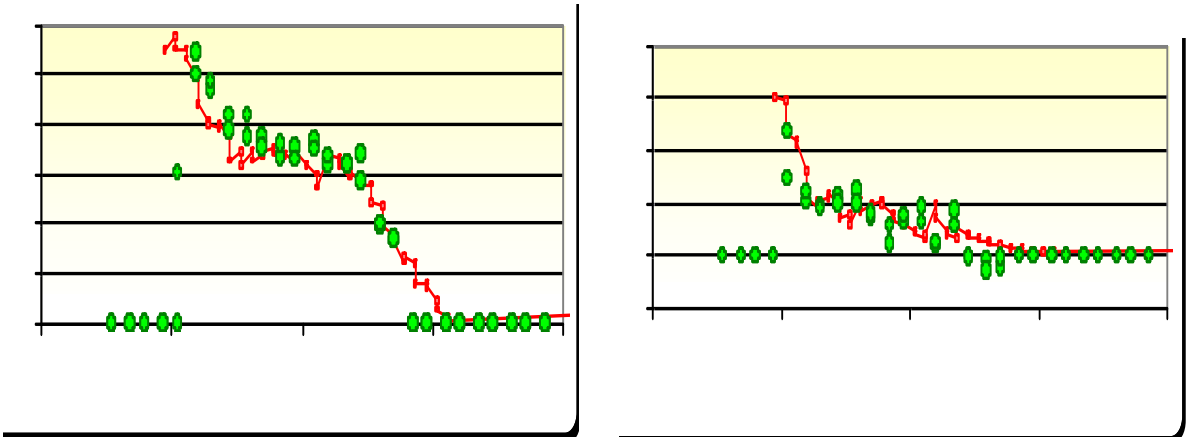

Figure 12.8. Z_h (left) and Z_{dr} (right) time series comparisons between 2DVD DSD based calculations (red) and the CP2 radar data at S-band, for the event given in Figure 12.6.

12.1.5 X-band alignment

Prior to the 25th of Feb 2008, there was a slight offset in the recorded azimuth of the X-band data compared with the S-band data, which typically gave an azimuth error of about 0.35 to 0.5 degrees in the surveillance mode. This offset, which is due to the signal processing software alone, has since been corrected. Figure 12.9 shows an example of the S- and X-band reflectivity profiles taken on the 26th of Feb 2008, as well as their difference in dB (the latter is the dual-wavelength reflectivity ratio or DWR expressed in dB). The red and the blue curves track each other well until 70 km, when the X-band signal goes below the noise level hence, indicating excellent alignment between the two radars. On this day there was significant rain-on-radome attenuating the X-band signal thus causing an initial difference or DWR of ~ 10 dB). (It has been noticed in prior studies that this is dependent on the rain intensity over the radome.) Nevertheless, the DWR can be seen to increase with range at least until 70 km, implying strong attenuation of the X-band signal due to rain (from 58 to 70 km).

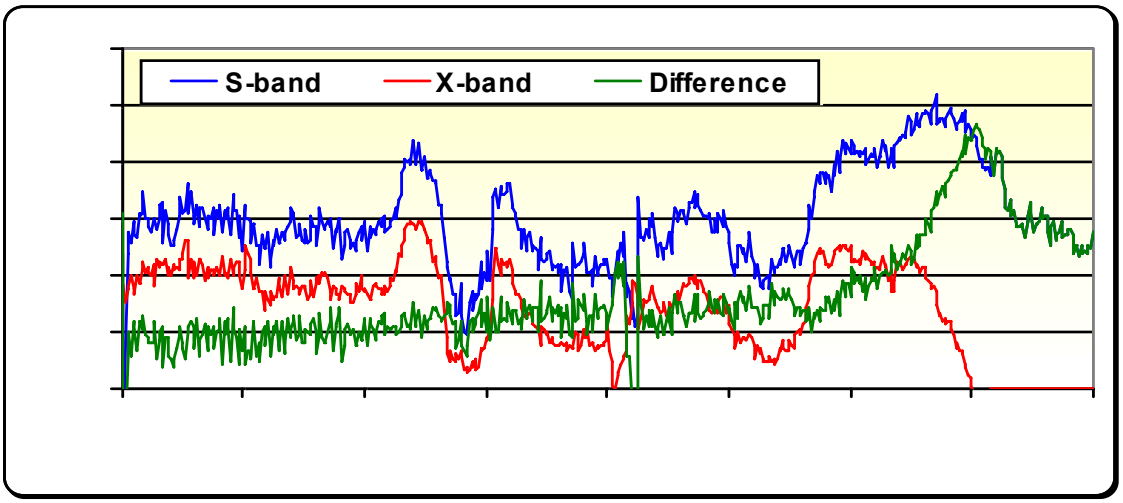

Figure 12.9. S- and X-band range profiles of Z_h showing the close alignment between the two, together with the difference (also referred to as the dual-wavelength reflectivity ratio or DWR in dB).

12.1.6 Using dual-wavelength ratio (DWR) for drop shape studies

If the S and X band data have sufficiently high accuracy, it may become possible to utilize simultaneously-sampled data to make inferences on 'effective' drop shapes. Here, we introduce a preliminary study using the X-band specific attenuation (A_H), K_{dp} and Z_{dr} data from the CP2 radar system. In theory, the ratio between the X-band specific attenuation, A_H , and the specific differential propagation phase K_{dp} varies with Z_{dr} at S-band, the variation being dependent on the probable drop shapes, i.e.

$$\frac{{A_H}^{X-band}}{{K_{dp}}^{S-band}} = f\left({Z_{dr}}^{S-band}\right) \quad \textbf{(13)}$$

where the function $f({Z_{dr}}^{S\text{-}band})$ is different for different drop shapes. The X-band specific attenuation is one-half the range derivative of the DWR just as the K_{dp} is one-half the range derivative of the differential propagation phase (assuming all raindrops and no Mie scattering due to hail).

This was attempted using the range profiles (such as shown in Figure 12.9) for range gates between 65 km and 69 km, where it was possible to derive the X-band specific attenuation by fitting a polynomial to the range profile of DWR and then taking one-half of the derivative. The results are plotted as green dots in Figure 12.10 and compared with theoretical calculations using the 1-minute DSDs from the 2DVD and assuming the drop shapes from the 80 fall experiment (blue stars) and the Andsager et al shapes (red crosses). The radar-based estimates lie within the theoretically predicted regions and, in particular, cluster around the predictions using the drop shapes obtained from the 80 fall experiment. However, to do more thorough analysis, range filtering or smoothing of the DFR needs to be done similar to the differential propagation

phase data. More detailed comparisons will be made in the future, conducted as part of a NSF-funded study on drop shapes.

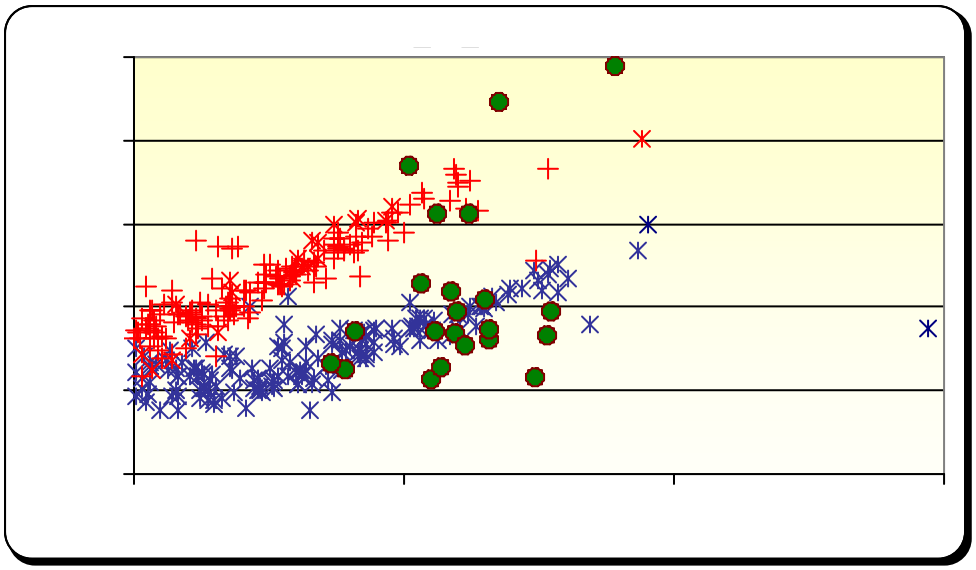

Figure 12.10. Theoretical variations corresponding to Eq. (1) using 1-minute DSDs from the 2DVD and using 2 different drop shape models (red and blue), compared with variation derived from CP2 S and X band data (green).

12.1.7 Zdr and vertically pointing data

Accurate hardware calibration is requisite for estimating rainfall and retrieving microphysical information with polarimetric radar. Of particular importance is the elimination of Z_{DR} bias. [A 0.1 dB bias creates a rain rate estimate bias of nearly 10%.] Radar calibration can be verified by: 1) pointing the radar antenna vertically during light precipitation, 2) examining the consistency among polarimetric variables (Z_H, Z_{DR}, and K_{DP}), 3) examining the consistency among polarimetric rainfall estimators, and 4) by comparing calculations of Z_H and Z_{DR} using disdrometer observations with radar measurements.

When viewed from below, raindrops are assumed to have no preferred orientation; and consequently, Z_{DR} should be 0 dB. This result is ensured by rotating the radar antenna through 360º as the data are collected. Vertically pointing data were collected on several days (Table 12.2). Measurements were averaged at each range location. The analysis is restricted to range locations less than 4 km above ground and measurements with $\rho_{HV} \geq$ 0.968. The table shows the number of profiles examined and estimates of the mean Z_{DR}. Biases that range from −0.15 to −0.37 are indicated. Bias time histories for the two days with numerous profiles are presented in Figure 12.11. The large temporal variations on 26 March are particularly disturbing. These results are preliminary; but clearly, they suggest that the measured Z_{DR} is too low.

The rain rate estimators have not yet been tested with rain gauge measurements. However, an alternate evaluation can be performed by comparing rain rates from the individual estimators. Brandes et al. (2002) show that, with a well-calibrated radar, long-term bias factors

for a suite of tuned polarimetric rainfall estimators converge to 1.0. Moreover, depending on which rain rate estimators may be high or low with respect to the others, it is possible to determine whether the problem lies with Z_H or Z_{DR}.

An alternate approach is to use the radar-measured Z_H and Z_{DR} values to estimate K_{DP}, and then compare the estimate to the radar-measured K_{DP}. A needed relation, developed from disdrometer observations, is

$$K_{DP} = 5.61 \times 10^{-5} Z_H^{0.927} Z_{DR}^{-1.48} \quad . \qquad \textbf{(14)}$$

This procedure readily detects problems, but does not necessarily isolate the problem as lying with Z_H or Z_{DR}. Tests with the two consistency methods and the direct comparison of disdrometer-calculated and radar-measured are Z_H and Z_{DR} are underway.

Table 12.2. Summary of raw (unadjusted) CP2 vertical pointing data. Only data points below 4 km height and with a correlation coefficient $\rho_{HV} \geq$ 0.968 are used in the analysis.

Date	Number of profiles	Estimated Z_{DR} bias (dB)
30 January 2008	2	−0.28
4 February 2008	1	−0.15
12 February 2008	3	−0.37
26 February 2008	11	−0.35
26 March 2008	18	−0.24

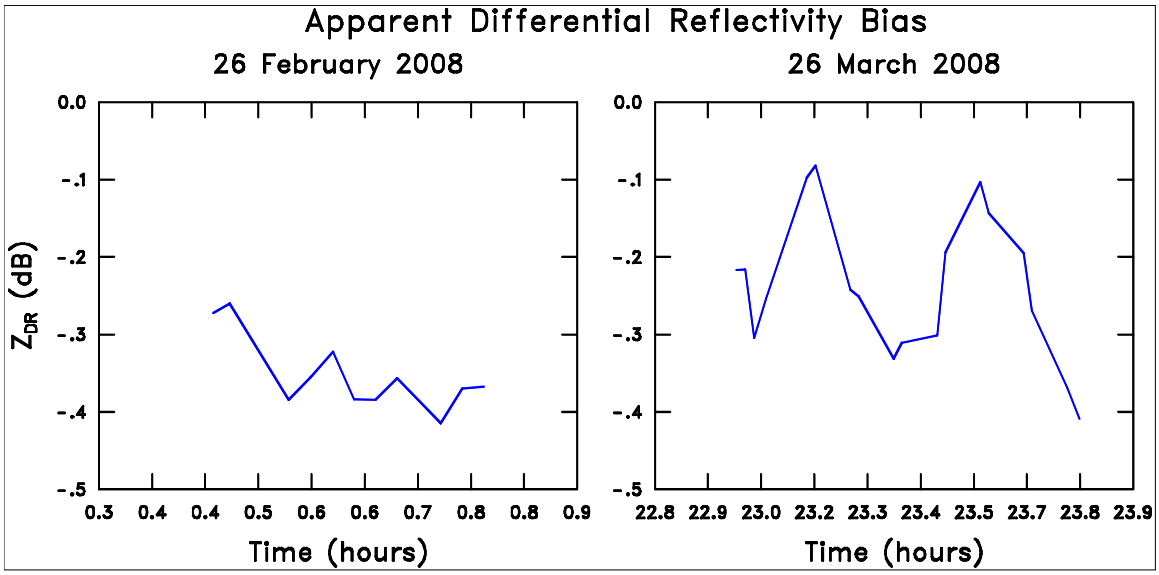

Figure 12.11. Mean Z_{DR} values computed from CP2 vertical pointing data.

12.1.8 LDR and vertically pointing data

Figure 12.12 shows one beam of vertical pointing data in light rain with distinct bright band at 3.7 km height. The LDR values are consistent with low values in rain below the bright band (close to -30 dB) with -16 dB at the peak of the BB. This implies that the cross-polarization channel is working as per expectations. The LDR system limit can be inferred to be close to -30 dB, which is the 'best' that the CP2 has ever achieved. Note that no LDR system offset has been applied to the data. Such an offset can occur because of differential gain between the 2 receivers or different waveguide losses from the 2 antenna ports to the input of the 2 receivers. Solar flux, being randomly polarized can be used to determine the LDR system offset provided the received solar power at X-band is around 5-10 dB above the noise floor. It is not clear if this is the case for the CP2 X-band system.

Figure 12.13 shows the average and standard deviation of LDR over 100 'similar' vertically pointing beams. It clearly illustrates the standard deviation of LDR as well as confirming the system limit of -30 dB in light rain. It also shows the peak of LDR at the BB and, also, the increase in the variance of LDR at the BB.

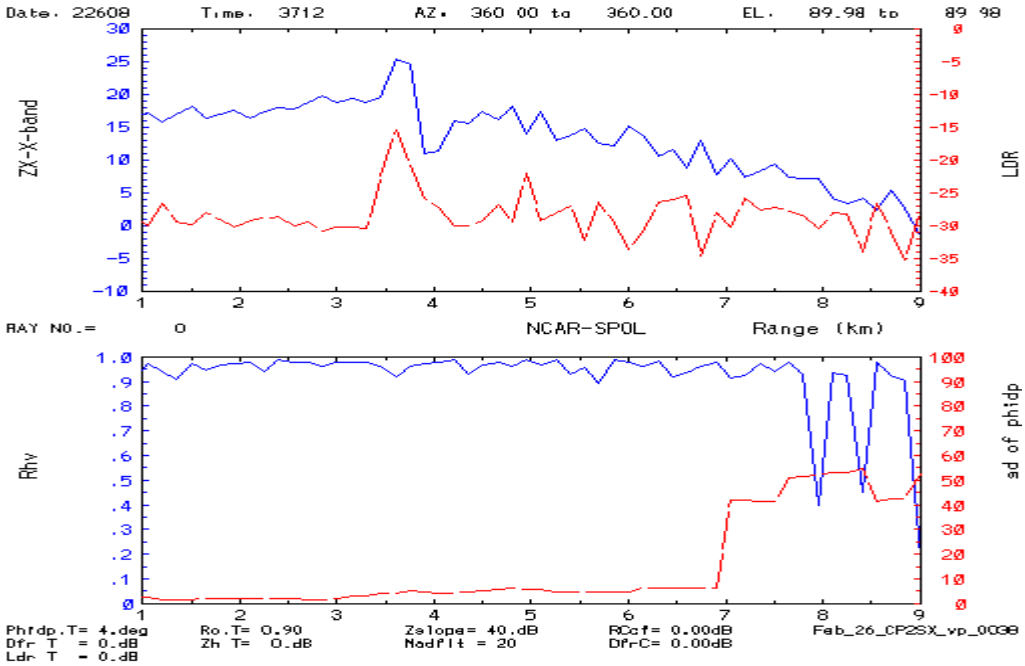

Figure 12.12. One beam of vertical pointing data with range representing the height above the radar. Top panel shows X-band Z (blue line) and X-band LDR (red line) clearly indicating the bright band at 3.7 km. Bottom panel shows ρ_{hv} (blue) and standard deviation of Φ_{dp} (over 10 gates).

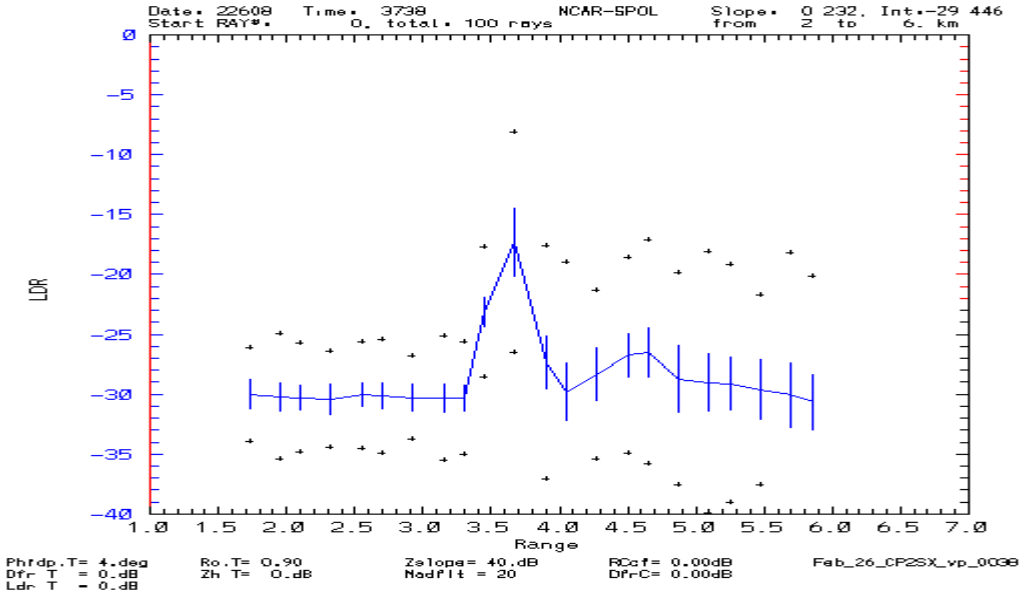

Figure 12.13. Averaged vertical pointing data (average over 100 beams: Figure 12.12 shows one example beam). It clearly shows the LDR bright band at 3.7 km and the system limit being reached in rain below the BB reaching -30 dB in light rain. The vertical bars are the estimated standard deviation (±1sigma bars) for LDR which is ± 1 dB as expected). The 'crosses' show extreme values in the 'bin' (range interval of 200 m).

The remaining figures are related to the S-band channel with Figure 12.14 showing the mean and standard deviation of ρ_{hv}. Note that the mean rhohv in light rain is around 0.97 and decreasing at the BB to around 0.94 and then around 0.96 in the snow region above the BB. These mean values are quite low in light rain and snow aloft which accounts for the large variance in Z_{dr} shown in Figure 12.15. In light rain the standard deviation is around 0.5 dB while in the BB and snow aloft it reaches 1 dB. These Z_{dr} fluctuations are quite high (and related to the rather low ρ_{hv} values in Figure 12.14) and most likely due to ground clutter and the rather poor side lobes of the 1970s era CP2 S-band antenna. The Z_{dr} fluctuations are believed to be a factor of 2 too large as compared with vertically pointing data from, say, SPOL or CHILL radars.

Range/azimuthal smoothing of the Z_{dr} data is a viable solution in the short term (as discussed earlier in Section 3.5.2.2) to reduce the high fluctuations in the 'raw' Z_{dr}. This is demonstrated rather vividly in Figure 12.16 with the standard deviations reducing by more than a factor of two. The FIR filter applied is for 100 m gate spacing and dampens the large gate-to-gate variability at the 150-300 m scale, but at the expense of poorer range resolution (~ retaining 1-2 km scale variability in range). The only long-term solution is an improved antenna of NEXRAD quality (e.g. as used in the Gematronik operational S-band systems).

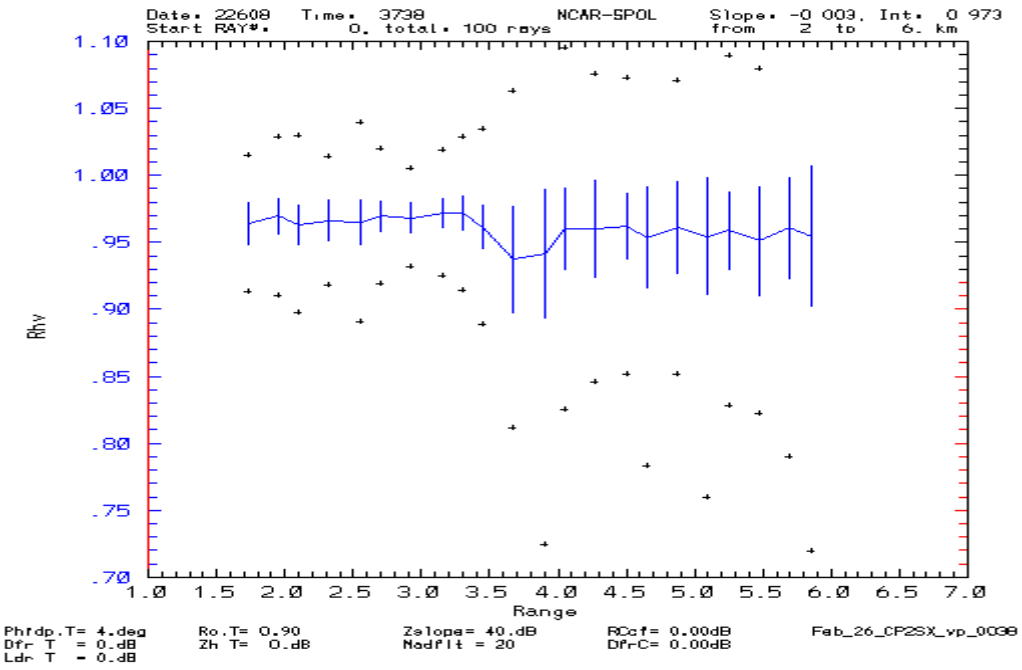

Figure 12.14. Average of ρ_{hv} using 100 beams of vertical pointing data showing the decrease in the BB.

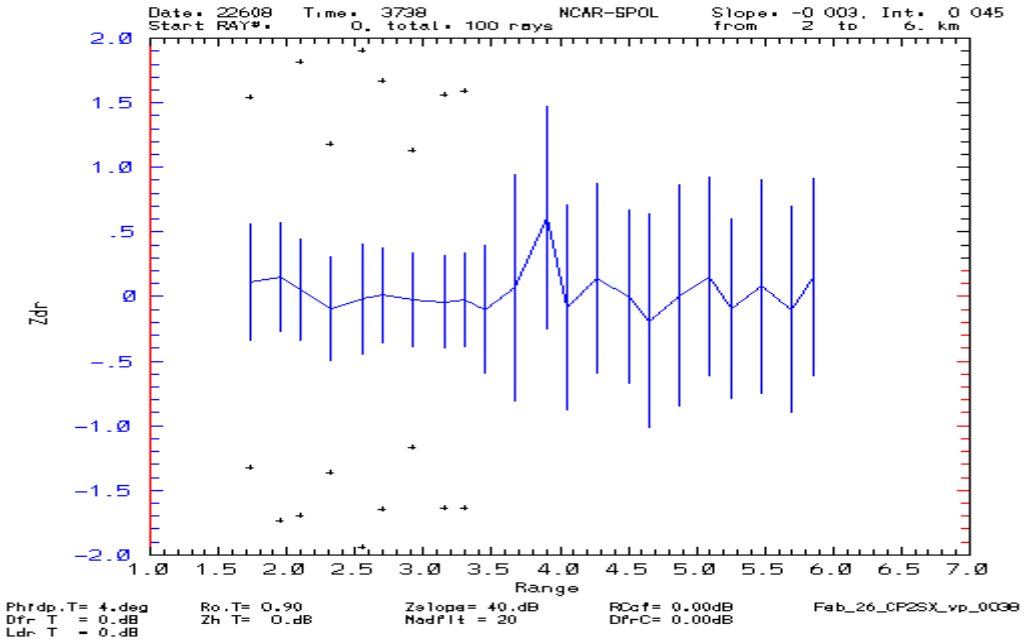

Figure 12.15. As in Figure 12.13 except showing the average and variance of Z_{dr} using 100 vertically pointing beams in light rain.

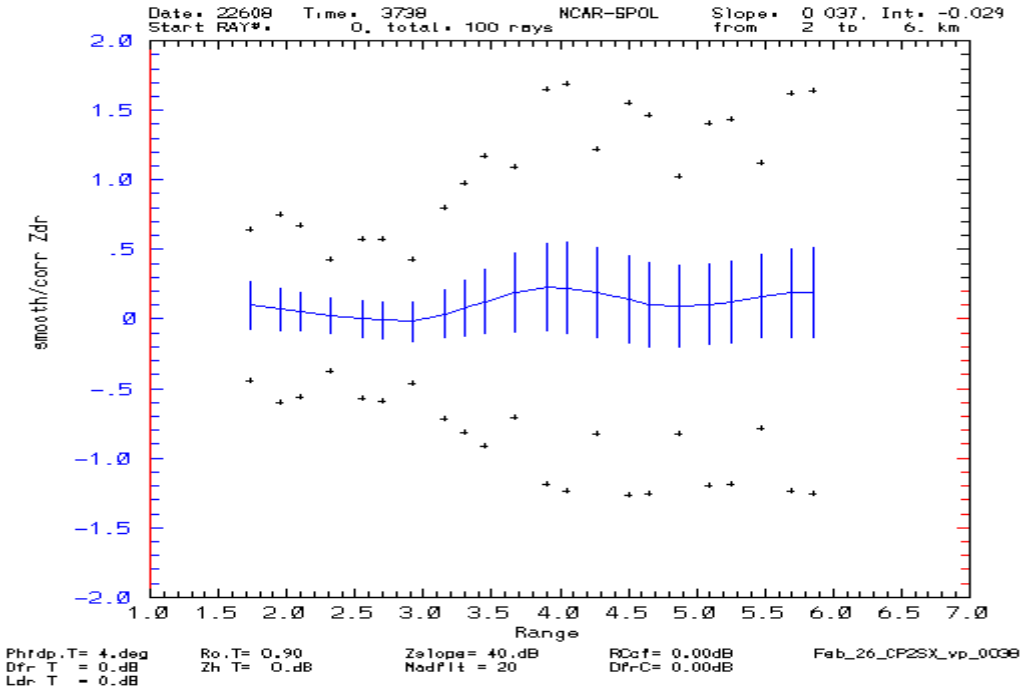

Figure 12.16. As in Figure 12.13 except mean and standard deviation of Z_{dr} after FIR smoothing is applied for the same 100 beams of vertically pointing data.

12.2 BACKGROUND MATERIAL

12.2.1 Impacts of aerosol and trace gases on precipitation

The atmosphere is made up of a combination of gaseous constituents and aerosol particles. Gases such as N_2, O_2, Ar, He, Ne, Kr, and Xe are present in the atmosphere in quasi-constant proportions up to about 85 km. Other gases such as, CH_4, O_3, N_2O, CO, CO_2, and H_2 vary slowly in the atmosphere, while gases such as SO_2, H_2S, NO, NO_2, and NH_3 vary rapidly in time and space due to their highly reactive nature. These gases all have sources and sinks that determine their local and regional concentrations in the atmosphere (Pruppacher and Klett, 1998; Warneck, 1988). Investigations of trace gases and their associated aerosols in the atmosphere are important for two reasons: 1) their influence on climate and clouds, and 2) their health and environmental impacts. Our focus here is their effect on clouds because aerosol particles affect the radiative properties and precipitation efficiency of clouds. The background pollution levels will also impact the efficiency of rainfall enhancement via cloud seeding with hygroscopic or glaciogenic flares.

Aerosol particles are injected into the atmosphere from either natural or anthropogenic sources. Aerosols also form in the atmosphere through gas-to-particle conversion. Dry aerosol particles can be classified into three size categories, nucleation or Aitken mode particles (radii < 0.1 μm), large or accumulation mode particles (0.1 < radii < 1.0 μm) and giant particles (radii > 1.0 μm) (Pruppacher and Klett, 1998). Atmospheric aerosols are significant in regional pollution and global radiative forcing. Potential radiative forcing and the efficiency of clouds to develop precipitation are complex functions of the size, chemical composition and other physical properties of aerosols. Within the climate change debate, the perturbing effects of forcing due to anthropogenic aerosols are of particular concern (Shine *et al.*, 1990). Penner *et al.* (1994) subdivided anthropogenic aerosols into four types and gave their main source and respective forcing mechanisms (see Table 12.3).

The effects of aerosols as agents of significant climatic perturbations have received increasing attention over the past decade (Charlson, 1990; Penner et al. 1992). Penner et al. (1994) estimated that the combined effects of anthropogenic and biomass burning aerosol emissions may cause a clear sky climatic forcing which is nearly equal in magnitude but opposite in sign (i.e., cooling) to the predicted greenhouse gas warming phenomenon. In addition, aerosols can also change the thermodynamic structure of the atmosphere and therefore atmospheric stability and associated cloud development.

Aerosols are thought to affect climate in two ways: directly through the scattering of incoming solar radiation and indirectly through changes to cloud microphysical processes. Carbonaceous aerosols also absorb solar radiation and re-radiate it as heat. This process has the potential of changing the vertical thermodynamic structure of the atmosphere. The absorption properties of aerosols are linked to the characteristics of the underlying surface. Absorption of solar radiation is more likely to occur above those surfaces with highly reflective properties, such as clouds and snow. Twomey (1977) estimated that underlying surfaces with an albedo of around 0.75 or more cause significant absorption by aerosols.

Table 12.3. Key anthropogenic aerosol types, their main sources and the possible climateforcing resulting from their presence in the atmosphere (Penner et al., 1994).

Anthropogenic aerosol type	Main sources	Forcing mechanisms
Water-soluble inorganic species – especially sulphate	Industrial fossil fuel burning, domestic fuel usage and transportation	a) Direct clear sky backscattering of solar radiation b) Indirect effect of CCN on cloud albedo c) Indirect effect of CCN on cloud lifetime
Elemental or black carbon	Industrial fossil fuel burning, domestic fuel usage, transportation and biomass burning	a, b and c
Organic species	Industrial fossil fuel burning, domestic fuel usage and transportation	d) Absorption of solar radiation
Mineral dust	Enhanced airborne mobility of soil due to land degradation	a, b, c, d and e) absorption and emission of terrestrial radiation

The indirect forcing of climate through cloud processes is complex and not well known. An increase in the total number concentration of particles in the accumulation mode at a given liquid water content, results in a decrease in the mean droplet radius in the cloud and a corresponding increase in the cloud albedo. Charlson et al. (1992) calculated that a 30% increase in the cloud droplet number would result in a 0.02 increase in the planetary albedo and a subsequent decrease in the mean surface temperature of approximately 1.3°C. In addition, the smaller cloud droplets will have the effect of a less efficient precipitation process in clouds.

Aerosols can decrease precipitation efficiency of clouds by inhibiting the warm-cloud coalescence mechanism (cloud droplet collisions), thus increasing cloud liquid water content and fractional cloud cover. This effect influences mainly low-level clouds where scattering of incoming solar radiation is expected to dominate over the potential of absorbing long wave radiation from the ground, resulting in a net cooling. An increase of 4% low cloud cover will increase the global albedo by 0.02 (Albrecht, 1989).

Other influences of increased aerosol concentrations are modifications of water and heat distribution in the atmosphere and thus the hydrological cycle as a whole. Water vapor is an important greenhouse gas, which if changed will have significant climatic implications. Indirect effects of aerosols on climate are complicated and associated with great uncertainties. At present, a concerted effort is directed to reducing these uncertainties by making in-situ measurements of aerosols and CCN concentrations and size distributions to determine their effects on clouds, rainfall efficiencies and planetary albedo (Albrecht, 1989; Hudson, 1991; Mather et al., 1997; Menon and Saxena, 1998; Terblanche et al., 2000). These effects are also being simulated in general circulation models to better understand their impacts and the uncertainties associated with current understanding. Boucher et al. (1995), for example, introduced cloud microphysical processes into a general circulation model to investigate the sensitivity of the model to cloud

droplet concentrations. They found that a fourfold increase in cloud droplet concentrations would lead to a 10% increase in the amount of cloud water stored in the atmosphere at any given time. This result is caused by a reduction in mean cloud droplet size and thus an inability of droplets to reach the threshold size at which they will precipitate. The model predicted a resulting 56.4% increase in global cloud cover that in turn resulted in a 14.4 Wm^{-2} global short-wave cloud radiative forcing change. At the same time, in this particular model, the amount of precipitation did not change significantly due to these alterations in cloud microphysics. Different categories of aerosols affect clouds in different ways.

12.2.2 Water-Soluble or Hygroscopic Particles in the Atmosphere

Water-soluble aerosol particles in the atmosphere consist mostly of sulfate derived from natural and anthropogenic sources. Anthropogenic sulfate in the atmosphere is produced mostly through gas-to-particle conversion of SO_2 emitted from fossil fuel combustion and metal smelting (Charlson et al., 1992). Sulfate and its associated cations occur in the atmosphere in the accumulation mode with a peak frequency of occurrence between 0.2 and 0.4 μm aerodynamic diameter (Warneck, 1988; Jaenicke, 1998). Determining SO_2 emissions in a specific region is important in understanding their impacts on clouds through their CCN activity and subsequently their formation of droplets and precipitation.

Sulfates have the greatest potential to contribute to global aerosol forcing due to the fact that sulfate aerosols are smaller than dust and sea salt aerosols and thus have a longer lifetime in the atmosphere (tens of days). Furthermore, the optical-scattering efficiencies of sulfates are an order of magnitude greater than those of dust. Lastly, sulfates are hygroscopic and therefore have twice the optical scattering per unit mass concentration as dry particles (White, 1990; Charlson et al., 1992).

12.2.3 Effects of mineral or desert dust on climate and precipitation

Emissions of crustal aeolian dust material, often termed “mineral dust”, are caused primarily by surface winds acting on dry soils where vegetation cover is or has become sparse (Tegen and Fung, 1995). The term “mineral dust” refers to a large range of species that are highly variable in their chemical composition and include such diverse compounds as quartz, clay, calcite, gypsum, hematite and others. Climate effects due to mineral dust are complex and diverse, ranging from heating of the atmosphere in some parts of the world to a net cooling in other parts. Presence of dust alters surface radiation budgets, which in turn, affects surface temperatures, surface-air exchange processes, thermodynamic structure and hence atmospheric dynamics (Tegen and Fung, 1995; Sokolik, 1999).

The complexity of the radiative effects of mineral dust on climate is determined by the uneven distribution of sources and sinks and the relatively short atmospheric life time of mineral dust (up to a few weeks) which lead to a complex spatial and temporal pattern (Guerzoni and Chester, 1996; Sokolik, 1999). In addition, when mineral dust exists in conjunction with other pollutants such as sulfates, the dust particles can be coated with the sulfate and become more active as CCN. This is especially important in desert regions where both sources exist and have a likely impact on the precipitation processes in clouds. In some instances, the coated dust particles

could enhance the precipitation efficiency of clouds, while in others they may have a negative impact.

12.2.4 Effects of organic nuclei on clouds and precipitation

Recent research has suggested an important role for organic aerosols as CCN (Cruz and Pandis, 1998; Facchini et al., 1999; Liu et al., 1996; Rivera-Carpio eta al., 1996; Shantz et al., 2003; Raymond and Pandis, 2002). Organic compounds either in mixed or free state, are a major source of atmospheric aerosol particles (Novakov et al., 1993). Novakov et al. (1993) calculated that approximately 65% of the CCN concentrations measured at 0.5% supersaturation in the marine atmosphere were due to organic aerosols. Cruz and Pandis (1997) implied that two hydrophilic compounds can be good CCN, while hydrophobic compounds are not good CCN. Raymond and Pandis (2002) showed how secondary organic aerosols with low carbon numbers and various functional groups are an excellent source of CCN, whereas longer carbon chains with fewer functional groups tend to be inactive under typical atmospheric conditions. Organic compounds in the atmosphere are very important; however, uncertainty about the chemical speciation and the solubility of the large organic component precludes a rigorous analysis of its contribution to nucleation activity. Recent studies in the Amazon have indicated that forests may be an important natural source of organic nuclei and this could be important for the forested regions of Southeast Queensland as well.

12.2.5 Background on precipitation development in clouds

Weather modification research requires the involvement of a wide range of expertise due to the multifaceted nature of the problem and the large range of scales that are addressed. Large-scale and mesoscale dynamics, which determine the characteristics of cloud systems, and small-scale microphysics, which determine the nucleation and growth characteristics of water droplets and ice particles, form part of the chain-of-events leading to precipitation development (Figure 12.17). Although our knowledge of the individual aspects in the chain has significantly increased in the past twenty years, there are still major knowledge gaps.

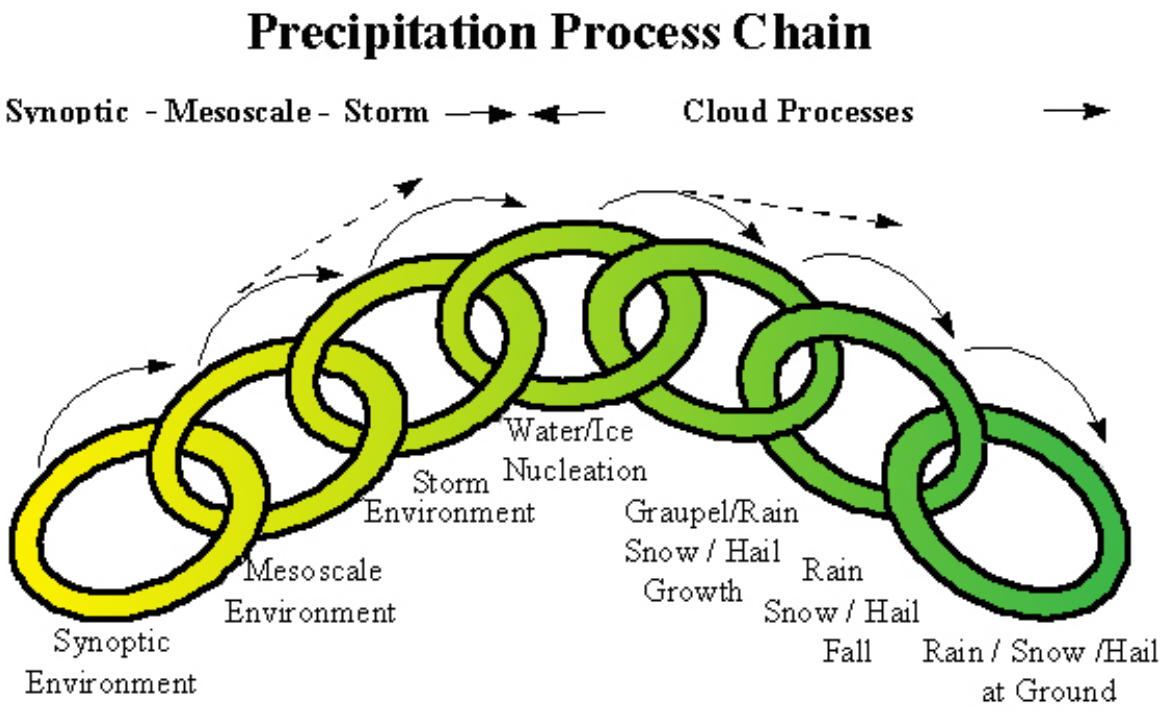

Figure 12.17. The "Precipitation Process Chain", illustrating the sequence of events, not necessarily independent, that leads to precipitation at the ground. Processes within each "link" or event often occur on different spatial and temporal scales.

Precipitation initiation and development can proceed via several physical paths (Figure 12.18). These involve various microphysical processes, which proceed simultaneously, but at different rates, resulting in one path becoming dominant because of its greater efficiency under given atmospheric conditions. The efficiency with which clouds produce rain at the surface varies greatly. Precipitation efficiency, defined as the ratio of the rate of rain reaching the ground to the flux of water vapor passing through cloud base (Marwitz, 1972), can range from zero in non-precipitating clouds to greater than unity for short times in very intense, convective systems (Cotton and Anthes, 1989). Some of the earliest studies showed that ordinary thunderstorms transform less than 20% of the in-flux of water vapor into rain on the ground (Braham, 1952). The principles of most, if not all, precipitation enhancement hypotheses are rooted in these efficiency factors, which in general, seek to improve the effectiveness of the precipitation evolution path. The seeding conceptual model (physical hypothesis) describes how this is accomplished by the seeding intervention, and specifically how the initiation and development of precipitation in seeded clouds differs from that in unseeded clouds and ultimately affects the dynamics of the cloud.

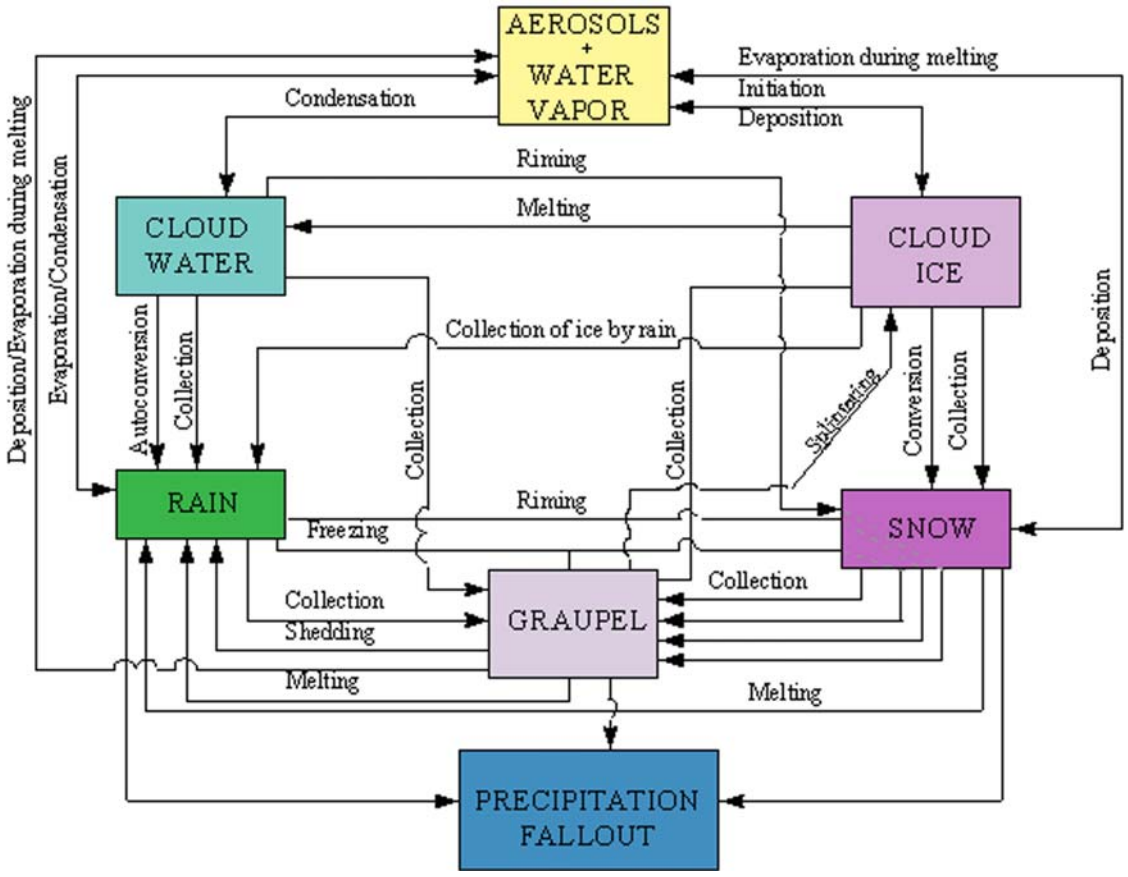

Figure 12.18. Various pathways by which water vapor is transformed into various types of cloud particles and precipitation. Adapted from Houze (1993, p. 96).

Precipitation formation mechanisms can differ dramatically from one location to another, and even at one location, depending on the meteorological setting. Precipitation growth can either take place through coalescence or the ice process or a combination of the two (Figure 12.18). In clouds with tops warmer than 0^{o} C, precipitation can develop only by means of the coalescence process. Clouds are further categorized as either continental or maritime, which describes their degree of colloidal instability. However, when cloud tops reach temperatures colder than 0^{o} C, ice may develop and precipitation can form through a different set of paths, as is depicted in Figure 12.18.

The number concentration and size spectrum of cloud droplets will influence the cloud's precipitation efficiency and can also vary dramatically, depending on the CCN size distribution. A maritime droplet spectrum will consist of fewer particles but more large drops than in a continental spectrum (Pruppacher and Klett, 1998) leading to a more efficient precipitation process. The vertical depth of the cloud also impacts how efficient it is at precipitation production (Cotton and Anthes, 1989). The deeper the cloud, the more likely precipitation will form. One way of inferring the depth of the cloud is to look at the horizontal scale of the convective core, defined by an elevated region of liquid water content and associated with the peak vertical velocities in the cloud. Generally, a cloud with an adiabatic core greater than 2 km is likely to form precipitation, with the likelihood increasing as the maximum liquid water

content increases. Another generality stated in Cotton and Anthes (1989) is that unless a cloud produces liquid water contents of 0.5 g m^{-3}, it is unlikely to precipitate.

12.2.6 Background on cloud seeding studies

Atmospheric water in the form of precipitation is one of the primary sources of fresh water in the world. However, a large amount of water present in clouds is never transformed into precipitation on the ground. This has prompted scientists and engineers to explore the possibility of augmenting water supplies by means of artificial cloud seeding. Although some projects have successfully documented increases in rainfall due to seeding, others have shown a decrease while the majority of projects indicated inconclusive results. The reason for this is that physical mechanisms of cloud and precipitation development in the atmosphere are much more complex than earlier anticipated, thus the initial optimism in the 1950's and 1960's has given way to a more cautious approach.

The early experiments treated the physical chain of events from seeding to rain at the surface as a "black box" (i.e., one does not attempt to learn what is happening in the "box"). However, in the late 1970's and 1980's scientists have turned to a physical approach that incorporates observations, modeling, and laboratory studies, to track the physical chain of events and the effects of seeding from formation of a cloud to precipitation at the surface.

In physical experiments such as those in the Cascade Mountains in Washington and to a lesser extent in Israel during the early 1970's, and in the 1980's and early 1990's, the High Plains Experiment, the Sierra Cooperative Pilot Project, and the Arizona Program, the aim was to test the fundamental cause-and-effect relations in the physical chain of events of cloud and precipitation development. Most past field and modeling studies concentrated on the links in the physical chain of events from the nucleation source to precipitation at cloud base and subsequently at the surface. However, to a large extent the forces (large scale and cloud dynamics) that determined the cloud formation were not taken into account. The existence and development of clouds largely depends on factors such as synoptic-scale disturbances, which determine the stability and moisture content of the air in which the clouds form, and mesoscale effects, such as orography and differential heating at the surface, which are primary forcing mechanisms in cloud development. Mesoscale convergence and divergence and interactions between clouds are also important.

Weather modification research requires the involvement of a wide range of expertise due to the multifaceted nature of the problem and the large range of scales that are addressed. The chain of events in precipitation development ranges from at least the mesoscale dynamics determining the characteristics of the cloud systems down to small-scale microphysics determining the nucleation and growth characteristics of water droplets and ice particles (e.g., see Pruppacher and Klett, 1998; Braham, 1979, 1986; Dennis, 1980; Rogers, 1976). Our knowledge of the individual steps in this chain has increased significantly in the past 20 years, but major gaps still exist in our understanding of certain physical processes (Bruintjes, 1999). Although most rainfall enhancement experiments focus on modifying the microphysical aspects of clouds, it is important to emphasize that cloud microphysical and dynamical processes are intimately linked, and that the major controls on precipitation occurrence and amounts are the mesoscale and synoptic-scale atmospheric dynamics (e.g., see Cotton and Anthes, 1989; Vali et al., 1988). At present, however, no theoretical framework or experimental methodology exists that could support any intentional modification of the atmosphere on these larger scales.

Precipitation enhancement from mixed-phase clouds (i.e., clouds or parts of the clouds containing temperatures below 0°C) has been the focus of most weather modification research

and operations around the world. The microphysics and dynamics of these cloud systems are complex and, especially in the case of convective storms, are characterized by large natural variability. Establishing cause-and-effect relationships through the complete chain of events leading to precipitation formation is extremely challenging. Glaciogenic seeding material is the most common seeding material used for precipitation enhancement. Hygroscopic seeding material, such as salt powders, has also been used, but its early applications generally proved to be less effective than glaciogenic seeding material. During the past decade, however, tests have been conducted on mixed-phase convective clouds using small (sub-micron to tens of microns in diameter) hygroscopic particles released by pyrotechnic flares with somewhat different results. The results of glaciogenic and hygroscopic precipitation enhancement techniques are distilled in the following sections.

12.2.7 Glaciogenic Seeding Experiments

Based on the quantity of glaciogenic seeding material used to enhance ice content, two seeding concepts have historically been proposed and widely referred to as "static" and "dynamic" seeding. In the static seeding concept the aim is to capitalize on the less-than-optimal ice crystal concentrations often present in nature that lead to prolonged periods of supercooled water, especially in orographic clouds. These regions of supercooled water have to exist for a sufficient length of time for ice crystal growth and precipitation to occur. In the dynamic seeding concept the emphasis is on the release of latent heat by rapid freezing, which enhances buoyancy and invigorates cloud growth, thereby increasing precipitation production. It should be noted that these concepts are not mutually exclusive because they both result in increased ice crystal concentrations and affect cloud dynamics. The same seeding material is used in both seeding concepts only the quantity of seeding material is varied. While the dynamic seeding concept primarily applies to convective clouds, the static seeding concept has been widely utilized in orographic and layer-type clouds as well as in convective clouds. In convective clouds, both "static" and "dynamic" responses can occur in a mutually interactive fashion (Rosenfeld and Woodley, 1993).

Static Seeding: Convective Clouds

The top half of Table 12.4 lists examples of static glaciogenic seeding experiments designed to test whether precipitation can be increased in convective clouds in response to seeding with ice nucleating agents. For static seeding of convective clouds, statistically significant rainfall increases were not obtained or, in the case of the Israeli experiments, continue to be debated (Gabriel and Rosenfeld, 1990; Rosenfeld and Farbstein, 1992; Rangno and Hobbs, 1995; Rosenfeld and Nirel, 1996; Levi and Rosenfeld, 1996).

In each case, however, important results or guidance was obtained which contributes to the current knowledge base in weather modification. Among these results are:

- that physical measurements in clouds are essential to provide an understanding of the underlying processes;
- that high concentrations of ice crystals occur naturally in some cumulus clouds at temperatures as warm as –10 °C thus allowing rapid production of precipitation particles;
- that the window of opportunity for enhancing rainfall from a given cloud (system) is limited;
- that treatment can both enhance and reduce rainfall; and
- that results based on small clouds might not be transferable to dynamically more vigorous and larger cloud complexes.

Table 12.4. Examples of static glaciogenic seeding experiments in precipitation enhancement

Type of cloud	Experiment	Reference
Convective clouds	Arizona projects	Battan and Kassander, 1967
	Israeli experiments	Gagin and Newmann, 1974
	Project Whitetop	Braham, 1964, 1979
	High Plains Experiment (HIPLEX) 1	Smith et al., 1984
	Puglia experiment	List et al., 2000
Winter orographic clouds	Lake Almanor experiment	Mooney and Lunn, 1969
	Sierra Cooperative Pilot Project (SCPP)	Reynolds and Dennis, 1986; Deshler et al., 1990; SCPP, 1982
	Climax I and II	Grant and Mielke, 1967; Mielke et al., 1981
	Bridger Range experiment	Super and Heimbach, 1983; Super, 1986
	Tasmanian experiments	Ryan and King, 1997

Static Seeding: Winter Orographic Clouds

In the case of static seeding of winter orographic clouds (bottom of Table 12.4), important results include:

- recognition of the complex interactions between terrain and wind flow in determining regions of cloud liquid water and, later, through microwave radiometer measurements, the existence of a layer of supercooled water;
- acknowledgment of the need to target and track the dispersion of seeding material and the demonstration that complex flows including ridge-parallel flows below the ridge crest exist in pronounced terrain;
- evidence of marked increases in ice particle concentrations leading to increased precipitation depending upon the availability of supercooled liquid water;
- re-emphasis of the need for physical data that can be used together with numerical models to identify the spatial and temporal changes in cloud structure;
- development of highly efficient silver chloro-iodide ice nuclei and other fast acting, highly efficient ice nucleating pyrotechnic and generator devices; and
- development of methods to detect traces of seeding agents in snowpack and rain water.

Dynamic Seeding

Table 12.5 lists four examples in which glaciogenic seeding was used in the expectation that an increase in cloud buoyancy would follow freezing of supercooled water drops. The intent was to seed supercooled clouds with large enough quantities of ice nuclei (100–1000 cm^{-3}) or coolant to cause rapid glaciation. Increased buoyancy was expected to cause the cloud to grow larger, ingest more water vapor, and yield more precipitation. It was postulated that increased precipitation would enhance downdrafts and outflows which, in turn, would initiate new convection and extend the effects of treatment (Woodley et al., 1982). Few of the hypothesized steps in the chain of events have been measured in experiments or validated by numerical models (Orville, 1996). However, as in the case of static seeding, dynamic seeding has contributed significantly to our current store of knowledge. Among the findings and results from dynamic seeding experiments that contribute to the current state of knowledge in weather modification are:

- the complexities of ice formation in clouds where ice and supercooled water have been found at temperatures as high as –10°C and as low as –38°C, respectively (Rosenfeld and Woodley, 2000);
- the dependence of ice formation upon CCN concentrations and sizes (e.g., freezing of large drops) and the role of primary and secondary ice formation in graupel production which have emerged from these experiments are areas of uncertainty;
- the importance of coalescence (and hence aerosols) on cloud structure, evolution and rain production (Rosenfeld and Woodley, 1993; Johnson, 1987);
- the importance and relationship between cloud dynamics and microphysics and the induced changes resulting from seeding; and
- the power and limitations of existing radar systems as integral experimental tools and as possible means of verification of seeding results.

Table 12.5. Examples of Dynamic Glaciogenic Seeding Experiments in Precipitation Enhancement.

Experiment	Reference
Florida Area Cumulus Experiments (FACE) 1 and 2	Woodley et al., 1982; Woodley et al., 1983; Gagin et al., 1986
Texas experiments	Rosenfeld and Woodley, 1993
South African experiments	Bruintjes et al., 1987; Krauss et al., 1987
Thailand experiments	Woodley et al., 1999

12.2.8 Hygroscopic seeding experiments: convective mixed-phase clouds

Hygroscopic seeding, as opposed to glaciogenic seeding, is directed at promoting the coalescence of water droplets in the cloud. The intention is to promote particle growth through coalescence and thereby improve the efficiency of the rainfall formation process. Appropriately sized salt particles, water droplets from sprays of either water or saline solution (Bowen, 1952; Biswas and Dennis, 1971; Cotton, 1982; Murty et al., 2000; Silverman and Sukarnjanasat, 2000),

and hygroscopic flares (Mather et al., 1997; WMO, 2000) have been used. Statistical results, observations and modeling results for large (>10 μm diameter) have provided some statistical evidence (Murty et al., 2000; Silverman and Sukarnjanasat, 2000) and evidence that under certain conditions with optimal seed drop size spectrums, precipitation can be enhanced (Farley and Chen, 1975; Rokicki and Young, 1978; Young, 1996). The hygroscopic flare particle seeding experiments have provided statistical support for rainfall increases due to seeding based on single cloud analyses, but the physical processes leading to these increases in precipitation are not well understood. Despite the wide use of hygroscopic seeding, the results have been inconclusive due to a lack of physical understanding and, in some cases, inconclusive statistical evaluations.

Table 12.6 lists examples of field experiments or operations in which hygroscopic seeding was employed. Among the results from these programs that have contributed to the current state of knowledge in weather modification are that:

- Both the South African and Mexican experiments produced remarkably similar statistical results in terms of the differences in radar estimated rainfall for seeded versus non-seeded groups (Bigg, 1997; Silverman, 2000; WMO, 2000);
- In the South African and Mexican experiments, reevaluation of the results showed an increase in rain mass 30–60 minutes after seeding, significant at the 96 percent level ($\alpha = 0.04$) or higher;
- Marked differences in concentrations of ice particles were found in maritime clouds (high) versus continental clouds (low) signifying the active role of collision and coalescence in maritime clouds compared to continental clouds (Scott and Hobbs, 1977; Cotton, 1972; Koenig and Murray, 1976);
- Freezing temperatures increased with increasing drop size because larger droplets contain or have a higher probability of colliding with ice nuclei;
- Relatively large droplets (>24 μm) played a role in ice multiplication processes, including mechanical fracturing during melting and evaporation and ice splinter formation during riming (Hallet and Mossop, 1974);
- Delayed response in radar-derived storm properties was a possible function of seeding-induced dynamic processes beyond the classical cloud physics results that links cloud condensation nuclei and droplet spectra to rain production (WMO, 2000); and
- Hygroscopic seeding might overcome inhibiting effects on rainfall of air pollution (Rosenfeld et al., 2002).

Table 12.6. Examples of Hygroscopic Seeding Experiments in Precipitation Enhancement

Experiment	Reference
South African experiments	Mather et al., 1997
Indian experiments	Murty et al., 2000
Thailand experiments	Silverman and Sukarnjanasat, 2000
Mexico experiments	WMO, 2000

12.2.9 Recent advances in cloud seeding

Our knowledge of cloud physics and statistics and its application to weather modification has increased substantially since the first cloud was seeded in 1946. Technology development (e.g. aircraft platforms with a variety of measuring systems, mesoscale and rain gauge network stations and remote sensing techniques from both space and the ground) has introduced a new dimension in our ability to describe the structure and evolution of cloud systems.

The last 10 to 15 years have seen significant progress in the development of new instruments to probe the atmosphere and cloud systems. Microwave radiometers, multi-parameter radars, and lidars make it possible to quantify seeding responses that previously could not be measured. In addition, these new remote sensors are capable of obtaining measurements at higher resolution in both time and space than earlier instruments. With improved airborne instrumentation it is possible to document the physical processes in clouds in much more detail than a decade or more ago.

Substantial work has also been conducted in the past ten years regarding the dispersion and transport of seeding material in both convective and orographic clouds. The use of tracer material to tag a seeded region has been particularly helpful in increasing the understanding of dispersion and transport of seeding material. The two tracer materials that are used most often are chaff and sulfer-hexafluoride (SF_6). Both materials can be released from an aircraft or at the surface. The dispersion and transport of the chaff is monitored by radar while the detection of the SF_6 is usually conducted with aircraft equipped to detect this gas at very low concentrations.

Equally important are the advances in computer systems that are now able to handle very large amounts of data at high speeds, making it possible to use increasingly sophisticated and detailed numerical models. In the past, weather modification experiments incorporating modeling efforts were primarily dependent on simple one- and two-dimensional models to help understand atmospheric processes and to give guidance during field experiments. However, three-dimensional, time-dependent numerical models are now used in the analyses of data from some projects. Field tests to run these large models in an operational mode in the field for weather modification efforts were conducted during recent field programs in Arizona. The preliminary tests were highly successful. These models may be used in the future to guide seeding operations in real time and to help in the analyses of seeding responses.

12.2.10 World Meteorological Organization's summary of weather modification

The World Meteorological Organization (WMO) in its meeting of the Executive Council in 2001 also approved a new statement on the status of weather modification. In this part we will only highlight some of the sections pertaining to rainfall enhancement. In the introduction of the statement some of the major problems and new opportunities in weather modification are highlighted. Amongst others they are:

"…The energy involved in weather systems is so large that it is impossible to artificially create rainstorms or to alter wind patterns to bring water vapour into a region. The most realistic approach to modifying weather is to take advantage of microphysical sensitivities wherein a relatively small human-induced disturbance in the system can substantially alter the natural evolution of atmospheric processes.

The ability to influence cloud microstructures has been demonstrated in the laboratory, simulated in numerical models, and verified through physical measurements in some natural

systems such as fogs, layer clouds and cumulus clouds. However, direct physical evidence that precipitation, hail, lightning, or winds can be significantly modified by artificial means is limited. The complexity and variability of clouds result in great difficulties in understanding and detecting the effects of attempts to modify them artificially. As knowledge of cloud physics and statistics and their application to weather modification has increased, new assessment criteria have evolved for evaluating cloud-seeding experiments. The development of new equipment - such as aircraft platforms with microphysical and air-motion measuring systems, radar (including Doppler and polarization capability), satellites, microwave radiometers, wind profilers, automated raingauge networks, mesoscale network stations - has introduced a new dimension. Equally important are the advances in computer systems that permit large quantities of data to be processed. New data sets, used in conjunction with increasingly sophisticated numerical cloud models, help in testing various weather modification hypotheses. Chemical and chaff tracer studies help to identify airflow in and out of clouds and the source of ice or hygroscopic nucleation as the seeding agent. With some of these new facilities, a better climatology of clouds and precipitation can be prepared to test seeding hypotheses prior to the commencement of weather modification projects.

If one were able to predict precisely the precipitation from a cloud system, it would be a simple matter to detect the effect of artificial cloud seeding on that system. The expected effects of seeding, however, are almost always within the range of natural variability (low signal-to-noise ratio) and our ability to predict the natural behaviour is still limited.

Comparison of precipitation observed during seeded periods with that during historical periods presents problems because of climatic and other changes from one period to another, and therefore is not a reliable technique. This situation has been made even more difficult with the mounting evidence that climate change may lead to changes in global precipitation amounts as well as to spatial redistribution of precipitation.

In currently accepted evaluation practice, randomization methods (target/control, crossover or single area) are considered most reliable for detecting cloud-seeding effects. Such randomized tests require a number of cases readily calculated on the basis of the natural variability of the precipitation and the magnitude of the expected effect. In the case of very low signal-to-noise ratios, experiment durations in the range of five to over ten years may be required. Whenever a statistical evaluation is required to establish that a significant change resulted from a given seeding activity, it must be accompanied by a physical evaluation to:

1. *Confirm that the statistically observed change is likely due to the seeding; and*

2. *Determine the capabilities of the seeding method to produce desired effects under various conditions.*

The effect of natural precipitation variability on the required length of an experiment can be reduced through the employment of physical predictors, which are effective in direct proportion to our understanding of the phenomenon. The search for physical predictors, therefore, holds a high priority in weather modification research. Physical predictors may consist of meteorological parameters (such as stability, wind directions, pressure gradients) or

cloud quantities (such as liquid water content, updraught speeds, concentrations of large drops, ice-crystal concentration or radar reflectivity).

Objective measurement techniques of precipitation quantities are to be preferred for testing weather modification methods. These include both direct ground measurements (e.g. rain gages and hail pads) and remote sensing techniques (e.g. radar, satellite)."

In the section that deals directly with an assessment of rainfall enhancement techniques, there are several important conclusions. It is important to note that although there are many claims to different rainfall enhancement techniques the WMO statement only addresses those techniques that have a scientific basis. The paragraphs that are important for the Southeast Queensland environment with mostly convective type of clouds to consider are:

"..In many regions of the world, cumuliform clouds are the main precipitation producers. These clouds (from small fair weather cumulus to giant thunderclouds) are characterized by strong vertical velocities with high condensation rates. They can hold the largest condensed water contents of all cloud types and can yield the highest precipitation rates. Seeding experiments continue to suggest that precipitation from single-cell and multicell convective clouds have produced variable results. The response variability is not fully understood.

Precipitation enhancement techniques by glaciogenic seeding are utilized to affect ice phase processes while hygroscopic seeding techniques are used to affect warm rain processes. Methods to assess these techniques vary from direct measurements with surface precipitation gauges to indirect radar derived precipitation estimates. Both methods have inherent advantages and disadvantages.

During the last ten years there has been a thorough scrutiny of past experiments using glaciogenic seeding. The responses to seeding seem to vary depending on changes in natural cloud characteristics and in some experiments they appear to be inconsistent with the original seeding hypothesis.

Experiments involving heavy glaciogenic seeding of warm-based convective clouds (bases about +10°C or warmer) have produced mixed results. They were intended to stimulate updraughts through added latent heat release, which, in turn, was postulated to lead to an increase in precipitation. Some experiments have suggested a positive effect on individual convective cells but conclusive evidence that such seeding can increase rainfall from multi-cell convective storms has yet to be established. Many steps in the postulated physical chain of events have not been sufficiently documented with observations or simulated in numerical modelling experiments.

In recent years, the seeding of warm and cold convective clouds with hygroscopic chemicals to augment rainfall by enhancing warm rain processes (condensation/collision-coalescence/break-up mechanisms) has received renewed attention through model simulations and field experiments. Two methods of enhancing the warm rain process have been investigated: first, seeding with small particles (artificial CCN with mean sizes about 0.5 to 1.0 micrometers in diameter) is used to accelerate precipitation initiation by stimulating the

condensation-coalescence process by favourably modifying the initial droplet spectrum at cloud base, and second, seeding with larger hygroscopic particles (artificial precipitation embryos about 30 micrometers in diameter) to accelerate precipitation development by stimulating the collision-coalescence processes. A recent experiment utilizing the latter technique indicated statistical evidence of radar estimated precipitation increases. However, the increases were not as contemplated in the conceptual model but seem to occur at later times (1-4 hours after seeding), the cause of this effect is not known.

Recent randomized seeding experiments with flares that produce small hygroscopic particles in the updraught regions of continental, mixed-phase convective clouds have provided statistical evidence of increases in radar-estimated rainfall. The experiments were conducted in different parts of the world and the important aspect of the results was the replication of the statistical results in a different geographical region. In addition, physical measurements were obtained suggesting that the seeding produced a broader droplet spectrum near cloud base that enhances the formation of large drops early in the lifetime of the cloud. These measurements were supported by numerical modeling studies.

Although the results are encouraging and intriguing, the reasons for the duration of the observed effects obtained with the hygroscopic particle seeding are not understood and some fundamental questions remain. Measurements of the key steps in the chain of physical events associated with hygroscopic particle seeding are needed to confirm the seeding conceptual models and the range of effectiveness of these techniques in increasing precipitation from warm and mixed-phase convective clouds.

Despite the statistical evidence of radar estimated precipitation changes in individual cloud systems in both glaciogenic and hygroscopic techniques, there is no evidence that such seeding can increase rainfall over significant areas economically. There are no evidence of any extra-area effects."

In addition to the above it is also important to consider the economic, social, and environmental aspects of a rainfall enhancement program. The statement also addresses some of these aspects.

"…Weather modification is sometimes considered by countries when there is a need to improve the economy in a particular branch of activity (for example: increase in water supply for agriculture or power generation) or to reduce the risks that may be associated with dangerous events (frosts, fogs, hail, lightning, thunderstorms, etc.). Besides the present uncertainties associated with the capability to reach such goals, it is necessary to consider the impacts on other activities or population groups. Economical, social, ecological and legal aspects should be taken into account. Thus, it is important to consider all the important complexity and recognize the variety of possible impacts, during the design stage of an operation.

Legal aspects may be particularly important when weather modification activities are performed in proximity to borders of different countries. However, any legal system aimed at

promoting or regulating weather modification must recognize that scientific knowledge is still incomplete."

The implications of any projected long-term weather modification operation on ecosystems need to be assessed. Such studies could reveal changes that need to be taken into account. During the operational period, monitoring of possible environmental effects should be undertaken as a check against anticipated impacts.

The statement in summary then concludes:

"…To answer the need for more water and less hail in many regions of the world, some progress has been made during the past ten years in the science and technology of weather modification. Large numbers of programmes in fog dispersion, rain, snow enhancement and hail suppression are in operation. Several research experimental programmes are supported in some countries and include randomized statistical evaluations. Improved observational facilities, computer capabilities, numerical models, and understanding now permit more detailed examination of clouds and precipitation processes than ever before, and significant advances are consequently possible. New technologies and methods are starting to be applied and will help to lead to further understanding and development in this field.

In light of this review on the status of weather modification, the following recommendations are made to interested Members of WMO:

(a) *Cloud, fog and precipitation climatologies should be established in all countries as vital information for weather modification and water resource studies and operations;*

(b) *Operational cloud-seeding projects should be strengthened by allowing an independent evaluation of the results of seeding. This should include measurements of physical response variables and a randomized statistical component;*

(c) *Education and training in cloud physics, cloud chemistry, and other associated sciences should be an essential component of weather modification projects. Where the necessary capacity does not exist advantage should be taken of facilities in other Members;*

(d) *It is essential that basic measurements to support and evaluate the seeding material and seeding hypothesis proposed for any weather modification experiments be conducted before and during the project;*

(e) *Weather modification programmes are encouraged to utilize new observational tools and numerical modelling capabilities in the design, guidance and evaluations of field projects. While some Members may not have access or resources to implement these technologies, collaboration between member states (e.g. multinational field programmes, independent expert evaluations, education, etc.) are encouraged that could provide the necessary resources for implementing these technologies*."

These guidelines provide a good roadmap to design and develop a cloud seeding program. During the 2007-2008 program in Southeast Queensland two seeding techniques were utilized to enhance rainfall. The primary technique used was seeding with hygroscopic flares to attempt to enhance the onset of the coalescence process and the second was with silver iodide flares to attempt to enhance rainfall by both the static and dynamic seeding methods. The latter technique was not utilized often, given the lack of conditions suitable for this technique. These methods were discussed in sections 12.2.7-12.2.8 and in the proceeding sections we will discuss the conceptual models in more detail and provide a preliminary evaluation and assessment of the use of these techniques in the Southeast Queensland region.